Abstract

We present the results of a systematic study of the Large Magellanic Cloud (LMC) with the X-ray satellite, Advanced Satellite for Cosmology and Astrophysics (ASCA). We analyzed all the available data in the vicinity of the LMC, obtained during the ASCA mission, the period from 1993 until 2000, including the data from the ASCA LMC survey and all archival pointing observations. The X-ray mosaic images in the soft (0.7−2.0 keV) as well as hard (2.0−7.0 keV) bands were constructed. In particular, the hard band image of the LMC is first revealed, thanks to the wide energy band of ASCA. We extracted 71 sources from these images with a criterion of S/N $>$ 5 and made systematic spectral analyses of them. From the information of spatial correlations as well as the spectra, the comparison with ROSAT PSPC and HRI source catalogues (Haberl and Pietsch 1999; Sasaki et al. 2000) are carried out. As a results, the first ASCA LMC source catalogue is revealed.

We made intensive spectral analyses for 9 SNRs, for which no detailed spectral analyses have been carried out (DEM L316A, DEM L316B, 0532−71.0, 0534−69.9, 0548−70.4, 0520−69.4, DEM L214, 0532−67.5, and N86; sample-1), applying the non-equilibrium ionization (NEI) model coded by Masai (1994). The NEI model well describes the ASCA spectra of sample-1 SNRs, allowing us to derive the plasma parameters within them, such as ages, and densities.

Among the sample-1 SNRs is included a pair of SNRs of considerable interest, a possible site for the collision between two remnants. The ASCA spectra of these two remnants exhibit totally different characteristics; one shows clear iron overabundance, while the other does not. These facts lead us to the conclusion that they were not due to a single supernova explosion into a pre-existing bubbles made by a stellar wind or SNe. We propose one of these have resulted from Type Ia explosion. We also examined the relation between the Balmer-dominated SNRs in the LMC and those which exhibit iron over abundances in the X-ray spectra. Based on the spatial correlations with OB associations or H II regions and those remnants, we found that it is highly possible that characteristic to show the dominant Balmer-lines in optical spectra does not always become the evidence for the Type Ia SNRs.

Our sample-1 SNRs together with 10 SNRs in Hughes et al. (1998) cover all the remnants for which the ASCA spectra with enough statistics are available. They exhibit various ages of $\sim 10^3$–10^5 yr. We found that the densities within them decrease as their ages increase, surely tracing the course of the evolution of the plasma within SNRs. The density of the oldest SNR in our sample should restrict the upper limit of the ambient plasma density, namely that of interstellar matter (ISM).

From all the available pointing observations, we accumulated a spectrum of diffuse X-ray emission which is widely spreading in the LMC body, whose origin is still uncertain, but probably arising from hot ISM in the LMC. The spectral analysis of the diffuse X-ray emission with such a good energy resolution and enough statistics is first attempted. We find that the

spectrum cannot be reproduced with a non-thermal model, instead, is well described with a NEI model ($kT_{\rm e} \sim 0.9$ keV and $n_{\rm e}t_{\rm i} \sim 10^{10.5}$ s cm^{-3}), showing that it is surely thermal in origin, which is a strong support for the diffuse X-ray emission to be arising from the hot ISM. We then attempted to interpret the diffuse X-ray emission in terms of sum of SNRs based on the derived plasma parameters. The diffuse X-ray emission cannot be described as an ensemble of either young, middle-aged, nor old SNRs; the expected temperature in young as well as old remnants differ from those of the diffuse X-ray emission. The potential candidates, middle-aged SNRs, though they have plasma parameters well resemble to those of the diffuse X-ray emission, also fail to be the major contributor of the diffuse X-ray emission, as long as we assumed that they follow the simple Sedov solution. The negative results to explain the diffuse X-ray emission with an ensemble of 'usual' SNRs are not surprising because most of them are considered to interact with other physical systems in the course of their evolution, thus the Sedov solution is not applicable. We suppose that most of the SNRs in the LMC do not end their lives normally to be silently merged into the cold or warm ISM, instead, they have merged into the hot tenuous medium in the course of their evolution, realized within the bubbles, giant shells, or super giant shells which themselves are formed by the repetitious merging of SNRs, and do not show the distinct remnants at all, thus have become a part of truly diffuse hot plasma. Indeed, only $\sim 10\%$ of the expected number of remnants to exist from the energy sustainment of the diffuse X-ray emission at this moment, are resolved in the LMC. The rest of them should be surely 'missing' within the truly diffuse hot plasma.

Contents

1 Introduction **15**

2 Review I
The Large Magellanic Cloud **17**

2.1 The Magellanic system 17

2.2 Previous X-ray Observations of the Large Magellanic Cloud 18

3 Review II
Supernovae and Supernova Remnants **25**

3.1 Supernova Explosion (SNe) 25

3.1.1 Classification 25

3.2 Progenitors of Supernovae 26

3.3 Nucleosynthesis in Supernovae 30

3.4 Shock Wave 32

3.5 Evolution of Supernova Remnants 35

3.5.1 Free Expansion Phase 35

3.5.2 Adiabatic Phase 36

3.5.3 Radiative Cooling Phase 36

3.6 SNRs in the LMC – Previous X-ray Observations 37

3.6.1 Imaging Analysis 38

3.6.2 Spectral Analysis 42

3.7 Diffuse X-ray emission 46

3.7.1 Bubbles, Giant Shells, and Super Giant Shells 48

4 Instrument **51**

4.1 ASCA 51

4.1.1 X-ray telescope (XRT) 51

4.1.2 Gas Imaging Spectrometer (GIS) 57

4.1.3 Solid-state Imaging Spectrometer (SIS) 60

4.2 ROSAT 66

5 Observations and Data Reduction **69**

5.1 Pointing observations and the LMC survey project 69

5.2 Data screening (GIS) 69

6 Analysis and Results I – X-ray Images and the first ASCA Catalogue **75**

6.1 X-ray Image & Source Extraction 75

6.1.1 X-ray Image 75

6.1.2 Source Extraction 77

6.1.3 The 1st catalogue of X-ray sources in the LMC 80

7 Analysis and Results II – Comments on specific SNRs **87**

7.1 Introduction of individual SNRs 87

7.1.1 DEM L316A and DEM L316B 87

7.1.2 SNR 0532−71.0 88

7.1.3 SNR 0548−70.4 88

7.1.4 SNR 0534−69.9 88

7.1.5 DEM L241 (SNR 0536−676) 89

7.1.6 SNR 0520−69.4 89

7.1.7 SNR 0532−67.5 . . . 89
7.1.8 N86 (SNR 0455−68.7) . . . 89
7.2 Observations & Data screening . . . 90
7.3 Analysis & Results . . . 91
7.3.1 DEM L316A and DEM L316B (0547−69.7A and 0547−69.7B) . . . 92
7.3.2 SNR 0532−71.0 . . . 97
7.3.3 SNR 0548−70.4 . . . 97
7.3.4 SNR 0534−69.9 . . . 99
7.3.5 DEM L241 (SNR 0536−67.6) . . . 103
7.3.6 SNR 0520−69.4 . . . 106
7.3.7 SNR 0532−67.5 . . . 106
7.3.8 N86 (SNR 0455−68.7) . . . 108
7.4 Nature of Individual SNRs . . . 111
7.4.1 DEM L316 A and DEM L316 B — Twin SNRs? . . . 111
7.4.2 SNR 0532−71.0 . . . 113
7.4.3 SNR 0548−70.4 . . . 114
7.4.4 SNR 0534−69.9 . . . 116
7.4.5 DEM L241 (SNR 0536−67.6) . . . 116
7.4.6 Dark SNRs — 0520−69.4, 0532−67.5, and N86 . . . 118
7.4.7 Summary . . . 119

8 Analysis and Results III – Diffuse X-ray Emission 123

8.1 Datasets used in diffuse X-ray emission analyses . . . 124
8.2 Results for spectral analyses . . . 128
8.2.1 Non-thermal model fit . . . 128
8.2.2 One-temperature CIE model fit . . . 129
8.2.3 One-temperature NEI model fit . . . 131

8.3 Systematic errors of the diffuse X-ray spectrum 131
8.3.1 Uncertainty of the ARF 131
8.3.2 Stray light from LMC X-1 132

9 Discussion **137**
9.1 Plasma parameters of the SNRs 137
9.2 Plasma parameters of the diffuse X-ray emission 139
9.3 Origin of the diffuse X-ray emission 143

10 Conclusion **151**

A Spectra and Images of Individual SNRs in the LMC **153**

B Pointing list of the data used for the CXB and NXB background **163**

C The diffuse X-ray and background spectra **167**

D 2-false-color X-ray image of the LMC **173**

acknowledgments **185**

List of Figures

2.1 Optical images of the Magellanic Clouds 20

2.2 H I distribution in the Magellanic System 21

2.3 The mosaic image taken with the ROSAT PSPC (Snowden & Petre 1994). . 23

3.1 Characteristic spectra of supernovae near maximum light. 27

3.2 The schematic classification scheme of supernovae based on early and late time spectra features. 28

3.3 The predicted relative abundances of synthesized heavy elements (Tsujimoto et al. 1995) 32

3.4 A schematic view around the shock front. 33

3.5 Cartoon showing the schematic stages of development of SNRs in a cloudy medium. 39

3.6 X-ray sizes of the LMC SNRs. 41

3.7 Mean metalicity vs. radius by Hughes et al (1998) 45

3.8 Average chemical abundances of the LMC by Hughes et al. (1998) 45

3.9 Surface brightness of diffuse X-ray emission and neutral hydrogen from Wang et al. (1991). 47

3.10 The super giant shells in the LMC from Meaburn et al. (1987). 49

4.1 Configuration of XRTs and the detectors aboard ASCA. 52

4.2 Walter type I optics. 53

4.3 Effective area of XRT. 54

4.4 Energy and position dependence of ASCA XRT effective area. 54

4.5 Point spread function of the ASCA XRT for four different off-axial angles. Approximate field of view is shown for GIS (circle) and SIS (square). 55

4.6 Four examples of XRT light paths: (a) normal path, (b) reflection only by primary mirrors, (c) reflection only by secondary mirrors, (d) multiple reflections by front and back surfaces of mirrors. 56

4.7 Observed stray light structures due to Crab taken with GIS. 57

4.8 The cross section of GIS-S. 58

4.9 Schematic diagram of the principle of the GIS detector. 59

4.10 GIS spectra of day earth, blank sky and night earth. 61

4.11 The effective area of the combination of XRT and GIS. 61

4.12 The cross section of the SIS camera. 62

4.13 The chip configuration of the SIS. 63

4.14 Grade definition and the rule to add pulse heights. The events out of these criteria are defined as Grade 7. 64

4.15 The quantum efficiency of SIS detector. 65

4.16 The effective area of a single SIS and XRT combined for three off-axis angles (0, 5, 10′) 65

4.17 Schematic view of the ROSAT spacecraft. 67

5.1 The GIS field of views of all the ASCA pointings in the vicinity of the LMC. 74

6.1 ASCA X-ray mosaic image of the LMC (0.7–2.0 keV band).. 78

6.2 ASCA X-ray mosaic image of the LMC (2.0–7.0 keV band). 79

6.3 Hardness ratio vs. Count rate for the known LMC and SMC sources. 80

7.1 DEM L316 image 93

7.2 The SIS and PSPC image of DEM L316. 94

7.3 The SIS X-ray spectra of shell A (a) and shell B (b) 95

7.4 Confidence contours between fitted electron temperature ($kT_{\rm e}$) and ionization timescale ($n_{\rm e}t_{\rm i}$). 95

7.5 0532−71.0 image. 98

7.6 The SIS and GIS X-ray spectra of 0532−71.0. 99
7.7 0548−70.4 image. 100
7.8 The SIS and GIS X-ray spectra of 0548−70.4. 101
7.9 0534−69.9 image. 102
7.10 The SIS and GIS X-ray spectra of 0534−69.9. 103
7.11 DEM L241 image taken with ASCA. 104
7.12 DEM L241 X-ray spectra, best-fit models and residuals. 105
7.13 0520−69.4 image 106
7.14 The SIS and GIS X-ray spectra of 0520−69.4. 107
7.15 0532−67.5 image. 108
7.16 The SIS and GIS X-ray spectra of 0532−67.5. 109
7.17 N86 image. 110
7.18 The GIS X-ray spectra of N86. 111
7.19 S II and Einstein HRI X-ray DEM241 images from Mathewson et al.(1985) . 118
7.20 The power spectrum of DEM L241. 119
7.21 The distribution of SNRs in the LMC (crosses) overlaid on the ROSAT X-ray map of LMC. 120

8.1 ASCA GIS pointing positions for the data used in the diffuse X-ray emission. 125
8.2 Change of GIS NXB since the launch. 126
8.3 The total diffuse X-ray spectrum and corresponding background spectrum. . 128
8.4 The background subtracted diffuse X-ray spectrum and folded power-law model.129
8.5 Same as Fig. 8.4, but for the CIE model fit. 130
8.6 The Spectral fitting results of diffuse X-ray emission. 132
8.7 The confidence contours between ionization age and temperature for left and column density and temperature right panels, respectively. 133
8.8 Counting rates of the Crab stray observations and the ray-tracing simulations in 0.7–10 keV energy band. 134

8.9 GIS field of views of observations for diffuse X-ray emission and the position of LMC X-1. 135

9.1 Radii vs the Sedov ages for the SNRs in the LMC. 138

9.2 Density and luminosity profile within the SNR, which follows the Sedov model. 140

9.3 Radii vs densities for the SNRs in the LMC. 140

9.4 A schematic view to show a relation between an observer and a differential volume of emitting region. 142

9.5 A schematic view to show the distribution of diffuse X-ray emission in the LMC. 142

9.6 Temperature and density distribution within SNRs in radiative cooling phase. 144

9.7 Constraints on the SNR interpretation of diffuse X-ray emission I. 148

9.8 Constraints on the SNR interpretation of diffuse X-ray emission II. 149

A.1 0509−67.5 154

A.2 N103B 154

A.3 0519−69.0 155

A.4 DEM71 155

A.5 N63A 156

A.6 N49 156

A.7 N23 157

A.8 DEML316A 157

A.9 N132D 158

A.10 0548−70.4 158

A.11 0453−68.5 159

A.12 0534−69.9 159

A.13 0520−69.4 160

A.14 N49B 160

A.15 DEML316B 161

A.16 0532−71.0 161

A.17 DEM241 & 0532−67.5 162

D.1 2-false-color X-ray image of the LMC. 174

List of Tables

2.1 Fundamental data for the LMC and the SMC. 19

3.1 Supernovae and Supernova Remnants (Lozinskaya 1992) 31

3.2 Classification of LMC SNRs by Williams et al. (1999) 40

3.3 Best-fit Parameters for the Sedov Models of LMC "Young" Remnants 43

3.4 Best-fit Parameters for the Sedov Models of LMC "Evolved" Remnants . . . 44

5.1 Observational log 71

5.1 Observational log (Continued from the previous page.) 72

5.2 GIS bit assignment. 72

5.3 The selection criteria for GIS data. 73

6.1 The 1st ASCA catalogue of X-ray sources in the LMC. 82

6.1 The 1st ASCA catalogue of X-ray sources in the LMC. (Continued from the previous page.) 83

6.2 The 1st ASCA catalogue of X-ray sources in the LMC. 84

6.2 The 1st ASCA catalogue of X-ray sources in the LMC. (Continued from the previous page.) 85

7.1 LMC SNRs Observational log for SISs 91

7.2 LMC SNRs Observational log – net exposure 92

7.3 Spectral fitting results of DEM L316 shell A and shell B. 96

7.4 Spectral fitting results of 0532−71.0. 98

7.5 Spectral fitting results of 0548−70.4. 100
7.6 Spectral fitting results of 0534−69.9. 102
7.7 Spectral fitting results of DEM L241. 105
7.8 Spectral fitting results of 0520−69.4. 107
7.9 Spectral fitting results of 0532−67.5. 109
7.10 Spectral fitting results of N86. 110
7.11 The SNRs in the LMC whose progenitors are, or the candidates of, Type Ia. 116
7.12 Summary of plasma paramters of the sample-1 SNRs. 121

8.1 Best-fit parameters of diffuse X-ray emission for CIE model. 130
8.2 Best-fit parameters of diffuse X-ray emission for Masai model. 133

9.1 A summary of the plasma parameters. 143

B.1 GIS blank-sky data 163
B.1 Observational log (Continued from the previous page.) 164
B.1 Observational log (Continued from the previous page.) 165

Chapter 1

Introduction

Hot ionized gas is an essential component of the interstellar matter (ISM). Supernovae (SNe) and their remnants (SNRs) as well as the stellar wind of the massive stars are the main cite for the formation of hot gas whose temperature is several times 10^6 K up to over 10^7 K, through their energetic interactions with ISM, such as ionizing, accelerating, and heating up.

SN explosions spew out the heavy elements into the interstellar space, thus the X-ray spectra of young SNRs strongly reflect the characteristics of the ejected matter. As the SNRs age, the amount of ambient matter engulfed by their shock fronts increase. Therefore, the X-ray spectra of middle-aged SNRs gradually change to reflect the characteristics of the ambient ISM. More older SNRs are then considered to gradually lose their identities by merging into the ambient ISM, thus the ISM are considered to be a wreck of SNRs.

The chemical enrichment as well as the energy input into the hot gas of the galaxy is considered to be going in this way. Therefore, we can trace the course of the formation of hot ISM in the galaxy by systematically investigating SNRs of various ages as well as the hot ISM in the galaxy. However, it is difficult to pursue the systematic study of SNRs and hot ISM for the case of our Galaxy, not only because we see the Galaxy from the edge-on view, but also because the strong obscuration along the galactic plane. The ideal site for pursuit this investigation is presented in the Large Magellanic Cloud (LMC), the neighboring galaxy of our own; its close proximity, nearly face-on view, small extinction toward it, and existences of plenty of hot ISM and SNRs.

One of our objectives in this thesis is to complete the systematic spectral study of the total LMC SNR sample with sufficient brightness for spectroscopy, part of which have already presented in Hayashi (1997) and Hughes et al. (1998). The aim of this study is to trace the course of the evolution of plasma within SNRs. The spectroscopy of these SNRs is meaningful not only because we can pursue the above objective, but also because we can reveal the individual natures of them, which are of great interest themselves. The other aim

is to investigate the spectrum of hot ISM in the LMC to examine whether it can be well explained as a wreck of SNRs, if not, to know what the reasons are.

The brief review of the LMC is given in chapter 2 and those of SNe and SNRs as well as the previous X-ray observations of SNRs in the LMC are presented in chapter 3. Chapter 4 is devoted for the overview of the ASCA satellite. Chapter 5 provides descriptions of observations and data reductions. The first ASCA X-ray source catalogue of the LMC as well as the images of the LMC in the soft (0.7–2.0 keV) and hard (2.0–7.0 keV) bands are presented in chapter 6. Chapter 7 contributes to the results and discussion of the individual natures of the 9 LMC SNRs; DEM L316A, DEM L316B, 0532−71.0, 0534−69.9, 0548−70.4, 0520−69.4, DEM L241, 0532−67.5, and N86. Among them are included the twin SNRs (DEM L316A and DEM L316B), which are of the considerable interest and provides the possible site for the collision between two SNRs. The analysis of the diffuse X-ray emission is described in chapter 8. In chapter 9, the evolution of the plasma within SNRs toward the hot ISM is discussed based on the results described in chapter 7 and 8. We finally make a concluding remarks in chapter 10.

Chapter 2

Review I
The Large Magellanic Cloud

The southern celestial sphere is much more spectacular than the northern hemisphere. The Milky Way is very marked in the south and it is flanked by two bright, diffuse visible clouds. These clouds took their name from their being mentioned in the accounts of Magellan's voyage around the world, the Large and Small Magellanic Clouds (hereafter, LMC and SMC). Here, we present a review on these clouds, the LMC and SMC as a whole, and we also present the review on previous X-ray observations particularly of the LMC.

2.1 The Magellanic system

Fig. 2.1 shows the visible image of the LMC and SMC taken at the Anglo-Australian Observatory. Both of them have bars seen in its optical images. The sizes of them are $\sim 3^\circ \times 1^\circ$ for the LMC and $\sim 2.5^\circ \times 1^\circ$ for the SMC.

The LMC and SMC are the satellite galaxies of our own. They are connected by the "Bridge" of gas. It would be more precise to say that the Clouds are drowned in an immense gas cloud. This cloud and its continuation towards our Galaxy from what is termed "the Magellanic Stream" (see Fig. 2.2) was discovered about 25 years ago (Mathewson et al. 1974). Two Clouds together with the stream are, as a whole, called the Magellanic System.

The past two decades have seen the number of viable mechanisms for the formation of this stream reduced to two – ram pressure stripping of material from the Magellanic System during its passage through the Galactic halo or extended ionized disk (Mathewson et al. 1974; Sofue 1994; Moore and Davis 1994), and tidal interaction of the Magellanic Clouds with the Milky Way (Murai and Fujimoto 1980; Gardiner and Noguchi 1996; Gardiner et al.

1994). Though the tidal models have been successfully explaining many characteristics of the Stream, they have two weak points, one is the absence of stars in the Stream, and the other is the lack of evidence for a leading arm (Murai and Fujimoto 1980; Gardiner and Noguchi 1996; Gardiner et al. 1994). Putman et al. (1998) recently discovered another stream, called " the Leading Arm" (see Fig. 2.2). The observed velocity of the Leading Arm, coupled with its velocity-space continuity with the Magellanic System clearly eliminates the possibility that the material is associated with the Milky Way disk. This continuous Leading Arm, extending $\gtrsim 25^\circ$ from the Magellanic System, is a natural prediction of tidal models (Putman et al. 1998). The argument made by Putman et al. (1998) against the absence of stars in the Stream is that the initial gas distribution is significantly more extended than the stellar component, as was confirmed in interferometer studies of spiral galaxies (Broeils and van Woerden 1994) and as is seen in other interacting systems (Yun et al. 1994).

From the existence of the common H I envelope, Murai and Fujimoto (1980) examined the possibility that a single Magellanic Cloud was split into two independent objects, the LMC and the SMC, by tidal disruption at a close passage to our Galaxy, but they found no orbits coalescing into a single one towards the past. The Magellanic Clouds may then be considered as having always been separated objects for a long time ($\sim$ 10 Gyr). They also mentioned that the two Clouds experienced a close encounter $\sim 2\times10^8$ yr ago, which synchronizes with the ages of stars in the Bridge, and that the Magellanic Stream was torn off from the SMC by tidal force. The recent observations made two kinds of constrains on this subject. Hipparcos satellite made a direct measurement of the proper motion of the Clouds (Kroupa and Bastian 1997) and found that those in equatorial longitude and latitude are $(1.94 \pm 0.29,\ -0.14 \pm 0.36)$ mas yr^{-1} and $(1.23 \pm 0.84,\ -1.21 \pm 0.75)$ mas yr^{-1}, for the LMC and the SMC, respectively. Girardi et al. (1995) studied the age distribution of star clusters in the LMC and mentioned that the LMC experienced enhanced cluster formation twice, $\sim 2\times10^9$ yr and $\sim 1\times10^8$ ago. Two close encounters may have triggered turbulence of interstellar matter, and then, such bursts of cluster formation might have resulted.

The fundamental data of the LMC and the SMC are shown in Table 2.1.

2.2 Previous X-ray Observations of the Large Magellanic Cloud

X-ray emission from the Magellanic Clouds was first detected in a five-minute rocket flight from Johnston Atoll in the South Pacific in 1968. The LMC shows slightly softer spectrum than that of diffuse X-ray background with the flux of $\sim 1.5 \times 10^{-9}$ ergs cm^{-2} s^{-1} (Mark et al. 1969). In 1971, Leong et al. (1971) resolved the LMC emission into four variable sources, LMC X-1, X-2, X-3, and X-4, with the Uhuru satellite. The successive satellites confirmed these hard X-ray sources in the LMC, however, it was not until 1975 that the

	LMC	SMC
Type	SB(s)m	SB(s)mp
Galactic coord. l,b	$280°.5, -32°.9$	$302°.8, -44°.3$
Distance moduli	18.5 ± 0.2 mag	18.9 ± 0.2 mag
Tilt	33°–45°	90°
Masses		
Total masses	2×10^{10} (6×10^9?)	2×10^9 $M_\odot$
H I mass	$< 8\%$ of total mass	$\sim 30\%$
H I (21cm)	7×10^8	6.5×10^8 $M_\odot$
H_2 (CO line)	1.4×10^8	6.5×10^8 $M_\odot$
Warm dust (IRAS)	$4–50 \times 10^3$	$8–10 \times 10^4$ $M_\odot$
Cold dust (mm)	$8–90 \times 10^5$	$9–100 \times 10^5$ $M_\odot$
Structure		
Disk:	Has a major disk made up of intermediate-age and young population (stars and gas)	Layers of H I are seen in depth; if there is a disk it will have to be in the line of sight.
H II regions	Large number	Few
Diffuse Hα emission	Yes, extended	Yes, extended
Molecular clouds	Several; strongest south of 30 Doradus and SW parts of the Bar	Few, mainly in NE
Bar:	Red stars ;superposed H II and starforming regions	Predominantly blue stars with a scatter of red stars
Halo : Stellar	Probably	Probably
: Plasma	Diffuse X-ray emission, gets softer away from the center. Optically thin thermal plasma with $\sim 2 \times 10^6$ K in western part;$\sim 10^7$ K near the active star forming region 30 Doradus	Diffuse X-ray emission optically thin thermal plasma of $\sim 10^6$ K halo plasma?

Table 2.1: Fundamental data for the LMC and the SMC. The galaxy types are from De Vaucouleurs and Freeman (1973).

The mass of the old, metal poor ([Fe/H] < -1.4) population in the LMC is $\times 6\%$ of its total mass (Frogel 1984); the mass of the old slightly more metal rich ([Fe/H] $\sim -1.0 \pm 0.5$) population, represented by the old long-period variables, is $\sim 2\%$ of the total mass (Hughes et al. 1991).

The average Magellanic normal dust is hotter than the galactic due to the high interstellar radiation field (Lequeux 1989). Small grains may have been destroyed by the abundant UV radiation.

The central region of the SMC are considerably bluer than the outer parts. This effect is less obvious in the LMC.

The high percentages of gas still unused in the Clouds show that they are far behind the Galaxy in evolutionary status. This is also evident in their lower metal content.

The SMC is much less evolved than the LMC.

No cold molecular clouds exist. SMC lacks H I and H_2 clouds heated by the far UV radiation of hot stars.

Figure 2.1: Optical images of the LMC (left) and the SMC (right). Optical Wing is protruding out from the main body of the SMC to the east (left side in the figure). (©Anglo-Australian Observatory)

soft X-ray (0.5–2 keV) emission was detected (Rappaport et al. 1975). Later, McKee et al. (1980) resolved a number of soft X-ray sources, including brightest supernova remnant (SNR) in the X-ray band in the LMC, N132D.

Thanks to the launch of the Einstein satellite and ardent pointing observations with IPC detector onboard, the X-ray population increased up to 105 (Long et al. 1981; Wang et al. 1991). About 10 % of sources were identified with galactic stars and three with background Active Galactic Nuclei (AGN). 28 SNRs and 9 X-ray binaries in the LMC have been confirmed through optical and radio observations. Nearly 20 X-ray sources are associated with OB associations and H II regions. 35 unidentified sources, which are probably background sources, remain. In addition, large scale diffuse X-ray emission was revealed, which was probably arising from hot gas with temperature of several 10^6 K.

During the ROSAT all-sky survey, the LMC was observed with high sensitivity by the Position Sensitive Proportional Counter (PSPC). Piestch and Kahabka (1993) analyzed a $13^\circ \times 13^\circ$ area centered on the LMC and found more than 500 X-ray sources. Using the Parkes 64 m radio telescope at different frequencies, Filipovic et al. (1995) carried out a large-scale radio surveys of the LMC. A comparison of the radio source catalogue with the ROSAT survey catalogue of Piestch and Kahabka (1993) yielded 71 sources within a correlation radius of $2.5'$ (Filipovic et al. 1996).

Another scientific program to cover the LMC field with ROSAT PSPC was carried out and provided us a beautiful mosaic image of the LMC (Snowden and Petre 1994; Fig 2.3). Beside bright point-like sources, one can easily notice the existence of plenty of diffuse X-ray emission in the LMC body, the origin of which is still uncertain.

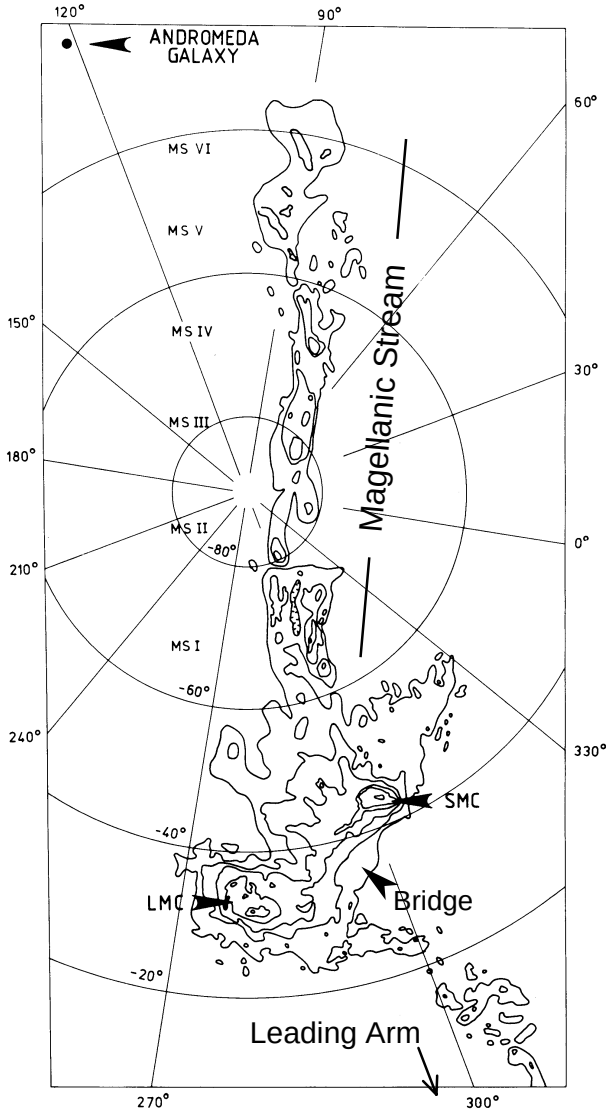

Figure 2.2: Global distribution of H I in the Magellanic System, taken from Mathewson (1985). Coordinates are in Galactic. The Leading Arm was discovered later on Putman et al. (1998).

Haberl and Pietsch (1999) analyzed more than 200 ROSAT PSPC observations in a 10 by 10 degree field centered on the LMC and derived a catalogue of X-ray sources. The number of point-like or few extended X-ray sources was up to 758. Based on the positional coincidence, 144 X-ray sources were identified using the SINBAD database. These identified X-ray sources include 46 SNRs and SNR candidates, 17 X-ray binaries, 9 Super Soft X-ray Sources (SSS), 56 foreground stars, and 15 background or extragalactic objects.

Using the 543 pointed observations of ROSAT High Resolution Imager (HRI) in the vicinity of the LMC, Sasaki et al. (2000) derived the catalogue, which contains 397 X-ray sources. Thanks to the high spatial resolution of HRI, the positions and the spatial extents of the sources were well determined. With the derived information of the sources and the hardness ratio derived in Haberl and Pietsch (1999), they identified 94 HRI sources with well known objects and improved the accuracy of their coordinates. They also suggested 5 new SNR candidates in the crowded region with many sources and diffuse X-ray emission, between 30 Dor and LMC X-1.

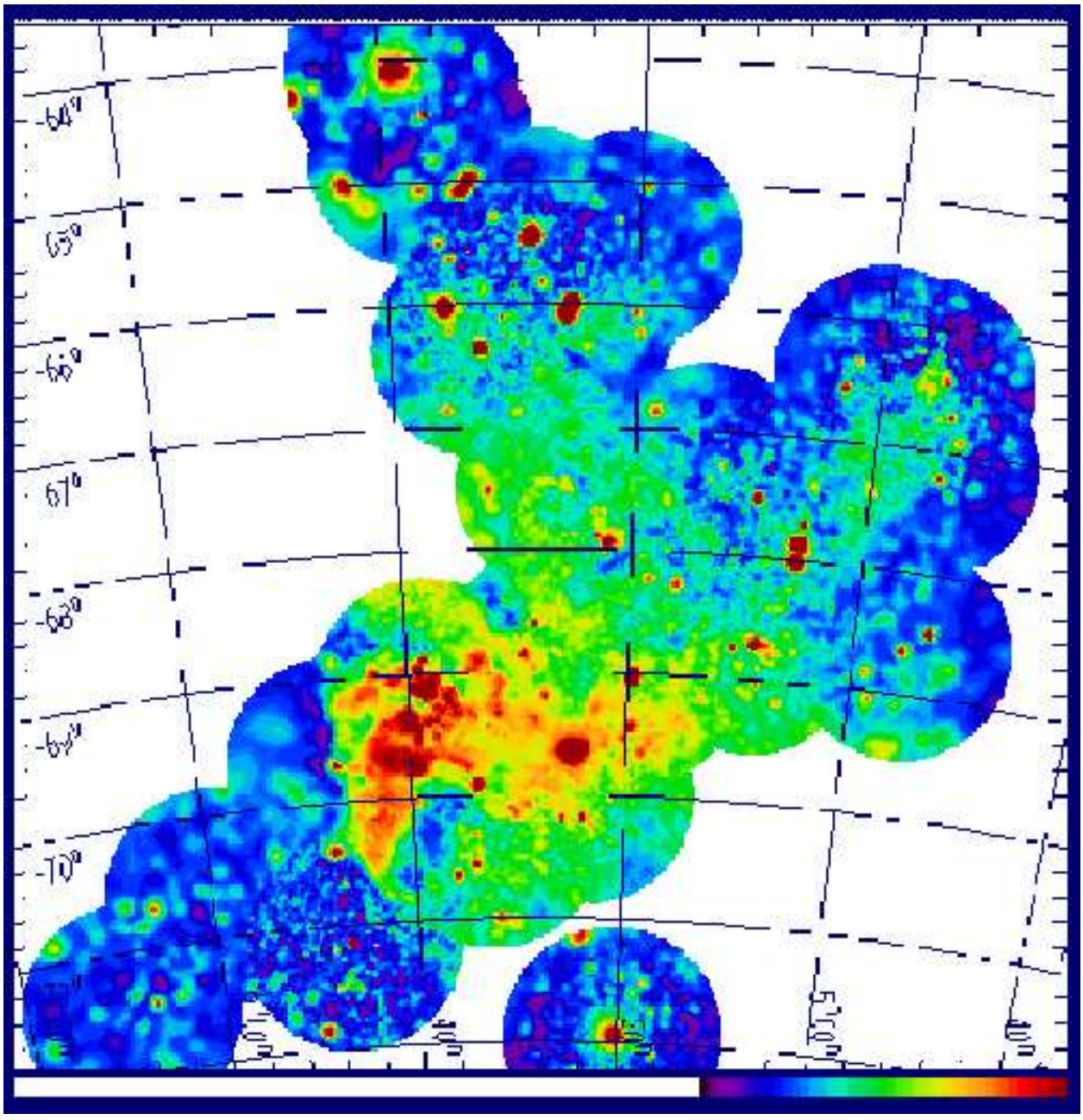

Figure 2.3: False-color logarithmic-scaled image of the LMC from the mosaic of ROSAT PSPC pointed observations, provided by Snowden & Petre 1994. The data are from 0.5–2.0 keV band. The data have been smoothed using adaptive-filter algorithm.

Chapter 3

Review II
Supernovae and Supernova Remnants

One of the most prominent differences between the LMC and the SMC, especially from view of X-ray wavelength might be, that the LMC has many bright SNRs in X-ray wavelength, while the SMC does only a few. Here in this section, we first make a general review of the supernovae (SNe) and their remnants. Later we review on the SNRs in the LMC mainly based on the previous X-ray observations. We further review on the hot interstellar matter (ISM) in the LMC which is commonly thought as a wreak of SNRs.

3.1 Supernova Explosion (SNe)

When a normal star comes to the end of its life, the explosive disruption takes place and it disappears from a visible sky. Baade (1934) who first mentioned a new word "supernova" to describe this extraordinary bright stellar outburst began a systematic search for these phenomena. In the ancient records from Europe, China, Japan, and Korea, only less than 10 such events took place in the Milky Way over the last two millenia. It tells us that SNe are relatively rare events (for a typical galaxy it is known that it occurs only once in every 25–100 yr).

3.1.1 Classification

SNe are classified based on their optical spectra into two families, Type I and Type II. The basis for the classification is the presence (Type II) or absence (Type I) of H lines in the spectrum near the maximum light. This is a fundamental criterion, not only because one or two high-quality spectra suffice for the classification, but because it is of clear-cut physical

importance as well.

Type I SNe have two subclasses, one and the other are Type Ia and Type Ib. This subclassification was succeeded only in the last 10 years (Elias et al. 1985; Branch 1986; Harkness et al. 1987; Porter and Filippenko 1987). Classical Type Ia events show a strong [Si II] absorption feature at 6150 Å, while Type Ib events do not. Another difference is a presence (Type Ib) or absence (Type Ia) of strong lines of He I (5876 Å) (Wheeler and Harkness 1987). Type Ib SNe usually take place in spiral galaxies and regions of star formation, typically showing strong non-thermal radio emission near optical maximum and somewhat weaker and redder than Type Ia events at maximum light. 25 days or more after the explosion, the most clear difference between Type Ia and Type Ib events shows up, the line of [Fe II] and [Fe III] dominate the spectra of Type Ia events, while lines of [O I] dominate the spectra of Type Ib events (Gaskell et al. 1986). Recently, a few Type I SNe with neither the 6150 Å[Si II] line nor detectable helium lines have been reported and have been tentatively classified as SN Ic.

Type II SNe can further classified into two categories, based on the shape of the light curve. Those with nearly linear decline in magnitude with time from peak are termed Type II linears, and those with a pronounced plateau have been termed Type II plateaus (Barbon et al. 1973). However, the recently exploded SN 1987A event falls neither of case. The light curve of SN 1987A was very different due to the blue compact nature of the progenitor, although it showed some similarity to Type II plateau on the exponential tail (Dopita 1988; Arnett et al. 1989). In addition, SN 1987A showed strong P-Cygni features of the Balmer lines from the first day, while traditional Type II plateau or linear events have shown a nearly pure continuum near maximum light, a week or two after the explosion.

3.2 Progenitors of Supernovae

A supernova releases spectacular energy, such as typical mechanical and radiative energy of $\gtrsim 10^{51}$ ergs. On a stellar scale, the energetic of the event might be associated with the gravitational collapse of the core. Think that a normal star is compressed within a size of a neutron star, the amount of the energy released is $\sim 10^{53}$ ergs, roughly equivalent to the Sun's energy output summed over 10 billion years then multiplied by 100.

We can estimate the masses of SN progenitors taking into account of the distribution of them among galaxies of different morphological types, and of the distribution within the individual galaxies. We also can estimate the lifetime of the progenitors, and thus the initial masses of them, from the fact that the Type II and Type Ib events cluster within spiral arms, while Type Ia events have no concentration towards the arms.

Type Ia SNe are often observed in the outskirts of the elliptical galaxies (Maza and van den Bergh 1976). This suggests us that the progenitors of them are old halo stars (10^{10} yr,

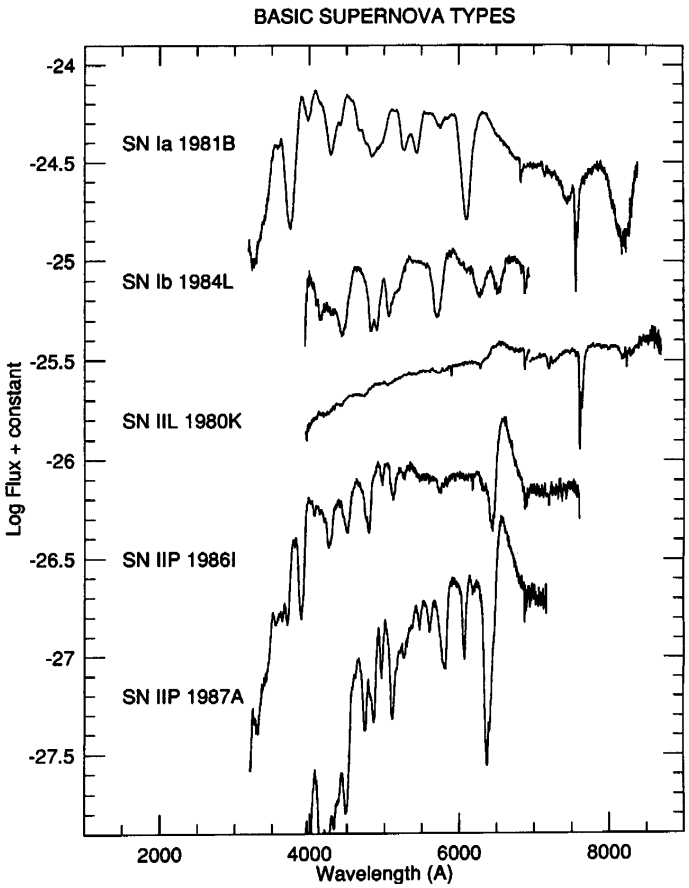

Figure 3.1: Characteristic spectra near maximum light are shown for the Type Ia SN and Type II SN. The SN Ia spectrum shown strong characteristic absorption line of ionized Si at 6150 Å, that is not seen in the spectra of SN Ib. The SN Ib has strong absorption lines of neutral helium at about 5700 Å[From Wheeler and Harkness 1990].

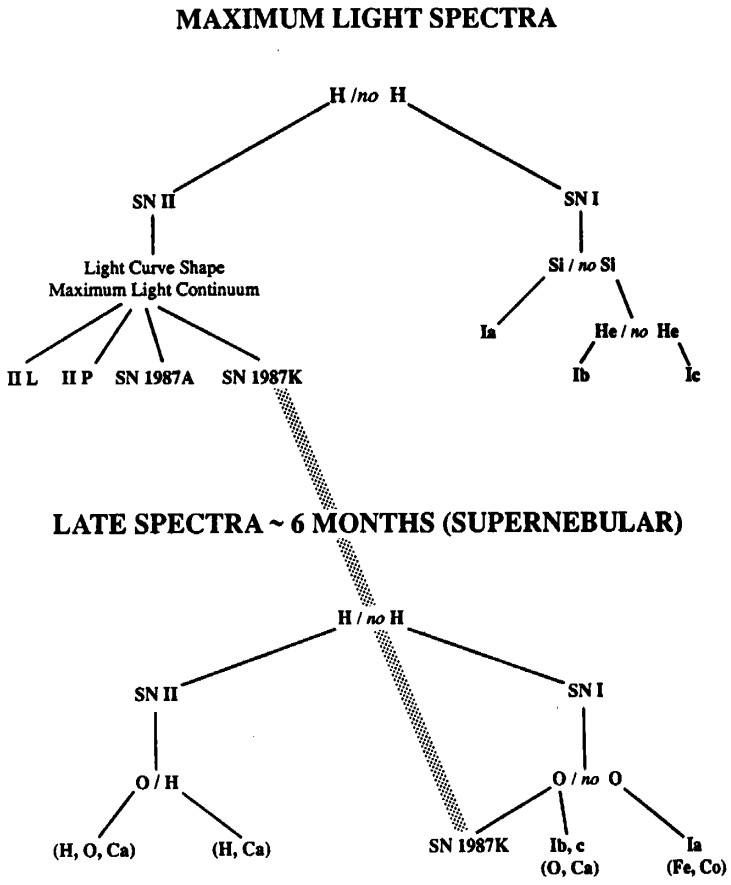

Figure 3.2: The schematic classification scheme of supernovae based on early and late time spectra features [from Harkness and Wheeler 1990].

~ 1 $M_\odot$). They are the only stars that have lifetimes approaching the age of an elliptical galaxy, where major activity of star formation stopped long ago; if star formation is presently taking place in the latter, the rate is very low, due to paucity of cold gas. The progenitors are believed to be mass-accreating white dwarfs, growing toward Chandrasekhar's limit. Light curves of Type Ia SN show a rapid rise to the maximum brightness and stay at maximum for a short time, fading by 3 mag in just 30 days but thereafter decreasing in an exponential function. This last-phase decline is thought to be caused by radioactive decay, of ^{56}Co which is followed by a decay of ^{56}Ni with half life of 6.6 days and decays into ^{56}Fe with half life of 78 days, created by the explosive ignition of the electro degenerate material. In order to explain the characteristics of light curve, the explosion must produce a nickel mass of $\gtrsim 0.5$ $M_\odot$(Arnett 1982; Arnett et al. 1985). Intermediate-mass elements (O, Mg, Si, S, Ca) must be present in the outer layers, as deduced from the spectra at maximum light (Branch et al. 1982; Wheeler et al. 1987). From the spectral characteristics, the progenitors must be devoid of hydrogen at the time of explosion. The estimate of maximum amount of hydrogen mass is $\lesssim 0.1$ $M_\odot$(it is still debatable in order to explain well the presence of Balmer lines.).

All of the characteristics above lead strong support to the white dwarf hypothesis - i.e., white dwarfs in the binary system, not a single ones, however a consistent scenario for evolution of the white dwarfs up to explosion is not present yet. In principle, the chemical compositions of the white dwarfs have quite various combinations (H, C+O, O+Ne+Mg), however, most of the studies are concentrated on C+O case. The reasons are that the H white dwarfs would almost certainly detonate after igniting to produce no intermediate mass elements, with too large expansion velocity, and that the O+Ne+Mg white dwarfs would rather collapse after igniting O at high densities (Miyaji et al. 1980; Miyaji and Nomoto 1987). On the other hand, C+O white dwarfs can ignite carbon at lower densities than O+Ne+Mg white dwarfs and can sustain subsonic burning fronts through either the whole or a fraction of their mass (Woosley 1990).

Type Ib events are thought to be associated with massive progenitors. They occur in the arms of spiral galaxies and often associated with H II regions, just like Type II events. At the present time, there is absolutely no evidence that the initial mass of a progenitor of Type Ib is less than that of a Type II, which is also thought to have a massive progenitor. Though the verdict is not yet on the possible identification of oxygen-rich remnants with those of Type Ib events, it is widely believed that these are identical. If the Type Ib remnants are really identical to the oxygen-rich remnants, the mass of the Type Ib progenitors might be $\sim$ 20–30 $M_\odot$. The reasons that these are thought to be identical are as follows; because Type Ib events are caused by the explosions of the massive stars, which are relatively compact and lack of outer hydrogen layers from the evidence of the light curve and spectra, because the progenitors of Type Ib events shed large amount of matter, and the SN shell interacts the dense gas supplied by this wind, which is verified by the radio observations, and because a significant amount of oxygen is expelled at the time of explosion ($\sim$ 2–5 $M_\odot$). These properties suggest that Wolf-Rayet stars and the helium cores of massive stars are likely

candidates for the Type Ib progenitors (Wheeler and Harkness 1987; Langer and El Eid 1986; Begelman and Sarazin 1986).

Type II SNe only flare up in spiral galaxies, never in ellipticals. They distribute toward the spiral arms. The rate of which Type II events occur strong correlates with the color of the galaxy, which is governed by amount of star-formation rate. From these, Shklovskii (1960), Tinsley (1975), and Tinsley (1977) concluded that the progenitors of the Type II SNe might be young, type O or early B high-mass stars on the main sequence, with mass of 6–8 $M_\odot$and lifetime of $\sim 3 \times 10^7$yr. The Hα flux from spiral galaxies can be determined by the number of OB stars and their ultraviolet luminosities. The rate of the Type II events is found to be well correlated with this Hα flux, a linear dependence (Kennicutt 1984). From this, the lower bound for the initial stellar mass resulting the Type II events can be estimated to be between 5–6 and 12 $M_\odot$, with the most probable value of $\gtrsim 8$ $M_\odot$. The upper limit of the initial stellar mass is obtained with less confidence, because it is supported by only one observational fact; CO observations of Galactic open clusters revealed that CO emission was found in 24 out of 28 clusters with young O stars, and was not found in 35 out of 38 clusters with the earliest stars of type B1 (Bash et al. 1977). This means that CO emission is present in young clusters with stars earlier than type B0, but not in those without such stars. Therefore, Wheeler and Harkness (1987) proposed that high-mass O stars with mass of $\gtrsim$ 15–25 $M_\odot$do not explode, and that gas is swept out of these clusters only after less massive stars that end their lives as SNe begin to leave the main sequence.

Table 3.1 shows the summary for these classification.

3.3 Nucleosynthesis in Supernovae

Just after the Big Bang, the universe contained only hydrogen and helium with tiny traces of other light elements like lithium. Heavier elements were, and continue to be, "synthesized" deep in the interiors of stars by step-by-step processes of nuclear fusion, so-called nucleosynthesis. These newly formed chemical species were spewed out into the interstellar space by the supernova explosions, together with still heavier atomic nuclei that were fused during the explosion.

How far the process of nucleosynthesis proceeds in a star depends on its mass. Stars like Sun normally produce elements as heavy as carbon and oxygen, but their densities and temperatures are too low to fuse these into heavier elements. More massive stars do support the required conditions to synthesize elements such as oxygen, magnesium, silicon, and iron, as well as some heavier ones. Therefore, different types of SNe have different progenitors, thus producing different heavy elements on different time-scales during the chemical evolution of galaxies.

Tsujimoto et al. (1995) predicted nucleosynthesis products of Type Ia and Type II

Table 3.1: Supernovae and Supernova Remnants (Lozinskaya 1992)

	Type Ia	Type II	Type Ib
Initial mass on MS $M_\odot$	∼4 to 6–7	6–8 to 12–(20?)	$\gtrsim 6$
Presupernova	WD (in a binary system?)	RSG(BSG)	WD+SG? WR?
Type of instability, explosion mechanism	Thermal, thermonuclear	Collapse, magnetorotational	Collapse? Thermonuclear? magnetorotational?
Stellar remnant	None	Neutron star	Black hole? Neutron star?
M_{ejecta} $M_\odot$	1.4(1–2)	1–10	(1–6?)
M_{Fe} $M_\odot$	0.4–1	0.04	0.2–0.3
M_O $M_\odot$	?	<0.2	1–5
Young remnant	Tycho SN1006 Kepler?	Crab, 3C 58, 0540-693 CTB80	Cas A? Oxygen-rich? (Kepler??)
Remarks	Why is Kepler different from Tycho and SN1006	Where is the fast-moving shell of the Crab? Are CTB 80 and SN 1408 related?	Was the supernova that produced Cas A anormalously weak? What are the earmarks of an asymmetrical SN explosion?

SNe, assuming that the stars initially more massive than 10 $M_{\odot}$ explode as Type II SNe if they are single stars, or as Type Ib/Ic SNe if they belong to close binary systems. Fig. 3.3 shows the predicted relative abundances of synthesized heavy elements by Tsujimoto et al. (1995), which are normalized to the corresponding cosmic abundances of Allen (1973). The abundance of Mg is normalized to 1.

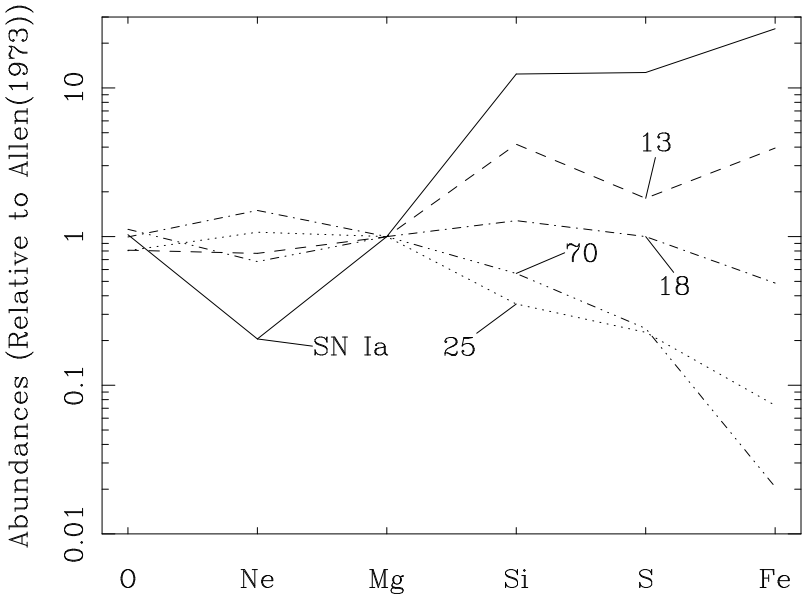

Figure 3.3: The predicted relative abundances of synthesized heavy elements (Tsujimoto et al. 1995) The ratios to the cosmic abundances of Allen (1973) are plotted for SN Ia and SN II of 13, 18, 25, and $70 M_{\odot}$ stars.

3.4 Shock Wave

A shock plays an important role in the dynamics within SNe and SNRs. It can be views as a transition region between upstream and downstream states of a fluid through which there is a net mass flux and across which mass, momentum, and energy flux are conserved but entropy per unit mass and mass density increases. Here we describe fluid equations and relations between some physical parameters.

In a coordinate at the shock front, the conservation of mass, energy, and momentum

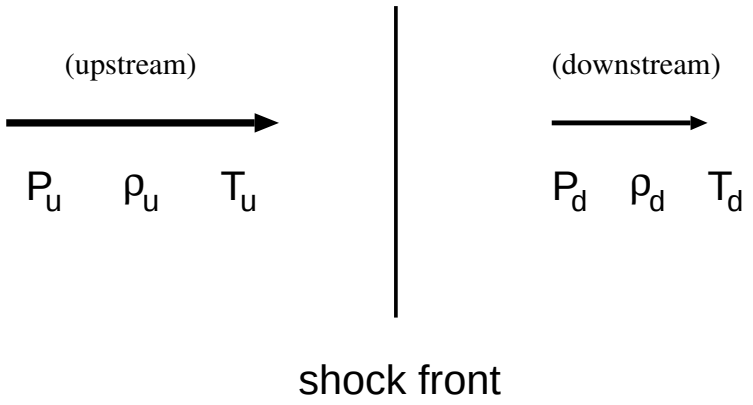

Figure 3.4: A schematic view around the shock front.

are described as

$$\frac{\partial \rho}{\partial t} + \frac{\partial (\rho v)}{\partial x} = 0 \tag{3.1}$$

$$\frac{\partial (\rho v)}{\partial t} + \frac{\partial (\rho v^2 + P)}{\partial x} = 0 \tag{3.2}$$

$$\frac{\partial}{\partial t}\{\rho(\frac{1}{2}v^2 + E)\} + \frac{\partial}{\partial x}\{Pv + \rho(\frac{1}{2}v^2 + E)v\} = 0 \tag{3.3}$$

where ρ, v, P, and E are density, velocity, pressure, and energy per unit mass, respectively. These continuity equation can be rewritten as follows in a Lagrangian coordinate for the situation in Fig. 3.4

$$\rho_{\rm u} v_{\rm u} = \rho_{\rm d} v_{\rm d} \tag{3.4}$$

$$\rho_{\rm u} v_{\rm u}^2 + P_{\rm u} = \rho_{\rm d} v_{\rm d}^2 + P_{\rm d} \tag{3.5}$$

$$v_{\rm u}\{P_{\rm u} + \rho_{\rm u}(\frac{1}{2}v_{\rm u}^2 + E_{\rm u})\} = v_{\rm d}\{P_{\rm d} + \rho_{\rm d}(\frac{1}{2}v_{\rm d}^2 + E_{\rm d})\} \tag{3.6}$$

where subscripts u and d denote upstream and downstream, respectively. The equation (3.6) for the ideal gas is changed to the formula, together with the equation (3.4)

$$\frac{1}{2}v_{\rm u}^2 + \frac{\gamma}{\gamma - 1}\frac{P_{\rm u}}{\rho_{\rm u}} = \frac{1}{2}v_{\rm d}^2 + \frac{\gamma}{\gamma - 1}\frac{P_{\rm d}}{\rho_{\rm d}} \tag{3.7}$$

where γ is specific-heat ratio. From the equations of (3.4), (3.5), (3.7), and the equation of state for ideal gas, we obtain

$$\frac{\rho_{\rm d}}{\rho_{\rm u}} = \frac{v_{\rm u}}{v_{\rm d}} = \frac{(\gamma - 1)P_{\rm u} + (\gamma + 1)P_{\rm d}}{(\gamma + 1)P_{\rm u} + (\gamma - 1)P_{\rm d}} \tag{3.8}$$

$$\frac{T_{\rm u}}{T_{\rm d}} = \frac{P_{\rm u}}{P_{\rm d}} \cdot \frac{(\gamma - 1)P_{\rm u} + (\gamma + 1)P_{\rm d}}{(\gamma + 1)P_{\rm u} + (\gamma - 1)P_{\rm d}}. \tag{3.9}$$

These formulae holds between thermodynamic quantities on the two sides of the surface of discontinuity and is known as Rankine-Hugoniot relations. For the velocities of the gas across the shock wave, we have

$$v_{\rm u}^2 = \frac{1}{2\rho_{\rm u}}\{(\gamma-1)P_{\rm u} + (\gamma+1)P_{\rm d}\} \tag{3.10}$$

$$v_{\rm d}^2 = \frac{1}{2\rho_{\rm u}}\frac{\{(\gamma+1)P_{\rm u} + (\gamma-1)P_{\rm d}\}^2}{\{(\gamma-1)P_{\rm u} + (\gamma+1)P_{\rm d}\}} \tag{3.11}$$

Here we supply some useful equations for the ratio of density, pressure, and temperature in terms of the Mach number $M_{\rm u} = v_{\rm u}/C_{\rm u}$, where $C_{\rm u}$ is the sound velocity.

$$\frac{\rho_{\rm d}}{\rho_{\rm u}} = \frac{(\gamma+1)M_{\rm u}^2}{(\gamma-1)M_{\rm u}^2+2} = \frac{4M_{\rm u}^2}{M_{\rm u}^2+3} \tag{3.12}$$

$$\frac{p_{\rm d}}{p_{\rm u}} = \frac{2\gamma M_{\rm u}^2}{\gamma+1} - \frac{\gamma-1}{\gamma+1} = \frac{5M_{\rm u}^2-1}{4} \tag{3.13}$$

$$\frac{T_{\rm d}}{T_{\rm u}} = \frac{\{2\gamma M_{\rm u}^2-(\gamma-1)\}\{(\gamma-1)M_{\rm u}^2+2\}}{(\gamma+1)^2 M_{\rm u}^2} \tag{3.14}$$

$$= \frac{(5M_{\rm u}^2-1)(M_{\rm u}^2+3)}{16M_{\rm u}^2} \tag{3.15}$$

The Mach number $M_{\rm d}$ is also given in terms of $M_{\rm u}$ by

$$M_{\rm d}^2 = \frac{2+(\gamma-1)M_{\rm u}^2}{2\gamma M_{\rm u}^2-(\gamma-1)} = \frac{M_{\rm u}^2+3}{5M_{\rm u}^2-1} \tag{3.16}$$

In the case of $P_{\rm u} \ll P_{\rm d}$ (strong shock),

$$\frac{\rho_{\rm d}}{\rho_{\rm u}} = \frac{v_{\rm u}}{v_{\rm d}} = \frac{\gamma+1}{\gamma-1} \tag{3.17}$$

$$v_{\rm u} = \sqrt{\frac{1}{2}(\gamma+1)\frac{P_{\rm d}}{\rho_{\rm u}}} \tag{3.18}$$

$$v_{\rm d} = \sqrt{\frac{1}{2}\frac{(\gamma-1)^2 P_{\rm d}}{(\gamma+1)\rho_{\rm u}}} \tag{3.19}$$

$v_{\rm u}$ and $v_{\rm d}$ are defined in a coordinate where the shock front has null velocity. In the observer's coordinate, $v_{\rm u}$ equals the shock velocity ($\equiv v_{\rm s}$) . Using the equation of state, the post-shock velocity $v_{\rm p} \equiv v_{\rm u} - v_{\rm d}$, post-shock pressure $P_{\rm p} \equiv P_{\rm d}$, and the post-shock temperature $T_{\rm p} \equiv T_{\rm d}$ are obtained as

$$v_{\rm p} = \frac{2v_{\rm s}}{\gamma+1} \tag{3.20}$$

$$P_{\rm p} = \frac{2\rho_{\rm u}v_{\rm s}^2}{\gamma+1} \tag{3.21}$$

$$kT_{\rm p} = P_{\rm p}\frac{\mu}{\rho_{\rm d}} = \frac{2(\gamma-1)}{(\gamma+1)^2}\mu v_{\rm s}^2 \tag{3.22}$$

where μ is the mean atomic weight, and k is the Boltzmann constant. In the case of $\gamma = \frac{5}{3}$ (monoatomic gas), we obtain

$$kT_p = \frac{3}{16}\mu v_{\rm s}^2 \tag{3.23}$$

$$\frac{\rho_{\rm d}}{\rho_{\rm u}} = \frac{v_{\rm u}}{v_{\rm d}} = 4 \tag{3.24}$$

The post-shock temperature is determined by the shock speed only.

3.5 Evolution of Supernova Remnants

At the time of supernova explosion, large amount of the mass of the progenitor star is ejected outward at high velocity. The evolution of the supernova remnant depends on the amount of ejected mass (M_0), the swept up mass ($M_{\rm b}$), and the radiated energy. Here we describe the brief summary of SNR evolution.

3.5.1 Free Expansion Phase

The first phase of the SNR evolution is called a free expansion phase. In this phase the evolution is mainly characterized by the free-expansion of the ejected matter whose mass is larger than that of the swept-up matter ($M_0 > M_{\rm b}$). The initial explosion energy is almost all manifested by kinetic energy of the ejected matter, i.e.- the velocity of the ejected matter is as high as $v_0 \sim$ (5–10) km s^{-1}. The deceleration of the shock front starts when the mass of swept-up matter becomes comparable to that of the ejected matter, which is the end of the first phase. The radius and age of the remnant at that point are

$$R_{\rm s} = \frac{(3M_0)^{(1/3)}}{(4\pi\mu m_H n_{\rm b})^{(1/3)}} = \left(\frac{M_0}{1M_\odot}\right)^{1/3} \left(\frac{\mu}{1.36}\right)^{-1/3} \left(\frac{n_0}{1\,{\rm cm}^{-3}}\right)^{-1/3} {\rm pc} \tag{3.25}$$

$$t \approx R_{\rm s} v_0^{-1} \approx 190\ {\rm yr} \tag{3.26}$$

here we assumed that the mean ambient hydrogen density $n_0 = 1\,{\rm cm}^{-3}$, and with $M_0 = 1M_\odot$, $v_0 = 10^4$ km s^{-1}, and $\mu = 1.36$ (mean atomic weight of cosmic material per H atom) (Allen 1973).

The ejecta heated by the shock wave makes an additional shock wave called reverse shock, which propagates toward the center of the SNR. The ejecta heated by the reverse shock radiates X-ray, hence the X-ray spectroscopy of this phase of SNRs can be a powerful tool to investigate the chemical composition of heavy elements synthesized by SN events.

3.5.2 Adiabatic Phase

The next phase of the SNR evolution is called a adiabatic phase. In this phase, the shock front is started to decelerate by encountering with the ambient interstellar matter. Shklovskii (1962) proved that the SN explosion within the interstellar matter can be linked to a powerful point explosion in a gas with constant heat capacity. He also proved that the self-similar Sedov (1959) solution was applicable to this phenomena. The Sedov solution describes the evolution of the remnant at adiabatic stage by assuming that the mass of swept-up matter is about 10 times that of the ejecta, and that the radiative energy losses are still negligible by comparison with the initial explosion energy (Gull 1973). Ostriker and McKee (1988) introduced the equations which describe the motion of this stage as follows,

$$R_{\rm s} = 0.31\ n_0^{-0.2}\ E_{51}^{0.2}\ t^{0.4}\ {\rm pc} \tag{3.27}$$

$$V_{\rm s} \equiv \frac{dR_{\rm s}}{dt} = \frac{2}{5}\frac{R_{\rm s}}{t} \tag{3.28}$$

$R_{\rm s}$, $V_{\rm s}$, n_0, E_{51}, and t are the radius, velocity of the shock front, ambient density, initial explosion energy in the unit of 10^{51} ergs, and the age in the unit of year, respectively.

With the the equation (3.23), the shock temperature is given as

$$kT_{\rm s} = \frac{3}{16}\ \mu\ V_{\rm s}^2 = 1.7 \times 10^4\ n_a^{-0.4}\ E_{51}^{0.4}\ t^{-1.2}\ {\rm keV} \tag{3.29}$$

In this stage, about 70% of the initial explosion energy is known to be converted into the thermal energy of swept-up matter (Chevalier 1974).

3.5.3 Radiative Cooling Phase

The remnant continues to expand adiabatically until the radiative cooling is dominant. At this moment, the shock velocity is decelerated down to ~ 200 km s^{-1} and the gas temperature is about $kT \sim (4\text{–}5) \times 10^{-2}$ keV. By this time, about half of the thermal energy has been radiated away, and cold, dense shell has been formed.

According to Falle (1981) and (1988), the age $t_{\rm cool}$, radius $R_{\rm cool}$, and expansion velocity $V_{\rm cool}$ of supernova remnant in the radiative cooling phase are expressed as,

$$t_{\rm cool} = 2.7 \times 10^4 E_{51}^{0.24} n_0^{-0.52}\ {\rm yr}, \tag{3.30}$$

$$R_{\rm cool} = 20 E_{51}^{0.295} n_0^{-0.409}\ {\rm pc}, \tag{3.31}$$

$$V_{\rm cool} = 277 E_{51}^{0.0554} n_0^{0.111}\ {\rm km\ s^{-1}}. \tag{3.32}$$

The cavity bounded by the thin, cold shell contains hot, tenuous gas that still continues to expand adiabatically. So-called "snowplow" model advocated by Cox (1972) describes quite

well the formation of the cold shell. The law of motion governing the shell at this state can be derived from the adiabatic expansion condition imposed on the interior hot gas,

$$\frac{\mathrm{d}E_{\mathrm{T}}}{\mathrm{d}t} = -4\pi R_{\mathrm{s}} P \frac{\mathrm{d}R_{\mathrm{s}}}{\mathrm{d}t}, \tag{3.33}$$

$$\frac{4\pi}{3} R_{\mathrm{s}}^3 P = (\gamma - 1) E_{\mathrm{T}} \tag{3.34}$$

and the equation for the mass and momentum of the shell

$$M = \frac{4\pi}{3} R_{\mathrm{s}}^3 \rho_0, \tag{3.35}$$

$$\frac{\mathrm{d}(MV_{\mathrm{s}})}{\mathrm{d}t} = 4\pi R_{\mathrm{s}}^2 P, \tag{3.36}$$

$$\frac{\mathrm{d}R_{\mathrm{s}}}{\mathrm{d}t} = V_{\mathrm{s}}. \tag{3.37}$$

Here P is the pressure of the hot gas, the thickness of the shell is assumed to be small compared to its radius, and the mass of the hot gas is assumed to be much less than that of the shell. With equation(3.34) and equation(3.37), McKee and Ostriker (1977) and Blinnikov et al. (1982) got a solution as follows,

$$R_{\mathrm{s}} = 38 (\epsilon E_{51})^{5/21} n_0^{-5/21} (\frac{t}{10^5 yr})^{2/7} \text{ pc}, \tag{3.38}$$

$$V_{\mathrm{s}} = \frac{2}{7} \frac{R_{\mathrm{s}}}{t}, \tag{3.39}$$

where $\epsilon = E_{\mathrm{T}}/E_0 = 0.2$–$0.35$.

When the expansion velocity is as small as $\sim$ 10–20 km s^{-1}, which is about the same as the velocity of proper motion of the ambient interstellar matter, the remnant begins to melt into the ISM. If the remnant structure does not interact with other ones, it will eventually disappear by fragmentation of the shell and by replacement of the cooling low-density gas by expanding cooler material from the ISM (Cox and Smith 1974).

3.6 SNRs in the LMC – Previous X-ray Observations

The LMC is one of the best sites for the systematic study of SNRs. The reasons are as follows; 1) the LMC is at the known distance of approximately 50 kpc (Bertelli et al. 1993), which allow us to regard that all the SNRs are at the same distance, thus enable us to make it easy to derive the physical parameters from the observable quantities, 2) the LMC has nearly face on view with a little inclination of $\sim 40^\circ$ from the plane of the sky (Feast 1999), 3) there is only little interstellar obscuration between the LMC and us, which allow us to

observe the LMC SNRs (not only just bright ones) in hard as well as soft X-ray energy bands, which is quite difficult for the case of Galactic SNRs.

Mathewson et al. (1983), (1984), and (1985) catalogued thirty-two LMC SNRs from their optical and radio observations. These SNRs were and have been observed also in X-ray wavelength. Here, we briefly describe about the recent systematic X-ray imaging analysis of the LMC SNRs with ROSAT by Williams et al. (1999) and the X-ray spectral analysis of the flux limited 10 SNRs with ASCA by Hayashi (1997) and Hughes et al. (1998).

3.6.1 Imaging Analysis

Williams et al. (1999) used archival ROSAT HRI or PSPC data of 31 LMC SNRs and carried out the systematic analysis of X-ray morphology of them. They categorized X-ray morphology of LMC SNRs into roughly 5 groups as follows,

Shell	limb is near complete and is brighter than face.
Diffuse face	face as bright as shell; limb sometimes indistinct from face.
Centrally brightened	center of face notably brighter than limb.
Peaked emission	emission dominated by central bright source of small diameter with respect to that of the entire SNR.
Irregular	incomplete or nonexistent shell, patchy emission.

with the designations for secondary X-ray features within the remnant defined as,

Gap	region of weaker emission in near-complete shell.
Hot spot	proportionally small region of bright diffuse emission.
Bright limb	elongated bright region along shell.
Nonlimb feature	patch of emission away from the limb.
Elongated extension	protrusion beyond shell limb.

Table 3.2 shows the X-ray morphological classification of LMC SNRs. They explained the physical implication from these morphology of SNRs as is shown in the cartoon (Fig. 3.5).

The younger and smaller remnants, such as 0509−675, 0519−690, and N103B, tend to show clear shell-type morphology in X-rays. In a very young remnant, in which the SN ejecta still dominates, the bulk of the X-ray emission arises from the reverse shock traveling back through this ejecta. Therefore, the fast expanding shock will have the brightest X-rays along the outer rim, as the front shocks the ambient relatively dense ISM to high temperatures (Raymond 1984 and references therein).

At the next stage of the SNR evolution, as the outer shock proceeds, cloudlets in the ambient medium may be left behind when the shock passes them. These cloudlets will then evaporate within the SNRs and produce detectable X-ray emission near these local maxima in the interior density, thus produce the sort of morphology, which they call “diffuse face“

SNRs.

At the far end of this "diffuse face" category, "Centrally-Brightened morphology" is placed. Because the clump emission raises the central surface brightness of the remnants to the point where the interior dominates the X-ray emission. They indicate that the best example of this type of SNR is N206 (0532−71.0).

They also show very interesting relation between X-ray sizes of SNRs, which can be an indicator of ages, and the morphology of them (Fig. 3.6). As is shown in Fig. 3.6, a loose correlation between remnant sizes and some of the morphological classes is seen. The smallest SNRs are all shell-type, and these are all at the lower end of the range of diameters. On the other hand, the remnants with centrally brightened morphology are all at the upper end of the range of X-ray sizes. Though the diffuse face remnants fill most of the range, however, roughly fall between the two cases above (both shell-type and centrally brightened SNRs), still, overlapping with them. Williams et al. (1999) thus insisted that the morphology does reflect the evolutionally trend.

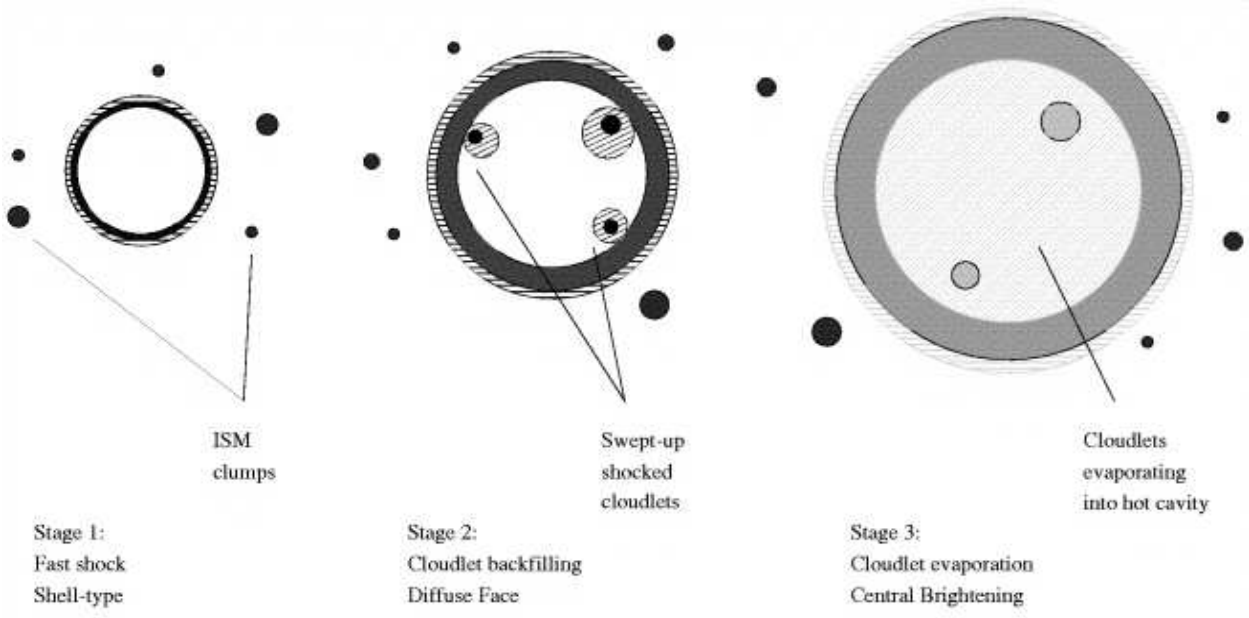

Figure 3.5: Cartoon provided by Williams et al. (1999), showing the schematic stages of development of SNRs in a cloudy medium. Stripped regions are those from which X-ray emission is expected, while solid regions indicate denser material, from which optical emission may be observed. The relative darkness of the shading indicated areas of higher (darker) and lower (lighter) density.

Table 3.2: Classification of LMC SNRs by Williams et al. (1999)

Object	Name	Category	Features
0450-709	SNR0450-709	No data	.....
0453-685	SNR0453-685	Diffuse face	
0453-669	SNR0453-669	Irregular	Bright limb
0454-665	N11L	Irregular	Elongated feature
0454-672	SNR0454-672	Centrally brightened?	Elongated feature
0455-687	N86	Irregular	Elongated features
0500-702	N186D	No data	.....
0505-679	DEM L71	Shell	Gap,nonlimb feature
0506-680	N23	Irregular	Bright limb, nonlimb feature
0509-675	SNR0509-675	Shell	Limb hot spot
0509-687	N103B	Shell	Limb hot spot
0513-692	SNR0513-692	No data	.....
0519-690	SNR0519-690	Shell	Gap
0519-697	N120	Centrally brightened?	.....
0520-694	SNR0520-694	Diffuse face	
0523-679	SNR0523-679	Diffuse face	Elongated feature
0524-664	DEML175a	No data	.....
0525-660	N49B	Diffuse face	Nonlimb feature
0525-661	N49	Diffuse face	Nonlimb feature
0525-696	N132D	Shell	Nonlimb feature
0527-658	DEM L204	No data	.....
0528-692	SNR0528-692	Unclassified	.....
0532-710	N206	Centrally brightened	
0534-699	SNR0534-699	Diffuse face	
0534-705	DEM L238	Unclassified	
0535-660	N63A	Diffuse face	Limb hot spot
0536-676	DEM L241	No data	.....
SN1987A	Special	Unresolved	Unresolved
0536-693	Honeycomb	Irregular	
0536-706	DEM L299	Unclassified	.....
0538-691	N157B	Peaked emission	Elongated feature
0540-693	N158A	Peaked emission	Unclassified shell
0540-697	SNR0540-697	Unclassified	Obscured by LMC X-1
0543-689	DEM L299	Unclassified	.....
0547-697A	DEM L316A	Diffuse face	Bright limb/hot spot
0547-697B	DEM L316B	Shell	Elongated feature
0548-704	SNR0548-704	Diffuse face	Gap?

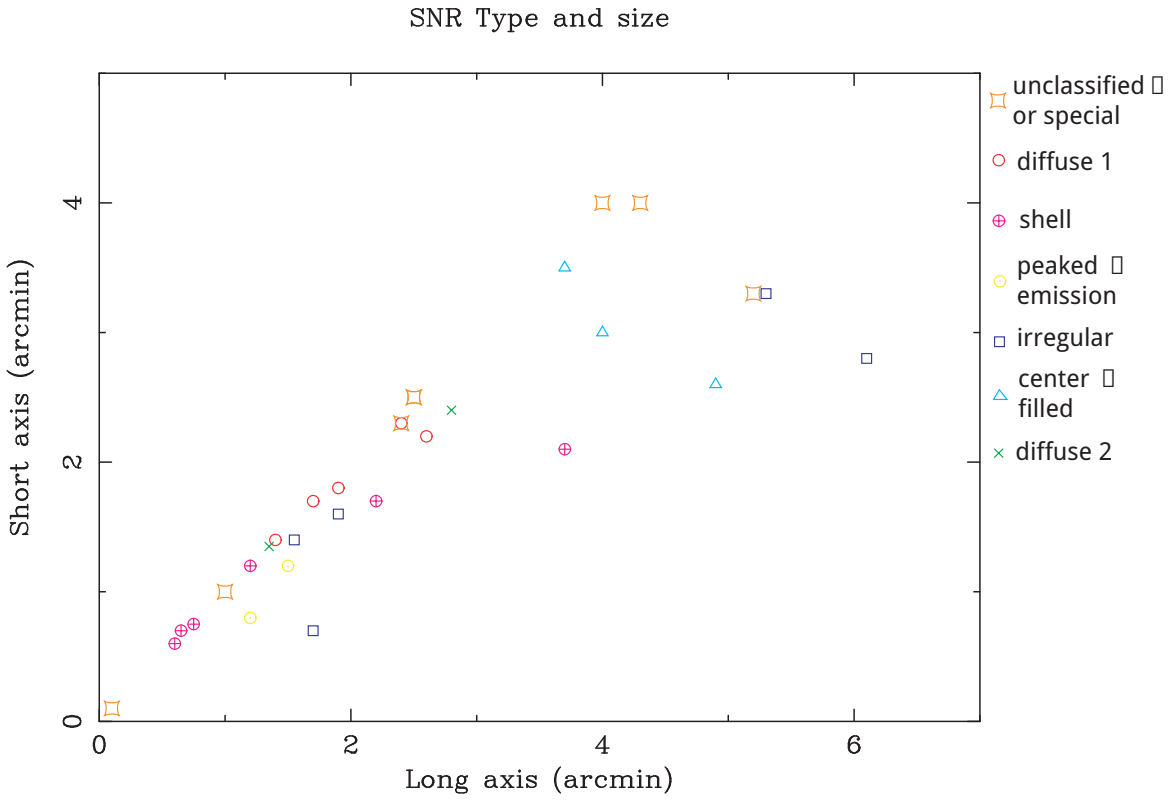

Figure 3.6: Plot of the X-ray sizes of the LMC SNRs. The symbols represent the different morphological classifications, provided by Williams et al. (1999)

3.6.2 Spectral Analysis

The systematic spectral analysis of flux-limited sample of three young SNRs and seven middle-aged SNRs were carried out using ASCA SIS instruments by Hayashi (1997) and Hughes et al. (1998). They constructed self-consistent nonequilibrium ionization SNR models assuming the Sedov solution for the dynamical evolution, and then applied the resulting spectral models to the data. In addition, they also tested the cases that the plasma at the shock front is in the equipartition or non-equipartition state. In the equipartition state, the temperatures of electrons and ions are equal at the shock front. On the contrary, in the non-equipartition state, the temperatures of them are assumed to be different. It is assumed that most of the energy is, at first, possessed by the ions at the shock front, whose masses are larger than those of electrons by more than three orders of magnitudes. The energy, then, is gradually transfered from ions to electrons through the Coulomb collisions.

All the remnants were reasonably well described by either of the models with the assumptions of equipartition and non-equipartition. From the fitting results, they derived physical parameters, such as, the Sedov ages ($t_{\rm sedov}$), ambient densities (n_0), initial explosion energies (E_0), and swept-up mass ($M_{\rm swept}$), using the following equations,

$$n_0 = 13 \left(\frac{N_S}{10^{12}{\rm cm}^{-5}}\right)^{1/2} \left(\frac{\theta_R}{10''}\right)^{-3/2} \left(\frac{D}{50\,{\rm kpc}}\right)^{-1/2} \left(\frac{\Omega}{4\pi}\right)^{-1/2} \ {\rm H\,cm}^{-3}, \tag{3.40}$$

$$t_{\rm sedov} = 1.0 \left(\frac{kT_1}{1\,{\rm keV}}\right)^{-1/2} \left(\frac{\theta_R}{10''}\right) \left(\frac{D}{50\,{\rm kpc}}\right) 10^3{\rm yr}, \tag{3.41}$$

$$E_0 = 0.33 \left(\frac{kT_1}{1\,{\rm keV}}\right) \left(\frac{N_S}{10^{12}{\rm cm}^{-5}}\right)^{1/2} \left(\frac{\theta_R}{10''}\right)^{3/2} \left(\frac{D}{50\,{\rm kpc}}\right)^{5/2} \left(\frac{\Omega}{4\pi}\right)^{-1/2} \ 10^{51}{\rm erg}, \tag{3.42}$$

$$M_{\rm swept} = 26 \left(\frac{N_S}{10^{12}{\rm cm}^{-5}}\right)^{1/2} \left(\frac{\theta_R}{10''}\right)^{3/2} \left(\frac{D}{50\,{\rm kpc}}\right)^{5/2} \left(\frac{\Omega}{4\pi}\right)^{1/2} \ M_\odot, \tag{3.43}$$

where Ω is a solid angle subtended by a remnant shell with respect to the remnant center, which takes an incompleteness of the spherical structure into account, and θ_R is a angular size of the remnant (in radius). The notations of D and kT_1 mean the distance to the LMC and the temperature at the shock front, respectively. and N_S is a normalization factor of the fitting model, which is defined as $N_S \equiv (n_0^2 V)/(4\pi D^2)$. They also determined the elemental abundances of the plasmas within individual SNRs. Table 3.3 and Table 3.4 shows the fitting results for the young and middle-aged SNRs with the self-consistent nonequilibrium ionization SNR models.

From the results of middle-aged SNRs, they found statistical evidence for enrichment of ISM by supernova ejecta in the sense that smaller remnants show a somewhat higher metalicity than the larger ones (Fig. 3.7). It is said that the derived abundances are in

general dominated by swept-up interstellar material, and so these middle-aged SNRs can be used for the estimation of the mean LMC gas-phase abundances. The elements are less abundant than the solar values by factors of 2–4 (Fig. 3.8). Overall these results are consistent with the derived results from the optical or UV observations. It is notable that this method of abundance determination with the X-ray observations is entirely independent of previous methods using UV or Optical observations. It is also notable that the X-ray data provide four independent constraints on the three independent parameters of the Sedov model, thus this abundance determination method is thought to be more reliable than other previous methods.

Table 3.3: Best-fit Parameters for the Sedov Models of LMC "Young" Remnants by Hayashi (1997).

SNR	R_1 (pc)	$N_{\rm H}$ ($10^{21}{\rm cm}^{-2}$)	kT_1 (keV)	$\log n_0 t_{\rm i}$ (${\rm cm}^{-3}{\rm s}$)	N_S ($10^{12}{\rm cm}^{-5}$)
N103B	3.0	3.1(0.3)	0.67(0.04)	11.29(0.15)	0.87(0.13)
		3.1(0.3)	1.23(0.35)	11.04(0.06)	0.88(0.22)
0509–67.5	3.3	2.5(0.5)	0.20(0.04)	10.92(0.13)	1.66(1.23)
		1.5(0.3)	1.94(1.14)	10.15(0.10)	0.21(0.09)
0519–69.0	3.6	1.1(0.3)	1.51(0.35)	10.42(0.07)	0.10(0.03)
		1.3(0.2)	4.75(2.96)	10.62(0.13)	0.15(0.04)

SNR	n_0 (${\rm H\,cm}^{-3}$)	$t_{\rm sedov}$ (10^3yr)	E_0 (10^{51}erg)	$M_{\rm swept}$ ($M_\odot$)	χ^2_ν/d.o.f.	$L_X[0.5-5\,{\rm keV}]$ ($10^{36}{\rm erg\,s}^{-1}$)
N103B	8.7	1.5	0.29	30	3.0/252	5.8
	8.7	1.1	0.53	30	3.3/252	
0509–67.5	11	3.0	0.13	50	2.7/147	1.4
	3.8	0.97	0.46	20	3.1/147	
0519–69.0	2.2	1.2	0.28	15	2.6/180	3.8
	2.8	0.69	1.1	20	2.6/180	

SNR	O	Ne	Mg	Si	S	Ar	Ca	Fe
N103B	0.31(0.10)	1.53(0.29)	0.68(0.14)	1.34(0.20)	2.47(0.37)	1.36(0.53)	7.2(2.7)	0.77(0.12)
	0.20(0.05)	0.83(0.10)	0.41(0.08)	0.89(0.11)	1.69(0.21)	0.85(0.37)	3.9(2.2)	0.69(0.09)
0509–67.5	0.11(0.03)	0.11(0.05)	0.06(0.09)	5.60(1.14)	5.24(1.75)			0.37(0.07)
	0.11(0.02)	0.17(0.05)	0.09(0.08)	4.43(0.77)	6.51(2.35)			0.57(0.12)
0519–69.0	0.21(0.03)	1.32(0.18)	1.07(0.28)	1.97(0.39)	2.81(0.39)			2.21(0.46)
	0.19(0.04)	1.05(0.18)	0.72(0.19)	1.51(0.27)	2.32(0.53)			1.58(0.28)

Notes: For each remnant, the values of the equipartition model are given in the upper line, while those of the non-equipartition model are given in the lower line. The distance of the remnants was taken to be 50kpc. The values in parentheses represent the 90% confidence statistical errors.

Table 3.4: Best-fit Parameters for the Sedov Models of LMC "Evolved" Remnants by Hayashi (1997).

SNR	R_1 (pc)	$N_{\rm H}$ (10^{21}cm^{-2})	kT_1 (keV)	$\log n_0 t_{\rm i}$ (cm^{-3}s)	N_S (10^{12}cm^{-5})	n_0 (H cm^{-3})	$t_{\rm sedov}$ (10^3yr)	E_0 (10^{51}erg)	$M_{\rm swept}$ ($M_\odot$)
N23	6.7	0.8(0.3)	0.53(0.10)	10.89(0.27)	0.33(0.12)	1.6	3.8	0.46	70
		0.7(0.3)	0.59(0.15)	11.16(0.21)	0.35(0.10)	1.7	3.6	0.53	70
N49	8.2	2.2(0.3)	0.58(0.05)	11.33(0.18)	1.59(0.28)	2.6	4.4	1.5	210
		2.1(0.3)	0.62(0.05)	11.52(0.13)	1.57(0.24)	2.6	4.3	1.6	200
N63A	8.5	1.4(0.1)	0.62(0.04)	11.23(0.17)	3.77(0.55)	3.9	4.5	2.6	330
		1.4(0.2)	0.68(0.07)	11.38(0.13)	3.95(0.49)	3.9	4.2	2.9	340
DEM71	10.4	0.4(0.3)	0.82(0.14)	10.58(0.11)	0.21(0.06)	0.67	4.7	1.1	110
		0.6(0.3)	0.83(0.41)	11.03(0.10)	0.35(0.13)	0.86	4.7	1.4	140
N132D	12.1	1.3(0.2)	0.68(0.06)	10.95(0.16)	4.70(0.79)	2.5	6.1	5.4	630
		1.3(0.1)	0.78(0.14)	11.19(0.07)	5.43(0.27)	2.7	5.7	6.7	680
0453-68.5	15.0	< 1.1	0.51(0.14)	10.68(0.30)	0.12(0.07)	0.30	8.7	0.91	140
		< 0.5	0.70(0.39)	11.01(0.34)	0.11(0.05)	0.28	7.4	1.2	130
N49B	17.0	2.6(0.4)	0.41(0.06)	10.78(0.11)	1.15(0.57)	0.75	10.9	2.7	520
		2.5(0.4)	0.44(0.10)	11.08(0.16)	1.37(0.55)	0.82	10.6	3.1	560

SNR	O	Ne	Mg	Si	S	Fe	χ^2_ν/d.o.f.	$L_X[0.5-5\,{\rm keV}]$ (10^{36}erg s^{-1})
N23	0.27(0.06)	0.47(0.09)	0.53(0.13)	0.38(0.11)	0.50(0.34)	0.31(0.08)	1.4/172	2.5
	0.32(0.08)	0.45(0.11)	0.50(0.13)	0.36(0.10)	0.52(0.32)	0.28(0.07)	1.3/172	
N49	0.32(0.04)	0.48(0.05)	0.44(0.09)	0.45(0.05)	0.61(0.10)	0.29(0.05)	2.4/247	6.3
	0.38(0.04)	0.48(0.09)	0.43(0.09)	0.43(0.07)	0.58(0.12)	0.29(0.05)	2.5/247	
N63A	0.25(0.05)	0.50(0.05)	0.50(0.06)	0.40(0.05)	0.29(0.07)	0.31(0.04)	2.8/146	20
	0.28(0.05)	0.45(0.08)	0.46(0.08)	0.36(0.05)	0.27(0.09)	0.30(0.04)	2.7/146	
DEM71	0.22(0.03)	0.55(0.08)	0.50(0.12)	0.26(0.09)	0.47(0.27)	0.62(0.12)	2.2/178	3.4
	0.27(0.05)	0.48(0.08)	0.39(0.11)	0.24(0.08)	0.57(0.26)	0.47(0.08)	2.1/178	
N132D	0.21(0.03)	0.44(0.06)	0.46(0.07)	0.34(0.05)	0.36(0.11)	0.30(0.04)	1.8/229	30
	0.24(0.02)	0.42(0.04)	0.41(0.04)	0.31(0.03)	0.36(0.09)	0.27(0.02)	1.8/229	
0453-68.5	0.21(0.05)	0.28(0.07)	0.33(0.13)	0.23(0.14)	< 0.78	0.26(0.08)	2.1/121	0.98
	0.26(0.09)	0.25(0.09)	0.33(0.15)	0.23(0.14)	< 0.71	0.28(0.10)	2.1/121	
N49B	0.22(0.03)	0.42(0.05)	0.74(0.10)	0.28(0.06)	< 0.30	0.21(0.04)	2.5/169	3.2
	0.23(0.05)	0.36(0.07)	0.63(0.12)	0.25(0.07)	< 0.39	0.16(0.03)	2.4/169	

Notes: For each remnant, the values of the equipartition model are given in the upper line, while those of the non-equipartition model are given in the lower line. The distance of the remnants was taken to be 50kpc. The values in parentheses represent the 90% confidence statistical errors.

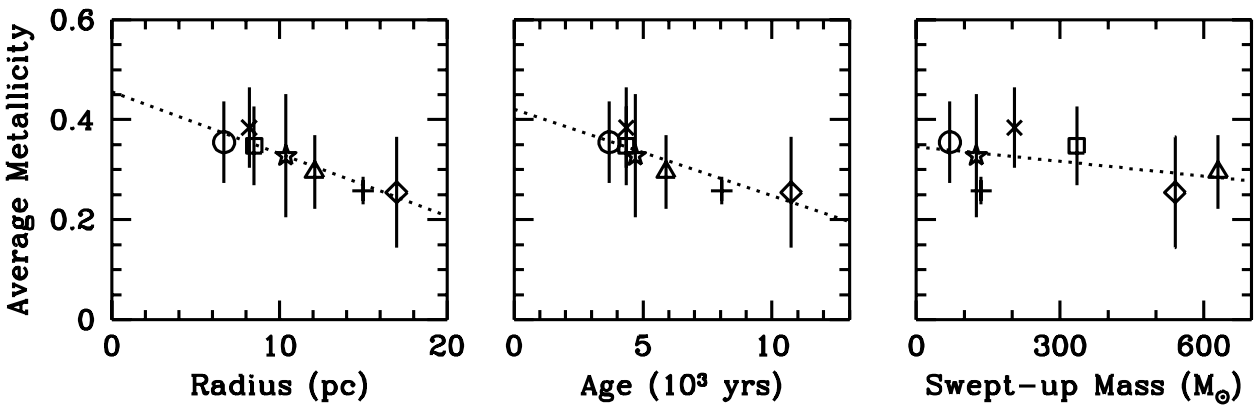

Figure 3.7: Mean metalicity (relative to cosmic values) vs. radius (left-hand panel), dynamical age derived from the Sedov solution (middle panel), and swept-up mass (right-hand panel), provided by Hughes et al. (1998). The different symbol types refer to the different remnants (circle, cross, square, star, triangle, plse sign, and diamond correspond to N23, N49, N63A, DEM71, N132D, 0453−68.5, and N49B, respectively). Error bars represent the rms scatter in the individual fitted abundances of the various elemental species considered. Results plotted are the average of the values obtained under the two different model assumptions about the timescale for electron-ion temperature equilibration. The only significant correlations are between metalicity and either radius or age.

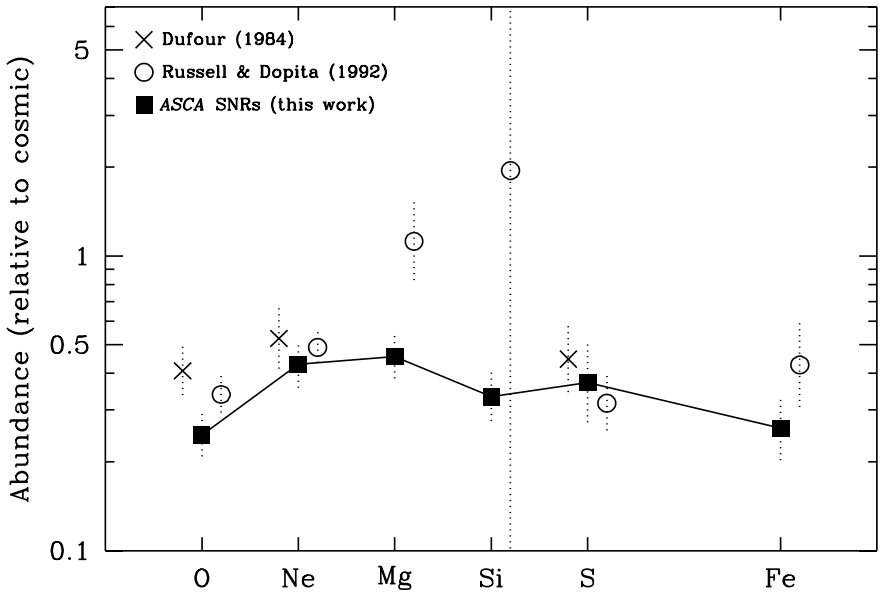

Figure 3.8: Average chemical abundances of the LMC relative to the cosmic value plotted as a function of elemental species by Hughes et al. (1998). The gas-phase abundances of the LMC derived from optical and UV studies of H II regions are shown as the crosses (Dufour 1984). More recent results from (Russell and Dopita 1992), shown as the circles, are based on the detailed modeling of optical/UV spectra from H II regions, SNRs, and supergiant stars.

3.7 Diffuse X-ray emission

Thanks to the imaging survey of the LMC with the Einstein satellite, it was revealed that the LMC hoards plenty of bright diffuse X-ray emission within its body. Wang et al. (1991) analyzed the LMC data of Einstein, extracted all the point-like sources from them, and found out that there remained large amount of diffuse X-ray emission in the LMC body. They examined the possible candidates which might be the major contributor of diffuse X-ray emission. Their discrete source survey with Einstein was complete to $\sim 3\times10^{35}$ ergs s^{-1}. They subtracted the contributions from these sources carefully. To account for remaining diffuse X-ray flux and to avoid being resolved into discrete sources, a new population of discrete contributors would have to have $\langle L_x \rangle \lesssim 10^{34}$ ergs s^{-1}, less than or equal to the fluxes of the faintest sources in their survey, and thus must be more numerous than $\sim 10^4$. They excluded the possibility of contribution from SNRs in a following way; 1) Assuming a SN rate of $\sim 1/500$ yr and a life time of even $\sim 10^5$ yr only 200 remnants are needed, while already 30 of which were detected at that time. 2) Pre-main-sequence, main-sequence, and post-main-sequence stars are known to emit X-rays, however, the integrated emission of the LMC stellar population falls at least an order of magnitude short of accounting for the X-ray luminosity observed. 3) They also excluded the case of low-luminosity X-ray binaries; For high-mass systems with neutron star companions (e.g., Be stars) , the life time of $< 10^7$ yr and an $\langle L_x \rangle \lesssim 10^{34}$ ergs s^{-1} (Van den Heuvel and Rappaport 1987) implies a birthrate of > 1 per 500 yr, implying (implausibly) that all SNs must lead to such systems; alternatively, a large class of low-mass (Population II) binaries would not show the observed correlation of diffuse X-rays with regions of star formation. Consequently, they proposed that an combination of discrete X-ray emitting sources can not account for the bulk of the diffuse emission.

They constructed hardness ratio map of the diffuse X-ray emission in the LMC and revealed that hardness ratio varied from place to place, the hardest around 30 Doradus region, and softest around the north-west part of the LMC. They also accumulated spectra from two regions with different values of hardness ratio. Both of the spectra were well described with the optically thin-thermal plasma model with temperature of ~ 0.3 (0.2–0.7) keV (at the north-west part of LMC) and ~ 0.95 (0.65–1.55) keV (around 30 Doradus), respectively. Therefore Wang et al. (1991) proposed that the diffuse X-ray emission was originated from the hot ISM within the LMC.

The interesting correlation between the surface brightness for the diffuse X-ray emission and the neutral hydrogen density was found as is shown in Fig. 3.9. Both of them fall to the field background level near the edges of the LMC, thus defining the extent of the galaxy, and both are brighter in the eastern half of the galaxy, where the optical light is dominated by Population I stars. The most interesting one is an anti-correlation on a scale of 0.5–1 kpc seen between their intensities in Fig. 3.9. Wang et al. (1991) explained that this is consistent with the picture in which X-ray bright areas represent regions in which large cavities filled

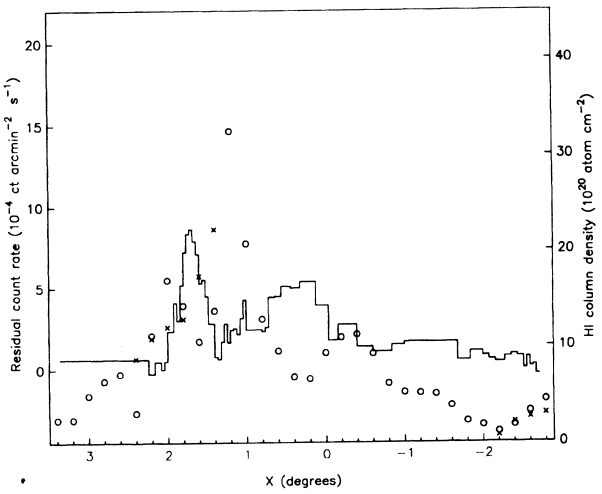

Figure 3.9: A plot of the surface brightness of the diffuse X-ray emission (solid curve) and the neutral hydrogen column density (open circles and crosses) in a slice $12'$ wide through the LMC at declination $-69.^{\circ}59'$ from Wang et al. (1991). The X-axis (in unit of degrees) refers to coordinate adopted by Rohlfs et al. (1984) and center of the LMC bar. The horizontal lines of varying length indicate the regions over which the X-ray surface brightness was determined (so that each has an equivalent statistical uncertainty). The two symbols for the H I distribution represent the two velocity components seen in some directions toward the LMC (open circles = low velocity; crosses = higher velocity). The anticorrelation for the X-rays and H I on scales of 0.5 to 1 kpc ($30'$ to 1°) is apparent, although on a global scale, the eastern half of the Clouds has both a higher H I column density and a higher mean X-ray emissivity.

with coronal gas have been excavated in the neutral interstellar medium by the combined action of stellar winds and SNe arising in spatially correlated massive star formation regions (McCray and Kafatos 1987).

They also estimated the energy budget of the diffuse X-ray emission. From the mean temperature of $\sim 4 \times 10^6$ K and a surface brightness of $S_X = 10^{-4}$ counts arcmin^{-2} s^{-1}, they calculated the total thermal energy of the diffuse X-ray emission within 37 deg^2 field to be $\sim 7 \times 10^{54}$ ergs, where they assumed that the depth of the diffuse X-ray emission to be 1 kpc. They also estimated the cooling time scale by the X-ray radiation and the heating time scale by the combined action of stellar wind and SNe to be $\sim 10^8$ yr and $\lesssim 10^7$ yr, respectively. Because the former is far larger than the latter value, they proposed that substantial amount of the energy which massive stars imparted to their surrounding medium left the galaxy in a form other than thermal radiation from gas at a temperature of 10^6–10^7 K. The rest of the energy should be applied, for example, to the galactic wind, to be deposited in the galactic halo, and so on.

3.7.1 Bubbles, Giant Shells, and Super Giant Shells

The LMC has many bubbles, giant shells (GSs) and super giant shells (SGSs) within its body, with the wide variety of scales; ~ 200 pc to $\gtrsim 1$ kpc. The smallest structure, "bubbles" are made by the stellar wind of one or a small number of massive stars or evolved SNRs, while "GSs" are made by the OB associations within them. The largest structure "SGSs" usually contain stellar populations resultant from multiple episodes of star formation distributed over an extended period of time and surface area. These SGSs are first identified by Meaburn (1980) from the H I observations as is shown in Fig. 3.10. The names of them are LMC 1, LMC 2, ..., and LMC 9, respectively. Among these SGSs, LMC2 and LMC4 were investigated in the X-ray band. Both of them exhibit diffuse X-ray emission. Assuming that they have thermal in origin, Bomans et al. (1994) and Points et al. (2000) derived the temperature of the plasma to be ~ 0.1–0.7 keV and ~ 0.1 keV for LMC2 and LMC4, respectively. The number densitied of the plasmas are obtained to be ~ 0.9–2×10^{-2} cm^{-3} and $\sim 8 \times 10^{-3}$ cm^{-3} for LMC2 and LMC4, respectively.

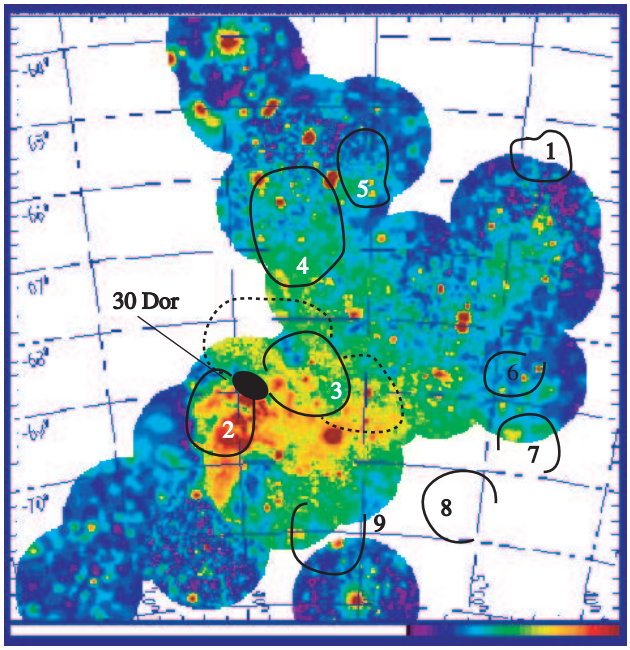

Figure 3.10: The super giant shells in the LMC from Meaburn et al. (1987) overlaid on the ROSAT X-ray map of the LMC. Total of 9 super giant shells are detected with H I observations.

Chapter 4

Instrument

4.1 ASCA

Advanced Satellite for Cosmology and Astrophysics – ASCA – is the fourth Japanese astronomical X-ray satellite, which was launched into orbit on 1993 February 20 by the Institute of Space and Astronautical Science (ISAS), with a perigee and apogee of 520 and 620 km, respectively, and an inclination of 31.1°. The orbital period is approximately 96 min.

The spacecraft mass is 417 kg, and its length is 4.7 m along the telescope axis. The spacecraft is three-axis stabilized; the pointing accuracy is approximately 30″ with a stability of better than 10″. Orientation of the spacecraft is limited by the power constraint that the direction of the solar paddles must be within 30° from the Sun. This limits the observable sky at a time in a belt within which the Sun angle is between 60° and 120°. Thus the entire sky is accessible every half year.

ASCA is equipped with two sets of the Gas Imaging Spectrometers (GISs) and the Solid-state Imaging Spectrometers (SISs) at the foci of four identical thin-foil X-ray telescopes (XRTs). All the XRTs are mounted in the same direction of the sky. The schematic view of the ASCA satellite is shown in Fig. 4.1.

With these instruments the ASCA covers a wide energy range from 0.5 to 10 keV. The general description of the ASCA are given in Tanaka et al. (1994).

4.1.1 X-ray telescope (XRT)

The X-ray Telescope (XRT) onboard ASCA was developed jointly by NASA/Goddard Space Flight Center (GSFC), Nagoya University, and ISAS. It opened the X-ray image with the energy of above a few keV up to about 10 keV for the first time (Serlemitsos et al. 1995).

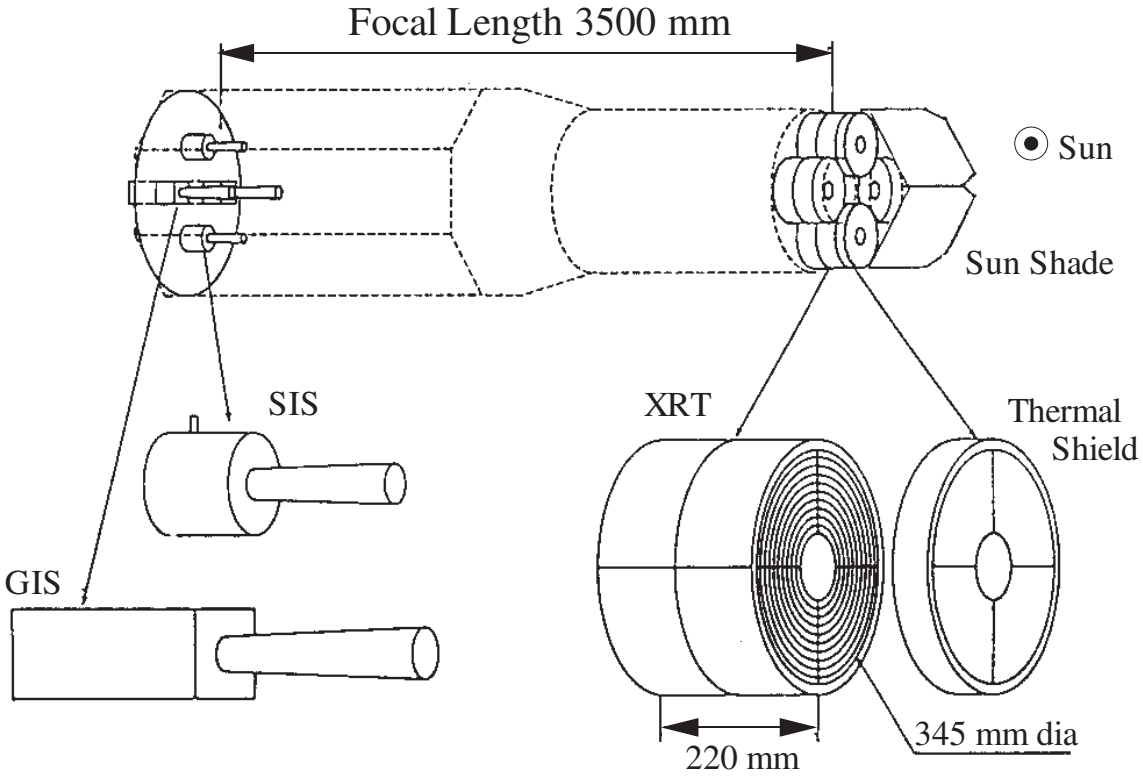

Figure 4.1: Configuration of XRTs and the detectors aboard ASCA.

Soft X-rays are totally reflected off a smooth surface, when their incident angle measured from the surface is shallower than a certain critical value. This phenomenon is known as grazing-incident reflection. The critical angle, typically of order 1 degree or so, is inversely proportional to the X-ray energy and increases with increasing free electron density of the reflecting material. X-ray telescope mirrors use this mechanism, so-called the Wolter type-1 configuration (Fig. 4.2).

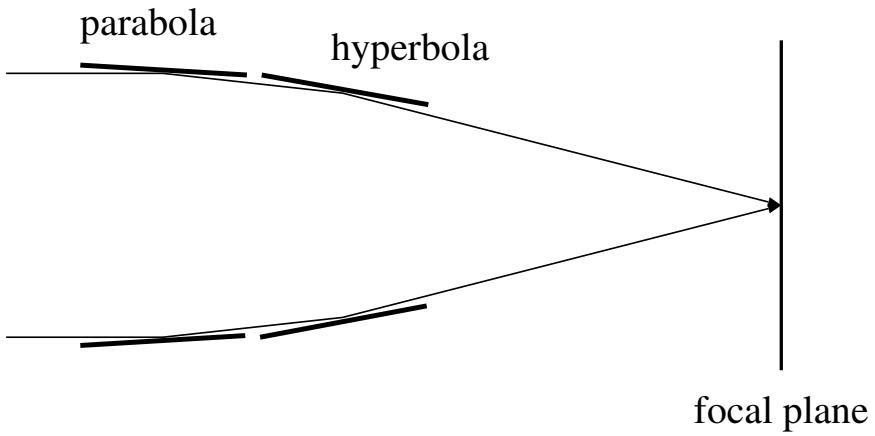

Figure 4.2: Walter type I optics.

In order to remove the first-order abberation, X-ray telescope mirrors employs paraboloid and hyperboloid surfaces as the primary and the secondary mirrors. These two kinds of mirrors have a common focus and reflect X-rays in series.

As the energy of X-ray photons increase it becomes more difficult to reflect them because the critical angle for the total X-ray reflection decreases with increasing the energy of X-ray photons. In order to ensure a high reflectivity for harder X-rays, we must operate the mirror shells under a very small incident angle, hence very small projected area. In order to achieve a high effective area up to higher energies, the number of mirror nesting is increased. This design of mirror is called multiple thin-foil optics. The reflector shells of the ASCA XRT are made of thin (127 μm) aluminum foils, bent in a conical form to approximate paraboloid or hyperboloid. Each foils are $\sim 10\mu$m lacquer-coated to improve the surface smoothness, and adding to that, the gold is evaporated over foils ($\sim 10\mu$m) to increase the reflectivity. One XRT is consists of 4 quadrants, in practice. Each quadrant is consists of 120 of these foils above. Thanks to this design of mirror, XRT has achieved a very large effective area and wide energy range (see Fig. 4.3). The effective area of mirrors depends on photon energy and incident angle as is shown in Fig. 4.4.

Fig. 4.5 shows a point source image (Point Spread Function: PSF) of XRTs. Because the XRTs consist of 4 parts (quadrants), PSF has a shape of 4-leaves pattern. Thanks to the sharp peak of the PSF, we can determine the source position by less than $20''$ at best,

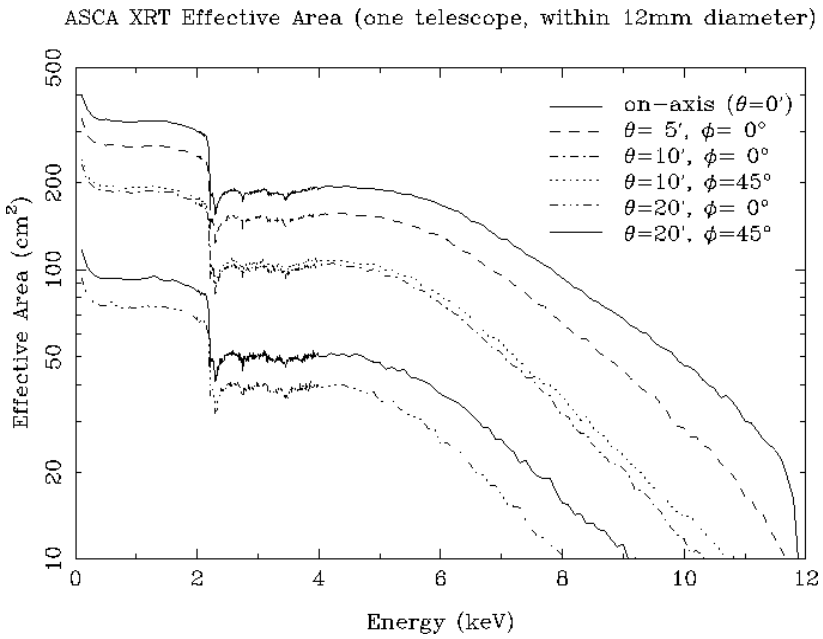

Figure 4.3: Effective area of XRT.

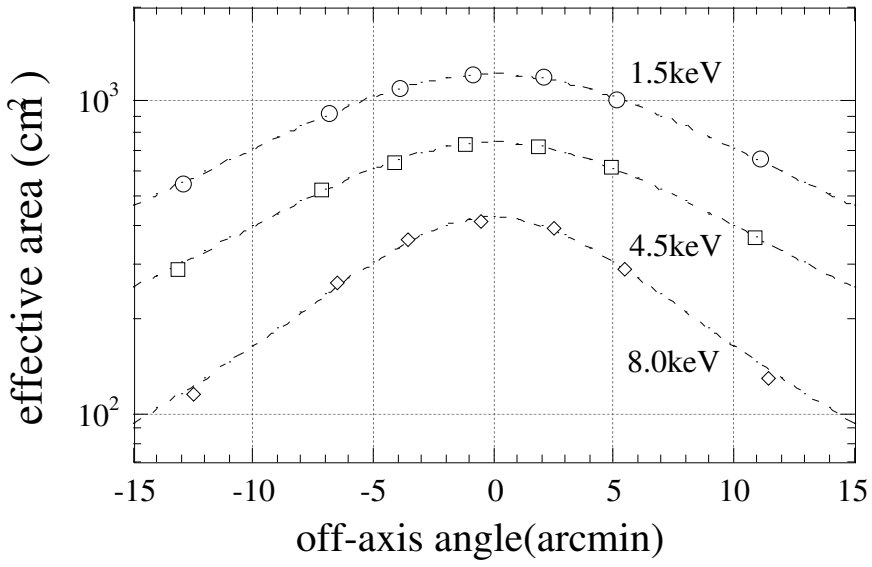

Figure 4.4: Energy and position dependence of ASCA XRT effective area.

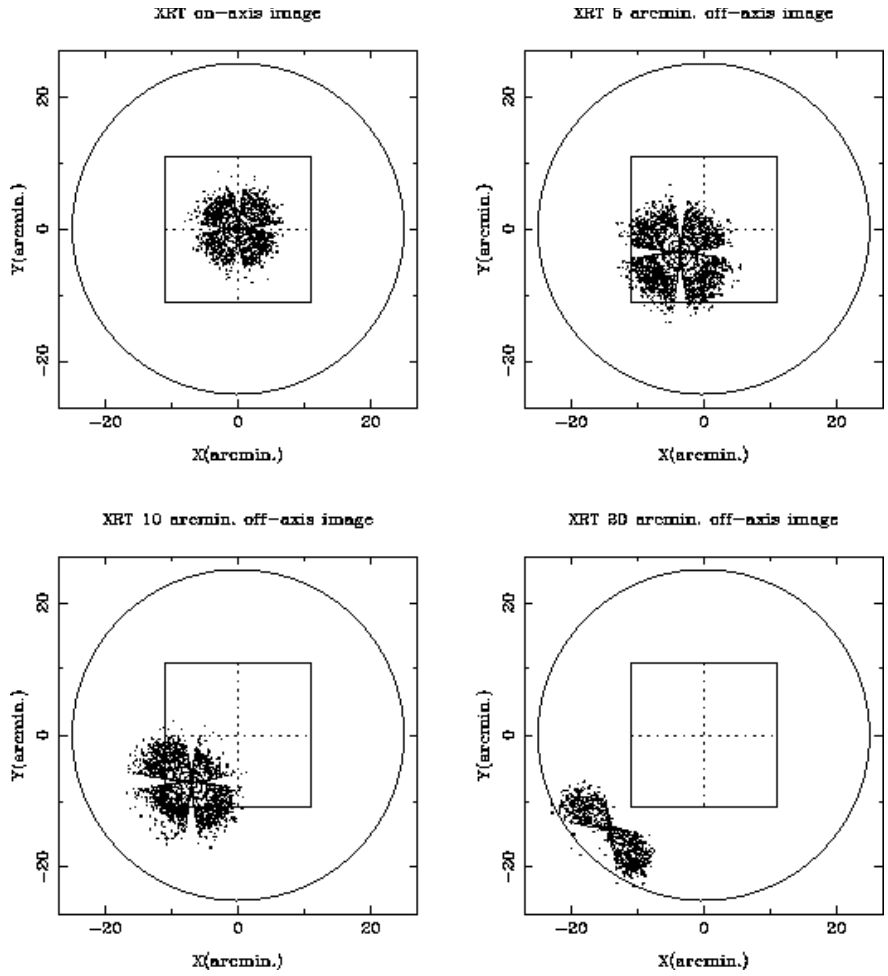

Figure 4.5: Point spread function of the ASCA XRT for four different off-axial angles. Approximate field of view is shown for GIS (circle) and SIS (square).

though PSF has a large outskirts.

The XRT allows some fraction of X-rays to reach the focal plane, even from outside of the fields of view. The X-ray photons are normally undergo the two successive reflections on the primary and the secondary mirrors of the Wolter type I optics. However, those which come from outside of the fields of view have gone through abnormal paths, as are shown in Fig. 4.6. Because both sides of the mirror foils are coated with acrylic lacquer before it is evaporated with gold only on the front side, soft X-rays can be reflected on the backside. These X-rays are called stray lights.

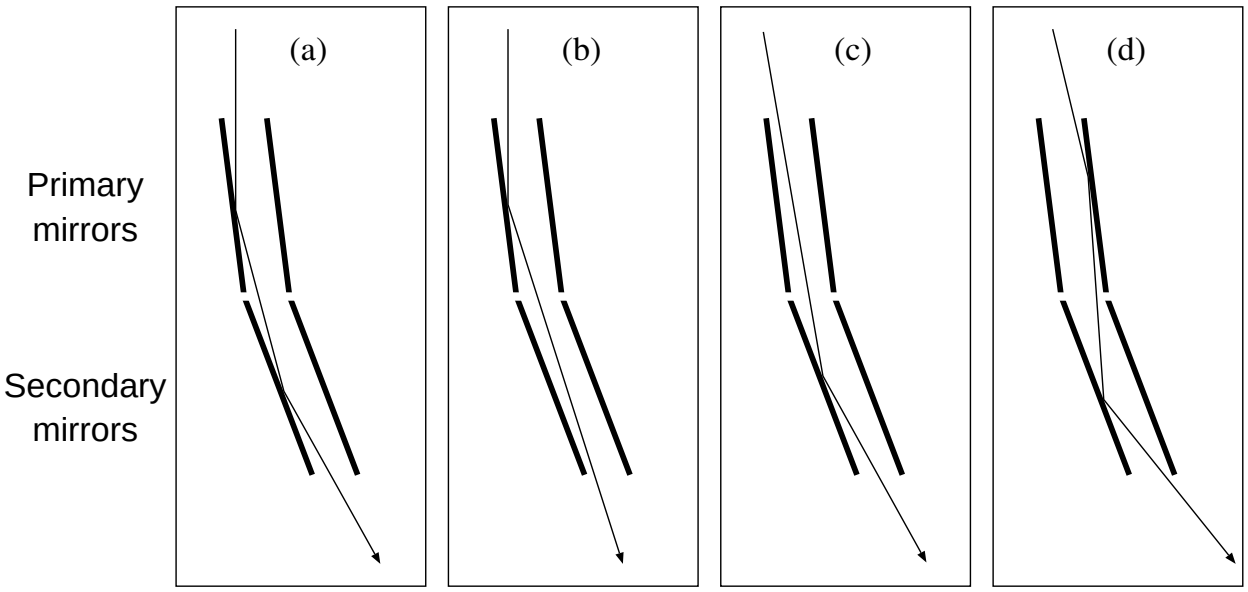

Figure 4.6: Four examples of XRT light paths: (a) normal path, (b) reflection only by primary mirrors, (c) reflection only by secondary mirrors, (d) multiple reflections by front and back surfaces of mirrors.

The stray light does not focus on the focal plane as an usual image. For the case of a point source out of the field of view, the stray light makes a shell-like pattern image depending on the source distance and the angle. In Fig. 4.7 the example of the stray light image from point source out of the field of view is shown. The source of stray light is Crab, which is placed at the position, $60'$ offset from the optical axis in the direction of $\phi = 45°$, $135°$ and $225°$ (Ishisaki 1997). On the other hand, the stray light from largely extended sources like cosmic X-ray background produces no distinct pattern on the image, instead, it extends smoothly over the focal plane, because of the large solid angle (Ishisaki 1997).

The influence of the stray light is not negligible, for the case of the bright point source outside of the fields of view or the case of the largely extended source. For example, in the case of cosmic X-ray background, about the half of the detected photons at the focal plane are originated from the stray light, because they are integrated over large solid angles.

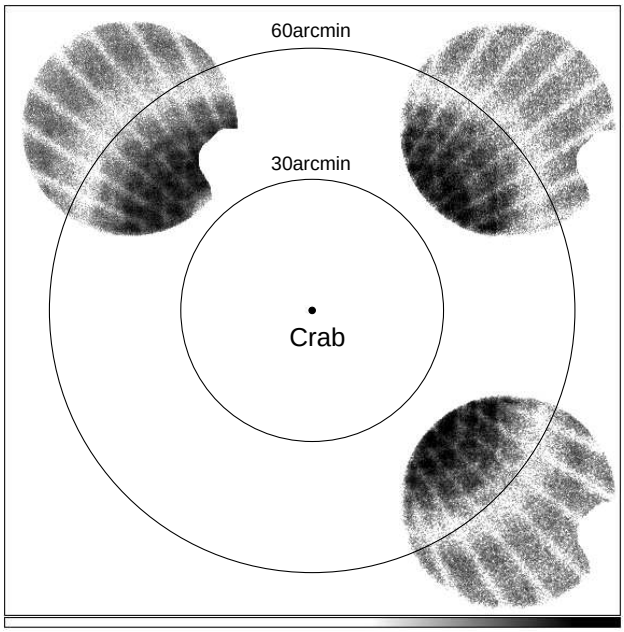

Figure 4.7: Observed stray light structures due to Crab taken with GIS (from Ishisaki 1997).

The ASCA XRT team has developed the ray tracing method to reproduce the stray light structure (Kunieda et al. 1995).

4.1.2 Gas Imaging Spectrometer (GIS)

The Gas Imaging Spectrometer (GIS) is an imaging gas scintillation proportional counter, mainly developed by the University of Tokyo, ISAS, Tokyo Metropolitan University, Meisei Electric Co. Ltd., and Japan Radio Corporation Co. Ltd. (Ohashi et al. 1996; Makishima et al. 1996). The GIS design is mainly based on the GSPC experiment onboard Tenma (Koyama et al. 1984). The structure of the GIS is shown in Fig. 4.8. GIS system consists of two identical detectors, called GIS2 and GIS3, and a signal processing part, GIS-E. Only difference between GIS2 and GIS3 is a radiation belt monitor (RBM) attached to the bottom of GIS2.

The schematic view of the GIS detector is shown in Fig. 4.9. The X-ray photons which enter the gas cell (filled with a mixture of 96 % xenon and 4 % helium) are first absorbed in the drift region, generating primary electrons (at a quantum efficiency of one per 21.5 eV). This electron cloud slowly drifts until it reaches to the intermediate mesh and then accelerated in the scintillation region because of the strong electric field. Because these electrons repeatedly excite xenon atoms, large number of scintillation UV photons are produced ($\sim$ 170 nm in wavelength). Finally these UV photons are collected by the imaging photo-multiplier tube

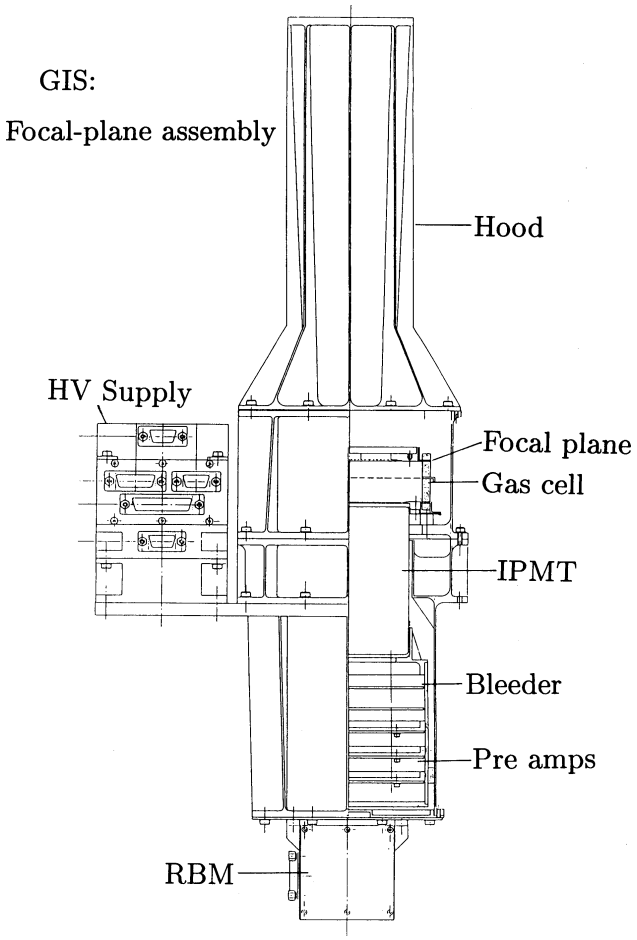

Figure 4.8: The cross section of GIS-S.

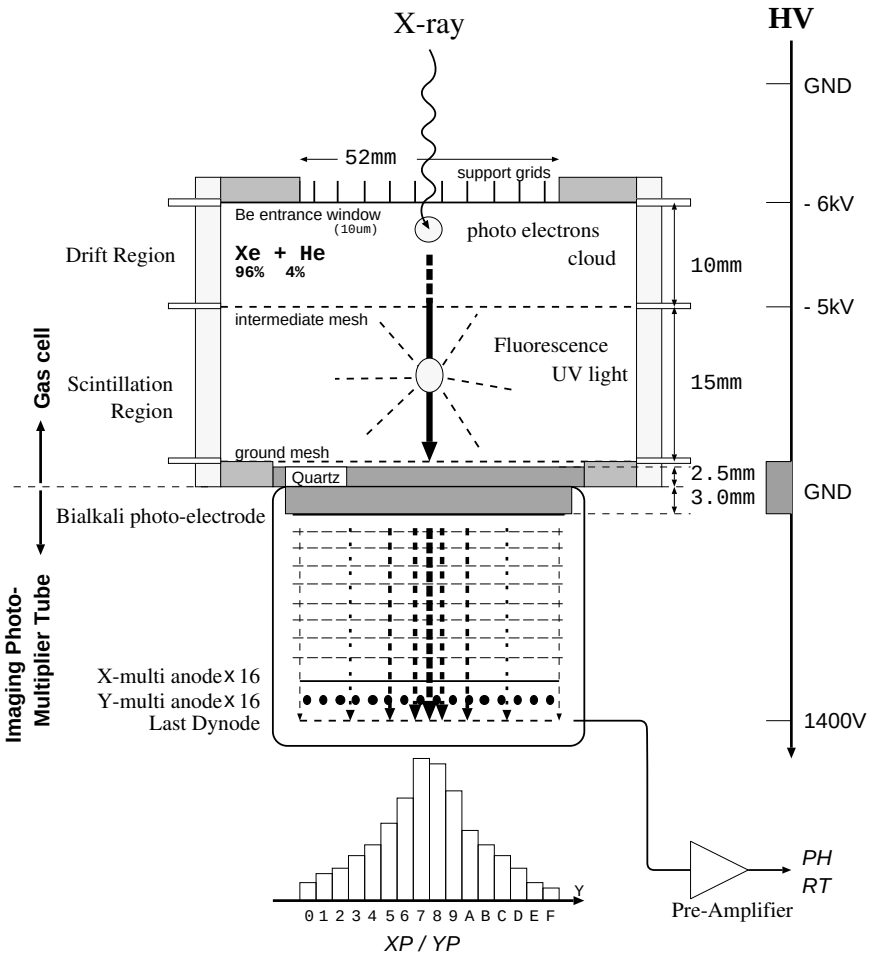

Figure 4.9: Schematic diagram of the principle of the GIS detector.

(IPMT) set below the gas cell. The energy information is obtained from the final dinode signal. The energy resolution is ~ 8 % at 6 keV, which is the highest value ever achieved with a gas counter. X and Y position information of the detected photons are calculated using outputs from 32 (16 for X and 16 for Y) multi-wire anodes, with an accuracy of 0.5 mm at 6 keV. The sensitivity of GIS is down to about 0.8 keV, which is thanks to the thin beryllium window as 10 μm, and up to 10 keV. It has higher efficiency at high energy range (above 3 keV), better timing resolution, and larger field of view than SIS (see the details in next section). GIS achieved a extremely low detector background similar to that of the LAC instrument onboard Ginga (Turner and Pounds 1989). To eliminate non-X-ray backgrounds, only signals with the rise time of limited band are selected to go out to the on-board CPU. With this process, about 90 % of backgrounds within the 2–10 keV band are eliminated. In addition, a certain discrimination method, called SPRD, is used on the CPU to eliminate the events whose position are outer than the certain radius or the spatial distribution of multi-anode output are larger than the certain length. With these discriminations, 99 % of non-X-ray backgrounds are eliminated and the residual non-X-ray backgrounds in the $17'$ radius from the detector center is achieved to be 5×10^{-4} cts s^{-1} cm^{-2} keV^{-1}. In Fig. 4.10 the GIS spectra of day earth, blank sky and night earth are displayed. The night earth data are thought to represent the non-X-ray events.

The gain of the GIS differs from position to position, hence the gain calibration by pointing Cas A in various positions were performed. Because the gain also changes with the pressure and the impurity of the counter gas and the phototube temperature, the gain of the GIS is monitored by the calibration source ^{55}Fe isotopes at the edges of the entrance windows of the each gas cell. In Fig. 4.11 we show the effective area of the combination of XRT and GIS.

The bit assignment for the GIS telemetry data represents the quantity of information on (sensor-ID), pulse height, X-Y position of the X-ray events on the detector, rise time, spread of light, and time stamp for each event. The standard bit-assignment is (1-)10-8-8-5-0-0. The time resolution of the observation can be selected by the observer. The best time resolution is achieved in high bit mode data, while the time resolution get worse by a factor of 8 or 32 in medium or low bit mode data. For standard bit-assignment, the time resolution is up to 65 ms in high bit mode data.

See Ohashi et al. (1996) and Makishima et al. (1996) for more detail of the GIS.

4.1.3 Solid-state Imaging Spectrometer (SIS)

The Solid-state Imaging Spectrometer (SIS) is the first CCD camera for the X-ray astronomy. It was developed under a collaboration of Massachusetts Institute of Technology (MIT), Pennsylvania State University, ISAS, and Osaka University. Each detector consists of a hybrid array of four-edge abuttable frame-store CCDs made at MIT's Lincoln laboratory.

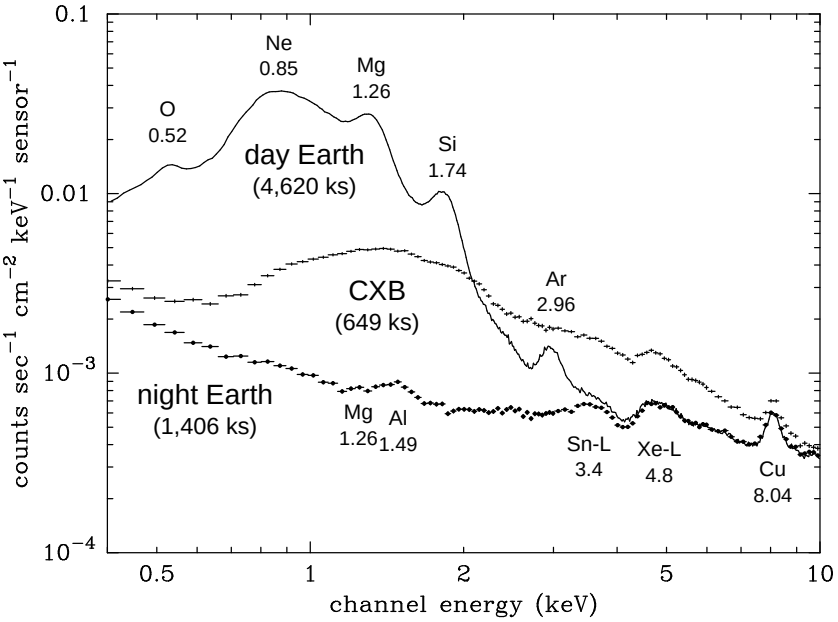

Figure 4.10: GIS spectra of day earth, blank sky and night earth from Ishisaki (1997).

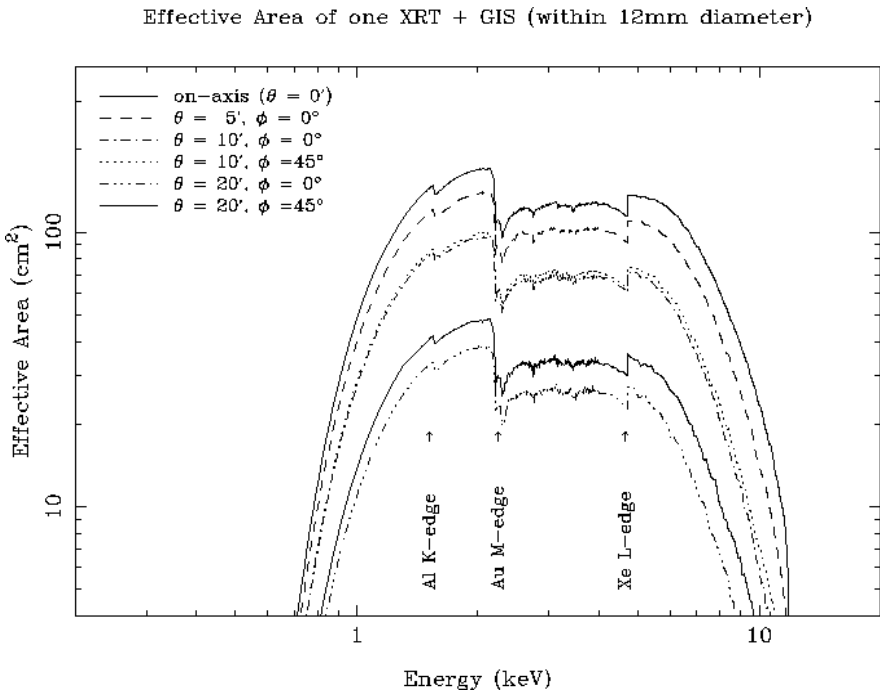

Figure 4.11: The effective area of the combination of XRT and GIS.

The CCD detector can be regarded as a 2-dimension array of solid state detectors. Each CCD has 27×27 μm^2 pixels and 18×24 μm^2 pixels in the imaging and framestore arrays, respectively. Both the imaging and the framestore arrays have 420×420 pixels. Geometrical area of each chip is 11×11 mm^2, corresponding to about $11' \times 11'$. The electron cloud produced by the incident X-ray photon is absorbed by the nearest pixels and carried to the readout gate by the driving external clock. Fig. 4.12 and Fig. 4.13 show the cross section of and the chip configuration of the SIS. Using the Peltier device (thermal electric cooler), the CCD chips are cooled down to -60°C in order to reduce the dark current. In front of the CCD chips, a Lexan film (1000 Å) coated by the aluminum (400 Å) on both sides, called Optical Blocking Filter (OBF), is placed in order to cut off the optical light.

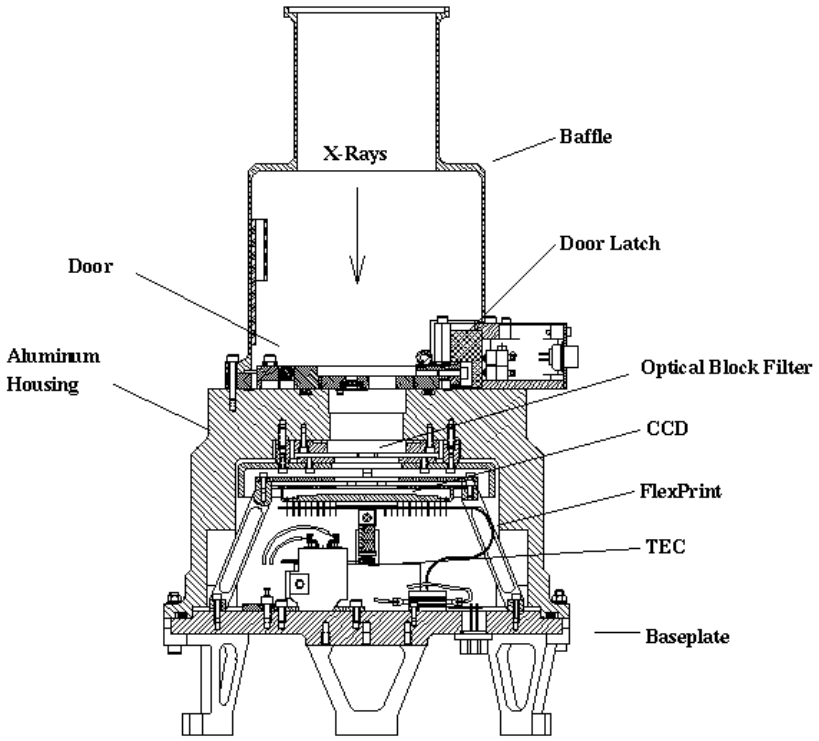

Figure 4.12: The cross section of the SIS camera.

The event extraction is carried out by SIS-DE and SIS-DP. When an incident X-ray photon is absorbed in the depletion layer by photo-absorption process, a primary electron cloud of $\lesssim 1$ μm in size is produced. This primary electron cloud grows in size to $\lesssim 5$ μm as it drifts toward the electrode. Because the sizes of electron clouds at the electrode are still smaller than the pixel sizes, most of the electron clouds are captured by one, two, or, at most four neighboring pixels. The pulse height patterns around the local maximum pulse height pixels are classified into 7 kinds of so-called grades (see Fig. 4.14). We generally regard grade

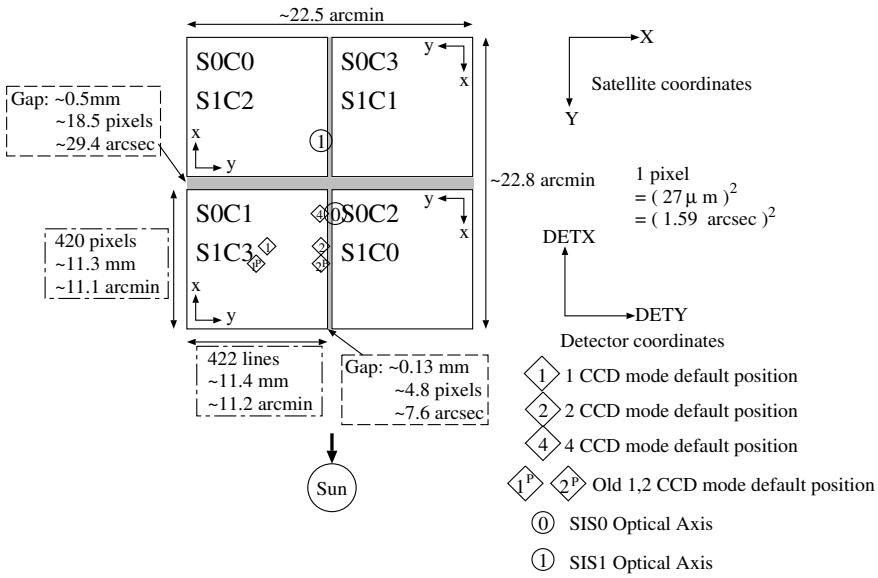

Figure 4.13: The chip configuration of the SIS.

0, 2, 3, and 4 events as X-ray events. On the contrary, charged particle events make a long tracks (long clouds), thus non-X-ray events can be removed from their grade patterns.

The SIS has three kinds of observation modes (FAINT, BRIGHT, and FAST). Here in this thesis, we do not use FAST mode, thus we omit the explanation for it. In the FAINT mode, the event information consists of the CCD ID, the addresses and 12 bit pulse heights of 3×3 pixels around the local maximum pulse height pixel. In this mode, all the pulse heights relating with the events can be obtained. On the other hand, this mode can be used only for the faint sources because of the telemetry limits. In the BRIGHT mode, the pulse heights of 9 pixels are summed up in onboard data processing. In this case, only the summed PH data, the grade information, and the addresses are transmitted.

The SIS can be operated in three clocking modes, 1, 2, and 4 CCD modes. The time resolutions for each clocking mode are 4, 8, or 16 s, respectively. All of the SIS chips can be operated in parallel, although only the selected chips are used in most of the cases in order to avoid the telemetry saturation.

The energy band of SIS detector is 0.4–10.0 keV. Fig. 4.15 shows the quantum efficiency of the SIS. The hard X-ray efficiency is determined by the depletion layer thickness, while the soft X-ray efficiency is limited by X-ray absorption in OBF, the dead layer in the CCD, and other components in front of it. Fig. 4.16 shows the effective area with the combination of the SIS and the XRT.

After the launch, several problems have been recognized with the SIS, such as, "hot pixels", "light leakage" and serious long-term degrading of the SIS performance due to the

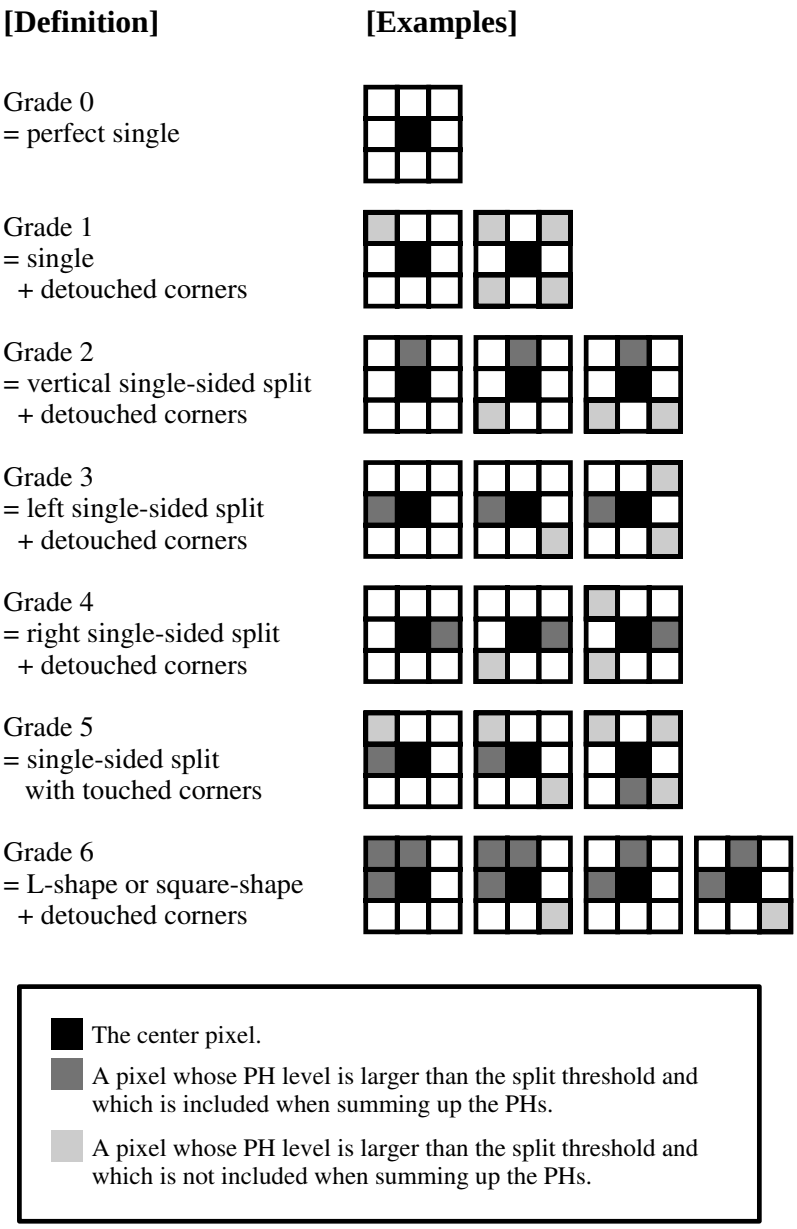

Figure 4.14: Grade definition and the rule to add pulse heights. The events out of these criteria are defined as Grade 7.

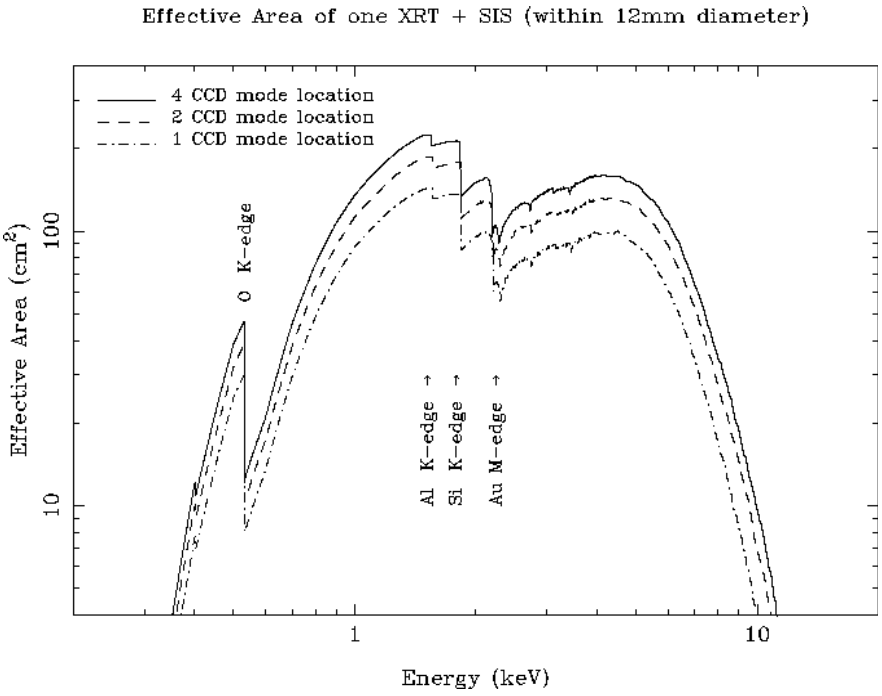

Figure 4.15: The quantum efficiency of SIS detector.

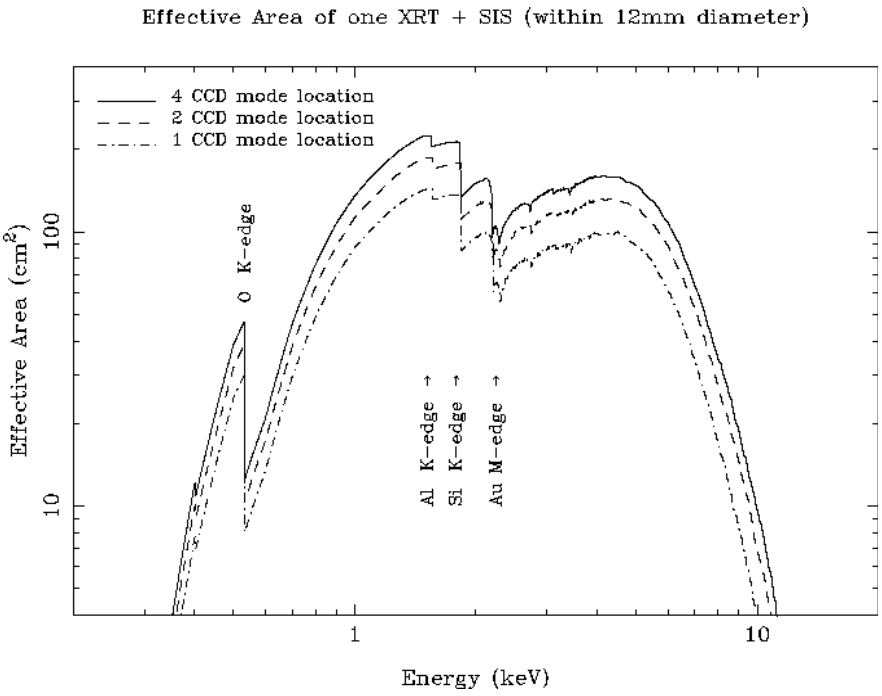

Figure 4.16: The effective area of a single SIS and XRT combined for three off-axis angles (0, 5, 10′).

accumulated radiation damage (Yamashita 1995; Yamashita 1998; Dotani et al. 1997). The "hot pixels" are the particular pixels, though not necessarily fixed ones, which report false event detections too frequently. These hot pixels are removed in the data analysis. Nowadays, because of the increasing of these hot pixels, we cannot obtain usable data in 4 CCD faint mode anymore. The "light leakage" is particularly notable in chip 2 and chip 3 of SIS0, probably caused by the damage in the OBF. When the day Earth is within ~ 25 degree from the target, it is almost impossible to make a observation with these chips. It also increases the dark current of all CCD chips in the daytime. The degradation of the SIS due to the accumulated radiation damage makes the large calibration uncertainty as well as the degradation of energy resolution, the detection efficiency, and the increase of the hot pixels.

4.2 ROSAT

ROSAT, an acronym for the German word *Röntgensatellit*, resulted from a proposal made by the Max-Planck-Institut für extraterrestrische Physik (MPE) in 1975 and developed through a cooperation among Germany, the United States, and the United Kingdom (Trüemper 1982). It was launched into the orbit in June 1990. The ROSAT carried three scientific instruments, Position Sensitive Proportional Counters (PSPC), the High Resolution Imager (HRI), and the XUV Wide Field Camera (WFC) (see Fig. 4.17). The former two kinds of instruments were placed at the foci of X-ray telescopes (XRT), but the WFC had its own mirror system. The XRTs consisted of 4 nested grazing incident Wolter-I mirrors with a maximum aperture of 83.5 cm and a focal length of 240 cm. All of the 8 mirror shells (four nested parabola/hyperbola pairs) are constructed of Zerodur, a glass ceramic with an almost negligible thermal coefficient, and are coated with a thin layer of gold to enhance the X-ray reflectivity. The effective area for X-ray collection was improved upto twice that of Einstein. The ROSAT mission turned off on 12th of February in 1999, however, it provided and have been providing us beautiful scientific results.

The PSPCs are multiwire proportional counters developed by MPE. The detectors provided the energy resolution of $\delta E/E = 0.43(E/0.93)^{-0.5}$ (FWHM) over the entire sensitive area, high spatial resolution ($25''$ at 1 keV) over a 2 degree diameter FOV, and time resolution up to 130 μs. The effective area of XRT/PSPC is down to ~ 0.1 keV.

The HRI was similar instrument to that carried by Einstein. It provided us a $38'$ square FOV, with good spatial resolution, as $\sim 2''$ (FWHM), however, It has no energy resolution.

See ROSAT USER's HANDBOOK 2 for more information about ROSAT mission.

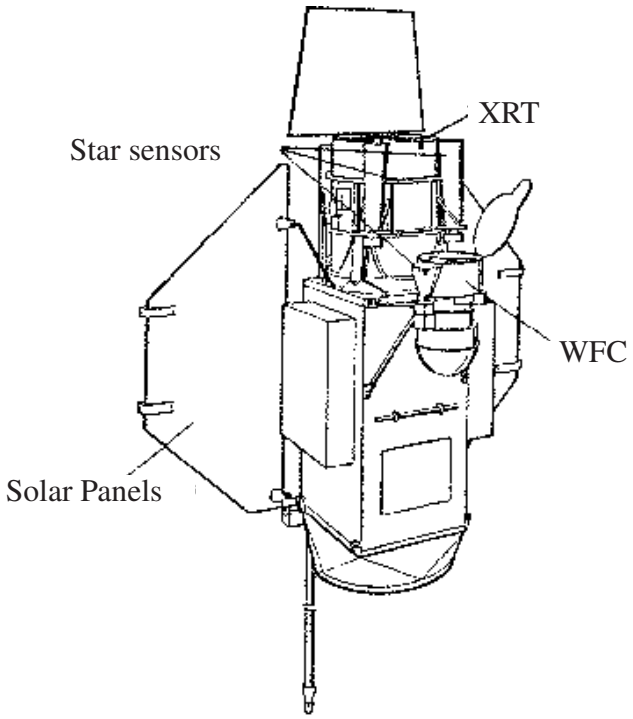

Figure 4.17: Schematic view of the ROSAT spacecraft (from ROSAT USER's HANDBOOK 2).

Chapter 5

Observations and Data Reduction

5.1 Pointing observations and the LMC survey project

ASCA observed the region in the vicinity of the LMC for 60 times since its launch up to Aug. of 2000. All the pointing observations shown in Table 5.1 include all the archival data as well as those which are the products of the LMC survey project. The LMC survey project was our own proposed observations, started in 1998, in the Announce of Opportunity 7 (AO7) observation phase of ASCA, whose original objectives are 1) to make the ASCA complete source catalogue in order to carry a X-ray source population study and 2) to carry out the spectral study of diffuse X-ray emission which widely spreads in the LMC body.

The exposure time of each pointing observation after filtering (see next section) is distributed from $\sim$ 4 ksec to 90 ksec, depending on the primary proposals for each pointing observation. The grand total exposure time of the LMC region is about 600 ksec.

5.2 Data screening (GIS)

Here in this section, we mention about data screening for only GIS data. The observation modes of SIS have many variations depending on the original proposals of each pointing. In addition, the ability of SISs is crucially affected with the radiation damage by charged particles, the amount of which depends on the date of observations (the amount of damage on SIS increases as time). For example, the detection efficiency of the SISs with 4-CCD mode in 1999 Jan. was degraded to only 30%–40% of that with 1-CCD mode in 1993 Dec. before RDD correction (Dotani 1999). Therefore, the way of screening for the SIS data varies from pointing to pointing. We mention about the screening for the SIS data later in the section

in which they are used.

The GIS modes of the observations are all PH mode with the standard bit-assignment (10-8-8-5-0-0) except for some pointings (see Table 5.2). We excluded the data, for example, affected by the South Atlantic Anormaly, earth occulation, and region of low geomagnetic rigidity (the standard criterion used in the ASCA REV2 pipe-line processing. See Table 5.3 for the detail.). We also applied a rise-time rejection to exclude particle events except for the observations which have no rise time information (see Table 5.2). In order to exclude the NXB events as many as possible, we further applied the "flare-cut" criteria (Ishisaki 1997; Ishisaki et al. 1997). Because the energy gain for each GIS changes with the temperature, the observation period, the position, and so on, we corrected the gain into the standard energy-channel relation, using "temp2gain" package with the gain history file released by NASA/GSFC. The telemetry limits for one GIS sensor are 4 c/s, 16 c/s. 128 c/s for low, medium and high bit-rate data, respectively. Almost of all the low bit-rate data are telemetry saturated, thus we did not use them. We used only high and medium bit-rate data in the analyses below.

All the pointing observations are summarized in Table 5.1. GIS fields of views of each observations are displayed in Fig. 5.1.

Table 5.1: Observational log

ID	Date		Coordinates		Exp.†	Name	Remark
	Start (UT)‡	End (UT)‡	*ra* (deg.)	*dec* (deg.)	(ksec)		
1	1995-11-25 /07:11:52	1995-11-26 /07:56:06	73.549	−68.530	4.0E+04	0453-68.5	
2	1993-11-09 /10:58:56	1993-11-10 /00:00:32	76.715	−68.040	2.9E+04	0506-68.0	
3	1993-11-10 /00:01:36	1993-11-10 /11:00:46	77.614	−67.525	2.4E+04	0509-67.5	
4	1993-11-08 /17:41:05	1993-11-09 /01:30:24	80.136	−69.040	1.9E+04	0519-69.0	
5	1997-05-12 /21:40:05	1997-05-14 /00:35:49	83.259	−69.886	3.8E+04	0534-69.9	
6	1993-11-21 /01:14:21	1993-11-21 /15:40:45	84.143	−66.060	1.5E+04	0535-66.0	
7	1997-05-11 /09:06:13	1997-05-12 /21:36:05	85.536	−69.007	4.4E+04	0543-68.9	
8	1995-08-24 /09:16:35	1995-08-25 /05:40:35	87.034	−70.328	1.6E+04	0548-70.4	
9	1993-06-13 /06:15:55	1993-06-14 /07:48:43	84.632	−69.164	3.3E+04	30_DOR	Yes
10	1995-02-03 /14:57:06	1995-02-04 /09:21:50	83.937	−66.954	3.4E+04	A0538-66	Yes
11	1995-10-07 /07:01:55	1995-10-08 /05:14:27	68.018	−61.427	2.3E+04	A3266	
12	1993-11-07 /12:43:45	1993-11-08 /06:30:57	82.390	−65.455	4.2E+04	AB_DRADUS	
13	1993-09-21 /16:39:00	1993-09-22 /11:02:54	85.592	−69.214	2.3E+04	BRIGHT_LMC_REGION	Yes
14	1997-06-21 /10:54:15	1997-06-22 /02:50:33	85.718	−68.309	2.0E+04	CAL83	
15	1996-09-06 /06:00:24	1996-09-08 /08:30:15	86.855	−71.076	6.4E+04	CAL87	
16	1995-10-08 /11:13:23	1995-10-09 /07:50:43	76.649	−67.846	1.3E+04	DEM71	
17	1995-08-25 /05:43:27	1995-08-26 /15:01:18	86.727	−69.127	4.2E+04	LMC-2_POINT_1	
18	1995-04-02 /23:24:13	1995-04-03 /10:40:45	84.667	−69.771	1.7E+04	LMC_X-1	
19	1993-11-09 /01:31:28	1993-11-09 /10:28:26	77.489	−68.730	2.2E+04	N103B	
20	1993-09-23 /00:27:58	1993-09-23 /05:20:14	81.522	−69.571	1.0E+04	N132D_1	
21	1993-09-23 /05:20:46	1993-09-23 /10:05:20	81.470	−69.732	6.1E+03	N132D_2	
22	1993-09-23 /10:05:44	1993-09-23 /17:43:00	80.948	−69.709	9.7E+03	N132D_3	
23	1993-09-23 /18:13:32	1993-09-23 /22:45:01	81.017	−69.546	8.2E+03	N132D_4	
24	1995-03-01 /10:44:51	1995-03-02 /15:20:45	80.478	−68.030	2.3E+04	N44	
25	1994-09-30 /22:58:32	1994-10-01 /08:50:32	85.095	−69.328	1.1E+04	PSR_0540_69_1	Yes
26	1994-10-02 /23:42:45	1994-10-03 /07:00:39	85.088	−69.337	9.1E+03	PSR_0540_69_2	Yes
27	1994-10-11 /06:25:09	1994-10-11 /11:10:29	85.085	−69.332	9.9E+03	PSR_0540_69_3	Yes
28	1994-10-12 /14:15:01	1994-10-12 /19:16:41	85.091	−69.340	9.3E+03	PSR_0540_69_4	Yes
29	1994-11-07 /02:47:26	1994-11-07 /07:17:41	85.090	−69.347	3.8E+03	PSR_0540_69_5	Yes
30	1994-10-01 /08:52:24	1994-10-02 /10:00:55	81.681	−65.943	3.5E+04	SGR0526-66_N49	Yes
31	1993-08-20 /22:54:47	1993-08-22 /02:00:23	84.068	−69.181	3.2E+04	SN1987A_1	Yes
32	1994-05-18 /02:30:54	1994-05-19 /04:30:53	83.616	−69.259	3.4E+04	SN1987A_2	
33	1995-04-23 /00:22:09	1995-04-25 /18:50:11	83.625	−69.264	8.4E+04	SN1987A_3	
34	1995-11-06 /08:10:03	1995-11-08 /12:36:43	84.118	−69.275	7.2E+04	SN1987A_4	
35	1996-11-06 /23:10:15	1996-11-09 /18:30:30	84.114	−69.274	9.2E+04	SN1987A_5	
36	1993-09-23 /22:48:45	1993-09-24 /22:35:25	85.095	−69.336	3.5E+04	SNR0540_693	Yes
37	1993-11-08 /06:34:09	1993-11-08 /14:40:01	62.496	−71.351	8.9E+03	VW_HYI_1	
38	1995-03-06 /12:17:16	1995-03-06 /19:56:06	62.092	−71.355	4.3E+03	VW_HYI_2	
39	1993-09-22 /11:43:00	1993-09-22 /20:53:18	84.932	−64.005	1.2E+04	X-3_1	
40	1995-04-14 /10:21:50	1995-04-15 /02:20:04	84.482	−64.115	1.5E+04	X-3_2	
41	1994-04-26 /09:21:30	1994-04-26 /21:00:04	83.040	−66.368	2.3E+04	X-4_1	
42	1994-04-26 /21:00:20	1994-04-27 /06:53:49	83.041	−66.367	2.0E+04	X-4_2	
43	1995-11-24 /21:33:26	1995-11-25 /07:10:20	83.362	−66.397	1.7E+04	X-4_3	
44	1996-05-24 /10:21:25	1996-05-26 /00:00:21	82.955	−66.308	7.0E+03	X-4_4	
45	1994-10-02 /11:10:53	1994-10-02 /23:05:49	74.893	−75.241	1.1E+04	YY_MEN	
46	1999-04-19 /17:29:39	1999-04-20 /18:59:46	79.252	−69.006	3.6E+04	LMC1	
47	1999-04-20 /18:55:14	1999-04-21 /20:25:02	82.000	−69.095	3.7E+04	LMC2	
48	1999-04-21 /21:01:54	1999-04-22 /21:19:34	81.751	−67.732	3.4E+04	LMC3	
49	1999-04-29 /01:25:20	1999-04-30 /04:24:32	84.779	−68.787	3.3E+04	LMC4	
50	1999-04-30 /10:45:06	1999-05-01 /15:09:03	84.473	−68.792	3.1E+04	LMC5	
51	1999-05-08 /01:31:25	1999-05-09 /04:25:01	83.427	−67.437	3.3E+04	LMC7	
52	1999-06-17 /23:13:24	1999-06-19 /00:10:58	81.242	−70.252	3.7E+04	LMC6	
53	1999-06-19 /00:11:46	1999-06-20 /02:41:06	82.991	−68.087	3.8E+04	LMC8	
54	1999-06-20 /02:41:38	1999-06-21 /04:35:45	84.246	−68.002	2.7E+04	LMC9	
55	1999-04-22 /23:05:44	1999-04-24 /02:20:49	82.726	−71.018	3.8E+04	0532-71.0	
56	1999-11-29 /04:30:45	1999-11-30 /09:10:41	266.72	−30.042	3.2E+04	LMC_10	
57	1999-11-01 /01:26:05	1999-11-01 /17:35:09	266.72	−30.042	1.0E+04	0520_69.4	

(Continuing to the next page.)

Table 5.1: Observational log (Continued from the previous page.)

ID	Date		Coordinates		Exp.†	Name	
	Start (UT)‡	End (UT)‡	*ra* (deg.)	*dec* (deg.)	(ksec)		
58	1999-09-01 /19:20:29	1999-09-04 /14:05:16	266.72	−30.042	8.4E+04	SGR_0526-66_2	Yes
59	1999-10-12 /04:00:02	1999-10-14 /00:10:26	266.72	−30.042	5.7E+04	DEM241	
60	1999-08-27 /14:19:27	1999-08-28 /12:40:46	86.948	−69.637	2.8E+04	0547_69.7	

†: The average of the exposures with GIS2 and GIS3 after the screening.
‡: (Year-Month-Date/Hour:Minute:Second).
§: Remarks; if "yes", GIS bit assignment is different from usual one and described in Table 5.2.

Table 5.2: GIS bit assignment.

ID	GIS bit assignment
9	8-6-6-1-0-10.
10	8-6-6-5-0-6.
13	8-6-6-1-0-10.
25-29	8-6-6-5-0-6.
30-31	8-6-6-1-0-10.
36	8-6-6-1-0-10.
58	8-8-8-5-0-2.

Table 5.3: The selection criteria for GIS data.

SAA	Excluded
GIS_RBMF	Excluded
COR	>4
ANG_DIST	<0.01 && >0
ELV	10
SFR	Excluded
HFR	Excluded

SAA : South Attlantic Anomaly passage
GIS_RBMF : GIS Radiation Belt Monitor Flag
COR : CutOff Rigidity
ANG_DIST : ANGular DISTribution
ELV : ELeVation from the rim of the earth
SFR : Soft Flare Region
(G2_H0+G2_H2+G3_H0+G3_H2<45 & RBM_CONT<100)
HFR : Hard Flare Region
(G2_H0+G2_H2+G3_H0+G3_H2<$0.45\times COR^2-13\times COR+125$)

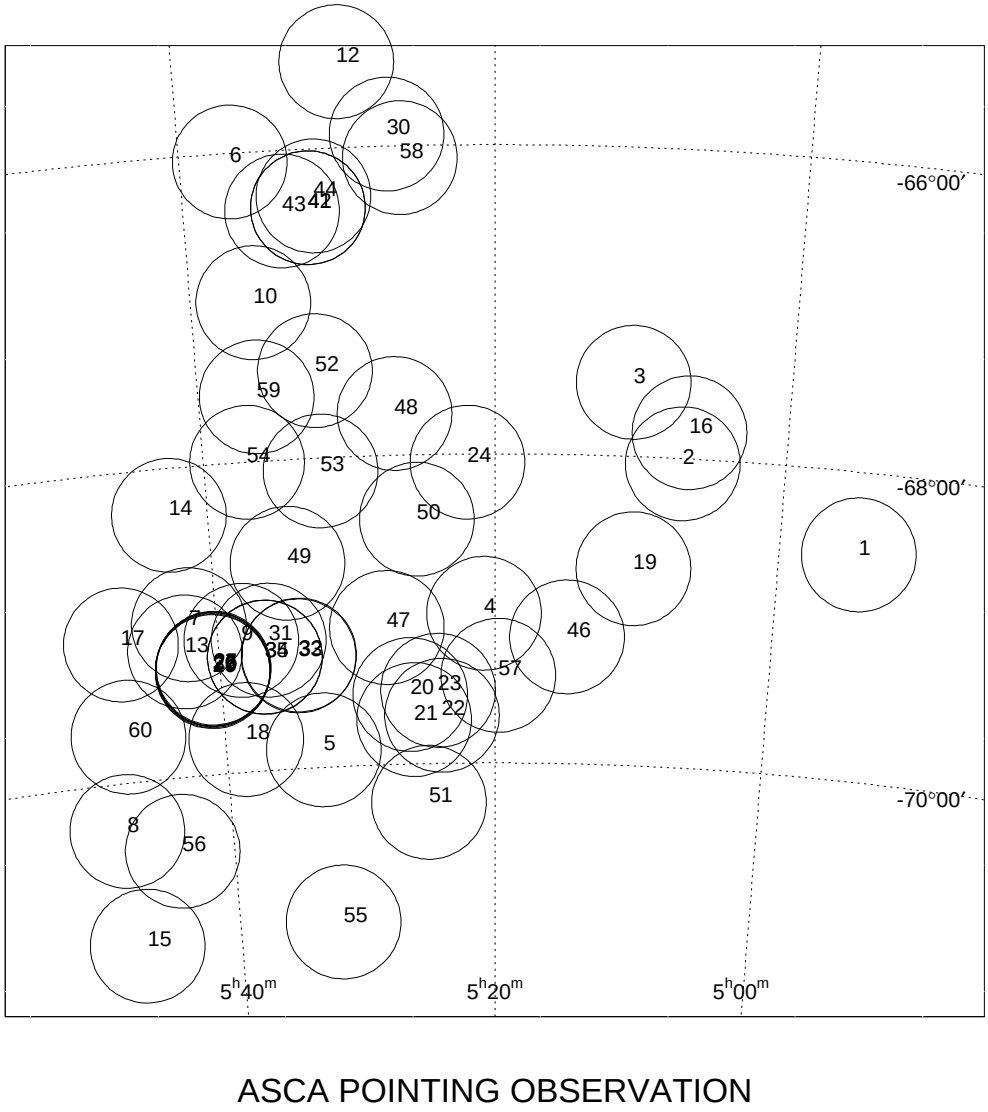

Figure 5.1: The GIS fields of view of all the ASCA pointings in the vicinity of the LMC. Each circle represents GIS field of view. The numbers shown in the ceter of each circle represent the observation IDs.

Chapter 6

Analysis and Results I – X-ray Images and the first ASCA Catalogue

6.1 X-ray Image & Source Extraction

Here in this chapter the overall figure of the LMC revealed from X-ray surveys with ASCA is reported; the X-ray images and the first ASCA catalogue of the LMC.

6.1.1 X-ray Image

In order to construct a mosaic image in wide field, we need to pay careful attentions on superposing many individual pointing images, because the response of the detectors have high dependency on the position on the detectors. In order to minimize this effect, we created X-ray mosaic images of the LMC region in the soft (0.7–2.0 keV) and hard band (2.0–7.0 keV) in the following way;

1. Make an X-ray image of each pointing observation for soft and hard bands along the usual method.

2. Make a mask image to choose the only region we need, namely we want to cut off the nearby region around calibration source, for example. Each pixel of the mask image has the value of either 1 or 0, corresponding to "selected" or "not-selected" pixel. We choose the region we need by multipling the X-ray image by mask image to make a "masked X-ray image".

3. Make a "NXB image" which must be also multiplied by the mask image.

4. Make a "corrected-exposure map image". A corrected-exposure map image is the product of a "raw-exposure map" image and a "efficiency map image". A exposure map image was made simply by scaling up a "masked X-ray image" by the exposure time. A "efficiency map image" expresses the position dependence of the effective area of mirror and the detection efficiency on a detector.

5. Each of the "masked X-ray image", the "NXB image" and the "corrected-exposure image" are convoluted to be the "convoluted X-ray image", the "convoluted NXB image" and the "convoluted corrected exposure image", respectively. The convoluting method is a simple smoothing with a Gaussian filter with $\sigma = 2.5$ pixel ($0.'625$).

6. The "convoluted NXB image" was subtracted from the "convoluted X-ray image" to be an "NXB-subtracted convoluted X-ray image".

7. Make the "NXB-subtracted convoluted X-ray images" and the "convoluted corrected exposure images" for all the pointing observations and both detectors (GIS2 and GIS3), and then, sum them up to make both kind of images for the LMC region (a "mosaic X-ray image" and a "mosaic exposure image").

8. Final convoluted mosaic image is obtained by dividing the "mosaic X-ray image" by the "mosaic exposure image".

Here, we explain more about the items coming up above.

- The mask image As the mask image, the so-called GIS good mask supplied by the GIS team (e.g., Ueda 1996), which excludes the region with higher NXB as well as the calibration isotope, was applied.

- The NXB image We used the night-earth GIS image supplied by NASA GSFC as the NXB image.

- The efficiency map The efficiency map takes account of the difference in detection efficiency, which arises, for example, from the decreasing of XRT effective area and the detection efficiency of GIS detectors themselves as the distance from the detector center increases, and from the supporting grid structure.

  The GIS images of blank sky for the soft and hard bands are constructed from many blank sky fields after all the bright sources have been subtracted (All the data was supplied by Dr. Ishisaki. see Ishisaki 1997). The image obtained by subtracting the NXB image from this blank sky image, is identical with that of Cosmic X-ray background (CXB) taken with GIS, accordingly includes the effects of vignetting by XRT and efficiency of GIS, thus should be regarded as the efficiency map.

Fig. 6.1 and Fig. 6.2 show the X-ray images in the LMC region with energy bands of soft (0.7–2.0 keV) and hard (2.0–7.0 keV) bands. The hard band image of the LMC is revealed for the first time.

6.1.2 Source Extraction

X-ray sources were identified from the soft/hard band images from each observation, with the criterion that the significance below should exceed more than 5σ.

$$\text{Significance} \equiv \frac{(\text{Counts}_{\text{sourceregion}} - \text{Counts}_{\text{BGDregion}})}{\sqrt{\text{Counts}_{\text{BGDregion}}}}. \tag{6.1}$$

Here the $\text{Counts}_{\text{sourceregion}}$ and $\text{Counts}_{\text{BGDregion}}$ are the X-ray photon counts of source region and background region, respectively. The source region was taken mostly as the circular region with radius of $2'$–$6'$ centered on the source. The eccentricity was taken to be larger if the source was located at larger off-axis angle because of the distortion of the point spread function. The background region was, in general, chosen as the annular region with radius of $3'$–$5'$ centered at the source position. However, due to the complicated background by diffuse emission and stray light structures, the background region was, sometimes, carefully chosen manually in order to avoid the effects from them.

The Hardness Ratio (HR)

The hardness ration (HR) was defined as

$$\text{HR} \equiv \frac{(\text{H} - \text{S})}{(\text{H} + \text{S})}, \tag{6.2}$$

where H and S are GIS photon counts after background subtraction in the hard (2.0–7.0 keV) and soft (0.7–2.0 keV) bands, respectively. From the definition of HR, one can easily see that HR takes the value between -1 to 1 and that the harder source takes larger value.

Spectral Analysis

In Fig. 6.3 we show the hardness ratio of the sources in the LMC and SMC as a function of the detected (raw) count rate of GIS in 0.7–7.0 keV. Those plotted in Fig. 6.3 have already known natures such as SNRs or X-ray Binaries (including both pulsating and non-pulsating ones). Yokogawa et al. (2000) established a simple and reliable method of source classification using HR as follows; XBPs fall in a upper region filled with confetti in Fig. 6.3, while thermal SNRs

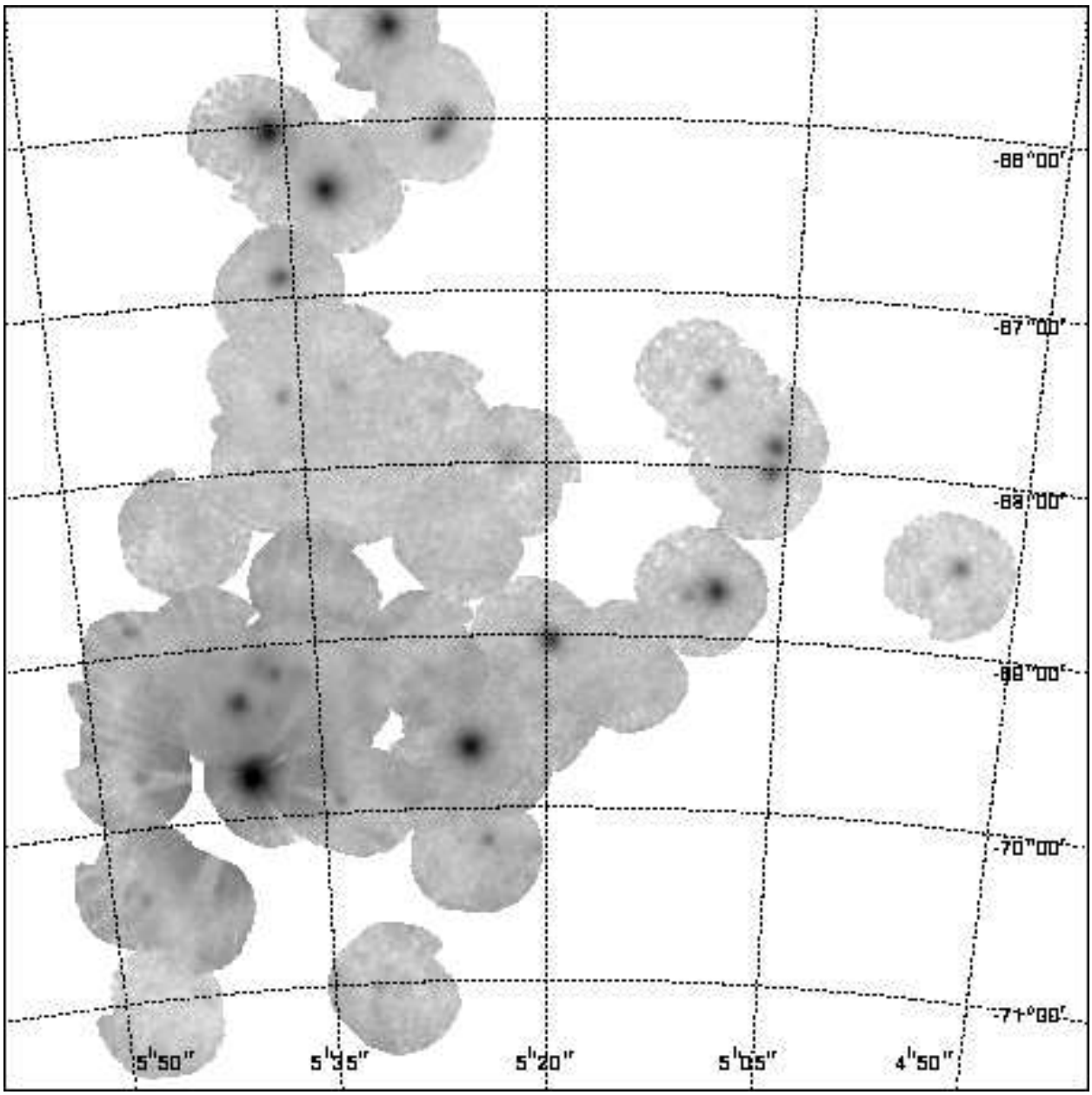

Figure 6.1: ASCA X-ray mosaic image of the LMC for the energy band of 0.7–2.0 keV with the equatorial coordinates (J2000). The color levels are logarithmic. The effects of non X-ray background, telescope vignetting and difference of exposure time among observations were corrected. The complex structure for sources near the edge of the detector fields is due to the point spread function of ASCA XRTs.

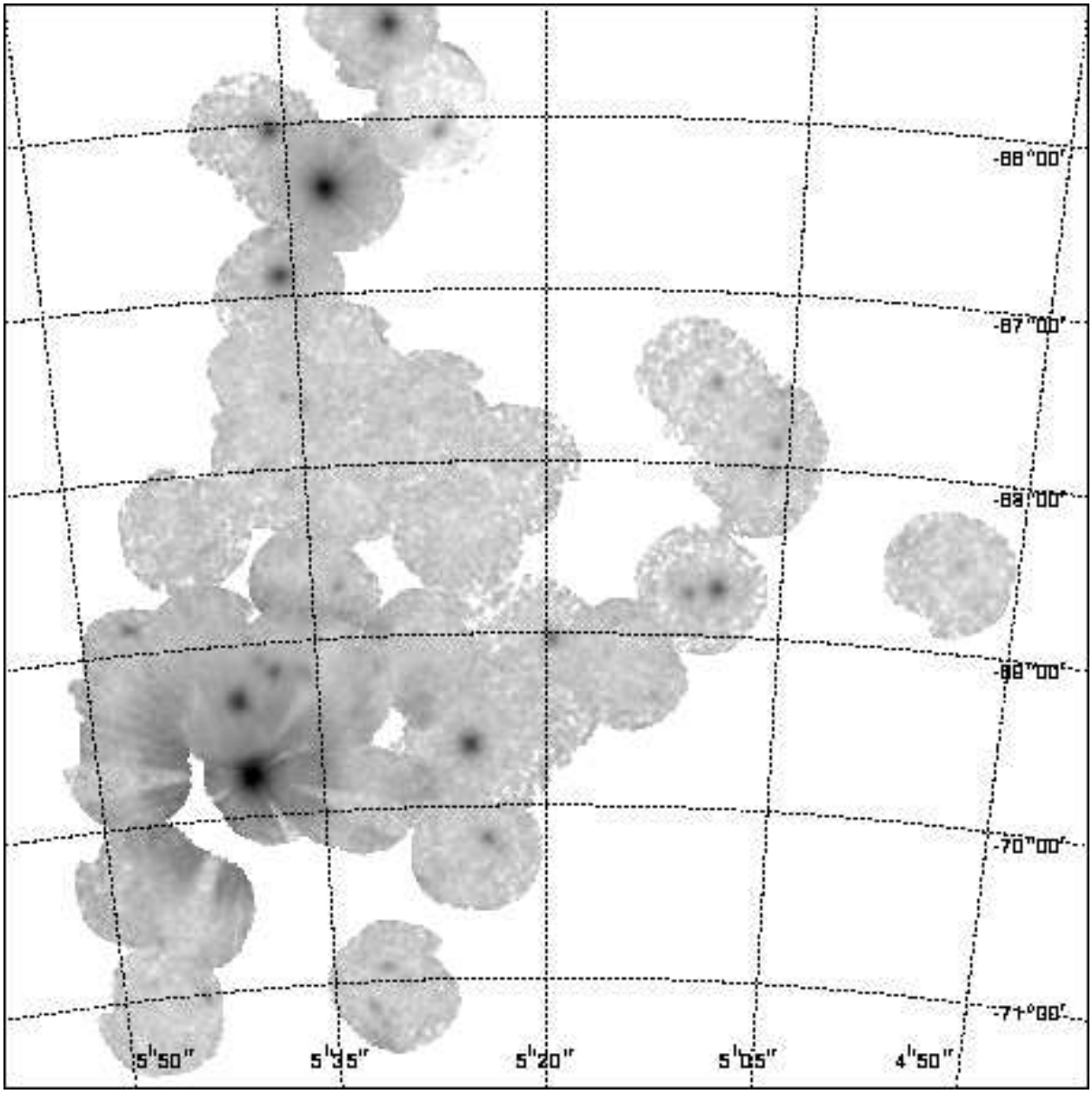

Figure 6.2: ASCA X-ray mosaic image of the LMC for the energy band of 2.0–7.0 keV with the equatorial coordinates (J2000). The color levels are logarithmic. The effects of non X-ray background, telescope vignetting and difference of exposure time among observations were corrected. The complex structure for sources near the edge of the detector fields is due to the point spread function of ASCA XRTs.

fall in a lower region filled with confetti. Therefore, we know the natures of unknown sources from their values of HRs. Sources, such as Black Hole candidates (BHCs), Crab-like SNRs, and AGNs fall between XBP and SNR regions. However, foreground stars are scattered in a quite wide region and part of them fall within the SNR region. From this classification method, we can see many candidates of SNRs or XBPs.

For known XBPs, foreground stars, AGNs and the candidates of them, we carried out simple spectral fittings with absorbed power-law model. For known SNRs and candidates of them, the spectral fitting with absorbed thin-thermal plasma model with Raymond-Smith plasma code was basically carried out with some exceptions, described as follows. The results from this simple spectral analyses are summarized in Table 6.1. For among known SNRs, the ASCA results of spectral analyses for 10 of them were already reported by Hughes et al. (1998) and Hayashi (1997), thus we applied their results. The detailed spectral analyses for additional 9 of them will be presented in the next chapter.

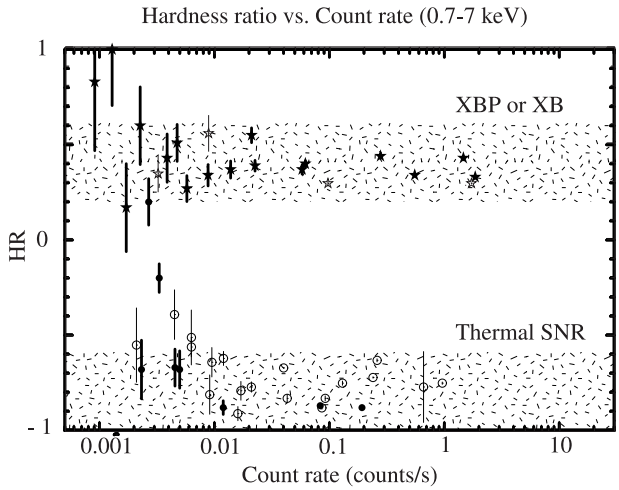

Figure 6.3: The plot of HR as a function of the Count rate for the known LMC and SMC sources. Open and filled symbols represent the LMC and SMC sources, respectively. Stars and circles represent X-ray Binaries (including XBPs) and thermal SNRs.

6.1.3 The 1st catalogue of X-ray sources in the LMC

Consequently 71 sources were found and listed in Table 6.1.
We carried out the identification of each sources with the ROSAT PSPC/HRI catalogues of LMC region, recently supplied in Haberl and Pietsch (1999) and Sasaki et al. (2000). The results are summarized in Table 6.1.

Column 1 Source number. Source extraction is shown in subsection 6.1.2.

Column 2–3 Equatorial coordinates (J2000). Radius of the error circle is $\sim 1'$ for on-axis sources and $\sim 2'$ for sources on the very edge of GIS.

Column 4 HR (hardness ratio) defined in subsubsection 6.1.2.

Column 5–7 Best-fit paramteres derived from the spectral fitting. The absorbed power-law model was applied for HMXBs, AGNs, foreground stars, and their candidates, while the absorbed thin-thermal plasma model was applied for SNRs and their candidates. Photon index Γ, temperature $kT_{\rm e}$ (keV) and column density (10^{21} H cm^{-2}) are presented. Note that more complicated model is applied for sources which are marked with †, *, and ‡.

Column 8 X-ray flux in 0.7–10 keV (erg cm^{-2} s^{-1}).

Column 9 Observed luminosity in 0.7–10 keV (erg s^{-1}).
$L_{\rm obs} \equiv F_{\rm x} \times 4\pi d^2$, where d is assumed to be 50 kpc.

Column 10 Source class.
SNR : Thermal SNR.
SNRc : Thermal SNR candidate.
HMXB : High Mass X-ray Binary.
BHC : Black Hole Candidate.
BP : XBP.
P : Pulsar which is not classified as an XBP.
NH : Non-pulsating HMXB.
UN : Unclassified sources.
FS : foreground stars.
AGN : Background AGN.
stellar : stellar sources.

Column 11 Name of the sources

Column 12 Source number used in ROSAT PSPC catalogue (Haberl and Pietsch 1999).

Column 13 Comments on individual sources.

Table 6.1: The 1st ASCA catalogue of X-ray sources in the LMC.

No.	R.A.	Dec.	HR	Γ	kT_e	N_H	F_X	L_X	Class
1	04 31 22.0	-61 26 20	0.04	1.7(1.7-1.8)	—	0.15(0.12-0.17)	6.1e-11	1.8e+37	HBP
2	04 52 26.1	-68 41 18	-0.11	—	1.83(0.1-7.5)	<5.0	1.7e-13	5.1e+34	UN
3	04 53 37.3	-68 28 58	-0.78	—	0.51(0.37-0.65)†	<0.11	3.5e-12	9.8e+35	SNR
4	04 55 41.6	-68 39 40	-0.56	—	0.65(0.34-1.27)	<0.97	1.8e-13	5.4e+35	SNR
5	05 05 06.9	-67 41 51	-0.35	2.6(1.6-4.8)	—	<1.7	4.9e-13	1.5e+35	UN
6	05 05 27.8	-67 43 07	-0.36	2.8(2.1-4.7)	—	<0.9	4.0e-13	1.2e+35	FS
7	05 05 44.1	-67 52 16	-0.84	—	0.82(0.68-0.96)†	0.04(0.01-0.07)	1.2e-12	3.4e+36	SNR
8	05 05 54.4	-68 01 27	-0.84	—	0.66(0.46-0.88)	<0.28	6.0e-12	1.8e+36	SNR
9	05 06 18.5	-68 15 00.	-0.74	—	—	—	—	—	UN
10	05 08 37.3	-68 02 19	-0.34	2.1(1.3-5.5)	—	<2.3	1.9e-13	5.7e+34	UN
11	05 09 02.6	-68 43 19	-0.64	—	0.67(0.63-0.71)†	0.3(0.28-0.34)	2.0e-11	6.0e+36	SNR
12	05 09 35.3	-67 31 03	-0.68	—	0.20(0.16-0.24)†	0.25(0.20-0.30)	5.0e-12	1.4e+36	SNR
13	05 10 30.3	-67 37 33	-0.09	1.8(1.2-3.4)	—	<0.75	2.1e-13	6.3e+34	UN
14	05 10 46.6	-68 44 53	0.20	—	3.61(2.65-5.41)	0.9(0.8-1.3)	1.1e-12	3.3e+35	SNRc
15	05 12 56.5	-69 20 53	-0.08	2.3(1.4-3.7)	—	<1.3	5.3e-13	1.6e+35	UN
16	05 13 49.3	-69 32 29	-0.32	2.4	—	0.0	6.6e-13	2.0e+35	FS
17	05 19 35.6	-69 01 43	-0.76	—	1.51(1.16-1.86)†	0.11(0.08-0.14)	1.4e-11	3.8e+36	SNR
18	05 19 55.1	-69 26 35	-0.52	—	1.89(1.17-3.51)*	1.37	5.1e-13	1.4e+35	SNR
19	05 22 15.0	-67 56 21	-0.57	—	0.79(0.65-0.87)	0.25(0.13-0.42)	1.4e-12	4.2e+35	SNRc
20	05 23 12.5	-70 15 12	0.18	1.4(0.8-2.6)	—	<1.59	4.7e-13	1.4e+35	UN
21	05 23 57.6	-70 10 42	-0.06	1.7(1.6-1.9)	—	<0.1	2.2e-12	6.6e+35	AGN
22	05 24 01.1	-69 56 50	—-	—	—	—	—	—	UN
23	05 24 52.9	-69 36 38	-0.80	—	0.68(0.62-0.74)†	0.13(0.11-0.15)	1.0e-10	3.0e+37	SNR
24	05 25 26.3	-65 59 25	-0.89	—	0.41(0.35-0.47)†	0.26(0.22-0.30)	1.1e-11	3.2e+36	SNR
25	05 25 59.1	-66 04 35	-0.73	—	0.58(0.53-0.63)†	0.22(0.19-0.25)	2.3e-11	6.3e+36	SNR
26	05 26 35.3	-67 40 16	-0.26	—	1.06(0.30-4.50)	0.90(<3.30)	2.4e-13	7.2e+34	UN
27	05 27 16.8	-65 52 19	0.01	1.8(1.3-2.7)	—	0.0(<1.24)	2.5e-13	7.5e+34	UN
28	05 27 48.8	-68 33 11	-0.51	3.3(2.5-4.5)	—	<0.37	9.8e-13	2.9e+35	UN
29	05 27 49.9	-69 12 15	-0.40	3.4(—)	—	0.38(—)	3.1e-13	9.3e+34	SNR
30	05 28 11.2	-69 28 17	-0.46	2.2(2.0-2.6)	—	0.0(0.0-0.03)	8.6e-12	2.6e+36	UN
31	05 28 23.8	-67 44 08	0.18	1.2(0.7-3.1)	—	0.10(0.0-2.0)	3.4e-13	1.0e+35	UN
32	05 28 47.9	-65 26 42	-0.49	3.1(3.1-3.1)	—	0e00(—)	4.2e-11	1.3e+37	FS
33	05 29 26.5	-68 53 10	-0.63	—	0.62(0.3-0.9)	0.26(0.0-0.62)	7.4e-13	2.2e+35	FS
34	05 29 42.9	-70 59 36	0.02	1.3(0.9-1.8)	—	<0.34	3.4e-13	1.0e+35	UN
35	05 29 50.1	-67 14 41	-0.24	2.1(1.2-3.9)	—	<0.85	4.2e-13	1.3e+35	stellar
36	05 31 03.4	-69 08 33	0.19	—	12.1(>1.0)	16.4(7.5-55.0)	1.4e-12	4.2e+35	UN
37	05 31 06.5	-70 54 33	0.55	1.3(0.9-1.8)	—	1.29(0.42-2.43)	8.4e-13	2.5e+35	UN
38	05 31 08.2	-66 08 00	0.55	0.9(0.3-1.5)	—	<2.6	2.0e-12	6.0e+35	XBP
39	05 31 52.1	-71 00 53	-1.01	—	0.62(0.19-0.56)*	0.10	5.3e-13	1.6e+36	SNR
40	05 32 16.2	-71 08 26	0.22	1.1(0.8-1.6)	—	0.0(0.0-0.60)	8.1e-13	2.4e+35	UN
41	05 32 25.0	-67 31 35	-0.65	—	1.95(1.06-3.58)	<0.30	8.4e-13	2.5e+35	SNR
42	05 32 46.1	-66 22 28	0.28	0.6(0.6-0.6)	—	<0.02	2.6e-10	7.8e+37	XBP
43	05 33 01.7	-67 24 33	-0.23	—	—	—	—	—	UN
44	05 33 18.8	-68 41 55	0.66	1.2(0.3-2.6)	—	3.0(0.3-10.6)	8.8e-13	2.6e+35	UN
45	05 33 55.2	-69 55 10	-0.92	—	0.71(0.52-0.81)*	0.13	1.5e-12	4.2e+35	SNR
46	05 34 30.6	-66 04 53	-0.79	5.7(4.5-9.1)	—	<0.87	1.8e-12	5.4e+35	UN
47	05 34 33.1	-67 38 06	-0.10	2.1(1.3-3.9)	—	<1.92	6.8e-13	2.0e+35	AGN
48	05 34 47.8	-67 01 38	0.16	—	—	—	—	—	UN
49	05 35 22.3	-66 50 39	0.29	1.6(1.3-2.0)	—	<0.06	1.2e-11	3.6e+36	XBP
50	05 35 27.6	-67 52 14	-0.78	—	—	—	—	—	UN
51	05 35 38.3	-69 11 40	-0.03	2.6(2.0-3.5)	—	0.55(0.31-0.83)	8.4e-13	2.5e+35	SNR
52	05 35 41.6	-67 34 38	-0.31	—	4.80(3.47-6.18)*	0.15	9.6e-13	2.7e+35	SNR
53	05 35 47.5	-66 14 44	-0.31	2.4(2.0-3.2)	—	<0.36	1.7e-12	5.1e+35	FS?
54	05 35 48.8	-66 01 49	-0.78	—	0.62(0.58-0.66)†	0.14(0.13-0.15)	7.1e-11	2.0e+37	SNR
55	05 36 09.5	-68 05 10	-0.07	2.0(1.4-2.8)	—	<1.07	2.6e-13	7.8e+34	UN
56	05 37 40.9	-69 10 27	0.07	—	13.1(???)	0.0(0.0-0.08)	8.8e-12	2.6e+36	SNR
57	05 37 45.7	-67 59 20	0.32	1.0(0.5-2.5)	—	<2.31	3.6e-13	1.1e+35	UN
58	05 38 13.6	-69 22 46	-0.35	2.8(2.6-3.1)	—	<0.08	1.2e-12	3.6e+35	FS
59	05 38 23.1	-69 05 40	-0.48	2.9(2.8-3.0)	—	0.0(0.0-0.03)	4.0e-12	1.2e+36	R140a2+Mrk34

(Continuing to the next page.)

Table 6.1: The 1st ASCA catalogue of X-ray sources in the LMC. (Continued from the previous page.)

No.	R.A.	Dec.	HR	γ	$kT_{\rm e}$	$N_{\rm H}$	$F_{\rm X}$	$L_{\rm X}$	Class
60	05 38 41.3	-68 53 54	-0.86	—	0.49(0.10-0.82)	0.09(<0.90)	1.2e-12	3.6e+35	FS?
61	05 38 54.9	-64 05 48	-0.17	3.0(2.9-3.1)	—	0.27(0.24-0.30)	4.3e-10	1.3e+38	HMXB(BHC)
62	05 39 54.6	-69 44 07	-0.01	2.7(2.5-2.8)	—	0.7(0.6-0.8)	5.7e-10	1.7e+38	HMXB(BHC)
63	05 39 59.6	-69 19 55	0.03	2.0(1.9-2.0)	—	0.4(0.3-0.4)	3.5e-11	1.1e+37	SNR
64	05 41 03.9	-70 40 27	-0.67	—	—	—	—	—	UN
65	05 41 21.2	-69 31 00	—	—	—	—	—	—	UN
66	05 44 05.1	-71 00 27	0.34	2.1(1.4-2.9)	—	1.6(0.7-2.8)	9.9e-12	3.0e+36	XBP
67	05 46 49.2	-68 51 29	-0.07	2.6(2.3-2.9)	—	0.75(0.51-1.03)	3.1e-12	9.3e+35	UN
68	05 47 02.3	-70 39 51	0.13	2.7(1.0-7.4)	—	1.15(<5.7)	2.2e-13	6.6e+34	UN
69	05 47 06.3	-69 41 43	-0.80	—	0.56(0.40-0.76)‡	0.27(0.07-0.49)	1.42-12	4.1e+35	SNRs
70	05 47 41.4	-70 24 31	-0.82	—	0.77(0.64-3.03)*	0.26	7.7e-13	2.3e+35	SNR
71	05 48 11.8	-70 18 46	-0.02	2.6(1.4-6.2)	—	<4.5	1.4e-13	4.2e+34	UN

† Results from Hughes et al. (1998) and Hayashi (1997). The model used in the spectral fitting is peculiar Sedov model (see section 3.6.2).

* The model used in the spectral fitting is Masai model (see Chapter 7 for the further details.).

‡ This object is consists of two SNRs, however, it is impossible to divide them with the poor spatial resolution of GIS. Here, we tentatively display the fitting results with Masai model for the spectrum including the X-ray photons from both of the SNRs. With SIS, the photons from each SNRs could be separated. See Chapter 7 for these results.

Table 6.2: The 1st ASCA catalogue of X-ray sources in the LMC.

No.	name	PSPC No.	Comments
1	A3266		
2		702	
3	SNR 0453-68.5	670	
4	SNR LHA 120-N 86	696	
5			
6	GSC 9161.1103	568	
7	SNR DEM L 71	592	
8	SNR LHA 120-N 23	614	
9		635	
10		615	
11	SNR LHA 120-N 103B, RX J0509.0-6844	707	
12	SNR 0509.0-67.5	542	
13			
14	CAL17	712	
15			
16	K1V RXJ0513.7-6932	943	
17	SNR 0519-69.0	789	
18	SNR 0520-69.4, RX J0519.8-6926	915	
19		603	SNR (s)? in HII complex LHA 120-N 44
20		1109	hard classify source in Haberl and Pietsch (1999)
21	AGN RXJ0524.0-7011	1094	z=0.151
22			
23	SNR LHA 120-N 132D, RX J0525.0-6939	977	
24	SNR LHA 120-N 49B	219	
25	SNR LHA 120-N 49	241	
26			
27		186	unknown source in Sasaki et al. (2000)
28			
29	SNR 0528-69.2	836	
30			
31	CAL41		
32	fgstar K0, AB Dor, HD 36705	122	
33	fgstar G2IV, HD 269620 RXJ0529.5-6852	749	
34			
35	stellar W529.8-6716, GSC 8891.3619	494	
36			
37			
38	EXO053109-6609	252	HMXB Be/X transient pulsar
39	SNR LHA 120-N 206, RX J0531.9-7100	1222	
40			
41	SNR? 0532-67.5, RX J0532.5-6731	540	
42	LMC X-4, HD269743 O8III	316	HMXB pulsar
43			
44			
45	SNR 0534-69.9, RX J0534.0-6955	1043	
46			
47	AGN RX J05348-6739, W534.9-6741?	561	z=0.0720
48		462?	HMXB?
49	A0538-66	436	HMXB Be/X transient pulsar
50			
51		840	SNR 30 Dor C brightest knot in X-ray ring No.270 in Sasaki et al. (
52	SNR DEM L 241 (C97), RX J0536.0-6735	551	variable
53	fgstar dM4e?	268?	
54	SNR LHA 120-N 63A, SNR0535-66.0	226	
55			
56	DEM L 263, RX J0537.8-6911, PSR0534-69.9 PSRJ0537-69 , SNR LHA 120-N157B, RASS254	826	Clab-like SNR ,16ms pulsar
57			
58	RXJ0538.3-6924(?)	902	

(Continuing to the next page.)

Table 6.2: The 1st ASCA catalogue of X-ray sources in the LMC. (Continued from the previous page.)

No.	name	PSPC No.	Comments
59	R140a2+Mrk34		
60	RXJ0538.6-6853, G2V	752	RS CVn?
61	LMCX-3	41	HMXB(BHC)
62	LMCX-1	1001	HMXB(BHC)
63	PSRB0540-69, SNR LHA 120-N158A	877	Crab-like SNR, 50ms pulsar
64			
65			
66	RX J0544.1-7100, 1SAXJ0544-71	1225	96ms pulsar, HMXB
67		747	hard souece (Haberl and Pietsch 1999)
68		1179	hard source (Haberl and Pietsch 1999)
69	DEM L316 shell A and shell B		each shells are resolved only in SIS data
70	SNR 0548-70.4	1137	
71			

Chapter 7

Analysis and Results II – Comments on specific SNRs

For the LMC SNRs, the X-ray observations with good imaging capability, such as ROSAT, had been extensively carried out. However, the spectral analyses of those SNRs with good spectral resolution have not been completed yet. The total number of the LMC SNRs observed with ASCA, which are bright enough for the spectral analysis, is 19. However, the spectral analyses have been carried out only for 10 of these (0509−67.5, N103B, 0519−69.0, N23, N49, N63A, DEM L71, N132D, 0453−68.5, N49B; hereafter sample-2) by Hayashi (1997) and Hughes et al. (1998) (also see the previous section 3.6.2). Here in this chapter, we report the spectral results of the rest of the SNRs (hereafter sample-1 SNRs; DEM L316A, DEM L316B, 0532−71.0, 0548−70.4, 0534−69.9, DEM L241, 0520−69.4, 0532−67.5, and N86) in order to complete the systematic spectroscopy of the LMC SNRs.

7.1 Introduction of individual SNRs

7.1.1 DEM L316A and DEM L316B

This emission nebula is of considerable interest, as it shows two overlapping shells at radio and optical wavelengths. These shells are called SNR 0547–69.7A and SNR 0547–69.7B, respectively (hereafter shell A and shell B). It has been proposed that these twin shells are (1) two independent remnants superposed along the line of sight (Mathewson and Clarke 1973), (2) a single SN that exploded into an interconnected bubble formed by a stellar wind or previous supernovae (Lasker 1981; Mills et al. 1984), or (3) "colliding remnants" (Williams et al. 1997). Because of the similarity in their mean radial velocities, some authors (Lasker 1981; Williams et al. 1997) have argues that the two shells are physically co-located. In fact

the individual mean radial velocities of the two shells are only poorly constrained, largely because they each come from averaging over the complex velocity field of an incomplete SNR shell expanding at a velocity of ∼200 km s^{-1} (Williams et al. 1997). Unfortunately Williams et al. (1997) did not assess quantitatively the level of difference in mean velocity of the two shells allowed by their data. These authors also found enhanced [O III] emission and a change in the magnetic field structure in the region between shell A and B, from which they inferred that the two shells in DEM L316 were indeed colliding SNRs.

7.1.2 SNR 0532−71.0

SNR 0532−71.0 is located near the OB association LH69 (∼ 80 pc) and in H II region DEM L221, thus considered to be a Population I [1] object. The radio spectral index was obtained to be −0.33 (Mathewson et al. 1983). Chu and Kennicutt (1988a) observed this with echellogram and found a continuous distribution of velocities, suggesting the presence of material that has fallen considerably behind the shock front. Williams et al. (1999) reported that this object shows quite large size (∼ 27 pc) and that it can be classified as the best candidate for a centrally brightened SNR in the X-ray band. Both of the results from optical and X-ray observations agree well in that it is a quite old remnant.

7.1.3 SNR 0548−70.4

SNR 0548−70.4 is one of the Balmer-dominated SNRs (the detail explanation for the Balmer-dominated SNR is in section 7.4.3) in the LMC, therefore, it is considered to be a Population II object. It has no spatial correlation with H II region nor OB association (Chu 1997). It is very faint in radio band (Mathewson et al. 1983) and only upper limit is obtained (< 0.19 Jy at 408 Hz). It shows patchy X-ray emission incompletely covering the face of it, thus is categorized in diffuse-face SNR (Williams et al. 1999). From the optical observations, Smith et al. (1991) showed that the shock velocity is relatively rapid as 500–1100 km s^{-1}. However, the outer shell is not clearly seen in X-ray band (Williams et al. 1999).

7.1.4 SNR 0534−69.9

SNR 0534−69.9 has more or less uniform (amorphous) image in optical band (Mathewson et al. 1983). It has also amorphous morphology in X-ray band, thus Williams et al. (1999)

[1] Population I stars contain much heavy elements while Population II stars (hereafter Pop I and Pop II, respectively) contain much. At the same time, Pop I stars are quite young, while Pop II stars are old. Therefore, that the more recent the stars are formed, the more heavy elements are contained in the gas which becomes the seeds of the stars, because more and more heavy elements are produced during the course of chemical evolution of the galaxy. The Pop II stars mostly consist of low-mass stars, which can survive longer.

categorized this SNR into diffuse-face SNR. It is located near an OB association, LH80. The radio spectral index is −0.60 (Mathewson et al. 1983).

7.1.5 DEM L241 (SNR 0536−676)

Mathewson et al. (1985) found that DEM L241 shows typical looped filamentary structure of an SNR in optical image. The [S III] to H α ratio is 0.6, which supports the identification that it is an SNR (Mathewson et al. 1985). The optical size was determined to be 1.6′ in radius (Mathewson et al. 1985).

A study of the echelle spectrum by Chu (1997) shows a relatively small expansion velocity and a large intrinsic velocity width, implying that the SNR may be expanding within the stellar-wind blown cavity, which suggests that the progenitor of DEM L241 is likely to be a massive star. Because ROSAT HRI did not make an observation of this object, no X-ray image with good spatial resolution exists.

7.1.6 SNR 0520−69.4

SNR 0520−69.4 is categorized in diffuse face SNR by Williams et al. (1999), showing fairly uniform X-ray distribution with some brighter patches. It has no spatial correlation with any OB associations nor H II regions.

7.1.7 SNR 0532−67.5

SNR 0532−67.5 was identified by its radio morphology and X-ray emission by Mathewson et al. (1985). The Hα image shows patchy diffuse emission over the field of view with little correspondence to the radio source. While the radio structure is suggestive of an SNR of diameter about 56 pc, it may also be possible to be a radio galaxy. The radio spectrum is compatible with either the SNR or the radio galaxy interpretation. Chu (1997) considered the SNR identification to be a more likely possibility because of its proximity to the OB association LH75. They suggested that the lack of optical counterpart of this SNR may be a result of a gas-poor environment. Therefore it is possible that it is an SNR in the superbubble blown by, but no longer ionized by, LH75.

7.1.8 N86 (SNR 0455−68.7)

This SNR is of much interest because it is considered to be a site showing a "breaking out" structure into its ambient medium. It is a large remnant with an optical angular diameter of

about 4′ showing very irregular morphology. Lasker (1977) observed northern and southern extensions of N86 with [O III] and [S II] to find that those parts represent breakouts of the expanding shell into a nearby region of low density within the ISM. A MOST observation by Mills et al. (1984) revealed that the radio spectral index of N86 was not as steep as those seen in most of the remnants in the LMC. Their explanation for this was that the radio flux density might be diluted by thermal emission. Williams et al. (1999) observed this SNR with optical, radio, and X-ray (ROSAT) wavelengths. The images taken in these wavelengths resemble with each other quite well. Optical image shows filamentary structures and a large jetlike feature extending to the north. From the Hα velocity, the age of N86 was approximated to be $\sim 8.6 \times 10^4$ yr assuming Sedov expansion. Their X-ray spectral analysis with ROSAT PSPC instrument revealed that the X-ray spectrum of N86 could be reproduced with an absorbed thin-thermal plasma model of $kT_{\rm e} \sim 0.2$–0.4 keV and $N_{\rm H} \sim 10^{21}$ cm^{-2}. The electron density was estimated to be ~ 0.16–0.49 cm^{-3}. The Sedov age estimated with the X-ray observation was ~ 2–5×10^4 yr. They also suggests that N86 may have expanded rapidly in its earlier stages, invalidating the simple Sedov relation, and would therefore be younger than its size would suggest. The H I column density found by Kim (1998) supports the picture, that it was exploded within very low density ambient medium, as it is on the low end of the overall LMC range.

7.2 Observations & Data screening

ASCA observed these SNRs at the time as is shown in Table 7.1. The observations were carried out both with GIS and SIS detectors. The modes for the SIS at each observation are also shown in Table 7.1.

The GIS data were screened with the criteria shown in section 5.2, so we do not repeat them here again. The SIS data were first screened with the usual criteria: data obtained during South Atlantic Anomaly passages, with a cut-off rigidity lower than 4 GV, or with an elevation angle to the limb of the Earth less than 5° were rejected. In addition, we also rejected events obtained when the elevation angle to the limb of the bright Earth was smaller than 25°. Hot and flickering pixels were removed and only standard events (grades 0, 2, 3, and 4) were used. The net exposure time after screening was shown in Table 7.2. We note here that, for the observations of 0534−69.9 and DEM L316A/B, because these SNRs are located quite near by bright HMXB LMC X-1, the roll angles were adjusted so that the stray lights from LMC X-1 were blocked by the mirror support housing at the position of SNRs.

The increase in the charge-transfer-inefficiency (CTI) of the SIS CCDs over the course of the ASCA mission has resulted in a number of deleterious effects including degraded spectral resolution and a decrease in the detection efficiency for X-ray photons (due to grade migration and on-board event rejection). We therefore, applied the RDD (Residual Dark Distribution) correction as described by Dotani et al. (1997) to recover some of the lost

spectral resolution for the data of the SNRs observed in Faint mode for both High and Medium bit data. This resulted in an energy resolution for the SIS of ∼7% (FWHM) at 1 keV. The decrease in X-ray photon detection efficiency was incorporated into the response function of the SIS. However, for the data of SNRs observed with Faint mode for High bit data but Bright mode for Medium bit data, we converted the Faint data to the Bright data format and treated both modes of the data uniformly in order to increase the statistics (The RDD correction cannot be applied for the Bright mode data.).

For DEM L316 shell A and B, we additionally used the ROSAT PSPC archival data (sequence number 500259) originally observed in October 1993 for 4.0 ks. The on-axis angular resolution of the PSPC was 13″ (50% encircled energy radius; Pfeffermann et al. 1987), which was sufficient to cleanly separate the X-ray emission from the two shells in DEM L316, which SIS could not do enough.

Table 7.1: Observational log with data mode, data selection etc. for SIS

SNR name	Observation Date	Data Mode
0532−71.0	1999-04-22	1CCD F/B
0534−69.9	1997-05-12	1CCD B/B
DEM L241	1999-10-12	1CCD F/F
0548−70.4	1995-08-24	1CCD F/F
0520−69.4	1999-11-01	1CCD F/B
DEM L316 A/B	1999-08-27	1CCD F/F
0532−67.5	1999-05-08	2CCD F/F[†]
N86	1995-11-25	—[*]

The notation "1CCD F/B" means that the data were taken with 1CCD Faint and Bright modes for High and Medium bit data.
[†] The SIS observation was operated with complementary 2CCD mode. The level discrimination is on (0.7 keV) only for Medium bit data.
[*] N86 was out of SIS fields of view.

7.3 Analysis & Results

In the successive sections we show the spectral analyses and results on the individual SNRs. The images on which spectra accumulated regions are overlaid are shown in each sections. The GIS and SIS spectra were simultaneously fitted to an optically-thin thermal plasma spectral model with the exception for the DEM L316 A, B and N86 data (we describe about this exception in section 7.3.1.). All spectral parameters were linked between the data sets for given SNRs with a few exceptions (we describe about these exceptions later in each corresponding sections.). Below we present the results based on the non-equilibrium

Table 7.2: The net exposure time after the screening for each observation.

SNR name	GIS exposure (s)	SIS exposure (s)
0532−71.0	7.7×10^4	7.0×10^4
0534−69.9	7.6×10^4	3.3×10^4
DEM L241	1.1×10^5	6.8×10^4
0548−70.4	3.3×10^4	4.9×10^4
0520−69.4	2.1×10^4	1.5×10^4
DEM L316 A/B	5.6×10^4	6.0×10^4
0532−67.5	6.7×10^4	2.0×10^4
N86	8.1×10^4	—

ionization (NEI) spectral code by Masai (1994) (hereafter referred to as the Masai model). The specific NEI model employed was the single-timescale, single-temperature model, which parameterized the NEI condition through a quantity called the ionization timescale ($n_e t_i$). Here n_e and t_i are the mean electron density and elapsed time after the plasma was heated to the temperature kT_e. The equilibrium ionization condition is attained for values of $n_e t_i > 10^{12.0}$ s cm^{-3}. In the following we refer to this as collisional ionization equilibrium (CIE).

7.3.1 DEM L316A and DEM L316B (0547−69.7A and 0547−69.7B)

SIS and PSPC X-ray Spectra

In Fig. 7.1 we show the ASCA SIS images in two energy bands; the soft (0.6–1.2 keV) and hard (1.2–7.0 keV) X-ray bands are shown as the grayscale and contour map, respectively. We see X-ray emission from both radio shells A and B. Since the half-power diameter of the ASCA XRT ($\sim 3'$) is comparable to the angular separation between the shells ($\sim 2.5'$), the SIS data do not cleanly resolve the two SNRs and therefore, each shell is contaminated by X-rays that spill-over from the other shell. In order to minimize this spill-over effect and take advantage of the sharp core of the ASCA XRT point-spread-function, we carefully selected the source and background regions. The source regions, as shown in Fig. 7.2 (a) were rather small ellipses with major axes of $1'$ centered on the peak emission from each shell. The background regions were the same size as the source regions, were situated beyond the remnant, and were located so that the source and background regions for one shell were roughly the same distance from the source region of the other shell. We note that the overall ASCA SIS fluxes are not well determined since only a portion of each shell was included in the small spectral extraction regions used. In order to obtain a more accurate estimate of the overall flux of each shell and to provide stronger constraints on the soft X-ray absorption toward the SNR, we thus extracted ROSAT PSPC spectra using the source and background

regions shown in Fig. 7.2 (b). Clearly the emission from shells A and B is cleanly separated in the PSPC data.

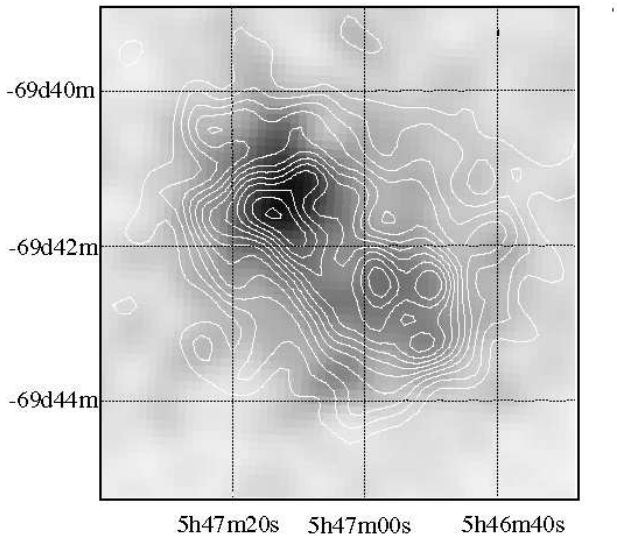

Figure 7.1: ASCA SIS image of DEM L316 (SNR 0547−69.7) after summing both detectors and smoothing with a gaussian filter of $\sigma = 15''$. The grayscale and contours represent the 0.6–1.2 keV and 1.2–7.0 keV bands, respectively. Contours are linearly spaced in steps of 2.8×10^{-4} cts s^{-1} arcmin^{-2} and sky coordinates are epoch J2000. The two X-ray sources correspond to shell A (northeastern source) and shell B (southwestern source), respectively.

The SIS and PSPC spectra were simultaneously fitted to an optically-thin thermal plasma spectral model. All spectral parameters were linked between the data sets for a given shell with the exception of the SIS and PSPC normalization factors (emission measure) which were each allowed to vary freely. Below we present results using the Masai model, although, as a cross check, the NEI model of Hughes and Singh (1994) was also used to verify results. In general there was good agreement between the two NEI spectral calculations and in particular we find roughly the same best-fit elemental abundances.

Shell A

In our NEI fits to the data of shell A, we first allowed the temperature, column density and ionization parameter to be free, while the abundances of all the elements were fixed to be 0.3 times solar, the average in the LMC (see Russell and Dopita 1992; Hughes et al. 1998; hereafter mean LMC value). This model, however, was statistically unacceptable (the χ^2 of 85.4 for 52 degrees of freedom can be rejected at the 99.7% confidence level), and furthermore the data showed an excess of emission relative to the model around 1 keV. This

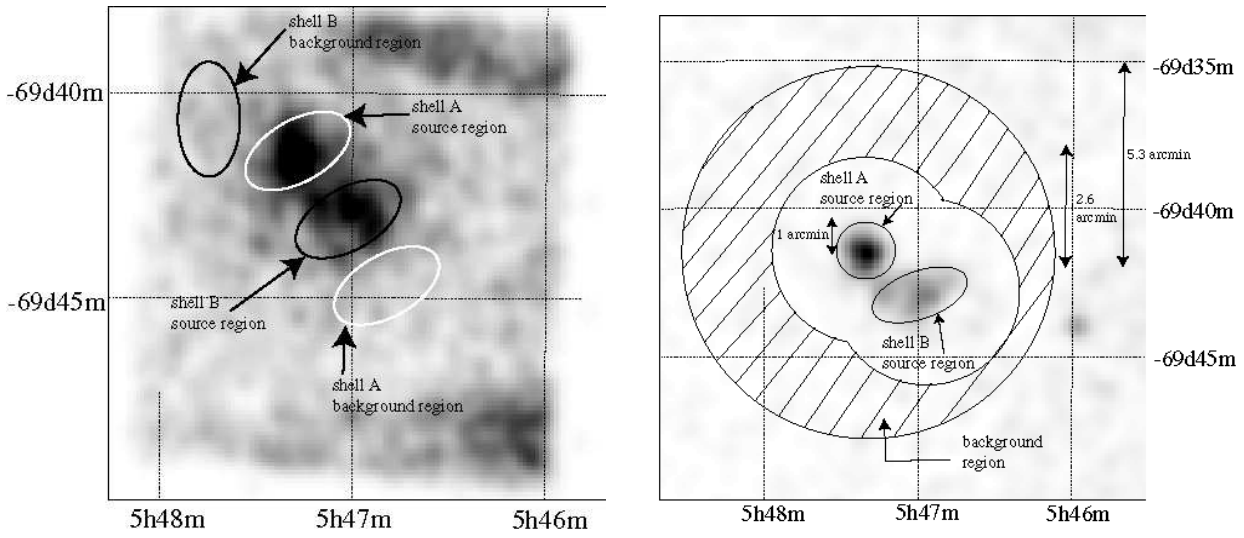

Figure 7.2: The source and background regions (see text) overlaid on the ASCA SIS (a) and ROSAT PSPC (b) total band images.

energy band contains the L-shell lines of iron and the Kα lines of neon, which raises the interesting possibility that one or both of these species may be relatively overabundant in shell A.

In order to test this hypothesis we tried several model fits including cases with (1) only the neon abundance free, (2) only the iron abundance free, and (3) both the iron and neon abundances free. In these fits the column density to shell A was fixed to $N_{\rm H} = 3.8 \times 10^{21}\,{\rm cm}^{-2}$, a value that is consistent with our preliminary fits (described in the preceding paragraph) and an independent estimate from the H I column to the SNR (Williams et al. 1997). The abundances of the other elemental species were fixed to be 0.3 times solar, as above. Model 1 was rejected since it was unable to account for the excess residual emission between 1 to 2 keV, while Models 2 and 3 were both acceptable from a statistical point of view. In the two latter cases, the iron abundance was found to be significantly higher than the LMC mean value. However, a similar statement about the abundance of neon in shell A could not be made, since the neon abundance determined in model 3 was not well constrained. In Table 7.3 we present the best-fit parameters from our case 2 model fits. Fig. 7.3 (a) shows the spectral data, best-fit model spectrum and residuals. The best-fit value of the iron abundance is $1.9^{+0.9}_{-0.6}$ times solar, a factor of 5 more than the mean LMC value, which clearly indicates a large overabundance of iron in shell A. We also note that the ionization timescale range allows for the possibility that the X-ray–emitting plasma is in CIE, as shown in the two-dimensional χ^2 contours of $kT_{\rm e}$ vs. $n_{\rm e}t_{\rm i}$ (Fig. 7.4 (a)).

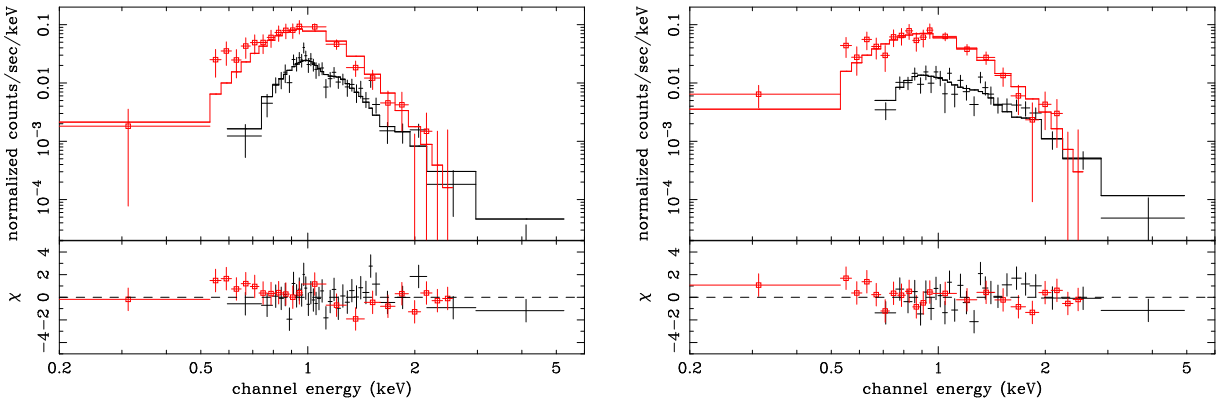

(a) (b)

Figure 7.3: X-ray spectra of shell A (a) and shell B (b) from the ASCA SIS (crosses) and ROSAT PSPC (boxes). The top panels show the data and best-fit models, while the lower panels shown the residuals. Errors are purely statistical at 1 σ confidence. The spectra appear to differ the most around 1 keV. We attribute the more sharply peaked emission from shell A near 1 keV to enhanced iron L line emission (see text for details).

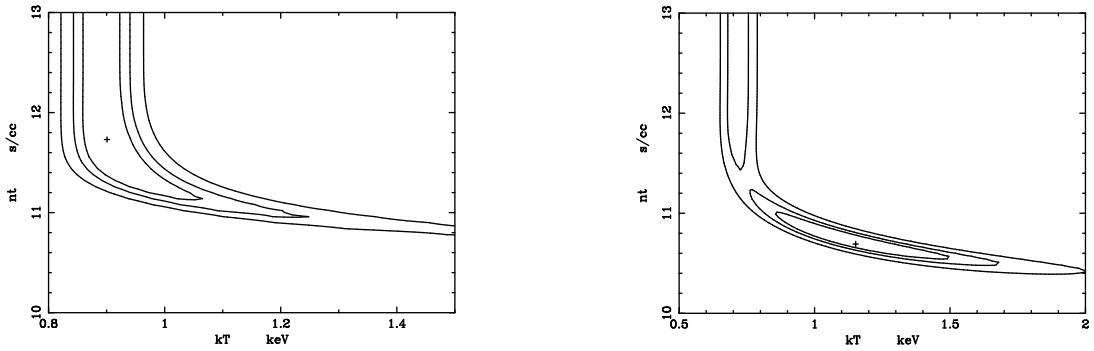

(a) (b)

Figure 7.4: Confidence contours between fitted electron temperature ($kT_{\rm e}$) and ionization timescale ($n_{\rm e}t_{\rm i}$) for shell A (a) and shell B (b). Contours are shown at the 68%, 90% and 99% confidence levels. The best-fit parameters are indicated by crosses.

Shell B

For this shell the NEI model with fixed abundances to mean LMC value provided an acceptable fit to the spectrum. As before the best-fit column was fixed to the value $N_{\rm H} = 3.8 \times 10^{21}\,{\rm cm}^{-2}$. The χ^2 confidence contours between ionization timescale and temperature are shown in Fig. 7.4 (b). This plot indicates that we could not constrain whether the plasma in shell B is in NEI or CIE condition because the confidence level for rejecting the CIE model is slightly low (68%), though the best fit ionization timescale favors the NEI case. Therefore, we also carried out the spectral fitting for the CIE case. The best fit parameters for both the NEI and CIE case are in Table 7.3. Fig. 7.3 (b) shows plots of the data, model, and residuals only for the NEI case, because the best-fit spectrum in CIE is almost the same as that in NEI.

X-ray spectra with GIS

The spatial resolution of the GIS is somewhat poorer than that of the SIS, which makes separating the X-ray emission from the two shells in DEM L316 nearly impossible. Thus we made a composite GIS spectrum containing the total emission from shells A and B again summing data from both detectors. We fit this GIS spectrum using the the best fit SIS/PSPC spectral parameters and found the fit to be acceptable, thereby establishing consistency between the GIS and SIS/PSPC data.

Table 7.3: Spectral fitting results of DEM L316 shell A and shell B.

	Shell A	Shell B (CIE)	shell B (NEI)
$N_{\rm H}$ ($10^{21}\,{\rm cm}^{-2}$)	3.8†	3.8†	3.8†
$kT_{\rm e}$ (keV)	0.90 (0.86–1.09)	0.72 (0.68–0.76)	1.13 (0.87–1.52)
log $n_{\rm e}t_{\rm i}$ (${\rm cm}^{-3}$ s)	11.74 (11.07–13.00)	13.00†	10.73 (10.53–11.07)
Fe *	1.9 (1.3–2.8)	0.3†	0.3†
Other species $^{\natural}$	0.3†	0.3†	0.3†
EM‡ (10^{10} ${\rm cm}^{-5}$)	6.9 (3.7–7.0)	16.6 (14.6–18.6)	8.4 (7.0–10.1)
χ^2 (d.o.f.)	50.9 (52)	46.1 (45)	43.4 (44)

Parentheses indicate 90% confidence intervals for a single relevant parameter ($\Delta\chi^2 = 2.71$)
† Fixed parameter
* Abundance of iron relative to the solar value.
$^{\natural}$ Abundances of other elements relative to the solar values.
‡ Emission measure, defined as: $(n_{\rm i}^2\ V)/(4\ \pi\ D^2)$. See text for details.

7.3.2 SNR 0532−71.0

GIS and SIS X-ray Spectra

In Fig. 7.5 we show the ASCA GIS (in 0.7–2.0 keV) and SIS images (in 0.5–2.0 keV) of 0532−71.0. The remnant is clearly detected at the center of both detectors. We also display the source and background spectra accumulated regions in the same figure. For the GIS, the source spectrum was accumulated from the region with radius of $3'$, while the background spectrum was accumulated from two different regions with the same radii ($3'$) in order to minimize the spill-over effect of the X-ray photons from nearby sources in the same field of view. For the SIS, the source and background spectra were accumulated from the circular region with radius of $4.4'$ and the rest of the region of SIS detector, respectively.

At the first glance of the SIS spectra of 0532−71.0, one can easily notice that the hump exists between 1 and 2 keV, from which one can aware of the relative overabundance of magnesium. As the first step, we allowed only temperature, ionization parameter and emission measure to be free for the NEI model fit, while the abundances of all the elements were fixed to the mean LMC value. All spectral parameters were linked between the data sets. Our SIS data are deficits below 0.5 keV because of the level discrimination at the observation. It is risky to determine the value of column density only from the ASCA data. We, therefore, fixed the column density to the value of $N_{\rm H} = 1.5 \times 10^{21}\,{\rm cm}^{-2}$, which is the sum of the Galactic H I column density toward the LMC ($N_{\rm H} = 5.0 \times 10^{20}\,{\rm cm}^{-2}$; Schwering and Israel 1991; hereafter we apply this value for the Galactic H I column density toward the LMC.) and column density in the vicinity of 0532−71.0 within the LMC provided by Rohlfs et al. (1984). This model was statistically unacceptable as we have expected (the χ^2 of 76.6 for 57 degrees of freedom can be rejected at the 99.7% confidence level) and the hump remained between 1 to 2 keV in the residuals (case 1, Fig. 7.6 (a)). We then allowed the abundance of magnesium to be free and found that the model this time was statistically acceptable, and that, at the same time, can well reproduce the data sets. The best fit parameters are shown in Table 7.4. The spectral data, best-fit model curve (in the upper panel) and residuals (in the lower panel) are shown in Fig. 7.6 (b) (case 2).

7.3.3 SNR 0548−70.4

GIS and SIS X-ray Spectra

Fig. 7.7 we show the ASCA GIS (0.7–2.0 keV) and SIS (0.5–2.0 keV) images of 0548−70.4. The regions from which source and background spectra were accumulated are also displayed in the same figure. In both of the detectors, 0548−70.4 was located at the center. The source spectra were accumulated from the circular regions with the radii of $3'$ and $3.5'$ for the GIS and SIS, respectively. In the GIS field of view, you see bright diffuse component at the right

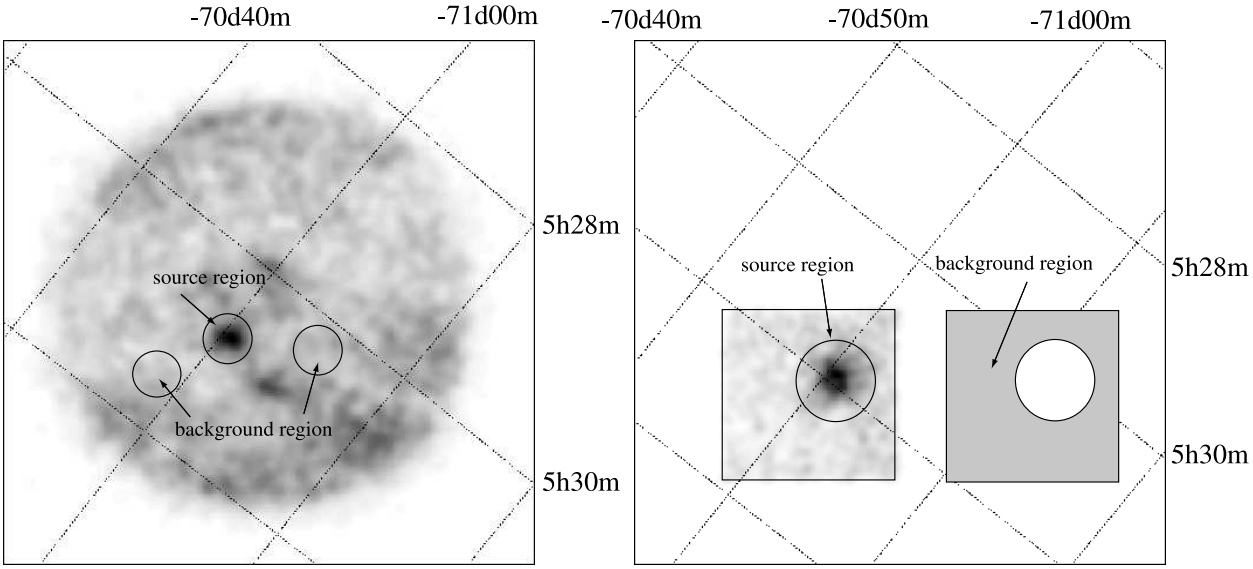

Figure 7.5: ASCA GIS and SIS image of 0532−71.0. Sky coordinates are epoch J2000. The source and background regions for the spectral analysis are shown.

Table 7.4: Spectral fitting results of 0532−71.0.

$N_{\rm H}$ (10^{21} cm^{-2})	1.5†
$kT_{\rm e}$ (keV)	0.55 (0.45–0.62)
log $n_{\rm e}t_{\rm i}$ (cm^{-3} s)	10.55 (10.38–10.80)
Mg *	1.23 (0.86–1.54)
Other species $^{\natural}$	0.3†
EM‡ (10^{10} cm^{-5})	7.1 (5.6–9.5)
χ^2 (d.o.f.)	67.19 (57)

Parentheses indicate 90% confidence intervals for a single relevant parameter ($\Delta\chi^2 = 2.71$)
† Fixed parameter.
* Abundance of magnesium relative to the solar value.
$^{\natural}$ Abundances of other elements relative to the solar values.
‡ Emission measure, defined as: $(n_{\rm i}^2\ V)/(4\ \pi\ D^2)$. See text for details.

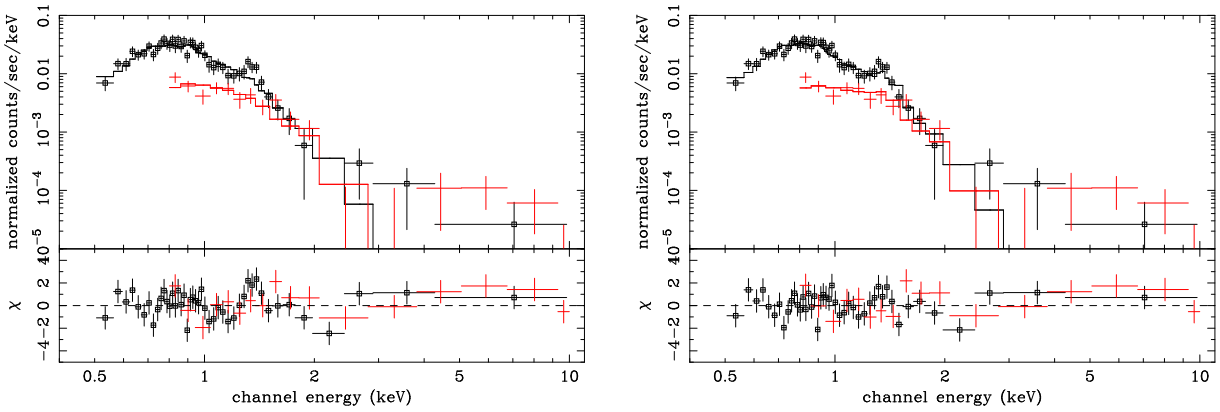

Figure 7.6: X-ray spectra of 0532−71.0 from the ASCA SIS (boxes) and GIS (crosses). Panels (a) and (b) show the case 1 and case 2, respectively. The top panels show the data and best-fit models, while the lower panels show the residuals. Errors are purely statistical at 1 σ confidence.

hand side. It is stray-light from the LMC X-1 out of the GIS field of view. With a careful look at the GIS field of view, one can find out quite dim point-like source at the upper part of 0548−70.4. In order to minimize the photon contamination from both of the components, the background region was chosen as is shown in the left panel of Fig. 7.7. For the SIS, the background spectrum was accumulated from the annulus region with radii of 3.5′ and 5.5′.

In our spectral fitting of 0548−70.4, we first allowed the temperature, ionization parameter and the emission measure to be free, while the column density was fixed to the value of $N_{\rm H} = 7.60 \times 10^{20}\,{\rm cm}^{-2}$, which is again sum of the column density within our Galaxy and that within the LMC in the vicinity of 0548−70.4 (Schwering and Israel 1991; Rohlfs et al. 1984). The abundances of all the elements were fixed to the mean LMC value. All spectral parameters were linked between the data sets. We found that this model can be accepted from the statistical point of view ($\chi^2 = 45.62$ with 53 d.o.f.) and well reproduce the data sets. The best fit parameters are shown in Table 7.5. The spectral data, best-fit model spectrum (in the upper panel) and residuals (in the lower panel) are shown in Fig. 7.8.

7.3.4 SNR 0534−69.9

GIS and SIS X-ray Spectra

We show the GIS (0.7–2.0 keV) and SIS (0.5–2.0 keV) images of 0534−69.9 in Fig. 7.9. The overlayed circles show the regions from which source and background spectra were accumulated. As we mentioned before, 0534−69.9 was just placed at the position on the

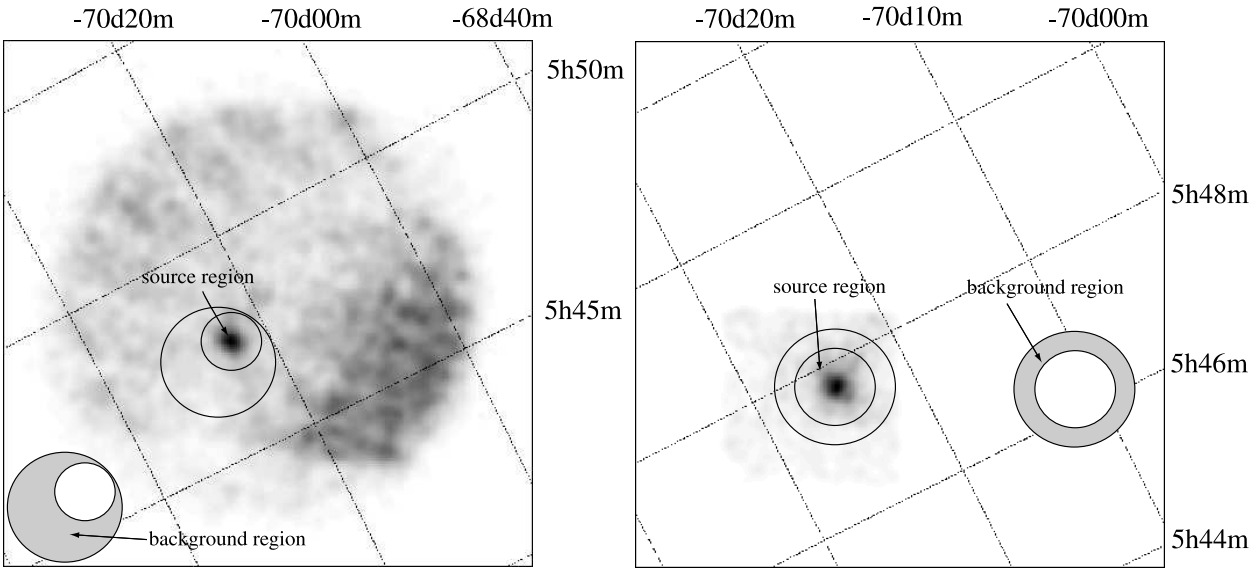

Figure 7.7: Same as Fig. 7.5, but for 0548−70.4

Table 7.5: Spectral fitting results of 0548−70.4.

$N_{\rm H}$ (10^{21} cm^{-2})	0.76†
$kT_{\rm e}$ (keV)	0.65 (0.61–0.71)
log $n_{\rm e}t_{\rm i}$ (cm^{-3} s)	11.25 (11.11–11.47)
Elemental abundances $^{\natural}$	0.3†
EM‡ (10^{10} cm^{-5})	10.8 (10.0–12.0)
χ^2 (d.o.f.)	45.62 (53)

Parentheses indicate 90% confidence intervals for a single relevant parameter ($\Delta\chi^2 = 2.71$)
† Fixed parameter
* Abundance of iron relative to the solar value.
$^{\natural}$ Abundances of elements relative to the solar values.
‡ Emission measure, defined as: $(n_{\rm i}^2\ V)/(4\ \pi\ D^2)$. See text for details.

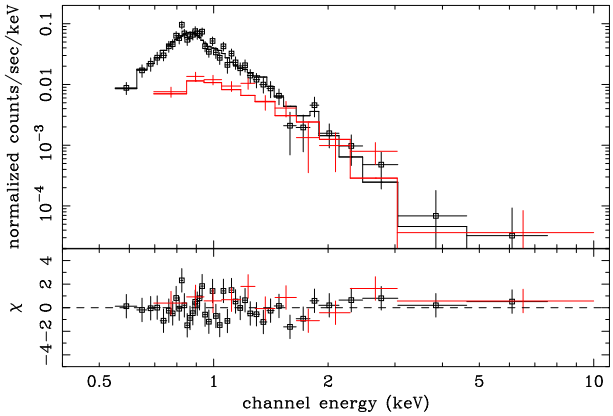

Figure 7.8: Same as Fig. 7.6, but for 0548−70.4.

detectors where the stray-light from LMC X-1 was blocked by the mirror support housing (see left panel of Fig. 7.9). For the GIS, the radii of the regions are 3′ for both source and background spectra. For the SIS, the source spectra was accumulated from the circular region with radius of 4.4′ and the background spectra was accumulated from the annulus region with radii of 4.4′ and 6.9′.

The NEI model with fixed abundance to the mean LMC value was first attempted in the spectral fitting of 0534−69.9. The free parameters are the temperature, ionization parameter, and the emission measure. The SIS data are devoid below 0.5 keV because of the level discrimination of SIS detectors at the time of observation. Therefore, we again assumed that it is risky to determine the column density only with the SIS and GIS data themselves. We fixed the column density to the value which is sum of the Galactic column density (Schwering and Israel 1991), and that derived from the H I observations in the vicinity of 0534−69.9 by Rohlfs et al. (1984) ($N_{\rm H} = 1.78 \times 10^{21}\,{\rm cm}^{-2}$). All spectral parameters were linked between the data sets. Though this model (hereafter case 1) is acceptable from the statistical point of view, the χ^2 shows quite large value (see Table 7.6 (a)) with the residuals showing waving behavior. This might be caused from the poor statistics of the data having no ability to exclude the case 1 model. We next allowed the elemental abundances of neon, magnesium, silicon, and iron to be free (case 2) to find more statistically confident model (Table 7.6 (b)). At the same time, the best-fit model can reproduce the data sets well because residuals showing less heaving behavior (see Fig 7.10). We hereafter adopt case 2 model fitting in discussing the nature of 0534−69.9.

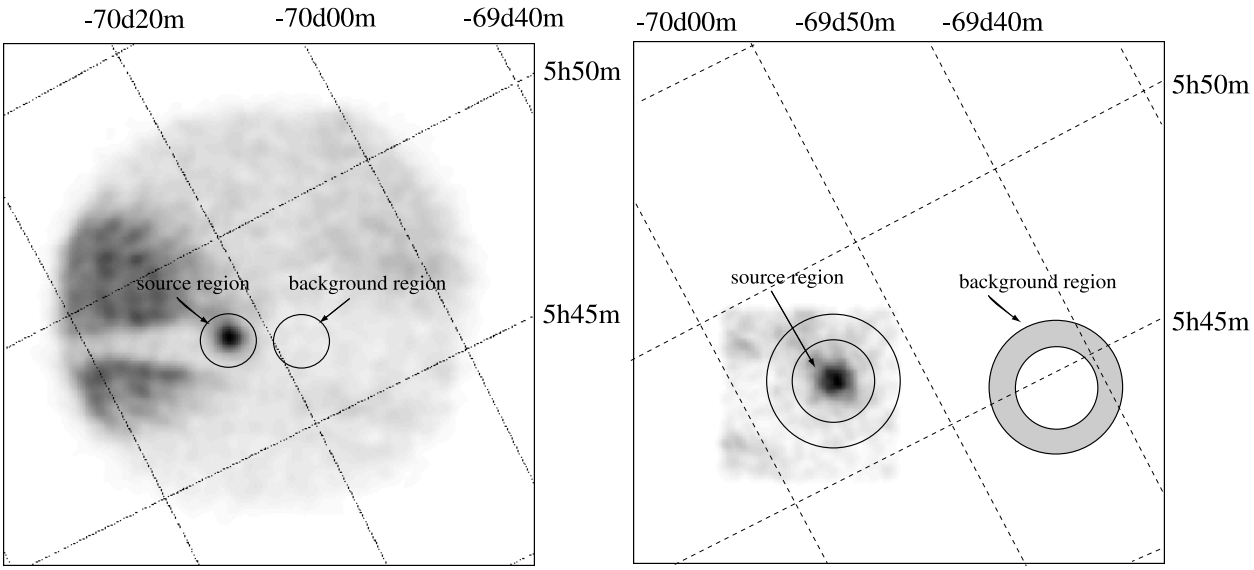

Figure 7.9: Same as Fig. 7.5, but for 0534−69.9.

Table 7.6: Spectral fitting results of 0534−69.9.

	case 1	case 2
$N_{\rm H}$ (10^{21} cm^{-2})	1.78†	1.78†
$kT_{\rm e}$ (keV)	0.57 (0.52–0.64)	0.60 (0.46–0.72)
log $n_{\rm e}t_{\rm i}$ (cm^{-3} s)	11.05 (10.87–11.24)	10.52 (10.18–11.01)
Fe *	0.3†	0.44 (0.34–1.05)
Ne *	0.3†	1.49 (1.06–2.09)
Mg *	0.3†	1.05 (0.51–1.51)
Si *	0.3†	1.16 (0.55–1.75)
Other species $^{\natural}$	0.3†	0.3†
EM‡ (10^{10} cm^{-5})	25.0 (18.1–24.8)	12.0 (10.0–20.0)
χ^2 (d.o.f.)	93.58 (69)	77.47 (65)

Parentheses indicate 90% confidence intervals for a single relevant parameter ($\Delta\chi^2 = 2.71$)
† Fixed parameter
* Abundance of iron, neon, magnesium and silicon relative to the solar value.
$^{\natural}$ Abundances of other elements relative to the solar values.
‡ Emission measure, defined as: $(n_{\rm i}^2\ V)/(4\ \pi\ D^2)$. See text for details.

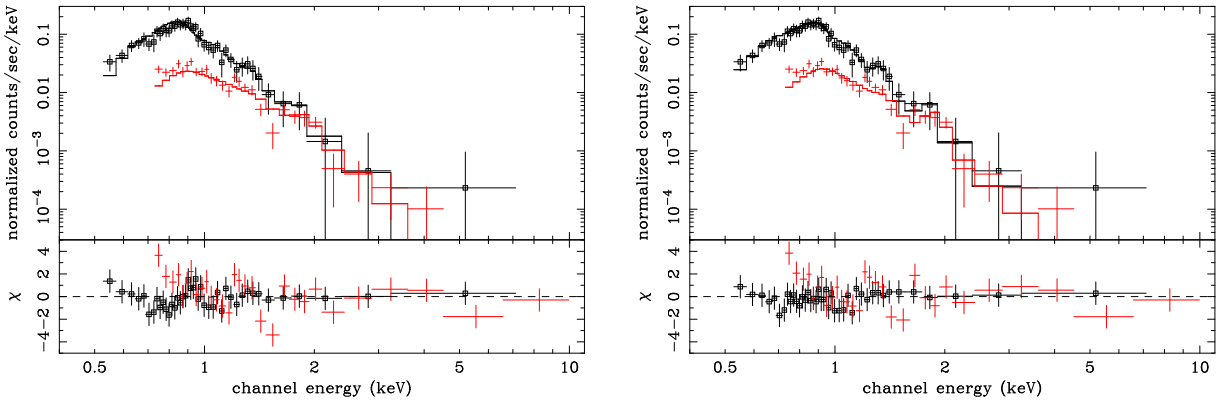

(a) (b)

Figure 7.10: Same as Fig. 7.6, but for 0534−69.9.

7.3.5 DEM L241 (SNR 0536−67.6)

In Fig. 7.11, the GIS (in 0.7–2.0 keV) and SIS (in 0.5–7.0 keV) images of DEM L241 are shown. We also displayed the source and background spectra accumulated regions in the same figure. The regions from which source spectra were accumulated were circles with radii of 5′ for GIS and 4.2′ for SIS. You see dim source within the same fields of view of both GIS and SIS at the left-lower side of DEM L241. We chose the background regions as are shown in Fig. 7.11 in order to minimize the contamination of the X-ray photons from this source.

The GIS and SIS spectra were simultaneously fitted to the NEI model. All spectral parameters were linked between the data sets. Our SIS spectrum is available only over 0.5 keV because of the level discrimination for the DEM L241 observation. Therefore, in our spectral fitting of DEM L241, the column density was fixed to the sum of the Galactic column density (Schwering and Israel 1991) and the value within the LMC which was reported by Rohlfs et al. (1984) in the direction of DEM L241 ($N_{\rm H} = 2.02 \times 10^{21}\,{\rm cm}^{-2}$). We first let only temperature, ionization parameter and emission measure be free and obtained the best-fit parameters. The elemental abundances were fixed to the mean LMC value. However, this model was rejected with the large χ^2 value (χ^2 of 191.30 with 74 d.o.f.). Therefore, we next let the abundances of oxygen, neon, magnesium, sulfur, iron, and argon be free parameters because it is likely to have resulted from massive star progenitor. This time, the model could reproduce the spectra better (hereafter case 1). The best-fit parameters are shown in Table 7.7. In the left panel of Fig. 7.12 we also show the spectra, best-fit model curves and the residuals between data and models.

Because the best-fit temperature of case 1 model fitting is quite high and also because the spectra has slight excess at harder energy band, we suspicious of the existence of hard

component. Therefore, we tested the additional thermal plasma model with higher temperature. Because the photon statistics are not enough, the elemental abundances were set to be common for both plasma components. We found that the spectra were reproduced with soft ($kT_{\rm e} \sim 0.85$ keV and $n_{\rm e}t_{\rm i} \sim 10^{10.75}$ s cm^{-3}) and hard ($kT_{\rm e} \sim 10.5$ keV and $n_{\rm e}t_{\rm i} \sim 10^{13.00}$ s cm^{-3}) plasma components. It is conceivable that the soft component represents the reverse shock, and the hard component fits the forward shock, as are often seen in the two-temperature plasma approximation for the spectra of SNRs. However, the model this time is quite unlikely because the temperature as well as the ionization timescale for the higher plasma component are much higher and larger than the values usually seen in other SNRs. Even the well known young SNRs, such as Cas A and Tycho exhibit the temperature of $kT_{\rm e} \sim$ 2–4 keV (Vink et al. 1996; Fink et al. 1994; Hwang and Gotthelf 1997). The value of ionization timescale for higher temperature component shows that the plasma is in CIE state, which is quite unrealistic. The fact that the apparent iron K-shell emission line component expected from the higher plasma component is not seen in the spectra also weaken the possibility of two-temperature model for the case of DEM L241.

Therefore, we next tested the additional power-law model to the NEI model. The free parameters are temperature, ionization timescale, elemental abundances of oxygen, neon and magnesium for the NEI model, and the photon index and normalization factor for the power-law model. The column density was again fixed to the value as before (hereafter case 2). This time, the model could reproduce the spectra quite well. The best-fit parameters are shown in Table 7.7. In the right panel of Fig. 7.12 we also show the spectra, best-fit model curves and the residuals between data and models.

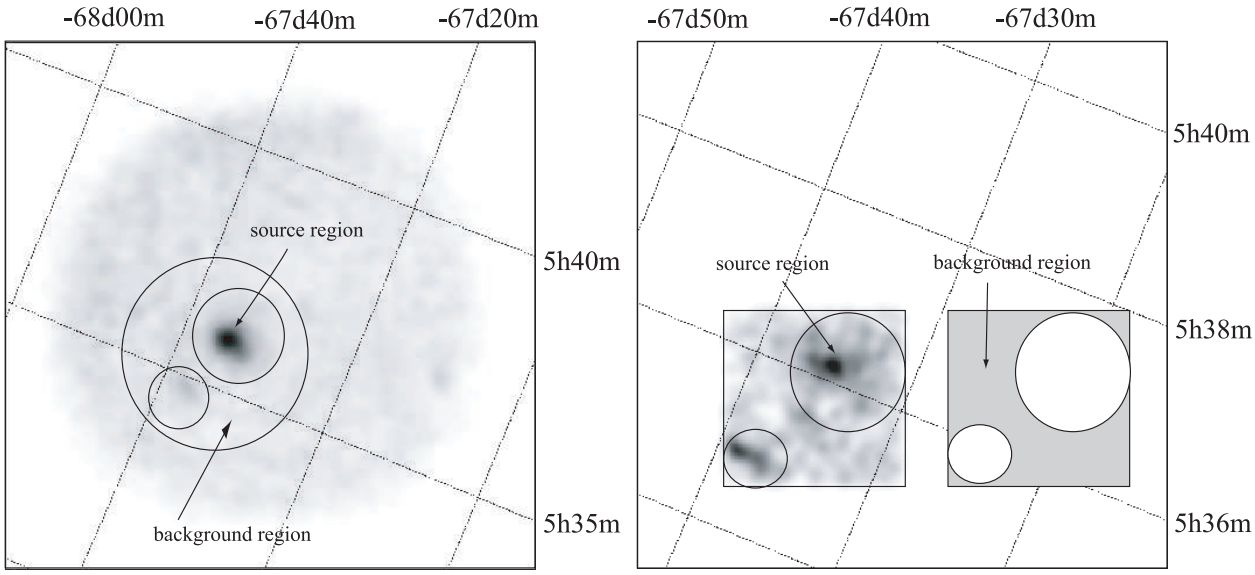

Figure 7.11: Same as Fig. 7.5, but for DEM L241

Table 7.7: Spectral fitting results of DEM L241.

	case 1	case 2
$N_{\rm H}$ (10^{21} cm^{-2})	2.02†	2.02†
$kT_{\rm e}$ (keV)	8.50 (5.07–15.52)	1.31 (0.40–2.64)
log $n_{\rm e}t_{\rm i}$ (cm^{-3} s)	10.30 (10.05–10.40)	10.40 (10.10–11.90)
O*	0.40 (0.21–0.64)	0.45 (0.22–1.25)
Ne*	1.67 (1.38–2.05)	3.38 (2.22–5.52)
Mg*	0.97 (0.73–1.27)	1.72 (1.19–3.37)
S*	0.39 (0.03–0.76)	0.3†
Ar*	1.74 (0.49–3.14)	0.3†
Fe*	0.60 (0.30–0.77)	0.3†
Other species $^{\natural}$	0.3†	0.3†
EM‡ (10^{10} cm^{-5})	2.8 (2.2–2.8)	2.33 (1.00–4.75)
$\Gamma^{\flat}$	—	1.63 (1.32–2.07)
Norm$^{\sharp}$	—	8.4 (1.00–20.6)
χ^2 (d.o.f.)	98.127 (68)	96.946 (69)

Parentheses indicate 90% confidence intervals for a single relevant parameter ($\Delta\chi^2 = 2.71$)
† Fixed parameter
* Abundances relative to the solar value.
$^{\natural}$ Abundances of other elements relative to the solar values.
‡ Emission measure, defined as: $(n_{\rm i}^2\ V)/(4\ \pi\ D^2)$. See text for details.
$^{\flat}$ Photon Index of power-law.
$^{\sharp}$ Normalization factor of power-law in the unit of 10^{-5} photons keV cm^{-2} s^{-1} at 1 keV.

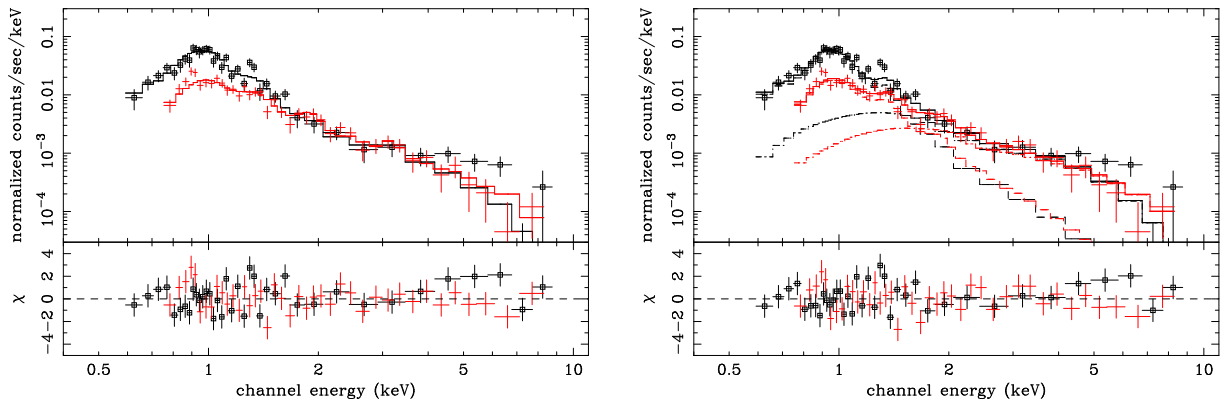

(a) (b)

Figure 7.12: Same as Fig. 7.6, but for DEM L241. Panels (a) and (b) show the case 1 and case 2, respectively.

7.3.6 SNR 0520−69.4

In Fig. 7.13 we show the GIS (0.7–2.0 keV) and SIS (0.5–2.0 keV) images of 0520−69.4. 0520−69.4 was detected at the center of both detectors as dim source. The bright sources in the same field of view of GIS are SNR N132D (upper side) and SNR 0519−69.0 (lower side). We also displayed the source and background spectral accumulated regions in the same figure. The radii for the source and background regions for GIS are both $3'$. The radii of the circles displayed in the right panel of Fig. 7.13 are $4.1'$ and $6.2'$, respectively.

Because the photon statistics of 0520−69.4 are quite poor, we fixed the column density to the value which is sum of the Galactic column density (Schwering and Israel 1991) and that within the LMC obtained from the H I observations by Rohlfs et al. (1984) in the direction of 0520−69.4 ($N_{\rm H} = 1.87 \times 10^{21}\,{\rm cm}^{-2}$). We also fixed the elemental abundances of the plasma to the mean LMC value. The free parameters were plasma temperature, ionization parameter, and the emission measure. The best-fit parameters are shown in Table 7.8. The spectra, best-fit model curves (in the upper panel) and the residuals between the data and the models (in the lower panel) are shown in Fig. 7.14.

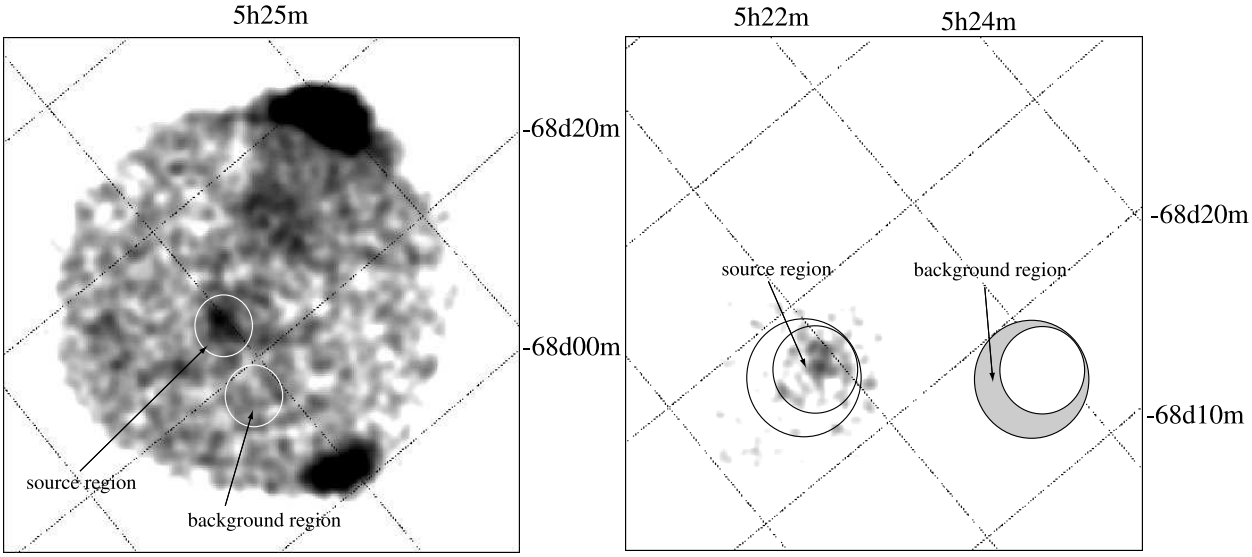

Figure 7.13: Same as Fig. 7.5, but for 0520−69.4.

7.3.7 SNR 0532−67.5

GIS and SIS X-ray Spectra

In Fig. 7.15 we show the ASCA GIS (in 0.7–2.0 keV) and SIS images (in 0.5–2.0 keV) of 0532−67.5. We also display the source and background spectra accumulated regions

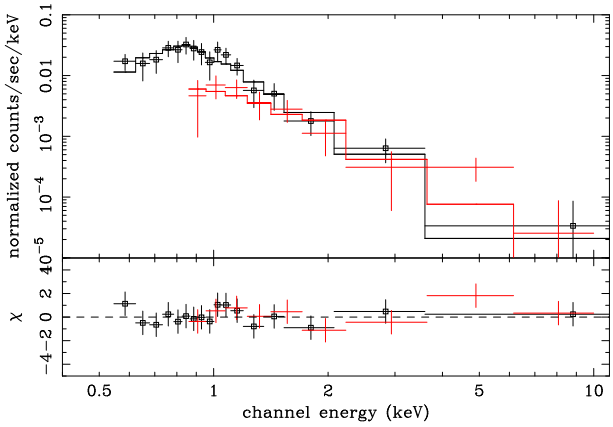

Figure 7.14: Same as Fig. 7.6, but for 0520−69.4.

Table 7.8: Spectral fitting results of 0520−69.4.

$N_{\rm H}$ (10^{21} cm^{-2})	1.87†
$kT_{\rm e}$ (keV)	1.42 (0.91–2.37)
log $n_{\rm e}t_{\rm i}$ (cm^{-3} s)	10.17 (10.00–10.54)
Elemental abundances $^{\natural}$	0.3†
EM‡ (10^{10} cm^{-5})	3.5 (3.0–5.0)
χ^2 (d.o.f.)	13.31 (23)

Parentheses indicate 90% confidence intervals for a single relevant parameter ($\Delta\chi^2 = 2.71$)
† Fixed parameter
* Abundances relative to the solar value.
$^{\natural}$ Abundances of elements relative to the solar values.
‡ Emission measure, defined as: $(n_{\rm i}^2\ V)/(4\ \pi\ D^2)$. See text for details.

in the same figure. The SIS observation was operated with complimentary 2CCD mode thus only Chip 0 of SIS 1 sensor detected 0532−67.5. The discrimination was 0.7 keV/off for Medium/High bit rate modes, respectively. Therefore, we accumulated the SIS spectra separately for Medium/High modes data and we made different responses for each. We then fitted the spectra of GIS, SIS High, and Medium bit data simultaneously to the NEI model. Because our spectra are poor in statistics, we fixed the elemental abundances to the mean LMC value. The column density was also fixed to the value of $N_{\rm H} = 1.5 \times 10^{21}\,{\rm cm}^{-2}$ (the sum of Galactic column density and the column density within the LMC; Rohlfs et al. (1984); Schwering and Israel (1991)). The model well reproduced the data sets. The best-fit parameters are shown in Table 7.9. The spectra, best-fit model curves (in the upper panel) and the residuals between the data and the models (in the lower panel) are shown in Fig. 7.16. The derived ionization timescale shows that the plasma within 0532−67.5 is in the CEI state.

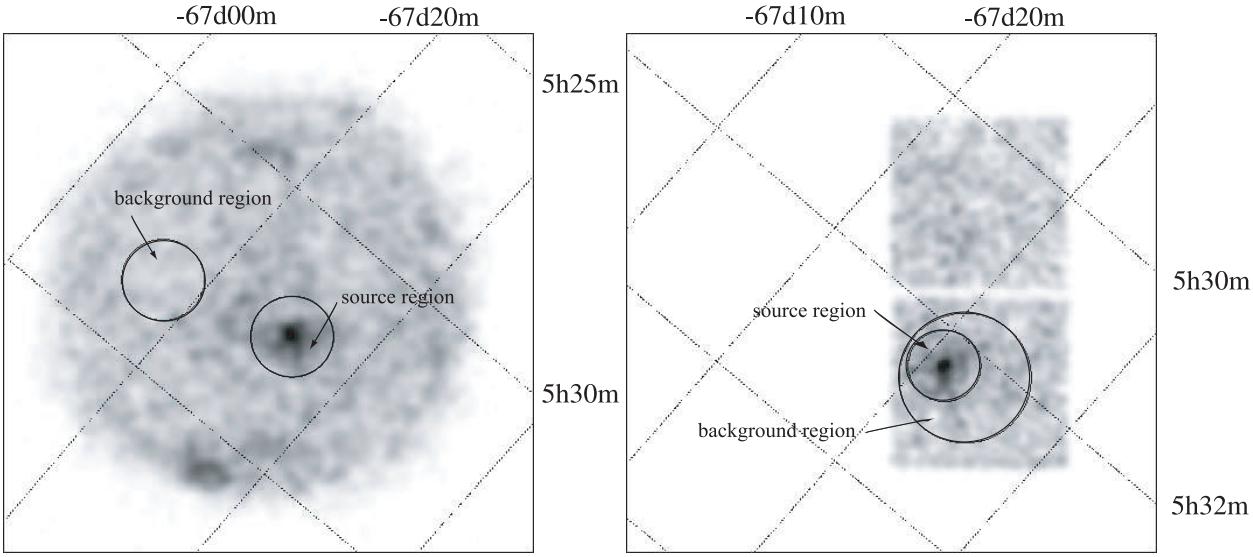

Figure 7.15: ASCA GIS and SIS image of 0532−67.5. Same as Fig. 7.5, but for 0532−67.5.

7.3.8 N86 (SNR 0455−68.7)

GIS spectrum

We show the the ASCA GIS (0.7–2.0 keV) image of N86 in Fig. 7.17. Because N86 was out side of the SIS fields of view at the time of observation, we used only GIS data. The regions from which source and background spectra were accumulated are also displayed in the same figure. The source detected at the center of the GIS field of view is SNR 0453−68.5.

Because the photon statistics of N86 are quite poor, and also because GIS data are devoid

Table 7.9: Spectral fitting results of 0532−67.5.

$N_{\rm H}$ (10^{21} cm^{-2})	1.5†
$kT_{\rm e}$ (keV)	0.69 (0.63–0.75)
log $n_{\rm e}t_{\rm i}$ (cm^{-3} s)	13.0 ($>$ 11.4)
Elemental abundances $^{\natural}$	0.3†
EM‡ (10^{10} cm^{-5})	12.0 (10.0–13.0)
χ^2 (d.o.f.)	44.70 (49)

Parentheses indicate 90% confidence intervals for a single relevant parameter ($\Delta\chi^2 = 2.71$)
† Fixed parameter
* Abundance of iron relative to the solar value.
$^{\natural}$ Abundances of elements relative to the solar values.
‡ Emission measure, defined as: $(n_{\rm i}^2\ V)/(4\ \pi\ D^2)$. See text for details.

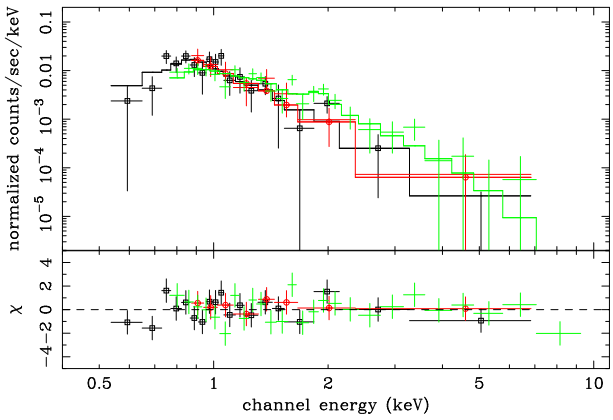

Figure 7.16: Same as Fig. 7.6, but for 0532−67.5. The SIS High and Medium bit data are shown with boxes and circles, while the GIS data are shown with crosses.

below 0.7 keV, we fixed the column density to the value of $N_{\rm H} = 1.76 \times 10^{21}\,{\rm cm}^{-2}$ (the sum of the value obtained from H I observations by Rohlfs et al. (1984) in the direction of N86 and the Galactic column density Schwering and Israel (1991)). We also fixed the elemental abundances of the plasma to the mean LMC value and the ionization timescale ($n_{\rm e}t_{\rm i}$) to be $10^{13.0}$ s cm^{-3}. The free parameters were plasma temperature and the normalization parameter. The best-fit parameters are shown in Table 7.10. The spectra, best-fit model curves (in the upper panel) and the residuals between the data and the models (in the lower panel) are shown in Fig. 7.18.

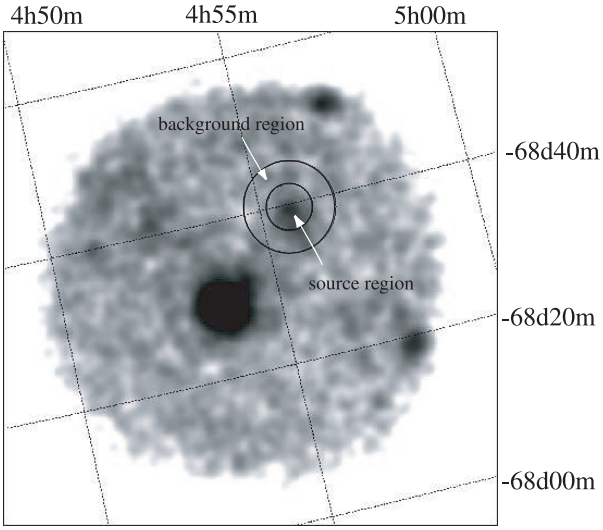

Figure 7.17: ASCA GIS image of N86. Same as Fig. 7.5, but for N86. Only GIS data are available.

Table 7.10: Spectral fitting results of N86.

$N_{\rm H}$ ($10^{21}\,{\rm cm}^{-2}$)	1.76†
$kT_{\rm e}$ (keV)	0.77 (0.60–1.05)
log $n_{\rm e}t_{\rm i}$ (cm^{-3} s)	13.0†
Elemental abundances $^{\natural}$	0.3†
EM‡ (10^{10} cm^{-5})	3.9 (2.8–5.0)
χ^2 (d.o.f.)	5.89 (9)

Parentheses indicate 90% confidence intervals for a single relevant parameter ($\Delta\chi^2 = 2.71$)
† Fixed parameter
$^{\natural}$ Abundances of elements relative to the solar values.
‡ Emission measure, defined as: $(n_{\rm i}^2\ V)/(4\ \pi\ D^2)$. See text for details.

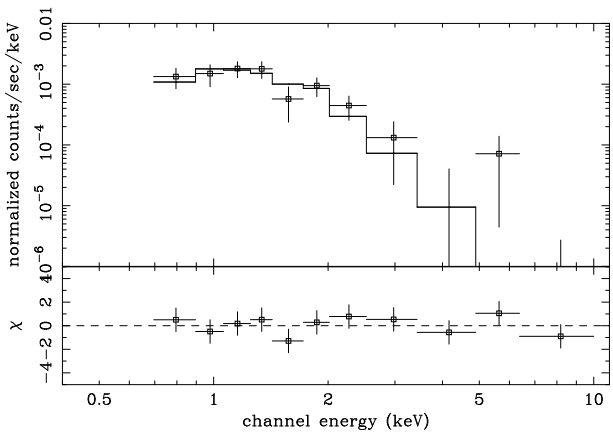

Figure 7.18: Same as Fig. 7.6, but for N86. Only GIS data are available.

7.4 Nature of Individual SNRs

Here, we discuss the individual natures of sample-1 SNRs.

7.4.1 DEM L316 A and DEM L316 B — Twin SNRs?

In this section, we mention about the nature of DEM L316 shell A and B, which are the possible site for the collision between two SNRs.

The main difference between the spectral characteristics of shell A and B is the strong emission line structure at about 1 keV seen in the spectrum of shell A. Our spectral analysis of shell A suggests an enhanced iron abundance. It is well known that Type Ia SNe are efficient producers of iron (Nomoto et al. 1984), while massive-star core-collapse SNe tend to produce proportionally more of the lower atomic number species, such as oxygen, neon, and magnesium (Tsujimoto et al. 1995). Therefore, one might argue that the emission line structure around 1 keV may be described by a combination of Kα lines from oxygen, and neon, which are major elements yielded by Type II SNe, rather than L shell lines from iron. To check this possibility, we further treated the abundances of neon, oxygen, and iron as free parameters and fitted the shell A spectra to the NEI model. Then we found that the abundance of iron was again significantly higher than the mean LMC value. However, a similar statement about the abundances of oxygen and neon could not be made, since the abundances of both of these elements were not well constrained. At least one other middle-aged LMC SNR (DEM L71) shows evidence for enhanced iron in its global integrated ASCA spectrum (Hughes et al. 1998). We, therefore, believe that the enhanced iron in shell A is

strong evidence in support of the origin of shell A as a Type Ia SN.

Assuming that the electron and ion densities in the plasma are identical (hereafter we use this assumption for the plasma within all the SNRs otherwise mentioned.), that the X-ray emitting plasma has uniform density, and that the distance to DEM L316 (D) is 50 kpc, we can estimate the electron ($n_{\rm e}$) and ion densities ($n_{\rm i}$) in both shells through

$$n_{\rm e} = n_{\rm i} = 1.7 N_{12}^{0.5} (V/10^{59}{\rm cm}^3)^{-0.5} (D/50{\rm kpc}){\rm cm}^{-3}, \tag{7.1}$$

where N_{12} is the emission measure derived from the spectral fits (in units of $10^{12}\,{\rm cm}^{-5}$), V is the volume of X-ray emitting plasma (in units of cm^3), defined as $V = V_{SNR} \times f$, where V_{SNR} and f are the whole volume of the SNR and the filling factor, respectively (hereafter we use this equation to derive the densities within the individual SNRs.).

We estimate the volume using the ROSAT HRI morphology (Williams et al. 1997) as follows. For shell A, we assume that the plasma fills a spherical region with a radius of 11 pc. Because shell B has limb-brightened morphology, we tentatively assumed that the Sedov model applies to shell B, i.e., the thickness of shell B is one twelfth of the shell radius (shell radius was assumed to be 15 pc; Williams et al. 1997). That is to say, we assumed the filling factors of 1 and 0.23 for shell A and shell B, respectively.

From equation (7.1), we obtain value for the ion density of the plasma in shell A to be $\sim$0.4 cm^{-3}. Adopting this density and the best-fit ionization parameter $n_{\rm e}t_{\rm i}$, we derive ionization timescale age for shell A of $\sim 3.9\times10^4$ yr.

For shell B, the spectral fitting gives two local minimums for the NEI conditions of $n_{\rm e}t_{\rm i}$ $\sim 10^{10.7}$ s cm^{-3} (case 1) and $n_{\rm e}t_{\rm i} \sim 10^{12.0}$ s cm^{-3} (case 2). Depending on these two cases, we obtain different physical parameters, particular on the ionization age. In case 1, the plasma density is ~ 0.5 cm^{-3}, then the ionization parameter ($n_{\rm e}t_{\rm i}$) gives the age ($t_{\rm i}$) to be $\sim 3.2\times10^3$ yr. While in case 2, the plasma density is ~ 0.8 cm^{-3} and the age is estimated to be $> 4.2\times10^4$ yr (the CIE condition is attained for values of $n_{\rm e}t_{\rm i} > 10^{12.0}$ s cm^{-3}). Since shell B has larger size and smaller surface brightness than those of shell A, it would be older than shell A. We thus infer that case 2 is more favored for shell B, hence the age would be $> 4.2\times10^4$ yr, which places shell B to be an older SNR than shell A.

Finally we propose, from the totally different spectral shapes of shell A and B, that these two shells were not due to a single supernova explosion into a pre-existing bubble made by a stellar wind or SNe. We also propose, from the iron over abundance seen in the spectrum, that the origin of shell A is a Type Ia. We could not obtain the evidence which positively supports the collision between two SNRs nor could we get a strong constraint for the shell B progenitor.

7.4.2 SNR 0532−71.0

SNR 0532−71.0 has center-filled morphology, and has large size (r $\sim$ 27 pc), thus Williams et al. (1999) categorized this SNR to be an old one which is at the far end of the stage of SNR evolution. Therefore, we assumed that the plasma fills a spherical region (namely, we assumed the filling factor of the plasma to be 1), and obtained the electron densitiy to be $\sim$0.08 cm^{-3}. From the ionization timescale derived from the fitting, we can also obtain the ionization timescale age $t_{\rm i}$ to be $\sim 1.3 \times 10^4$ yr, which is consistent with the assumption by Williams et al. (1999) that it is an old remnant.

Therefore, it is expected that the X-ray spectrum of 0532−71.0 strongly reflects the elemental abundances of ambient medium ($\sim$ 0.3 solar; the mean LMC value). However, we found enhanced emission line of magnesium. The abundance of magnesium was more than factor of 4 larger than the mean LMC value, while those of other elements, such as oxygen, neon, and silicon, were consistent with the mean LMC value. From the predicted relative abundances of synthesized heavy elements (Tsujimoto et al. 1995), this kind of pattern of elemental abundances, namely, the excess abundance of only particular element, cannot be produced in any kind of supernova explosions, if the ejecta is uniformly mixed up. To explain this unusual overabundance of magnesium, there must be two possible cases as follows.

One of the explanation is that there must be a local magnesium-rich plasma somewhere in the SNR. This kind of overabundance of only particular elements is also seen in the plasma of Galactic SNR, Vela (Tsunemi et al. 1999). Tsunemi et al. (1999) found prominent silicon-K emission lines from a clump in a Vela, called "shrapnel A", which was first identified by Aschenbach et al. (1995). They explained that the shrapnel A is a debris of the explosion of the massive progenitor star. This analogy might be also adopted to the case of 0532−71.0.

The other explanation is as follows. Williams et al. (1999) explain that the SNRs categorized in the center-filled morphologies have engulfed ambient cloudlets during the course of their evolution. These cloudlets have evaporated and increase the density of the interior of SNR, thus raise the brightness of the remnant toward its center. Williams et al. (1999) argue that 0532−71.0 is the best example of this type. If there was (or were) a cloudlet (or cloudlets) which contained plenty of magnesium around the progenitor of 0532−71.0, these cloudlets have engulfed by the shockfront and evaporated within the 0532−71.0, thus have raised the abundance of magnesium.

However, because of the lack of spatial resolution of ASCA, as well as, the lack of spectral resolution of ROSAT, we cannot determine which story explains the case of 0532−71.0. More spatially as well as spectrally sensitive observations, such as with Chandra satellite, are needed.

7.4.3 SNR 0548−70.4

Williams et al. (1999) categorized 0548−70.4 into SNRs with diffuse-face morphology. It is quite uncertain how much volume X-ray emitting plasma occupies within the total volume especially for the SNRs having diffuse-face morphologies, that is to say, we do not know the value of the filling factor of the X-ray emitting plasma. However, filling factor should be smaller than 1, if we take into account of the clumpieness of the morphology. Therefore, hereafter, we assume that the filling factor is ~ 0.1 for all the SNRs with diffuse-face morphologies. From the emission measure derived from the fitting, we can obtain the electron density of the plasma to be ~ 1.0 cm^{-3} (the electron and ion densities decrease by a factor of $\sim$3 if the filling factor is ~ 1).

The optical spectra of typical SNRs exhibit forbidden emission lines of oxygen, nitrogen, and sulfur, as well as the hydrogen Balmer series (Fesen et al. 1985). These lines come from shocked interstellar material that is cooling radiatively (Raymond 1979; Dopita 1977). On the contrary, few SNRs show strong Balmer lines with little or no evidence of the forbidden lines seen in radiative shock spectra. The typical example of such an SNR is a Galactic SNR, SN 1572, also known as Tycho. Other examples of such Balmer-dominated Galactic SNRs are Kepler, SN1006, RCW86, and Cygnus loop (Smith et al. 1991; Hwang et al. 1998; Tuohy et al. 1982; Kinugasa and Tsunemi 1999; Bocchino et al. 2000; Bamba et al. 2000; Miyata 1996). The nature of these Balmer-dominated shocks was explained by Chevalier and Raymond (1978), who proposed that the spectrum was due to a collisionless shock moving into partially neutral interstellar material.

Tuohy et al. (1982) searched the catalogue of LMC SNRs (Mathewson et al. 1983) to find 4 such examples (0509−67.5, 0519−69.0, DEM L71, and 0548−70.4) that exhibit dominant Balmer-lines. They found that all of them are faint radio sources. They made a restriction of one of the progenitor masses from optical and X-ray observations. Their quantitative estimate revealed that the progenitor mass of 0519−69.0 lay between 1.2 $M_\odot$and 4 $M_\odot$. Therefore, they proposed 0519−69.0 resulted from a Type Ia progenitor. Because the optical, radio, and X-ray properties of the four remnants resemble, with few exceptions, the three historical SNRs in the Galaxy (Tycho, Kepler, and SN1006) which are thought to be the results of Type Ia explosions, they proposed that the four LMC remnants all resulted from Type Ia. The detailed X-ray spectroscopy of ASCA of three of them (0509−67.5, 0519−69.0, and DEM L71) by Hayashi (1997) afterward revealed that they exhibit strong iron-L shell lines, thus confirmed their progenitor types to be Type Ia.

Because 0548−70.4 is one of those four LMC remnants, we are suspicious of lacking of iron overabundance in its X-ray spectrum. Therefore, we additionally tested the model fitting in which the iron abundance was allowed to be free in order to check the existence of more confident model with iron overabundance. At this time, also neon abundance was allowed to be free, because the iron L-shell emission lines and neon Kα emission line both fall around $\sim$ 1 keV, thus either of them can produce the excess emission around 1 keV.

However, the abundances of iron as well as neon were consistent with the mean LMC value within the error against our expectation.

One possible explanation for the absence of clear overabundance of iron in 0548−70.4 spectra might result simply from its older age than any other SNRs in the LMC which exhibit iron overabundance. That is to say, the shock front of 0548−70.4 has engulfed much enough ambient ISM that the ejecta has already been diluted.

However, we cannot completely exclude the possibility that 0548−70.4 resulted from the explosion of a massive star. In Table 7.11 we summarize all the LMC remnants, which have resulted, or with possibilities to have resulted from Type Ia explosions. We also show their associations with H II regions and OB associations in the same Table. Apart from the characteristic to show Balmer-dominated optical spectra, that to exhibit iron overabundance in X-ray spectra can be the direct evidence for the SNRs to have resulted from Type Ia explosions. The interesting point is that not all of the remnants which resulted from Type Ia progenitors do show the dominant Balmer-line optical spectra, and viceversa, yet many SNRs possess both of the characteristics at the same time.

As mentioned before, the Balmer-dominated optical spectra are results of collisionless shock moving into partially neutral interstellar material, thus it should have direct physical connection, not with progenitor types, but with ambient interstellar conditions. Indeed, as is shown in Table 7.11, all the LMC remnants which exhibit iron overabundance with Balmer-dominated optical spectra have no correlation with OB association nor H II regions. On the contrary, those exhibiting iron overabundance but no Balmer-dominated optical spectra have correlation with OB association, or H II regions, or both of them. This is a quite natural consequence considering the progenitor stars of Type Ia SNe. Type Ia progenitor stars are considered to be old low-mass stars. They are likely to be isolated from H II regions or young stars (OB stars) which ionize ambient medium with their stellar winds or supernova explosions. Therefore, some amount of matter around old low-mass stars are likely possibility to be left without being ionized (neutral matter). This brings us the Balmer-dominated optical spectra when those explode as SNe. That is to say, the Balmer-dominated optical spectra can also be observable from the SNRs which resulted from massive stars, if some amount of neutral matter are left around them, like Cygnus loop (Miyata 1996). We therefore, should not come hastily to a conclusion that 0548−70.4 have resulted from Type Ia explosion. It should be noted that the mass estimate for the progenitor star by Tuohy et al. (1982) should be handled with caution because the mass restriction was succeeded only for 0519−69.7 case, not for the other three Balmer-dominated SNRs, and also because their estimation was based on the observed bulk velocities with high uncertainty.

Table 7.11: The SNRs in the LMC whose progenitors are, or the candidates of, Type Ia. Their correlation with OB associations and H II regions are also shown.

		Balmer line	Fe overabundance	progenitor type	OB association	H II regions
LMC	0509−67.5	◯	◯	Type Ia[1]	–	–
	N103B	×	◯	Type Ia[1]	near NGC1850	in DEM L84
	0519−69.0	◯	◯	Type Ia[1]	–	–
	DEM L71	◯	◯	Type Ia[1]	–	–
	DEM L316A	×	◯	Type Ia[2]	–	near LMC2
	0548−70.4	◯	×	Type ?[2]	–	—

1. Hayashi (1997) and Hughes et al. (1998).
2. this work.

7.4.4 SNR 0534−69.9

The X-ray spectra of 0534−69.9 show clear overabundance of neon, magnesium and silicon. The remarkable point is that the abundance of neon is larger than that of iron, which is clear evidence for 0534−69.9 to be resulted from a massive star progenitor.

From the derived emission measure, we obtained the electron density of $\sim$0.76 cm^{-3}, here we assumed that the filling factor is 0.1 in the analogy of other diffuse-face SNRs.

7.4.5 DEM L241 (SNR 0536−67.6)

DEM L241 has not been observed with ROSAT HRI, thus the detailed morphology of this SNR is unknown. However, Mathewson et al. (1985) observed this SNR with radio, optical, and X-ray (using Einstein HRI) wavelengths. The radio and optical morphology resemble with each other quite well, showing elongated from north-east to south-west direction. At the north-east part lies a fairly dense H II region which is radiatively excited by a loose cluster of young stars. In Fig. 7.19 we show the [S II] photograph (left panel) and Einstein X-ray image (right panel). The shock waves of the SNR can be seen in the [S II] photograph tunneling through the H II region creating a tangle web of filaments (Mathewson et al. 1985). On the other hand, the X-ray morphology is concentrated at the south-west region with the size of about $\sim 1.7'$ (in diameter), which corresponds to 25.5 pc at the LMC distance. Therefore, we hereafter use this size for discussing characteristics of the plasma within DEM L241.

From the spectral fitting, we obtained two possible models which explain the DEM L241 spectra; case 1 and case 2. Because both models show the overabundance of oxygen, neon, and magneisum relative to the iron, they do not contradict to the hypothesis which is based on its surrounding condition that DEM L241 has resulted from a massive star progenitor.

The fitting results from case 1 model provide us the Sedov age, ionization timescale

age, and electron density of the plasma to be $t_{\rm sedov} \sim 1.8 \times 10^3$ yr, $t_{\rm i} \sim 1.1 \times 10^3$ yr, and ~ 0.59 cm^{-3}, respectively, where the filling factor is assumed to be 0.1. In this case, $t_{\rm sedov}$ as well as $t_{\rm i}$ show that the remnant is quite young comparable to the three youngest remnants in the LMC. Though we cannot indicate a strong argument against the case 1 model, the extremely high temperature is quite unrealistical. On the other hand, the case 2 model provides us more reliable temperature of ~ 1.3 keV. We, therefore, assume that the case 2 model is more probable for DEM L241. From the case 2 model, the Sedov age, ionization timescale age, and electron density of the plasma to be $t_{\rm sedov} \sim 4.5 \times 10^3$ yr, $t_{\rm i} \sim 1.5 \times 10^3$ yr, and ~ 0.54 cm^{-3}, respectively (again, filling factor is assumued to be 0.1).

DEM L241 is known to be an SNR within the bubble and reported to exhibit quite lower expansion velocity of ~ 70 km s^{-1} from the echelle observation by Chu (1997). However, the derived temperature of X-ray plasma was quite high. They are apparently inconsistent results with each other. The possible explanation for the lower expansion velocity of DEM L241 by Chu (1997) is that they detected the velocity of the bubble. DEM L241 could be interacting with the inner walls of a bubble to reproduce the SNR signature. Therefore, the optically observable shell are dominated by the bubble dynamics. The derived electron density of ~ 0.54 cm^{-3} increases to be ~ 1.70 cm^{-3}, if the assumption of the X-ray emitting volume changes from 10% to 1% of the total volume. However, in either case above, the expected Hα emission is well below the detection limit of the echelle observation by Chu (1997) (the detection limit of Hα observation by them corresponds to an emission measure of 50–100 cm^{-6} pc for a 10^4 K gas.). Therefore, it would be probable that the echelle observation by Chu (1997) failed to detect the high velocity component of Hα emission which arises from the SNR itself, but they detected only the bubble component which shows lower velocity.

We next discuss the hard X-ray component seen in the spectra. The hard X-ray emission was well reproduced with power-law model, thus we consider it has non-thermal origin. The plausible mechanism of non-thermal X-rays is synchrotron emission from high energy electrons. Such electrons are realized in Crab-like SNRs or SN 1006-like SNRs. From the electrons accerelated within the Crab-like SNRs, the X-ray synchrotron radiation whose spectral shape is the power-law with typical photon index of ~ 2 is observed. On the other hand, the electrons within the SN 1006-like SNRs are accelerated at the shock front through Fermi-process up to $\sim$ 100 TeV and emit X-ray photons through synchrotron radiation whose spectral shape is the power-law with typical photon index of ~ 3 (Koyama et al. 1995; Koyama et al. 1997). In the case of DEM L241, the derived photon index of ~ 1.63 is somewhat smaller than those seen in the SN 1006-like SNRs. SN 1006-like SNRs are known to exhibit clear shell morphology in X-ray band. However, we could not recognize the shell-shape morphology from its ASCA image, instead, it seems at least to show diffuse or center-filled morphology, though we must admit that the detail morphology is unknown because of the lack of spatial resolution of ASCA XRT. Therefore, we assume that the Crab-like case is more probable for DEM L241 case. It is expected that the point-like source is

observed in the Crab-like SNRs. However, we could not confirm any point-like sources in its ASCA image. We also performed the pulsation search using the GIS data to find no significant peak in the power density spectrum in the range of 0.125–2048 s. Fig. 7.20 shows the power density spectrum in 1.0–7.0 keV band.

From our data, it is impossible to conclude the origin of hard X-ray component, thus more spatially sensitive observations with much photon statistics are required.

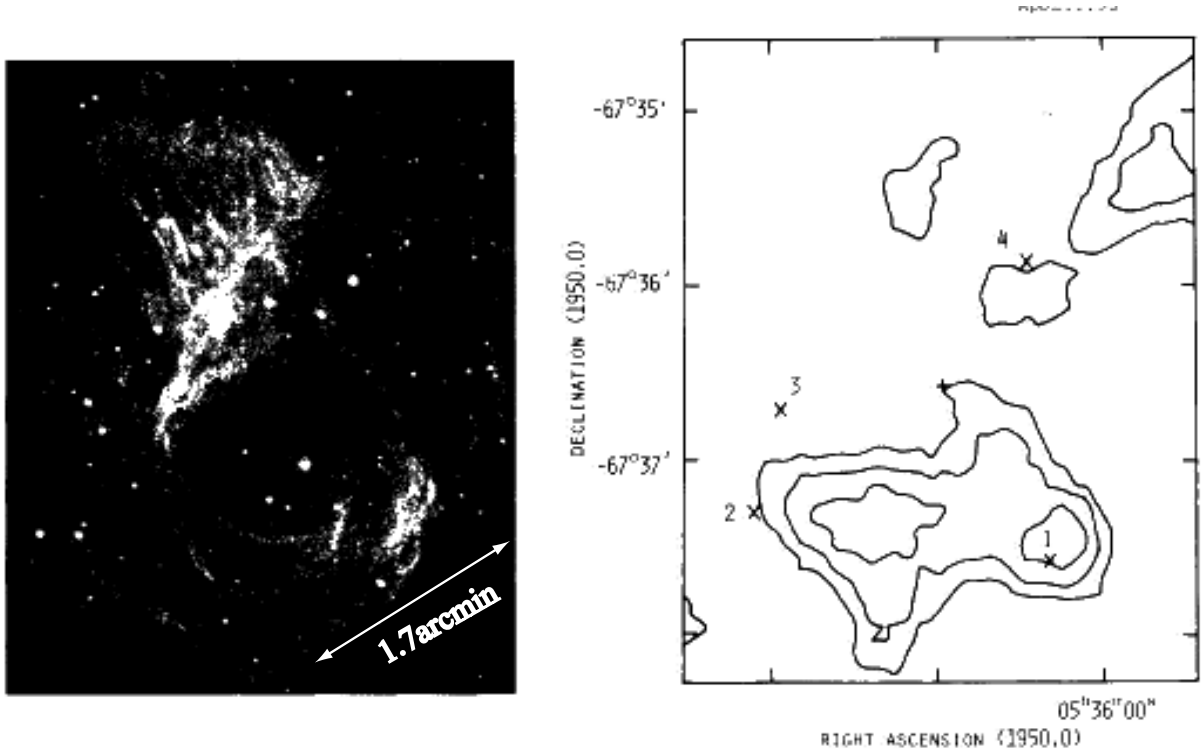

Figure 7.19: S II (left panel) and Einstein HRI X-ray (right panel) DEM241 images from Mathewson et al. (1985).

7.4.6 Dark SNRs — 0520−69.4, 0532−67.5, and N86

0520−69.4 and 0532−67.5 were categorized to have diffuse-face morphology, while N86 was categorized to have irregular morphology by Williams et al. (1999). We assumed that the filling factor of the X-ray emitting plasma to be 0.1 for all the SNRs. The electron densities were obtained from the fitting normalization parameter to be $\sim 0.40, 0.37$, and 0.17 cm^{-3} for 0520−69.4, 0532−67.5, and N86, respectively. The Sedov ages were estimated to be $\sim 6.0 \times 10^3, 1.4 \times 10^4$, and 1.5×10^4 yr, and the ionization age of the plasmas within them were obtained to be $\sim 1.2 \times 10^3$, $> 8.6 \times 10^4$, and $> 2.0 \times 10^5$ yr, for 0520−69.4, 0532−67.5,

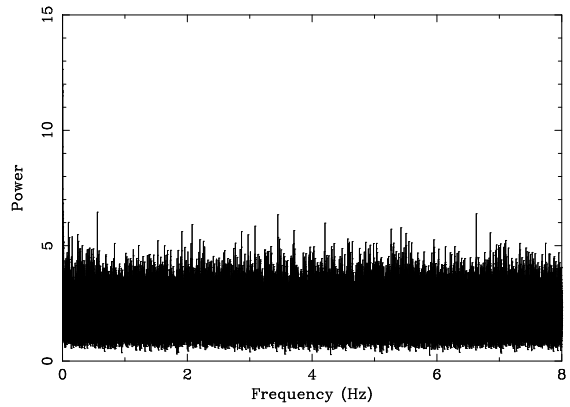

Figure 7.20: The power spectrum of DEM L241 in the 1.0–7.0 keV band.

and N86, respectively. For N86, the derived Sedov age and the density are consistent with the previous results by Williams et al. (1999). The derived ionization ages of 0532−67.5 and N86 are at least factor of 6 greater than the Sedov ages (See Fig. 9.1 in the subsequent chapter 9; you see a clear trend that the increasing rate of Sedov age hits its peak.). This suggests us that the hypothesis by Williams et al. (1999) for N86, that the remnant has younger age than its size would suggest, is suspicious. We consider the explanation for the age discrepancy is that both 0532−67.5 and N86 are really old remnants as the ionization ages show, and that they have already entered the stage of momentum-conserving expansion, as this stage of expansion proceeds more slowly.

7.4.7 Summary

Plasma parameters of sample-1 SNRs

Here we summarize the plasma parameters of individual sample-1 SNRs (Table 7.12).

Comments for Spatial distribution of Type Ia SNRs

We show the spatial distribution of SNRs from Type Ia explosions in Fig. 7.21. The SNRs are shown with crosses which are overlaid on the ROSAT X-ray map of the LMC. Those which are, or have possibility of being caused by, Type Ia explosions are encircled. One can easily notice that encircled SNRs distribute just at the edge of the region filled with bright diffuse X-ray emission. Another interesting point is that the younger SNRs from Type Ia explosions all lay at the northwest side and older ones lay at the southeast side.

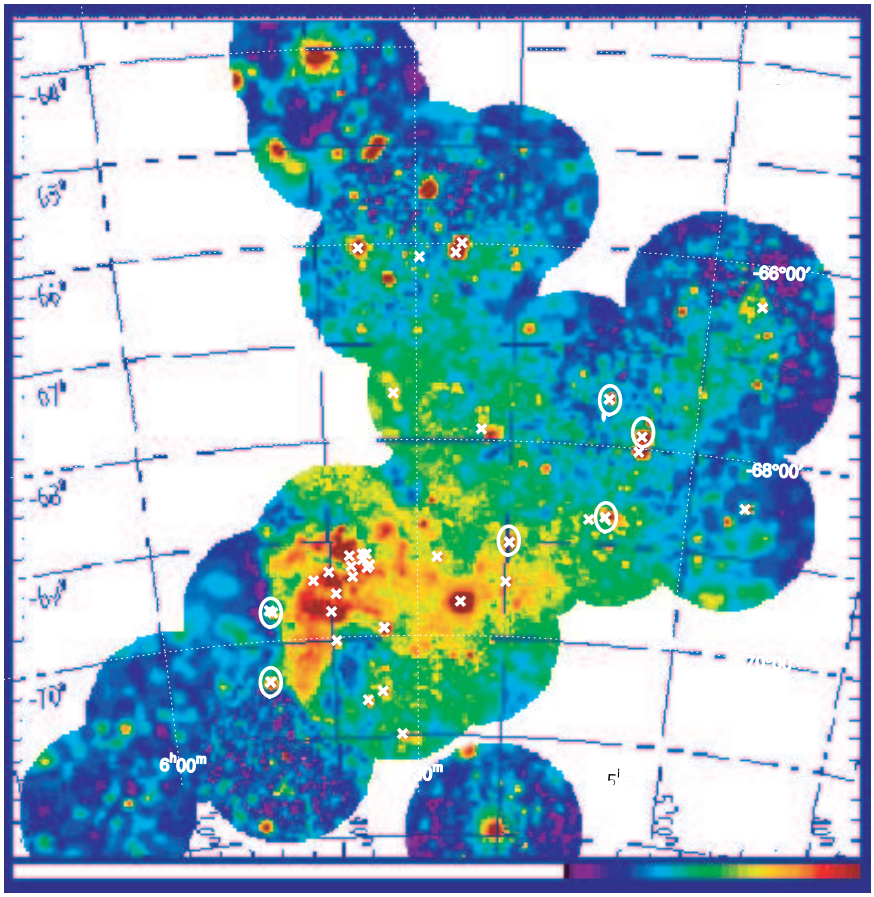

Figure 7.21: The distribution of SNRs in the LMC (crosses) overlaid on the ROSAT X-ray map of LMC. The crosses encircled indicate SNRs from Type Ia progenitor or candidates. These SNRs from Type Ia progenitors tend to lay at the age of bright diffuse X-ray region.

Table 7.12: Summary of plasma paramters of the sample-1 SNRs.

Name	$kT_{\rm e}$ (keV)	$n_{\rm e}$ (cm^{-3})	$t_{\rm sedov}$ (yr)	$t_{\rm i}$ (yr)
DEM L316 A†	0.90 (0.86–1.09)	0.37	4.6×10^3 (4.2×10^2)	3.9×10^3 (1.3×10^4)
DEM L316 B‡	0.72 (0.68–0.76)	0.75	7.1×10^3 (2.0×10^2)	$> 4.2 \times 10^4$
0532−71.0†	0.55 (0.45–0.62)	0.09	1.5×10^4 (1.5×10^3)	1.2×10^4 (1.8×10^3)
0548−70.4*	0.65 (0.61–0.71)	1.04	6.9×10^3 (3.0×10^2)	5.4×10^3 (5.1×10^2)
0534−69.9*	0.60 (0.46–0.72)	0.76	9.1×10^3 (1.3×10^3)	1.4×10^3 (4.0×10^2)
DEM L241$^{\natural}$	1.31 (0.40–2.64)	0.54	4.5×10^3 (3.6×10^3)	1.5×10^3 (6.9×10^2)
0520−69.4*	1.42 (0.91–2.37)	0.40	6.0×10^3 (1.5×10^3)	1.2×10^3 (2.3×10^3)
0532−67.5*	0.69 (0.63–0.75)	0.37	1.4×10^4 (6.4×10^2)	$> 8.6 \times 10^4$
N86*	0.77 (0.60–1.05)	0.17	1.5×10^4 (2.2×10^3)	$> 2.0 \times 10^5$

The notation $kT_{\rm e}$, $n_{\rm e}$, $t_{\rm sedov}$, and $t_{\rm i}$ represent the temperature, electron density, Sedov age, and ionization timescale, respectively. Parentheses indicate the error. Errors include only the statistical uncertainty from the spectral fitting results (at the 90% confidence level).

† Center-filled morphology. Filling factor of 1 was assumed.

‡ Shell-shaped morphology. Filling factor of 0.23 was assumed.

* Diffuse-face morphology (only N86 has irregular morphology). Filling factor of 0.1 was assumed.

$^{\natural}$ No HRI observations. Filling factor of 0.1 was assumed.

Chapter 8

Analysis and Results III

After getting rid of the point-like and extended objects, the diffuse X-ray emission widely spreading over the whole LMC disk remains. Though its existence has been well known since the observations of the Einstein satellite, no detailed spectroscopy of the diffuse X-ray emission has been carried out.

Though Wang et al. (1991) carried out a simple spectral analyses of diffuse X-ray emission, their results must be handled with caution because of the following reasons; 1) they did not mention whether the non-thermal model, such as power-law model, surely failed to reproduce the diffuse X-ray spectrum, 2) the energy resolution of the Einstein IPC was not so high, 3) the statistics in their spectrum were quite poor. Therefore, no one can get a sufficient answer to such a simple question, as to whether the origin of the diffuse X-ray emission is thermal or not.

Even if their assumption that the diffuse X-ray emission has thermal origin is valid, another problem remains as follows. The simple thin-thermal plasma model in their spectral fitting did not account for the NEI effect. For an ionizing plasma, the characteristic timescale for realizing ionization equilibrium is

$$t \sim \frac{10^{12}}{n_{\rm e}}\ {\rm s} = \frac{3 \times 10^4}{n_{\rm e}}\ {\rm yr} \tag{8.1}$$

(Masai 1994). For the value of the density of $\sim 10^{-2}$ cm^{-3} (the previously derived densities of the diffuse X-ray emission within super giant shells LMC-2 and LMC-4 are $\sim 9 \times 10^{-3}$ and $\sim 8 \times 10^{-3}$ cm^{-3}, respectively; Points et al. 2000.), the ionizing time scale becomes $\sim 3 \times 10^6$ yr, which is comparable to the escape time scale of the plasma (see below for the detail). It is not until the time when the plasma escapes from the LMC body that it finally reaches to the CIE state. Therefore, large amount of the plasma remaining within the LMC body should stay at the NEI state.

Here, we report on the spectral analysis of the diffuse X-ray emission with better spectral

resolution than ever achieved, taking into account of the NEI effect.

8.1 Datasets used in diffuse X-ray emission analyses

The SIS data for most of the pointing observations were obtained with 1-CCD faint mode because the original purposes for these are the investigations for the bright point-like sources, such as SNRs, XBPs and so on. We can not accumulate the spectra of diffuse X-ray emission with enough statistics from the rest of the region after subtracting these bright sources in following two reasons. The field of view of SIS, especially when it is used in the 1CCD mode, is quite small. Because of the wide-based point spread function of ASCA XRT, almost all the region on the detector is filled up with the X-ray photons from primary target sources when they are bright. Adding to that, the mode of SIS data taken during the LMC survey project were complementary 2-CCD faint mode in order to cover as wide field as possible with SIS. However, since the SIS was heavily damaged by proton irradiation while in orbit, the energy resolution and dark current of the SIS at the time of LMC survey project were significantly degraded and increased compared with those just after the launch of ASCA (Yamashita 1995; Dotani et al. 1997; Tomida et al. 1997). Therefore, we did not use the SIS data for the study of diffuse X-ray emission.

In 11 out of 60 pointing observations, the bit assignment of GIS telemetry was changed to achieve higher time resolution at the sacrifice of spatial information of detectors because the original targets were highly time variable sources, such as pulsars. Therefore, we could not separate the diffuse X-ray emission clearly from the sources in the same field of view. Other 17 pointing observations were not available because the entire fields of view of GIS were heavily polluted by the bright glaring point or extended sources in the same field of view. In addition, 21 pointing observations were also unavailable because those were heavily polluted by the stray light from bright HMXB LMC X-1, or SNR N132D, or both. As a results, we used only 11 out of 60 pointing observations for the spectral analysis of the diffuse X-ray emission. The selected regions are shown in Fig. 8.1.

For the data of each pointing, we made X-ray spectra of the diffuse X-ray emission using the events within $17.5'$ from the center of the field of view (within this radius, we can get a warranted ARF file by GIS calibration team with the 'ascaarf' command provided in HEASOFT 5.0 package by NASA/GSFC.) after excluding contaminations from the sources within the circular region centered on them whose radius is typically $3'$. For bright or extended sources, we used larger radius than $3'$.

The accumulated spectra for each 11 pointing observations include not only the X-ray photons from the diffuse X-ray emission itself, but those from cosmic X-ray background (CXB) and non X-ray background of the GIS detectors (NXB). In order to subtract the X-ray photons from CXB and NXB as a background, we accumulated the background spectra

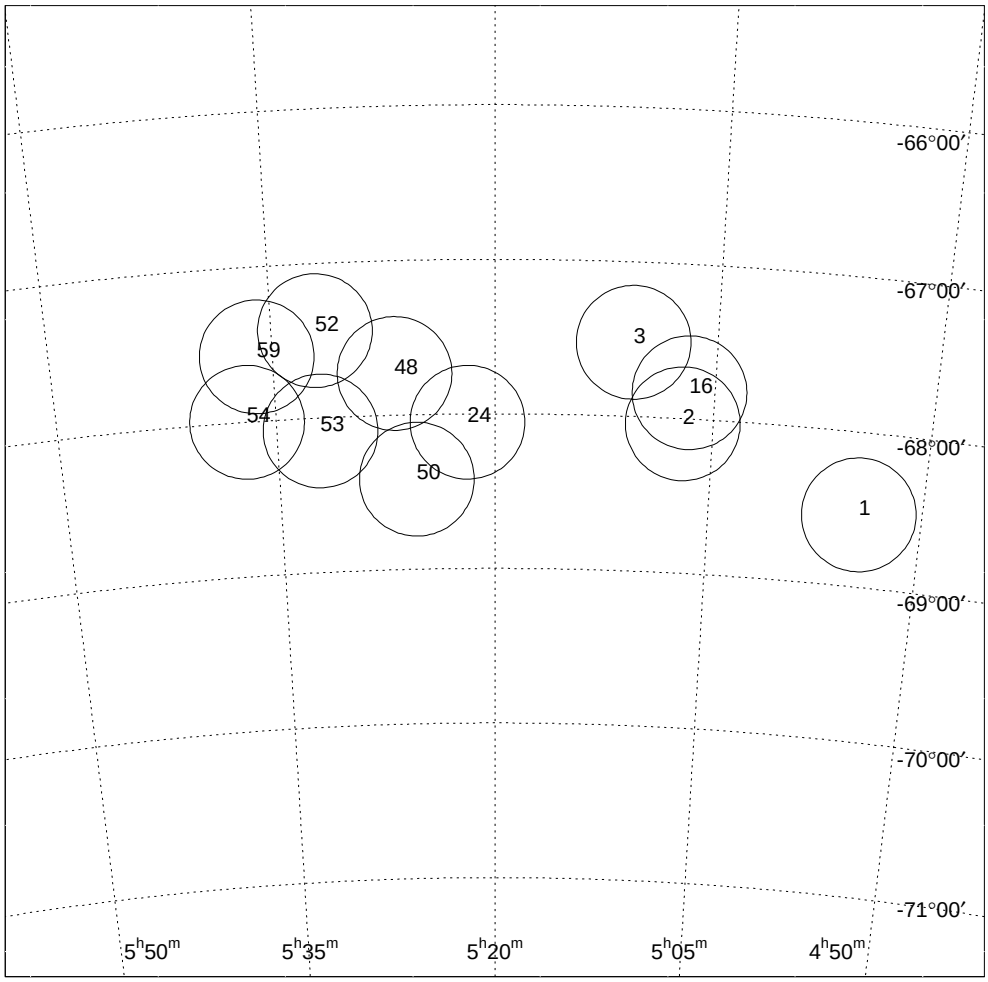

Figure 8.1: ASCA GIS pointing positions for the data used in the diffuse X-ray emission. Each circle represents the GIS fields of view. The numbers displayed in the circle show the observation IDs in Table 5.1.

from the data of blank-sky observations provided by the ASCA Guest Observer Facility (GOF) of NASA in a following way.

The blank-sky data set includes GIS high latitude observations taken between 1993 June and 1995 December which was first provided by Dr. Ishisaki (Ishisaki 1997) during the course of CXB analyses in his PhD thesis (See Table B.1). The data were available in the form of event files after the sources brighter than $\sim 1 \times 10^{-13}$ erg s^{-1} cm^{-2} in 2–10 keV were removed (The 'mask file' supplied by Dr. Ishisaki, which were used to remove the contaminations from the sources are explained in Ishisaki (1997).). These blank-sky event files were screened with the standard criteria which are the same as those used for the data from which diffuse X-ray emission spectra were accumulated (See Table 5.3).

The background spectra were accumulated from the same selected regions in the GIS detector as those from which the spectra of diffuse X-ray emission were accumulated (for example, we must take account of the effect of masking-out the point sources, and so on). This so-called "vignetting effect" has quite large influence on the spectral shape. The actual command used for taking this step is 'mkgisbgd' provided in HEASOFT 5.0 package. 'mkgisbgd' reads the WMAP of the each input diffuse X-ray spectra and make sure the detector regions to use. It, then, creates exposure corrected blank sky spectra and images for each input spectral file, using point-source removed blank sky data set (Table 5.3 in Appendix. B) described above.

The blank-sky data set includes the data taken at different time, which extend over a long period of time. The NXB of GIS is known to have been increasing since the launch with its spectral shape unchanged (Ishisaki 1997; Ishisaki et al. 1997; see also Fig. 8.2). However, if we use only the limited blank-sky data which falls within the limited time span

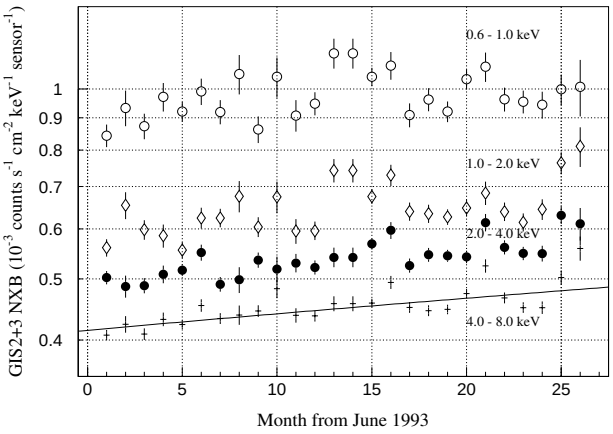

Figure 8.2: Change of GIS NXB fluxes with several energy bands since the launch. NXB shows gradual increase since the launch. This figure is adopted from Ishisaki (1997).

which encompasses each pointing observation, the resulted background spectra have only

poor statistics. Moreover only a part of the data from the blank-sky data set cannot cover whole GIS field of view because each blank-sky data has quite a lot of masked-out regions.

The CXB spectrum is known to be reproduced with the combination of soft and hard power-law models, whose photon indices are ∼6.0 and ∼1.4, respectively. The hard component does not fluctuate much, while the soft component varies from field to field, due to the Galactic contributions (Ishisaki et al. 1997). There are only a few blank-sky data which were taken from the regions of which the values of Galactic latitude are close to that of the LMC (the data with IDs QSF3, see Table B.1). With the same reason we mentioned above, we cannot cover the whole GIS fields with these limited data sets. Moreover, the resulted background spectra are again poor in statistics. The total exposure time of the background spectra of, for example, 0453−68.5 region (ID No.1) resulted from only the data of QSF3 region is 1.5×10^5 s, while that from all the blank-sky data set is 3.3×10^6 s. The exposure time of the former is more than an order of magnitude less than that of the latter. Therefore, we finally decided to use all the blank-sky data. All the diffuse X-ray and corresponding background spectra accumulated from each selected 11 pointings are displayed in Appendix. C.

The shape of diffuse X-ray spectrum of each pointing resembles to the corresponding background spectra quite well in higher energy band. It suggests us that the diffuse X-ray emission does not continue to harder energy band, or that, at least, it is quite weak. It is also good evidence for that the resulted background spectra take into account of the vignetting effect very well. Because the statistics of diffuse X-ray spectra accumulated from each pointing are poor, and also because their spectral shapes are not largely different from pointing to pointing, we decide not to discuss the difference among them. We sum them up to concentrate on discussing the characteristics of diffuse X-ray emission as a whole, instead. The total exposure time of the summed up and background spectra are 7.7×10^5 s and 3.6×10^7 s, respectively.

Since the X-ray emission of the LMC extends over a region much larger than the ASCA field of view, stray lights occupy a significant fraction of the photons detected at each region. For example, in the case of the uniformly extended CXB, if we integrate X-ray photons with the radius of $20'$ from the optical axis, the number ratio of the X-ray photons which come from the region outer than $20'$ to that of the total X-ray photons is about 45% at 1 keV (Ishisaki 1997). According to Ishisaki (1997), it is enough to take into account stray lights which come from the region within $180'$ from the optical axis, assuming the uniform spectrum and a constant brightness throughout the area. This value of $180'$ was determined in such a way that the leakage flux become almost negligible ($< 1\%$ at 1 keV).

However, from the ROSAT PSPC image of LMC, the extent of the diffuse X-ray emission is something smaller than $180'$. Therefore we assumed a slightly smaller extent of $120'$, a constant spectrum and brightness within the area for the diffuse X-ray emission in the LMC. To calculate the ARF, we used the 'ascaarf' in HEASOFT 5.0. 'ascaarf' in HEASOFT 5.0

reads the series of raytracing image data (at the 300 energy steps from 0.1 keV to 12 keV) and calculates the leakage of X-ray photons from the outer field of view into the selected region on the GIS detector. We used the standard RMF provided by the GIS team.

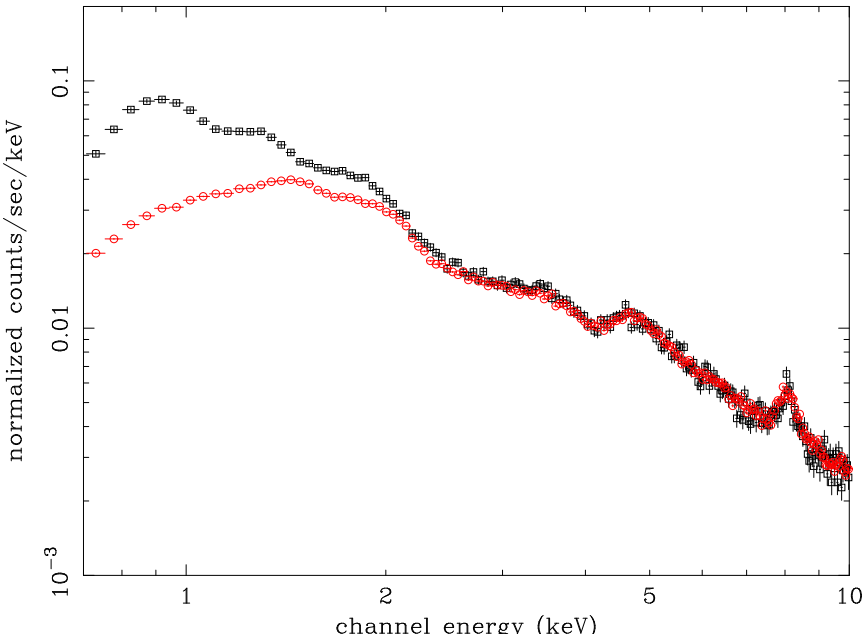

Figure 8.3: The total diffuse X-ray spectrum (marked with squares) and corresponding background spectrum (marked with circles). The excess emission above the background spectrum shows the emission from diffuse X-ray in the LMC.

8.2 Results for spectral analyses

8.2.1 Non-thermal model fit

First of all we fitted the X-ray spectrum in the 0.7–10.0 keV band with power-law model in order to investigate the possibility that the diffuse X-ray emission has non-thermal origin. The χ^2 value of this model was 318.71 with 96 degrees of freedom, which is far from acceptable. There was large discrepancy between the model curve and the data. In addition we

see that the residuals show a waving behavior which suggests the existence of emission lines from heavy elements in the thin-thermal plasma (Fig. 8.4). Therefore, we insist that the diffuse X-ray emission is not non-thermal but thermal in origin, which is a strong support that it is arising from hot ionized plasma in the LMC.

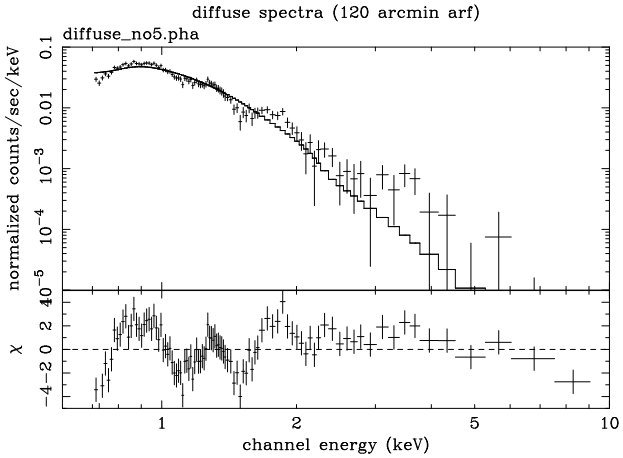

Figure 8.4: The background subtracted diffuse X-ray spectrum and folded power-law model are displayed at upper panel. The lower panel shows the residuals from the model. The power-law model is statistically rejected with large χ^2 value of 318.71 (for 96 d.o.f.).

8.2.2 One-temperature CIE model fit

We next tested the thin-thermal plasma model in the CIE state in the spectral fitting. In order to unify the spectral code used with the subsequent analysis, we used the Masai model with fixed ionization parameter of $n_e t_i = 10^{13.0}$ s cm^{-3}, which represents the thin-thermal plasma spectrum in the CIE condition. In the spectral fitting, we assumed that the elemental abundances of the plasma are identical to the mean LMC value (see Russell and Dopita 1992; Hughes et al. 1998). The free parameters are temperature, column density and emission measure per unit solid angle, defined as $EM' \equiv (n_i^2 V')/(4\pi D^2)$ where n_i, V' and D are the ion number density in the plasma, plasma volume per unit solid angle, and distance to the plasma, respectively. However, this model could not sufficiently well reproduced the spectrum, and was rejected with large χ^2 value ($\chi^2 = 142.87$ with 96 d.o.f.). The fitting results are shown in Table 8.1 and Fig. 8.5.

Table 8.1: Best-fit parameters of diffuse X-ray emission for CIE model.

$kT_{\rm e}$ (keV)	0.55 (0.53–0.56)
$EM'^{\dagger}$ (10^{15} cm^{-5})	3.8 (3.7–4.1)
$N_{\rm H}$ (10^{20} cm^{-2})	0.0 (< 3.0)
χ^2 (d.o.f)	142.87 (96)

Parentheses indicate 90% confidence intervals for a single relevant parameter ($\Delta\chi^2 = 2.71$).
The elemental abundances are fixed to mean LMC value.
† Emission measure per unit solid angle, defined as: $(n_{\rm i}^2\ V^{'})/(4\ \pi\ D^2)$. See text for details.

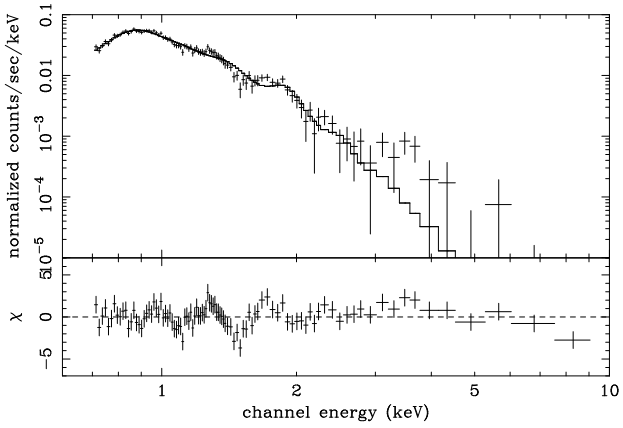

Figure 8.5: Same as Fig. 8.4, but for the CIE model fit.

8.2.3 One-temperature NEI model fit

Based on the results derived in previous subsection, we next let the ionization parameter vary freely. In the spectral fitting, we assumed that the elemental abundances in the plasma are, again, identical to the mean LMC value (see Russell and Dopita 1992; Hughes et al. 1998). The best-fit parameters and model curves are shown in the middle column of Table 8.2 and Fig. 8.6, respectively. To let the ionization parameter be free improved the χ^2 value by 16.5. Therefore, from the F-test, the fitting result was improved by 99.9% than using the CIE model, thus NEI model is more reliable. The χ^2 value is slight larger than the acceptable range and we also see that the residuals show a bit heaving behavior, which was hardly reduced by letting the elemental abundances vary freely. We, then, tested the further model fitting with additional plasma component with fixed elemental abundances to the mean LMC value. In order to reduce the humps seen in the residuals, a plasma component with lower temperature and ionization parameter is expected. However, the fitting results with such an additional plasma component could not be obtained. Instead, we got the fitting results with the combination of higher temperature ($kT_{\rm e} \sim 2$ keV and $n_{\rm e}t_{\rm i} \sim 10^{9.0}$ s cm^{-3}) and lower temperature ($kT_{\rm e} \sim 0.5$ keV and $n_{\rm e}t_{\rm i} \sim 10^{11.0}$ s cm^{-3}) plasma components. This two-temperature NEI model still failed to reduce the heaving behavior in the residuals and only a little reduction was seen in the χ^2 value compared with one-temperature NEI fitting ($\chi^2 = 114.49$ with 92 d.o.f.). Therefore, we are quite skeptical in applying additional plasma model component in the spectral fitting to explain the spectrum. Moreover, to take into account that the systematic errors in the experimental data due to calibration uncertainties, for example, have not been included, the only a slight larger χ^2 value seen in the one temperature NEI fitting results, together with the slight heaving behavior in residuals might be acceptable. Therefore, we regarded that the results of one temperature NEI fitting is more simple and realistic to approximate the overall diffuse X-ray spectral shape. Hereafter, we adopt the results from one temperature NEI fitting.

8.3 Systematic errors of the diffuse X-ray spectrum

Here in this section, we examine the effects of the systematic errors on the diffuse X-ray spectrum.

8.3.1 Uncertainty of the ARF

One may argue against the reliability of the assumption of the extent of diffuse X-ray emission ($120'$) which we tentatively used. To study this, we examined the effects of the systematic errors on the fitting parameters, which arise from the different assumptions for the extent of diffuse X-ray emission. When we made ARF files, we assumed additional 2 cases for the

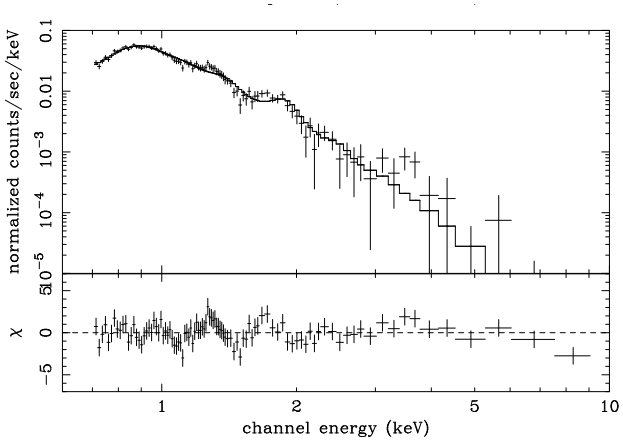

Figure 8.6: Spectral fitting results of diffuse X-ray emission for one-temperature NEI model. The top panel shows the data and best-fit model, while the lower panel shows the residuals.

extent, 60′ and 180′. (hereafter we call case 1, 2, and 3 which correspond to the assumptions of the extent 60′, 120′ and 180′.). We again tested the NEI model fit with those different ARFs. The best-fit parameters are shown in Table 8.2. The confidence contours between ionization age and temperature show that those fitting results with different ARFs do not differ drastically (see Fig. 8.7), while the confidence contours between column density and temperature, together with the values of $EM^{'}$ differ only in the case 1 fitting result. This shows us that the X-ray photons coming from out of the GIS field of view increases as the source extent becomes larger, however, the increasing rate hits its peak when the source extent is close to 120′. Therefore, the fitting results do not change much regardless of what value is assumed for the extent of diffuse X-ray emission, as long as it is between 120′ and 180′. Because the ROSAT X-ray image shows us that the extent is between 120′ and 180′, the value which tentatively used (120′) does not influence on the derived fitting results.

8.3.2 Stray light from LMC X-1

Here in this section, we estimate the stray light effect of LMC X-1. In Fig. 8.8 we show the counting rates of the Crab stray-light observations and the ray-tracing simulations in 0.7–10 keV band (from Ishisaki (1997)). In the ray-tracing simulation, the spectral shape of Crab was assumed to be an absorbed power-law model (power-law index, normalization at 1.0 keV and the column density were $\Gamma = 2.10$, 9.7 cts s^{-1} cm^{-2} keV^{-1}, and $N_{\rm H} = 3.0 \times 10^{21}$ cm^{-2}.). From Fig. 8.8, you see that the counting rate of stray-light decreases to about 0.01 and 10^{-3}cts s^{-1} GIS^{-1} at the offset angle from the Crab of 70′ and 80′, respectively. Because the spectral shape of LMC X-1 resembles to that of Crab, we can apply the above results by Ishisaki (1997) to the case of LMC X-1. In Fig. 8.9 we show the position of LMC X-1 (with cross) and the GIS field of views of observations used for diffuse X-ray emission. In the same

Table 8.2: Best-fit parameters of diffuse X-ray emission for Masai model. ARFs with different assumption for the extent of diffuse X-ray emission, such as 60, 120, and 180 arcmin, were used (case 1, case 2, and case 3).

	case 1	case 2	case 3
$kT_{\rm e}$ (keV)	0.83 (0.72–0.89)	0.91 (0.77–1.00)	0.89 (0.75–1.01)
log $n_{\rm e}t_{\rm i}$ (cm^{-3} s)	10.53 (10.42–10.69)	10.49 (10.36–10.63)	10.50 (10.36–10.65)
$EM'^{\dagger}$ (10^{15} cm^{-5})	2.20 (2.06–2.77)	1.63 (1.55–2.15)	1.69 (1.53–2.21)
$N_{\rm H}$ (10^{20} cm^{-2})	0.0(<4.0)	0.2 (< 5.2)	1.4 (< 6.4)
B^{*}(10^{-8} ergs s^{-1} cm^{-2} str^{-1})	4.2	3.4	3.4
χ^2 (d.o.f)	128.35 (95)	126.35 (95)	126.54 (95)

Parentheses indicate 90% confidence intervals for a single relevant parameter ($\Delta\chi^2 = 2.71$).
The elemental abundances are fixed to mean LMC value.
† Emission measure per unit solid angle, defined as: $(n_{\rm i}^2\ V^{'})/(4\ \pi\ D^2)$. See text for details.
* Unabsorbed X-ray surface brightness in 0.7–10 keV band.

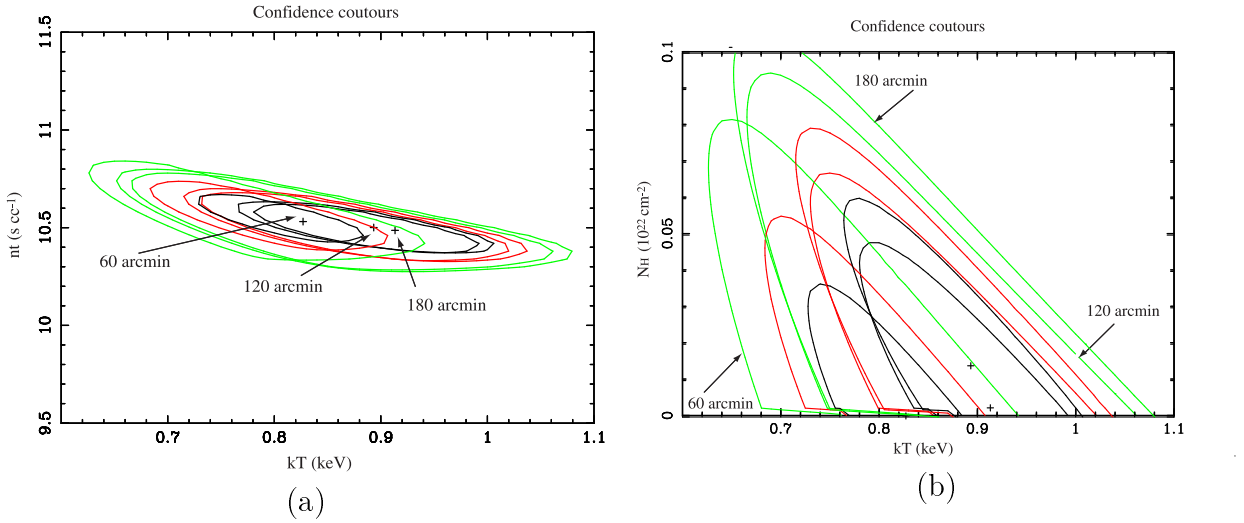

Figure 8.7: The confidence contours between ionization age and temperature for left and column density and temperature right panels, respectively. The results from the fitting using ARFs with assumption for the different extent of the diffuse X-ray emission. Contours corresponds to 68%, 90%, and 99% levels, respectively. Best-fit parameters are indicated by plus signs.

figure, circles which show the offset angle of $70'$ and $100'$ from LMC X-1 are displayed. The offset angle between the edge of the pointing which is nearest to LMC X-1 and LMC X-1 itself is more than $100'$. At the offset angle of $100'$, the counting rate of LMC X-1 decreases by orders of 4 as is shown in Fig. 8.8, thus becomes to be $\sim 8 \times 10^{-4}$ cts s^{-1} GIS^{-1}, which is about 1% of that of the diffuse X-ray emission. Taking into account that the counting rate of stray-light drops drastically as the offset angle increases, the contamination from LMC X-1 is negligible small in our diffuse X-ray spectrum.

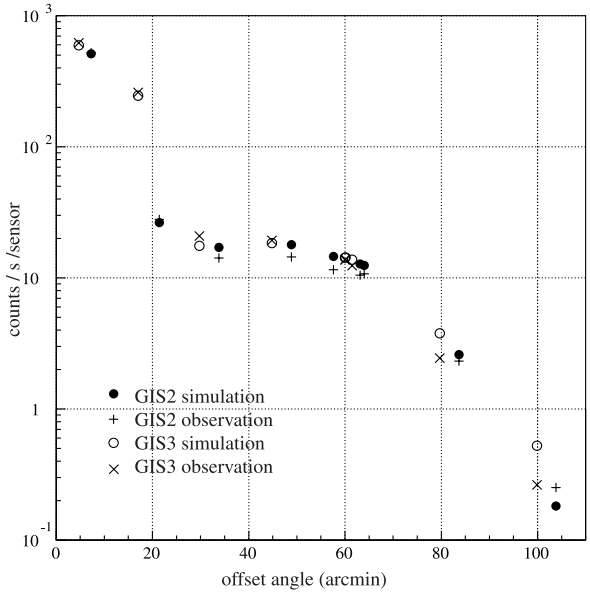

Figure 8.8: Counting rates of the Crab stray observations and the ray-tracing simulations in 0.7–10 keV energy band, plotted versus offset angle of the Crab nebula (Ishisaki 1997).

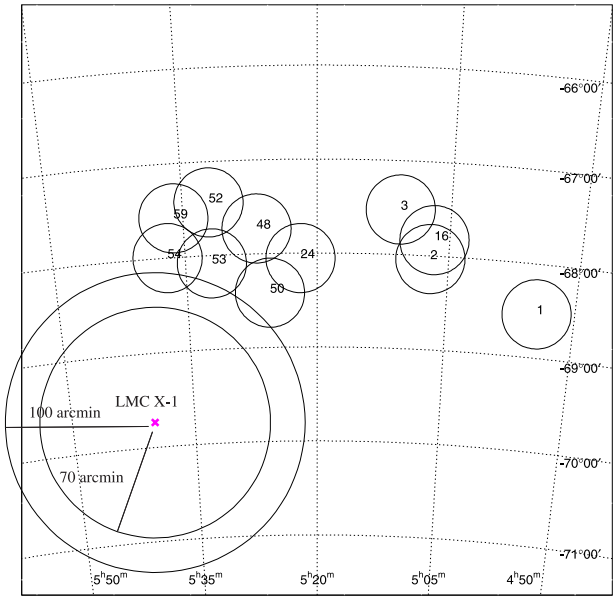

Figure 8.9: GIS field of views of observations for diffuse X-ray emission and the position of LMC X-1. The positions whose distances are 70′ and 100′ from LMC X-1 are displayed with circles.

Chapter 9

Discussion

9.1 Plasma parameters of the SNRs

In chapter 7, we have studied the individual nature of sample-1 SNRs. The sample-1 SNRs together with the sample-2 SNRs include all the LMC SNRs for which spectral analyses with ASCA are available. These samples cover SNRs of various ages, from younger to older ones. From the spectroscopy of individual sample-1 SNRs (chapter 7) and also from the results of sample-2 SNRs by Hughes et al. (1998) and Hayashi (1997), we can diagnose the plasma conditions within SNRs. As the SNRs age, the plasma within them are thought to show less characteristics of their incident progenitors, but show more characteristics of the ambient ISM because the swept-up mass increases. At the same time, the X-ray images of SNRs provide us important information, the X-ray sizes of them, which can be an indicator of their ages. Therefore, we are sure to trace the course of evolution of plasma in the SNRs using both of the information.

First of all, we plot the relation between radii and the Sedov ages of LMC SNRs in order to confirm that the sizes of SNRs can certainly be a tracer of their ages using the equation (3.41) (shown in Fig. 9.1). Angular sizes of SNRs were applied from the results with HRI observations (Williams et al. 1999). Most of the sample-1 SNRs do not show shell-shaped morphology which is one of the strong supports that they are in the Sedov phase, but show, instead, diffuse-face morphology. Therefore, one may argue that the derived the Sedov ages for sample-1 SNRs are meaningless. However, an excuse for this is that most remnants over 8 pc in radii show velocity-size relationships similar to what is expected for a Sedov remnant (Lozinskaia 1980; Rosado 1986) (the Sedov age is a function of shock radius and velocity). Because $1'$ is equivalent to 15 pc at the LMC distance, all the SNRs in sample-1 fall well in this range. Therefore, the derived Sedov ages for sample-1 SNRs are not meaningless. For sample-2 SNRs, we did not adopt the Sedov ages given in Hayashi (1997) and Hughes et al. (1998), because they used the SNR sizes from radio observation (Mathewson et al. 1983) in

order to obtain the Sedov ages (the Sedov age strongly depends on the size of SNR). Instead, we adopted the Sedov ages, which we re-calculated with the radii from X-ray observation (Williams et al. 1999). As we have mentioned in section 7.4.6, the ionization ages are more reliable indicator for the ages of SNRs which have already entered the stage of momentum-conserving expansion (e.g. 0532−67.5 and N86). Therefore, this fact together with Fig. 9.1 show that total SNR samples in the LMC include those with various ages, scattering from about 10^3 to more than 10^5 yr, and also suggests that the SNRs having grown within the average LMC environment stay within the Sedov stage for about 10^4 yr.

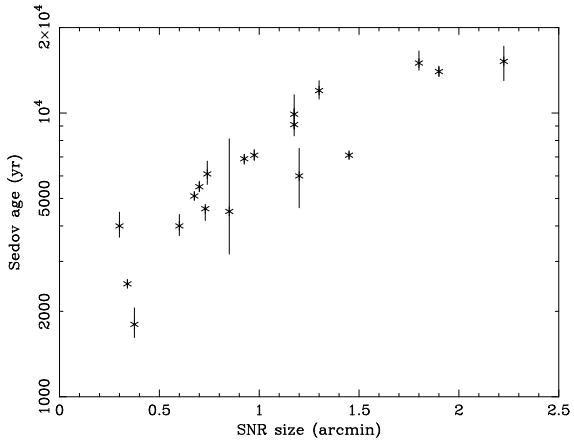

Figure 9.1: Radii vs the Sedov ages for the SNRs in the LMC. For the sample-2 SNRs whose analyses were already reported, we used the results in the papers (Hayashi 1997; Hughes et al. 1998). Error bars include only the statistical uncertainty (at the 90% confidence level) for the temperature. See the detail in the text.

We next investigate the relation between SNR size and the density of plasma within them, namely, the relation between age and the density. The densities for sample-1 SNRs were derived in chapter 7. We re-calculated the ambient densities for sample-2 SNRs with equation (3.40) using the normalization factor obtained by Hughes et al. (1998) and Hayashi (1997) and the radii derived by Williams et al. (1999).

However, there is one point that we must make clear before making comparisons among densities (it is also same for other plasma parameters) of SNRs from two different samples altogether. The model used in Hayashi (1997) and Hughes et al. (1998) for spectral analyses is a peculiar model (hereafter we call model-2), which consider the dynamical evolution of plasma in the SNR to follow the Sedov model as is described in subsection 3.6.2. On the other hand, the model used in our analyses assumes the plasma spreading uniformly in the SNRs (model-1), because sample-1 SNRs have diffuse-face morphology, thus the Sedov model is not applicable to these cases. Therefore, we must be careful in taking up altogether the plasma parameters derived from these different models. However, because model-2 assumes that the dynamical evolution of plasma follows the Sedov model with well known formulae,

it is possible to extract the densities which we can directly compare with the model-1 results in a following way.

The densities re-calculated with equation (3.40) for sample-2 SNRs are the ambient densities of SNRs, while those obtained with equation (7.1) for sample-1 SNRs are the values within the SNRs. We, therefore, should extract the densities within the SNRs from those around sample-2 SNRs. The normalized density profile within the SNR which follows the Sedov model is shown in Fig. 9.2. In the Sodov model, the density immediately behind the shock front is 4 times that of ambient density (strong shock limit), and quickly decreases toward the center of the remnant. It is clear that most of the plasma emitting volume stays just close to the shock front. The normalized luminosity profile within the SNR is also calculated and shown in Fig. 9.2. We determined an average density ($\overline{n_{\rm e}}$ and $\overline{n_{\rm i}}$), assuming that the distribution function of density follows the luminosity profile of the Sedov model, as follows,

$$\overline{n} \equiv \frac{\int_0^{R_s} L_{\rm X}(r) \cdot n(r)\ {\rm d}r}{\int_0^{R_s} L_{\rm X}(r)\ {\rm d}r} \sim 2.6 \times n_0, \tag{9.1}$$

where $L_{\rm X}(r)$ and $n(r)$ are luminosity and density at the radius r within the SNR, and n_0 represents the ambient density. The densities derived from model-2 results in this way (modified density) can be directly compared with the ones from model-1 results. They are shown in the right panel of Fig. 9.3. It is clearly shown that the densities of the plasma within SNRs decrease as the SNRs age. It is a natural consequence, because younger SNRs have swept up only a little ambient ISM, thus the plasma within them show larger density which resulted from the ejecta. On the contrary, because older SNRs have swept up much more ambient ISM, they have forgotten all the details at the SN explosions. Therefore, it is expected that the value of density within SNR gets closer and closer to that of the ISM, as SNR ages. Therefore, the average ISM density should not exceed the value within, at least, the oldest SNR in our sample, ~ 0.1 cm^{-3}.

9.2 Plasma parameters of the diffuse X-ray emission

From the observed quantities, we can calculate the basic parameters of the plasma. Fig. 9.4 shows the differential volume ${\rm d}V$ whose direction is within a solid angle ${\rm d}\Omega$ at a distance of r from us. The volume emissivity ε can be derived from the surface brightness B. The luminosity from the infinitesimal volume is

$${\rm d}L_X = \varepsilon\eta {\rm d}V = \varepsilon\eta r^2 {\rm d}r{\rm d}\Omega, \tag{9.2}$$

where η means a filling factor of the plasma. The differential flux is, then expressed as

$${\rm d}f = \frac{{\rm d}L_{\rm X}}{4\pi r^2} = \varepsilon\eta {\rm d}r\frac{{\rm d}\Omega}{4\pi}. \tag{9.3}$$

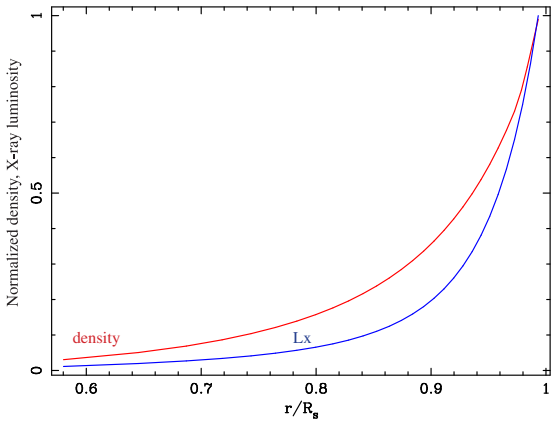

Figure 9.2: Density and luminosity profile within the SNR, which follows the Sedov model. The horizontal axis shows the distance from the center of the SNR (r) normalized by the shock radius ($R_{\rm s}$) and the vertical axis shows density and luminosity normalized by the values at shock front. The density and luminosity decrease immediately behind the shock front.

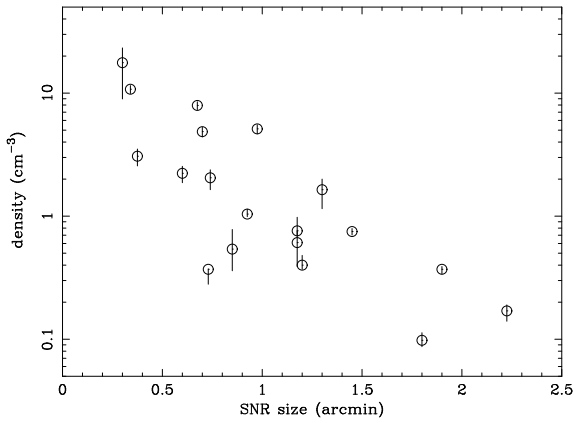

Figure 9.3: Radii vs densities for the SNRs in the LMC. For sample-1 SNRs, the results derived in chapter 7 are applied. While, for sample-2 SNRs, the results from Hayashi (1997) and Hughes et al. (1998) are applied. See the detail in the text. Error bars include only the statistical uncertainty (at the 90% confidence level) from fits for emission measure.

The observable flux (f_Ω) is an integrated one along the line of sight. If we express the depth of the plasma as l, f_Ω is written as

$$f_\Omega = \frac{\eta \mathrm{d}\Omega}{4\pi} \int \varepsilon \mathrm{d}r = \frac{\eta \mathrm{d}\Omega}{4\pi} \bar{\varepsilon} l, \tag{9.4}$$

where $\bar{\varepsilon}$ is the average volume emissivity along the line of sight. The surface brightness is, then, expressed as follows,

$$B = \frac{f_\Omega}{\mathrm{d}\Omega} = \frac{\bar{\varepsilon}\eta l}{4\pi}. \tag{9.5}$$

From the surface brightness B, derived from the spectral fitting (see Table 8.2), the volume emissivity of the plasma is calculated to be $\bar{\varepsilon} = 1.4 \times 10^{-28} \eta^{-1}$ ergs s^{-1} cm^{-2}, where η is the filling factor of the plasma. Here, we assumed the depth of the plasma l to be 1 kpc, which was first applied by Wang et al. (1991).

The plasma density can be derived from the fitting parameter, $EM^{'}$ as

$$n = (\frac{4\pi D^2}{V^{'}} \times EM^{'})^{0.5} = (\frac{4\pi D^2}{D^2 l \eta} \times EM^{'})^{0.5}, \tag{9.6}$$

to be $2.6 \times 10^{-3}\ \eta^{-0.5}$ cm^{-3}, where $EM^{'}$ and $V^{'}$ are the emission measure per unit solid angle and volume per unit solid angle, respectively. We now take the distance to the plasma, r to be identical to that of the LMC, D.

The schematic view of the X-ray emitting plasma is assumed as is shown in Fig. 9.5, thus the volume is $7.6 \times 10^{65}\ \beta$ cm^3, where β represents the uncertainty of the volume. Then, the total luminosity of the plasma L_X is estimated to be

$$L_\mathrm{X} = \bar{\varepsilon} V \eta = 1.1 \times 10^{38} \beta \text{ ergs s}^{-1}. \tag{9.7}$$

Wang et al. (1991) reported that the lower limit of the X-ray luminosity of the plasma to be $\sim 2 \times 10^{38}$ ergs s^{-1} from the Einstein observations. Considering that the accumulated region for our diffuse X-ray spectrum does not include the brightest region around 30 Dor, and that our assumption for the constant brightness of diffuse X-ray emission throughout the whole region, it is natural that the derived luminosity shows somewhat lower value than the Einstein result, thus our result should be the lower limit.

The total plasma energy, defined as

$$U = 3 n_\mathrm{e} k T_\mathrm{e} V, \tag{9.8}$$

can be calculated to be $8.6 \times 10^{54}\ \eta^{0.5}\ \beta$ ergs. Therefore, the radiative cooling time scale (t_cool), defined as U/L_X, becomes $2.5 \times 10^9 \eta^{0.5}$ yr. The plasma pressure, defined as $p = 2 n_\mathrm{e} k T_\mathrm{e}$, is also derived to be $7.5 \times 10^{-12} \eta^{-0.5}$ ergs cm^{-3}. We summarize the plasma parameters in Table 9.1.

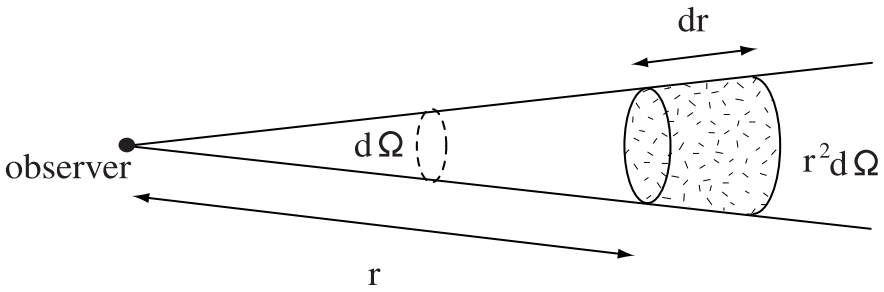

Figure 9.4: A schematic view to show a relation between an observer and a differential volume of emitting region.

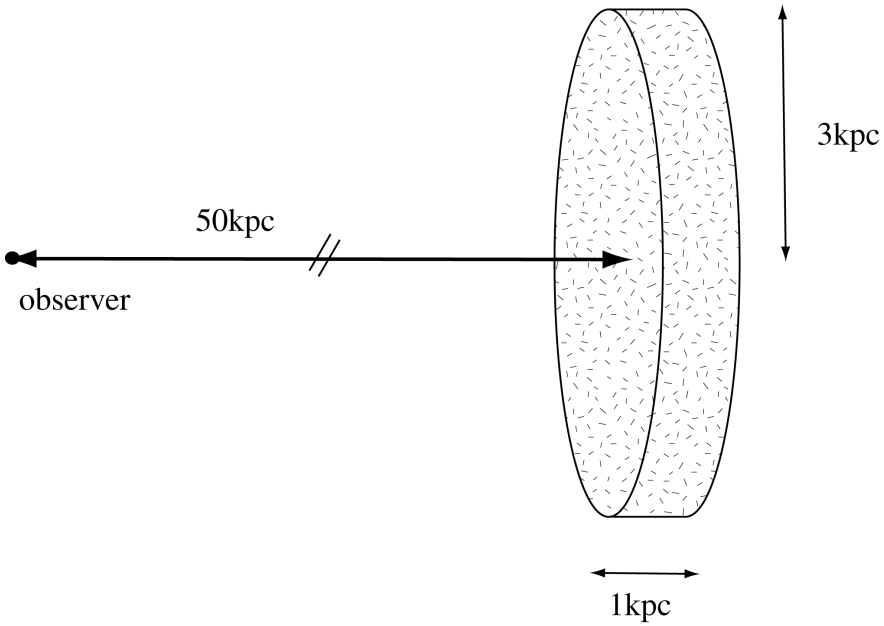

Figure 9.5: A schematic view to show the distribution of diffuse X-ray emission in the LMC.

Table 9.1: A summary of the plasma parameters.

$B^{\dagger}$ (ergs cm^{-2} s^{-1} str^{-1})	3.4×10^{-8}
$\bar{\varepsilon}^{*}$ (ergs cm^{-3} s^{-1})	$1.4 \times 10^{-28}\ \eta^{-1}$
$n_{\rm e}^{\natural}$ (cm^{-3})	$2.6 \times 10^{-3}\ \eta^{-0.5}$
$P^{\ddagger}$ (erg cm^{-3})	$7.5 \times 10^{-12}\ \eta^{-0.5}$
$V^{\diamondsuit}$ (cm^{3})	$7.6 \times 10^{65}\ \beta$
$L_{\rm X}^{\flat}$ (erg s^{-1})	$1.1 \times 10^{38}\ \beta$
$U^{\sharp}$ (erg)	$8.6 \times 10^{54} \beta \eta^{0.5}$

† Unabsorbed surface brightness in 0.7–10.0 keV band.
* Volume emissivity of the plasma. Depth of the plasma was assumed to be 1 kpc. η represents the filling factor.
$^{\natural}$ Electron density. The ion and electron densities are assumed to be identical.
‡ Plasma pressure.
$^{\diamondsuit}$ Plasma emitting volume, where β represents the uncertainty of the volume.
$^{\flat}$ Overall luminosity.
$^{\sharp}$ Total energy.

9.3 Origin of the diffuse X-ray emission

Since Einstein detected diffuse X-ray emission in the LMC, it appeared unlikely that an combination of discrete X-ray sources can account for the bulk of diffuse emission (see the discussion in Wang et al. 1991). Alternatively, it has been suggested that they are formed by the collective action of fast stellar winds and supernova explosions of massive stars. The diffuse X-ray emission is thought to be the shock heated plasma by the stellar winds, SNe, and SNRs. However, it has been long time merely "suggestion", because of lack of detailed spectral information with previous observations. Here we examine the validity of this suggestion.

It has been commonly cited that stellar winds are as important a source of energy as SNe. However, a simple order-of-magnitude comparison between stellar wind energy and SN energy shows that SN energy is higher than the cumulative stellar wind energy. From the typical stellar wind terminal velocity of $\sim$ 2000 km s^{-1} and the typical mass loss rate of $\sim 10^{-7}$ M$_{\odot}$ yr^{-1}, the cumulative mechanical energy of the stellar wind within the typical lifetime of a massive star ($\sim 10^{6}$ yr) is $\sim 4 \times 10^{48}$ ergs, which is far less than the canonical explosion energy of one SN. Therefore, hereafter we consider only the contribution from SNe.

In the first place, are the spectral features of diffuse X-ray emission consistent with those of plasma in the SNRs? SNRs are known to emit variable X-ray spectra depending on their ages. Younger SNRs (with the typical age of $\sim$ 1000 yr) might not be the major contributor of diffuse X-ray emission, because the elemental abundances and temperature

seen in diffuse X-ray emission are quite lower than those seen in the plasma of typical young SNRs (e.g. 0509−67.5, 0519−69.0, and N103B).

Then how are the old SNRs, which are in the radiative cooling phase? The SNRs at radiative cooling phase made cold and dense shells around themselves, within which gas remains at high temperature for a long time, because the radiative loss of such hot and low density plasma is quite small (Cox and Smith 1974). It might be possible that they are observable in the form of diffuse X-ray emission; the observed temperature of diffuse X-ray emission is comparable to that of the hot plasma inside SNRs. However, the mass within the SNRs is so heavily concentrated near the edges (shock front) that only a small fraction is hotter than twice the post-shock temperature (the typical post shock temperature is $\lesssim 0.1$ keV; also see Fig. 9.6; Cox 1972). Therefore, the SNRs in the radiative cooling phase also fail to be the major contributors of the diffuse X-ray emission.

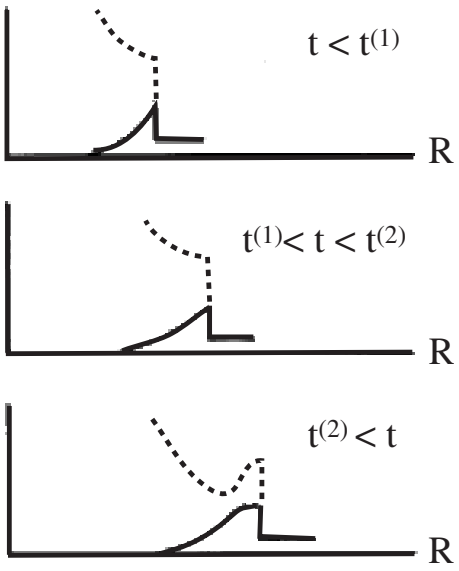

Figure 9.6: Temperature (dotted line) and density (solid line) distribution within SNRs in radiative cooling phase by Cox (1972). The top, middle, and bottom panels show those at the adiabatic phase, the time when the cooling of SNRs begins to be dominated not by the expansion of the shells, but by the radiative cooling (t^1), and the time when dynamical evolution of SNRs is completely governed by the radiative cooling (t^2). Though the temperature increases inside of the SNR, the most of the matter is concentrated near the shock front, where the temperature is lower.

Then the still remaining candidate might be SNRs which are in the adiabatic phase. Their spectra show similar temperature and elemental abundances to those of diffuse X-ray emission, thus it might be possible that ensemble of unresolved SNRs in the adiabatic phase are the origin. If so, various constraints exist, as are shown on the n_0–t plane in Fig. 9.7. From the Sedov's similarity solution (Sedov 1959) the expansion radius R_s pc and temper-

ature $kT_{\rm s}$ keV of the shock front of an SNR in the adiabatic phase is expressed as equation (2.25) and (2.27);

$$R_{\rm s} = 0.31 n_0^{-0.2} E_{51}^{0.2} t^{0.4} \ {\rm pc} \tag{2.25}$$
$$kT_{\rm s} = \tfrac{3}{16}\mu V_{\rm s}^2 = 1.7 \times 10^4 n_0^{-0.4} E_{51}^{0.4} t^{-1.2} \ {\rm keV} \tag{2.27}$$

Here, the shock temperature can be defined as

$$T_{\rm s} = \frac{n_{\rm e} T_{\rm e} + n_{\rm i} T_{\rm i}}{n_{\rm e} + n_{\rm i}}, \tag{9.9}$$

where $T_{\rm e}$ and $T_{\rm i}$ are the electron and ion temperatures, respectively.

The dotted lines in Fig. 9.7 represent the conditions where the temperature just behind the shock front ($kT_{\rm s}$) takes 0.7 keV and 1.5 keV, which include the range consistent with temperature obtained ($kT_{\rm e}$) from the fitting of diffuse X-ray emission. In the case where an external disturbance is mechanical such as shock heating, ions are heated more rapidly than electrons (It arises from the difference between electron and ion mass, $kT_{\rm i,e} = (3/16) m_{\rm i,e} V_{\rm s}^2$, where $m_{\rm e}$ and $m_{\rm i}$ are the electron and ion masses), and electrons are gradually thermalized due to Coulomb collisions with ions. The timescale for the ion and electron temperature of the gas behind the shock front to reach energy equipartition is

$$t_{\rm eq} = 9.9 \times 10^{12} \langle \ \frac{A_{\rm i}}{Z_{\rm i}^2} \ \rangle \ \frac{(kT_{\rm e})^{1.5}}{n_{\rm e} \ln \Lambda} \ {\rm s}, \tag{9.10}$$

where $A_{\rm i}$ and $Z_{\rm i}$ are the ion mass in atomic units and ion charge, respectively. $\ln \Lambda$ is the Coulomb logarithm ($\ln \Lambda \simeq 30$), which is a function insensitively depending on $T_{\rm e}$ and $n_{\rm e}$ (Spitzer 1978). $\langle \ \rangle$ means the average value over the various ions (we assume $\langle A_{\rm i}/Z_{\rm i}^2 \rangle \simeq 1$). The units for electron temperature and the number density of the electrons are keV and cm^{-3}, respectively. Because the temperature derived from the fitting is $kT_{\rm e} \sim 0.9$ keV, $n_{\rm e} t_{\rm eq}$ is calculated from equation (9.10) as $\sim 3 \times 10^{11}$ s cm^{-3}, while the ionization timescale parameter ($n_{\rm e} t_{\rm i}$) derived from the fitting is $\sim 3 \times 10^{10}$ s cm^{-3}, which is about one order less than $n_{\rm e} t_{\rm eq}$. Therefore, we must take into account of the non-equipartition effect. Masai (1994) reported that $T_{\rm e}$ increases to be $0.7 T_{\rm s}$ at the time of $\sim 0.1 t_{\rm eq}$, thus the dotted line in Fig. 9.7 which corresponds to the shock temperature ($kT_{\rm s}$) of 1.5 keV represents the extreme non-equipartition case. The shock temperature $kT_{\rm s} = 0.7$ keV is from the lower limit of the spectral fitting results of $kT_{\rm e} = 0.7$ keV and also from the extreme assumption that the plasma has reached to the energy equipartition; $kT_{\rm e} = kT_{\rm i} = kT_{\rm s}$.

The other constraint is from the ionization parameter derived from the fitting. We show this constraint with dashed lines in Fig. 9.7. The conditions which satisfy $\log n_{\rm e} t_{\rm i} = 10$ and $\log n_{\rm e} t_{\rm i} = 11$, are pointed out to encompass a range consistent with the observation.

The last constraint corresponds to the filling factor of the plasma, shown with solid lines in Fig. 9.7. One of the lines signed as $\eta = 0.6$ corresponds to one-fourth the mean plasma

densities derived from the volume emissivity with the filling factor of 0.1; $\bar{\varepsilon} = \Lambda(T) n_{\rm e}^2 = 1.4 \times 10^{-28} \eta^{-1}$, where $\Lambda(T)$ represents the cooling function ($\Lambda(T) = 2.6 \times 10^{-23} (kT)^{-0.6}$, 0.01 keV$< kT <$ 3 keV). The other lines signed as $\eta = 0.01$ is a constraint coming from the study of plasma densities within the individual SNRs (section 9.1); the plasma density of the ISM should be smaller than the one-fourth the density of the oldest SNR in our sample (~ 0.1 cm^{-3}). The allowable range of the ambient gas density and the age of the SNR are shown with the region filled with confetti.

With the emissivity (ε) formula from McKee and Cowie (1977), which took account of the relatively low temperature and ionization degree, X-ray luminosity is expressed as

$$L_{\rm X} = \frac{\pi}{3} R_{\rm s}^3 \varepsilon = 4.6 \times 10^{30} n_0^{1.64} E_{51}^{0.36} t^{1.92} \ {\rm ergs \ s^{-1}} \tag{9.11}$$

where the thickness of emitting region at the shock front is equal to $R_{\rm s}/12$ and the plasma density $n_{\rm e}$ at the shock front is taken as $n_{\rm e} = 4 n_0$. We show the constant-luminosity locus for 10^{36} ergs s^{-1} with the dot-dashed line. In addition the locus which expresses the detection limit of our survey is shown.

Finally, the conditions which the candidate must satisfy are, the age of $\sim 2 \times 10^4$ yr, the ambient density of ~ 0.01 cm^{-3}, the temperature of ~ 0.9 keV, and the luminosity of $\lesssim 10^{36}$ ergs s^{-1}. From the equation (3.27), we derive the size of the candidate to be ~ 40 pc, which corresponds to $\sim 3'$ at the LMC distance. However, the X-ray emitting sources which are as large as $\sim 3'$ and whose luminosity are as large as $\lesssim 10^{36}$ ergs s^{-1}, should be certainly detected and resolved with ASCA (the point spread function is $\sim 3'$ in radius), unless they are overlapping closely with each other. Then a simple doubt might easily occur to everyone such that the total luminosity far exceeds the observed value, if ensemble of such bright SNRs exists densely overlapping with each other. Therefore, in order to exclude such a case, we examine the allowable range on the log $L_{\rm X}$–log ρ plane, where ρ is the source density in the unit of pc^{-3}. At first, the luminosity range allowed from Fig. 9.7 are shown in Fig. 9.8 as region (a). Secondly, the energy density of the diffuse X-ray emission ($3 n_{\rm e} k T_{\rm e}$) is $\sim 1.1 \times 10^{-11} \eta^{-0.5}$ ergs cm^{-3}, which is equivalent to the number density of the SNe (ρ) of $\sim 3 \times 10^{-7} \eta^{-0.5}$ pc^{-3}. Again from the allowable range of η (0.01–0.6), the constraint of the space density is shown as region (b). Another constraint is from the volume emissivity of the diffuse X-ray emission; $\varepsilon \eta = \rho L_{\rm X}$ and shown as region (c) in Fig. 9.8. The last constraint is from calculated $R_{\rm s}$ value, ~ 40 pc. Assuming the thickness of $\sim R_{\rm s}/12$ for the X-ray emitting region at the shock front, the filling factor is expressed as

$$\eta = \frac{\pi}{3} R_{\rm s}^3 \rho. \tag{9.12}$$

The allowable range from this relation is shown as region (d). It is obvious that there is no region which satisfies all the constraints shown above, apparently indicating that it is impossible to explain the origin of diffuse X-ray emission with the ensemble of middle-aged SNRs.

Is it really impossible that the SNRs are the origin of diffuse X-ray emission? The answer might be "Yes, it is possible.", because there are some things left unnoticed in the argument made above, which are by far the most important; the above story is based on the assumption that the SNRs are surrounded within uniform and cold or warm (not hot) matter and isolated from other physical systems. However, this kind of situation is quite unrealistic, especially for the case of the LMC, which contains many OB associations and star clusters as well as GSs and SGSs. As is seen in previous study of such SNRs, many of them fail to end their lives normally; they fail to silently melt into the ambient cold or warm ISM, instead, they encounter with other SNRs, OB associations, or HII regions in the course of their evolutions (Williams et al. 1997; Williams et al. 1999; Chu 1997), thus for which the simple Sedov solution is no longer applicable. For example, the SNR which encounters one of the "bubble" made by older remnant, evolves in this way. The shock driven by the new remnant will propagate preferentially into the old cavity. The thermal energy remaining in the interior of the new remnant is quickly redistributed between the two; the pair of remnants then have a temperature and pressure comparable to that of an isolated remnant, and their interior will remain hot and diffuse for a comparable time. Significantly, the volume formed by this conjunction is larger than that of an isolated SNR and thus more likely to be struck by yet another supernova shock (Cox and Smith 1974). This step is repetitious to form very large bubbles (GSs and SGSs) filled with hot tenuous medium; SNe occurring just close to the bubbles will not form dense shell by radiating X-rays in a critical epoch, instead, will break into the bubbles and disperse their energies there (Cox and Smith 1974). If SN occurs within such bubbles, they are submerged into the hot tenuous gas to become unrecognizable as distinct remnants at all because the X-ray emission measure is too small to produce a detectable remnant, unless the shock front of the remnant hits the wall of the cavity (e.g. the estimated X-ray luminosity of the remnant exploded at the center of the superbubble is $\lesssim$ 4–5 $\times$ 10^{33} ergs s^{-1} (Chu and Mac Low 1990), which is well below the detection limit of our observations.). The shock velocities of most of the remnants may have fallen to the local speed of sound before reaching the wall of the cavity, implying that the SN mechanical energy has all gone into heating the bubble's coronal gas to form truly diffuse hot ionized gas (Wang and Helfand 1991). Indeed, massive stars are often formed in groups, such as OB associations and clusters thus they often explode within such environments as SNe and become 'missing'. The negative result to explain the origin of diffuse X-ray emission with an ensemble of 'normal' SNRs, for which the Sedov solution is applicable, is not surprising. On the contrary, it strongly suggests us that the large amount of the LMC SNRs are in the form of such 'missing' SNRs, ultimately in the form of truly diffuse hot plasma.

We now check the energy sustainment of the diffuse X-ray emission. The sound velocity equivalent for the temperature of $\sim$0.9 keV obtained from the spectral fitting is $\sim$ 400 km s^{-1}. If we assume that the escaping velocity is almost equal to the sound velocity, the escaping time ($t_{\rm escape}$) is estimated as $\sim$ 2 $\times$ 10^6 yr (the scale height of $\sim$ 1 kpc is assumed). On the other hand, the cooling timescale of the diffuse X-ray plasma ($t_{\rm cool}$) is estimated to be $\sim$ 2.5 $\times$ $10^9 \eta^{0.5}$ yr. Because $t_{\rm cool}$ is far larger than $t_{\rm escape}$, it is reasonable that the plasma

with an age of older than $t_{\rm escape}$ should be slip outward before it is cooled down.

The total energy of the diffuse X-ray emission is $U \sim 8 \times 10^{54} \beta \eta^{0.5}$ ergs which is equivalent to the energy input from $\sim 8 \times 10^{3} \beta \eta^{0.5}$ SNe. The average SN rate of one per $\sim 250 \beta^{-1} \eta^{-0.5}$ yr is required to replenish this number of SNe in the typical escape time of $\sim 2 \times 10^{6}$ yr. On the other hand, the predicted SN rate in the LMC is $\gtrsim$ one per ~ 500 yr (Chu and Kennicutt 1988b). Therefore, we can assume the filling factor of the plasma to be ~ 0.25–1 (where we assumed $\beta \sim 1$.). The age of an oldest (and at the same time isolated) SNR in our sample, N86, is $\sim 10^{5}$ years old. Assuming that oldest SNRs have $\sim t_{\rm escape}$ of age, about $(10^{5}$ yr$)/t_{\rm escape} \sim 10$ % of SNRs should be observable at present time. However, about 40 SNRs have been detected in the LMC and a bit more SNRs are expected to be resolved with Chandra satellite, which is or still less than 1% of the expected number of SNe. Therefore, we suppose that the remaining SNRs should be surely 'missing' ones which have already melt into truly diffuse hot gas.

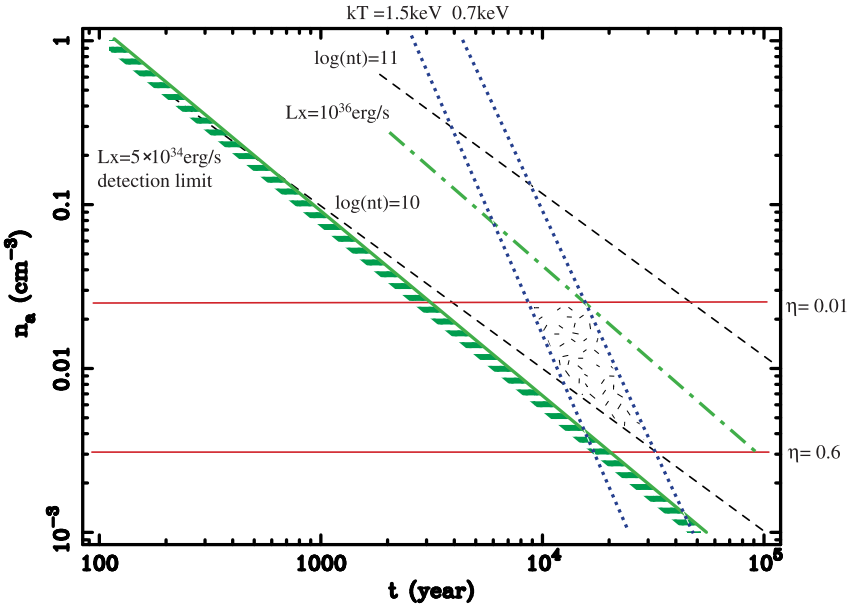

Figure 9.7: Constraints on the SNR interpretation of diffuse X-ray emission, shown in the log n_a – log t plane. n_a and t are the ambient density and age of the SNR. The dotted lines represent the observational constraint from the plasma temperature, the dashed lines from the ionization parameter, and the solid lines from the derived mean plasma density for different filling factors. Constant luminosity loci for individual SNRs are shown in dot-dashed lines. The allowable regions are also shown in a region filled with confetti.

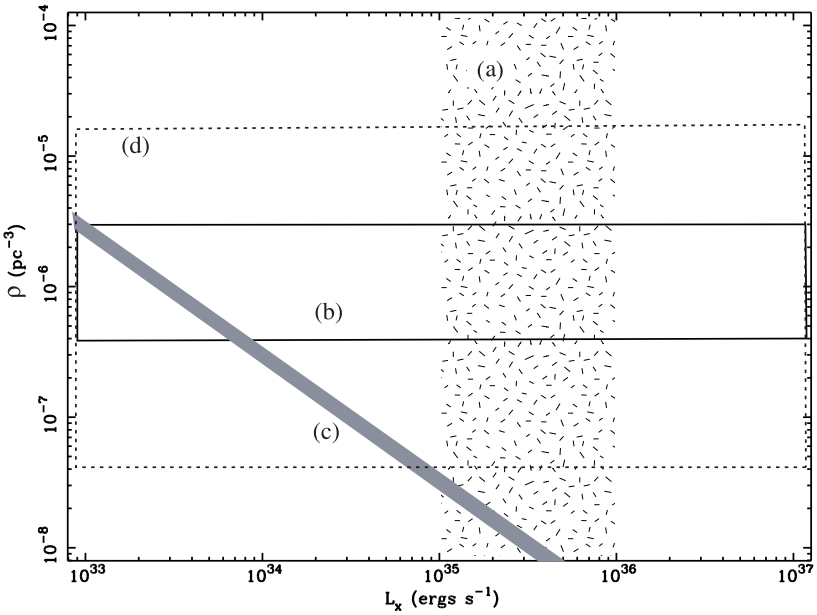

Figure 9.8: Constraints on the SNR interpretation of diffuse X-ray emission, shown in the log $L_{\rm X}$ − log ρ plane. $L_{\rm X}$ and ρ are the X-ray luminosity and the space density of the SNRs in the adiabatic phase. Region (a), (b), (c), and (d) represent the allowable region of luminosity from Fig. 9.7, of total energy density of the diffuse X-ray emission, of the observed surface brightness, and of the Sedov solution on $R_{\rm s}$.

Chapter 10

Conclusion

With all the available data of ASCA in the vicinity of the Large Magellanic Cloud, we performed the systematic study of X-ray sources within the galaxy. The principle results are summarized as follows;

- We obtained the image of the LMC in harder energy band (2.0–7.0 keV). The figure of LMC in the harder energy band is revealed for the first time.
- We detected 71 point or point-like sources in the LMC region with the criterion of $S/N > 5$. The systematic X-ray spectral analyses for those sources were performed. The results are summarized in the first ASCA catalogue of the LMC region. We also carried out the comparison with the previously obtained ROSAT catalogues of LMC (Haberl and Pietsch 1999; Sasaki et al. 2000).
- We carried out the detailed spectral analyses for the SNRs in the LMC, for which X-ray spectroscopy of ASCA have not been carried out yet. The number of such SNRs are 9, including DEM L316A, DEM L316B, 0532−71.0, 0534−69.9, 0548−70.4, 0520−69.4, DEM L241, 0532−67.5, and N86 (sample-1). From the X-ray spectral fits to the NEI model, we obtained the plasma parameters within them, for example, the age and density. We found that our sample-1 SNRs together with the sample-2 SNRs for which Hayashi (1997) and Hughes et al. (1998) carried out the X-ray spectral analyses, include the SNRs whose ages scatter from $\sim 10^3$–10^5 yr. We also found that the densities within those SNRs decrease as their ages increase. The density of the oldest SNR in our sample (~ 0.1 cm^{-3}) might be the upper limit of the average density of the ISM in the LMC.
- We further accumulated the X-ray spectrum of diffuse X-ray emission which is widely spreading over the LMC body. The spectrum can be reproduced with the NEI model, whose temperature and ionization timescale were $kT_{\rm e} \sim 0.9$ keV and $n_{\rm e}t_{\rm i} \sim 10^{10.5}$ s cm^{-3},

respectively. From the resemblance of plasma parameters with those of middle-ages SNRs, we tried to explain the origin of diffuse X-ray emission with ensemble of those SNRs. However, we found no allowable range on the log L_X–log ρ plane for the the SNRs which are within the approved range on the log t–log n_0 plane. We consider that the negative results to explain the origin of diffuse X-ray emission with an ensemble of SNRs surely arise from the fact that most of them does not follow the simple Sedov solution during the course of their evolution, instead, they have exploded into or within the hot tenuous medium realized within the OB associations or SGSs, and have merged into it.

- Our sample-1 SNR includes DEM L316 A and B (shell A and B), which is of considerable interest because it is a possible site for the collision between two SNRs. From our X-ray spectral analyses, shell A and B exhibit totally different X-ray spectra; shell A exhibits strong L-shell lines of iron while shell B does not. Therefore, we concluded that these two shells were not due to a single supernova explosion into a pre-existing bubble made by a stellar wind or SNe. We also proposed, from the iron over abundance seen in the spectrum, that the origin of shell A is a Type Ia. However, we could not obtain the evidence which positively supports the collision between two SNRs nor could we get a strong constraint for the shell B progenitor.

- SNR 0548−70.4 had been long time considered to have resulted from Type Ia explosion because it shows Balmer-dominated spectra in optical wavelength. Our spectral analysis for 0548−70.4 revealed that it does not show clear iron overabundance (the overabundant of iron in the X-ray spectrum strictly restricts the type of the explosion to be Type Ia). We suspect that it might be caused by its quite older age thus it forgot all the details at the explosion. However, we also suspect that 0548−70.4 might not have a Type Ia progenitor star, because exhibiting Balmer-dominated spectra cannot be a strong constraint for its progenitor star. SNRs with any kind of progenitor stars have possibility to exhibit Balmer-dominated spectra if they are surrounded by some amount of cold matter; Cygnus loop exhibits Balmer-dominated spectrum but have a massive progenitor star. Therefore, we argue that we should not hasten to conclude that 0548−70.4 have resulted from Type Ia explosion.

Appendix A

Spectra and Images of Individual SNRs in the LMC

We show the spectra and images of individual SNRs in the LMC. Left panels show spectra accumulated from the GIS and the SIS, while right panels show the ROSAT HRI images provided by Williams et al. (1999) with some exceptions. For DEM L316 the spectra from SIS and ROSAT/PSPC are displayed. For DEM241 and 0532−67.5, no HRI images are obtained thus only the spectra are displayed.

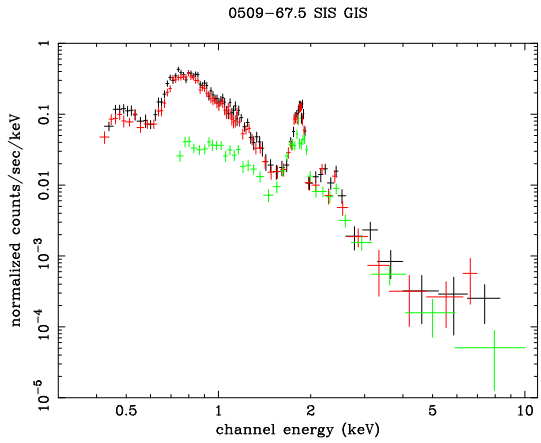

(a)

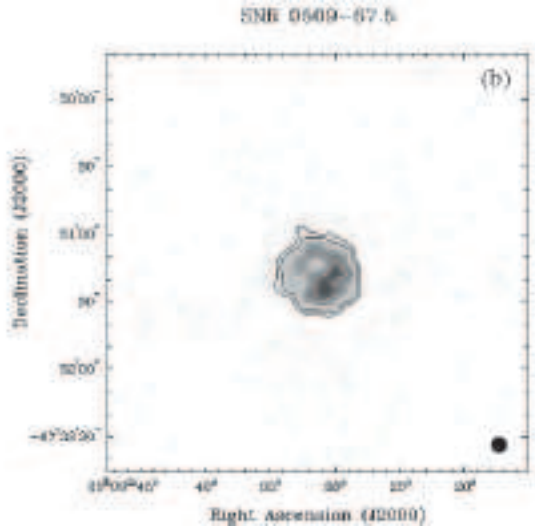

(b)

Figure A.1: 0509−67.5

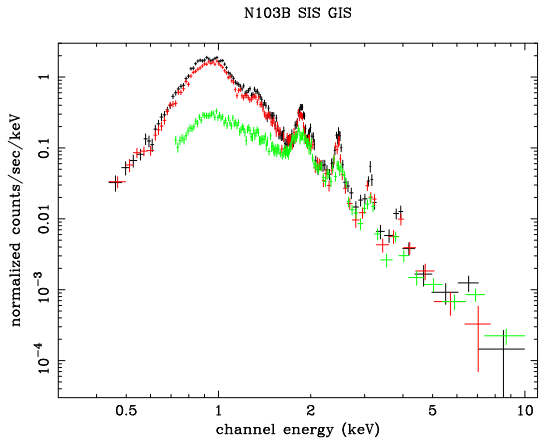

(a)

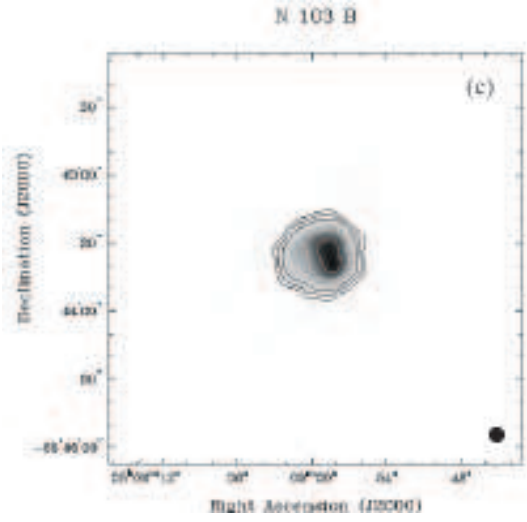

(b)

Figure A.2: N103B

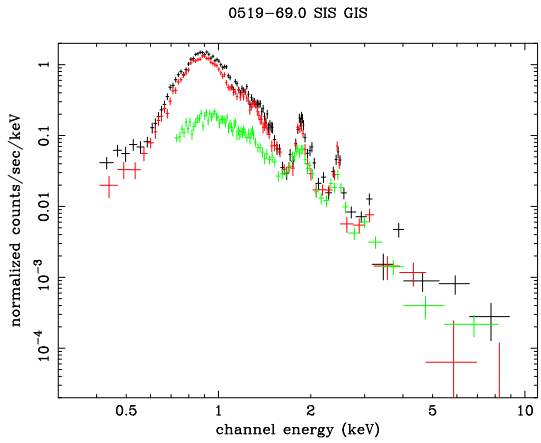

(a)

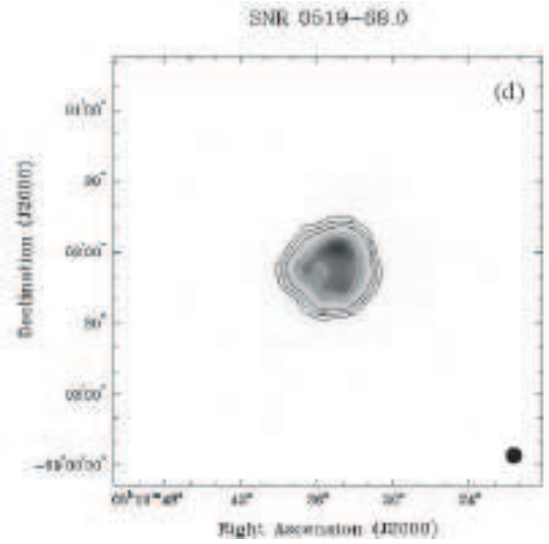

(b)

Figure A.3: 0519−69.0

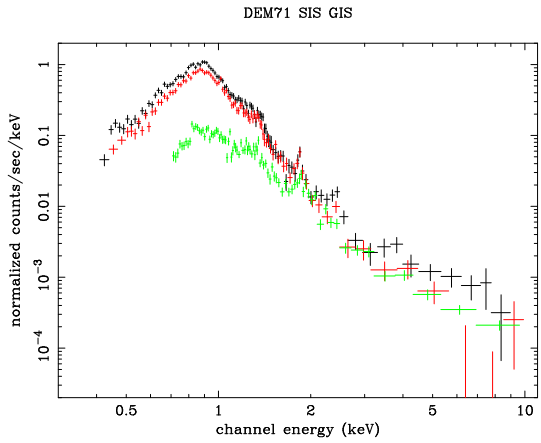

(a)

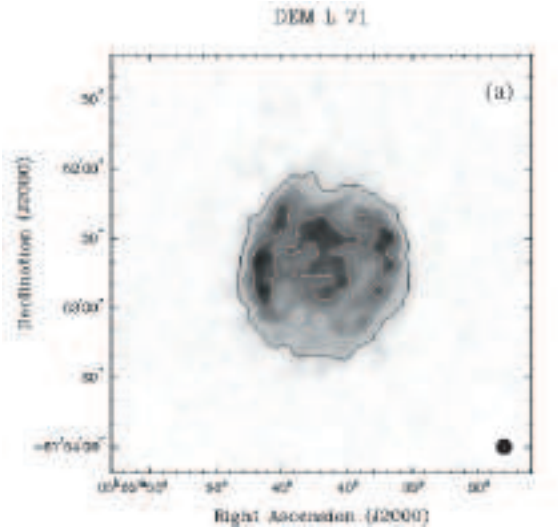

(b)

Figure A.4: DEM71

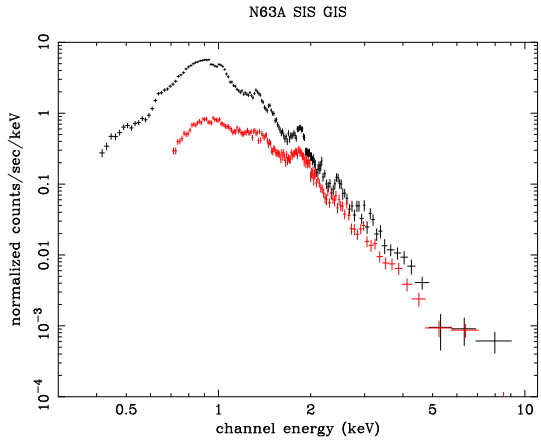

(a)

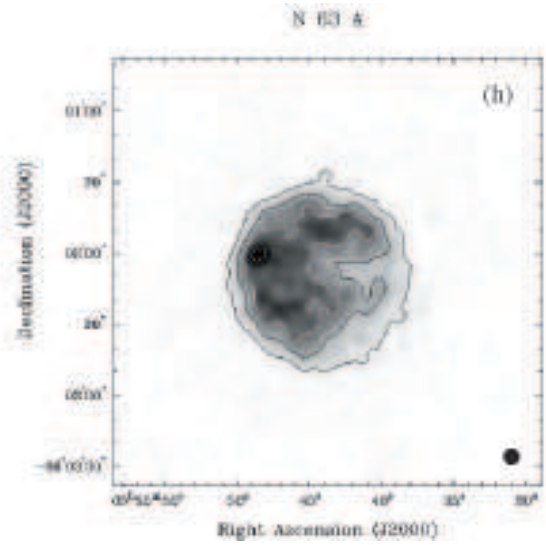

(b)

Figure A.5: N63A

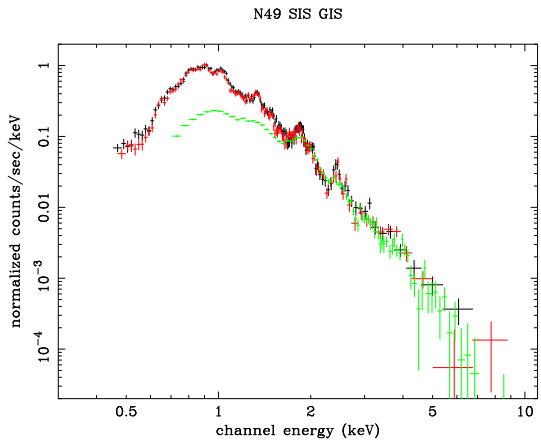

(a)

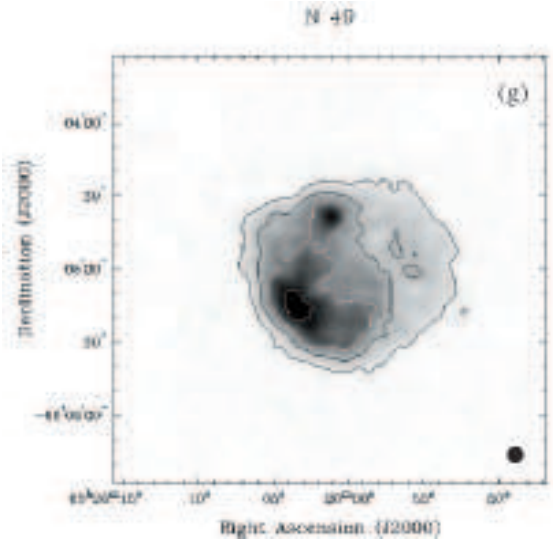

(b)

Figure A.6: N49

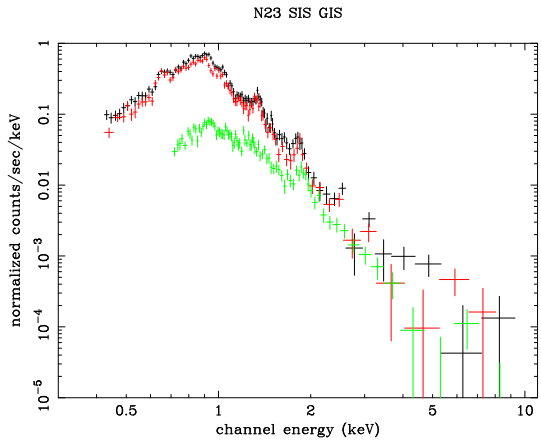

(a)

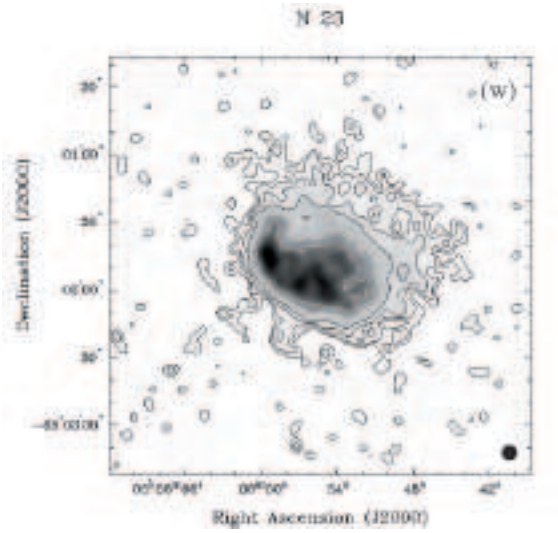

(b)

Figure A.7: N23

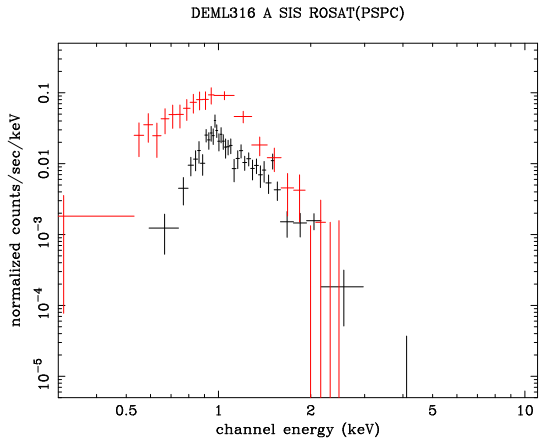

(a)

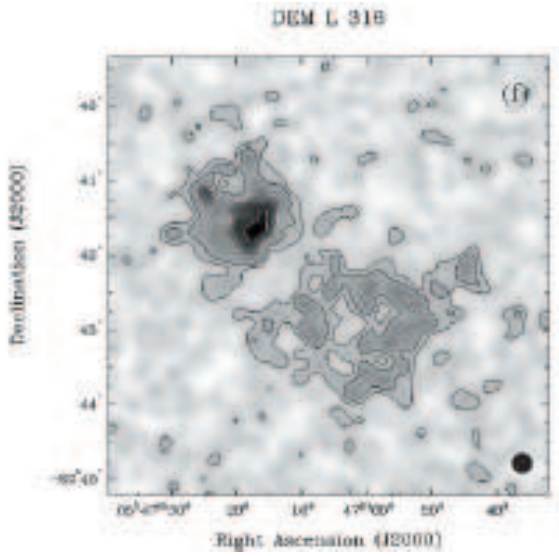

(b)

Figure A.8: DEML316A

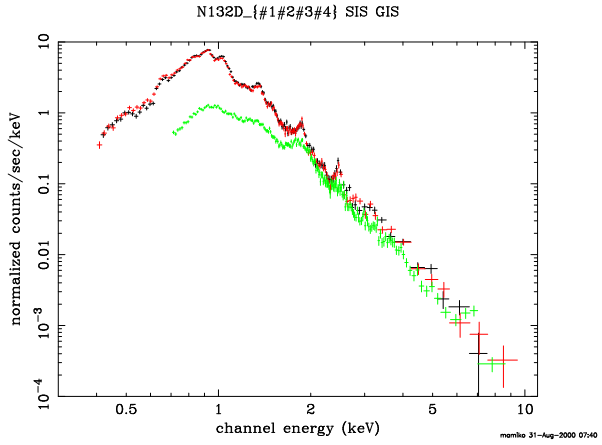

(a)

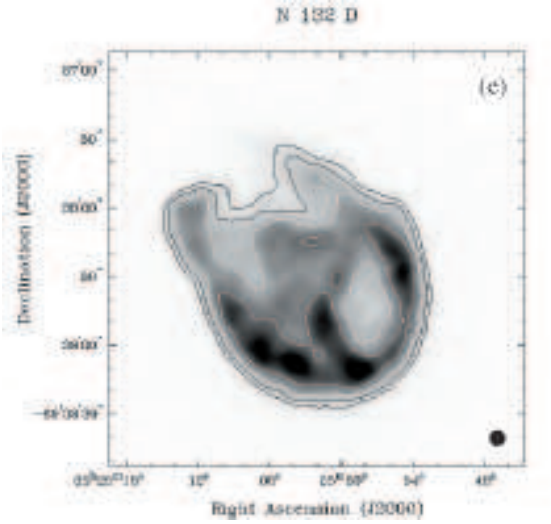

(b)

Figure A.9: N132D

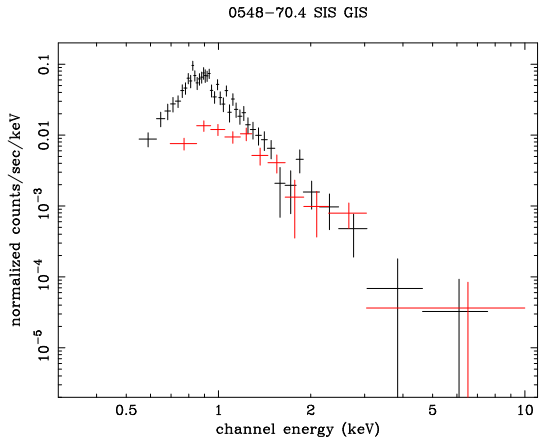

(a)

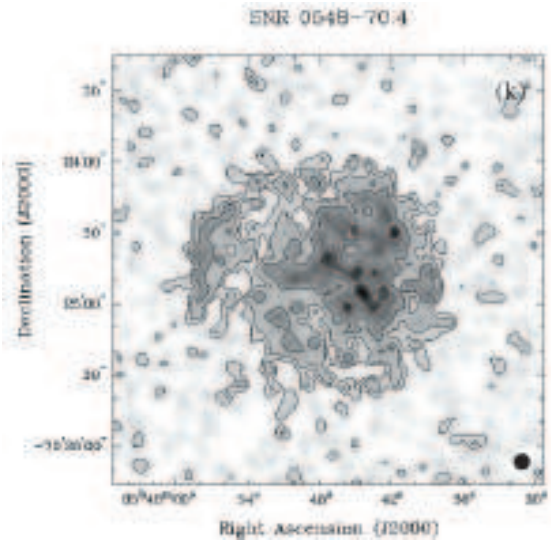

(b)

Figure A.10: 0548−70.4

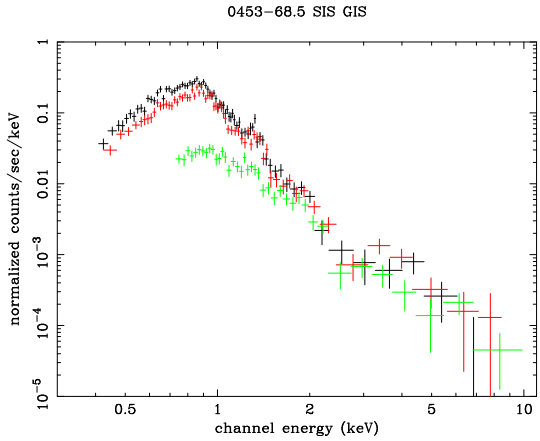

(a)

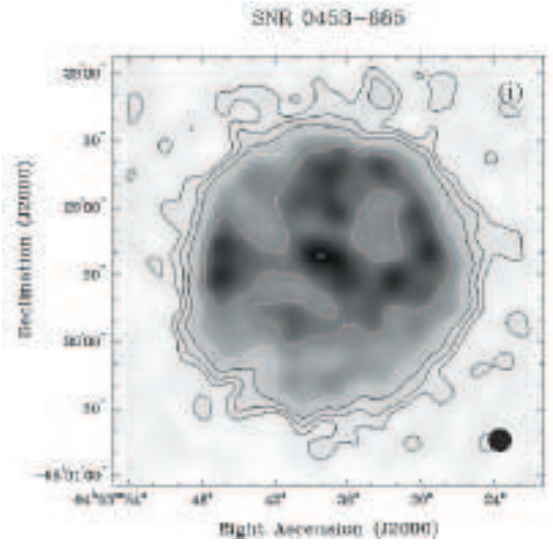

(b)

Figure A.11: 0453−68.5

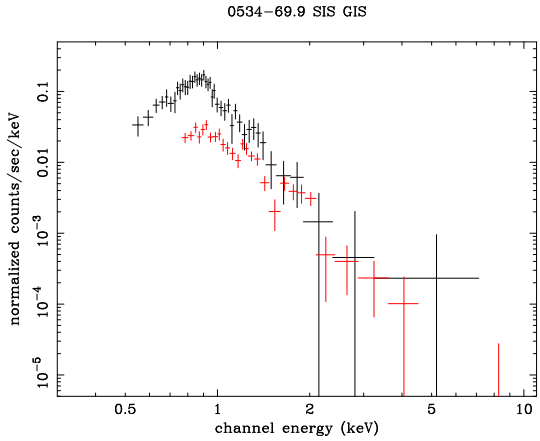

(a)

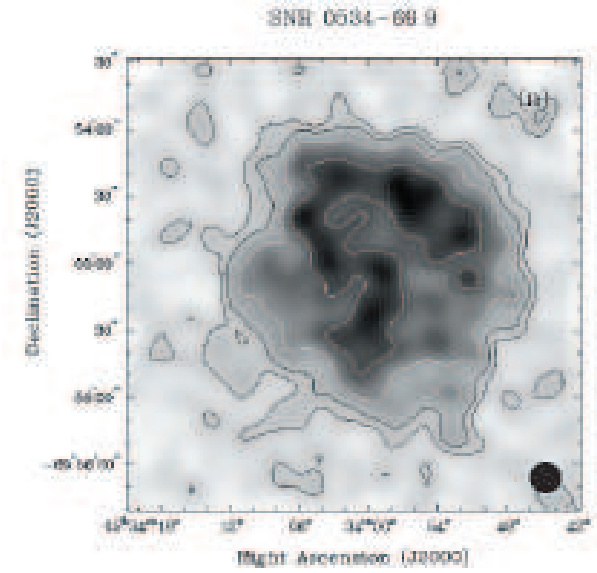

(b)

Figure A.12: 0534−69.9

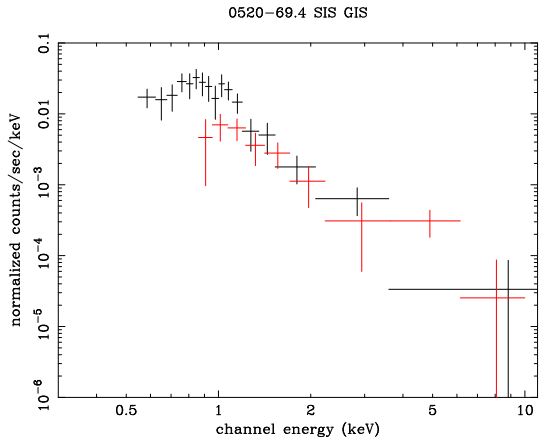

(a)

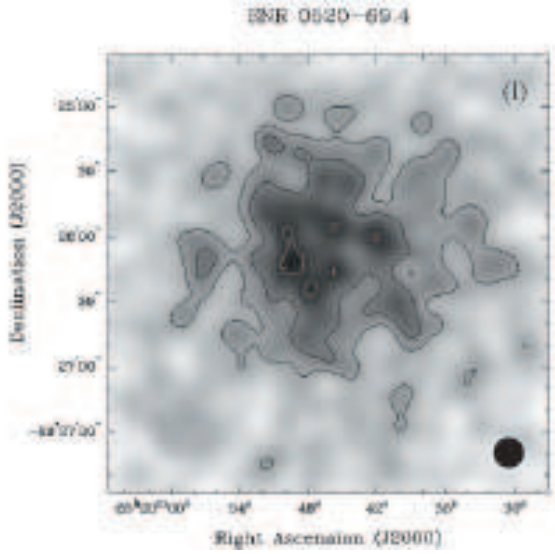

(b)

Figure A.13: 0520−69.4

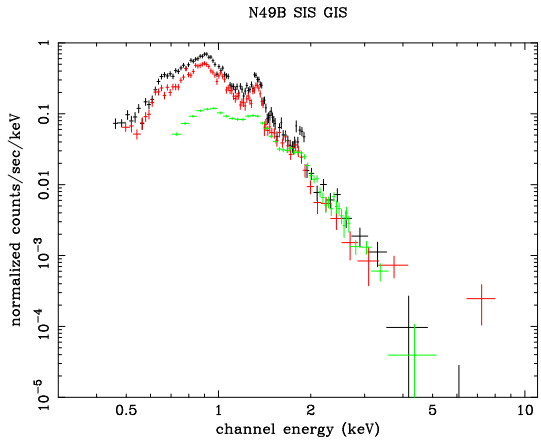

(a)

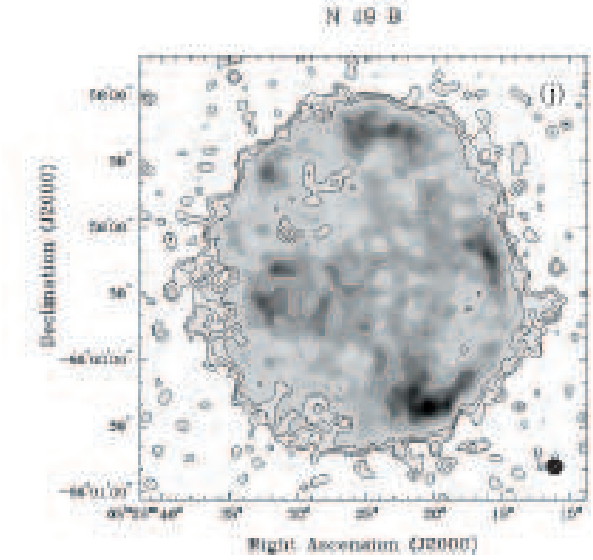

(b)

Figure A.14: N49B

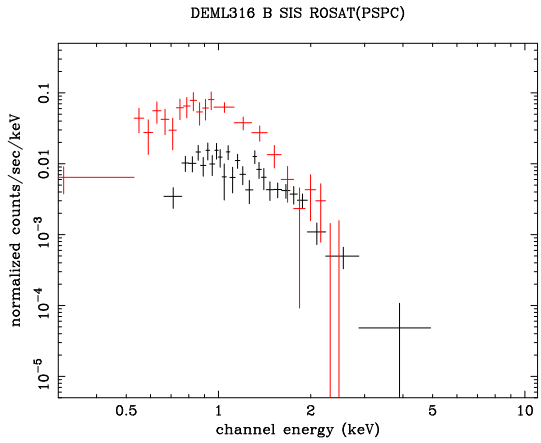

(a)

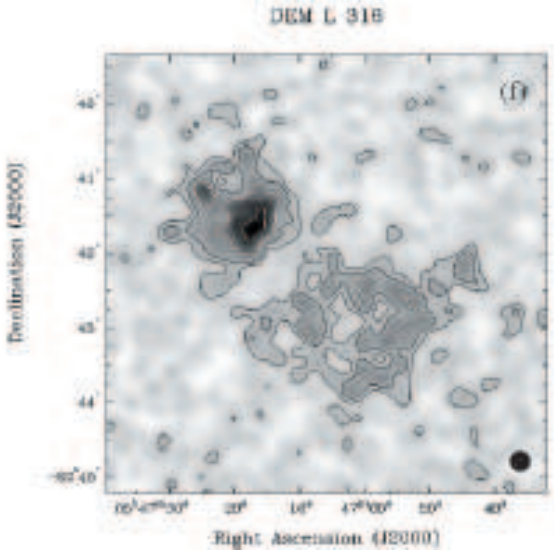

(b)

Figure A.15: DEML316B

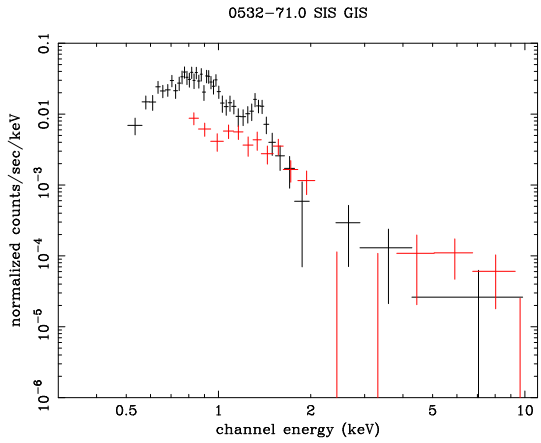

(a)

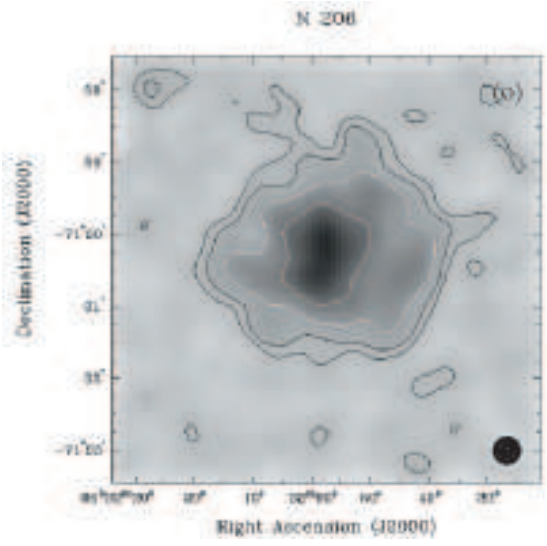

(b)

Figure A.16: 0532−71.0

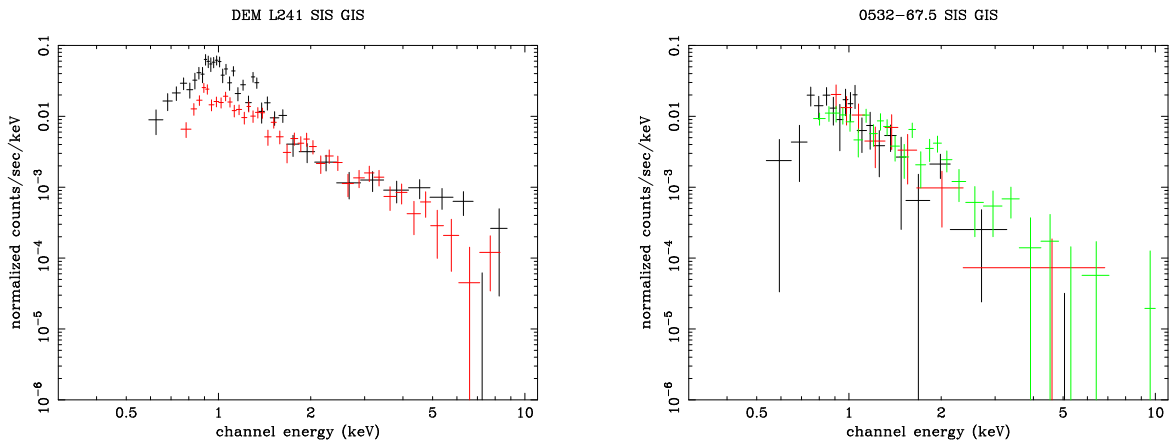

(a) (b)

Figure A.17: DEM241 & 0532−67.5

Appendix B

Pointing list of the data used for the CXB and NXB background

Here we show the pointing list of the data used for the CXB and NXB background spectra.

Table B.1: GIS blank-sky data

ID	Name	Euler Anlges			Sequence No.
		ϕ	θ	ψ	
sa57p1	ft931221_1025.0650	196.872	60.660	339.983	91001010
sa57p2	ft931224_1340.1020	196.739	60.624	340.035	91001000
sa57p3	ft931228_1320.1030	197.012	60.712	339.899	91001040
sa57p4	ft940116_0512.0325	196.825	60.782	339.996	91001020
sa57p5	ft940118_0326.0100	196.923	60.553	339.949	91001030
sa57ao3_1	ft950602_1609.2019	197.586	60.699	138.582	93001000
sa57ao3_2	ft950604_2020.2150	197.586	60.699	138.582	93001020
sa57ao3_3	ft950611_0406.0520	197.586	60.699	138.582	93001010
sa57ao3_4	ft950613_0520.0659	197.586	60.699	138.582	93001030
sa57ao3_5	ft950615_0700.1200	197.586	60.699	138.582	93001040
bfn1	ft950526_1942.0833	196.512	54.510	134.792	93000010
bfn2	ft950528_0835.1525	194.631	54.504	124.307	93000000
bfn3	ft951222_1351.1820	195.192	54.201	331.569	94000000
bfn4	ft951221_0905.1350	194.572	54.497	331.848	94001000
zsys1	ft940809_0548.0220	39.629	112.886	11.419	72010020
zsys2	ft940810_0220.0720	39.843	113.253	11.402	72010000
zsys3	ft940811_0721.0355	39.550	113.854	11.149	72010010
zsys4	ft950728_0201.2240	40.400	113.543	16.901	73005000
zsys5	ft950727_0444.0200	39.609	112.481	16.711	73006000
draco1	ft930604_1413.0233	256.939	19.289	109.068	90022000
draco1	ft930605_0233.0910	256.939	19.289	109.068	90022000
draco2	ft930605_0910.1901	257.587	19.196	108.476	90023000
draco3	ft930605_1902.1535	258.229	19.096	107.878	90024000
nep1jun	ft930609_2339.1051	270.205	23.712	79.027	90014000
nep1jul	ft930720_2008.0545	270.588	23.596	117.658	90016000
nep1oct	ft931021_2058.0810	270.381	23.196	209.708	90020000
nep1mar	ft940328_0803.2050	269.426	23.603	8.028	90018000
nep2jul	ft930702_0425.1243	270.025	23.665	100.391	90015000
nep2jul	ft930702_1243.1536	270.025	23.665	100.391	90015000
nep2aug	ft930816_1344.0035	270.289	23.500	139.619	90017000
nep2sep	ft930930_0505.1742	270.178	23.282	185.975	90019000

(Continuing to the next page.)

Table B.1: Observational log (Continued from the previous page.)

ID	Name	Euler Anlges			Sequence No.
		ϕ	θ	ψ	
nep2nov	ft931116_1031.2200	269.593	23.155	240.536	90021000
qsf3n1	ft930711_1217.1350	55.283	134.381	39.660	90011000
qsf3n2	ft930915_1500.0155	55.045	134.174	343.463	90011010
qsf3n3	ft930910_2221.1145	55.041	134.163	341.008	90011020
qsf3n4	ft930921_0635.1620	55.046	134.139	335.801	90011030
lss101	ft931226_1022.1749	197.653	59.667	330.298	91002000
lss102	ft931226_1750.2200	197.458	59.952	330.391	91002010
lss103	ft931226_2200.0150	197.274	60.244	330.486	91002020
lss104	ft931227_0150.1000	197.083	60.533	330.578	91002030
lss105	ft940104_1032.1549	197.316	59.500	330.468	91003000
lss106	ft940104_1550.2022	197.124	59.791	330.560	91003010
lss107	ft940104_2022.0241	196.935	60.080	330.653	91003020
lss108	ft940105_0241.1320	196.751	60.375	330.744	91003030
lss109	ft940105_1321.1742	197.579	59.439	330.330	91004000
lss110	ft940105_1742.2330	197.386	59.728	330.432	91004010
lss111	ft940105_2330.1042	197.200	60.017	330.520	91004020
lss112	ft940106_1043.1600	197.010	60.309	330.620	91004030
lss113	ft940106_1601.2050	197.053	59.563	330.598	91005000
lss114	ft940106_2050.0426	196.862	59.851	330.692	91005010
lss115	ft940107_0426.1529	196.676	60.147	330.781	91005020
lss116	ft940107_1530.1930	196.487	60.434	330.871	91005030
lss201	ft940616_1636.0412	198.548	59.395	150.196	92002000
lss202	ft940617_0412.0742	198.741	59.101	150.100	92002010
lss203	ft940617_0742.1059	198.930	58.812	150.001	92002020
lss204	ft940617_1059.1540	199.114	58.528	149.905	92002030
lss205	ft940617_1540.0410	199.325	58.239	149.798	92002040
lss206	ft940618_0411.0742	198.987	58.072	149.976	92002050
lss207	ft940618_0743.1207	198.793	58.364	150.074	92002060
lss208	ft940618_1207.1710	198.594	58.649	150.176	92002070
lss209	ft940618_1710.0410	198.401	58.941	150.273	92002080
lss210	ft940619_0410.0831	198.210	59.229	150.372	92002090
lss211	ft940627_2312.0404	198.471	59.163	150.238	92001000
lss212	ft940628_0405.0839	198.667	58.877	150.135	92001010
lss213	ft940628_0839.1337	198.863	58.586	150.036	92001020
lss214	ft940628_1337.0048	199.060	58.299	149.930	92001030
lss215	ft940629_0049.0535	199.259	58.010	149.832	92001040
lss216	ft940629_0536.1049	198.721	58.131	150.114	92001050
lss217	ft940629_1051.2025	198.521	58.424	150.220	92001060
lss218	ft940629_2026.0228	198.322	58.709	150.324	92001070
lss219	ft940630_0228.0738	198.863	58.589	150.037	18940630
lss220	ft940630_0738.1320	197.946	59.290	150.505	92001090
lss301	ft941225_2135.0600	198.212	57.823	330.016	93006060
lss302	ft941226_0601.1325	198.412	57.541	329.912	93006050
lss303	ft950106_0816.1430	198.604	57.257	329.815	93006070
lss304	ft950107_2055.0501	198.804	56.959	329.706	93006030
lss305	ft950108_0502.1110	199.008	56.673	329.598	93006020
lss306	ft950109_1054.1250	199.212	56.383	329.491	93006170
lss307	ft950109_1251.2050	199.278	56.612	329.452	93006080
lss308	ft950109_2051.0320	199.080	56.906	329.563	93006040
lss309	ft950110_0321.0800	198.877	57.189	329.665	93006120
lss310	ft950110_0801.1551	198.677	57.476	329.771	93006010
lss311	ft950110_1552.2220	198.752	57.708	329.731	93006000
lss312	ft950110_2221.0441	198.948	57.417	329.623	93006100
lss313	ft950111_0442.1100	198.481	57.763	329.868	93006190
lss314	ft950111_1102.1721	199.149	57.128	329.517	93006180
lss315	ft950111_1722.2350	199.353	56.840	329.408	93006160
lss316	ft950111_2351.0611	199.553	56.554	329.300	93006150
lss317	ft950112_0612.1240	198.820	57.934	329.690	93006140
lss318	ft950112_1241.1900	199.021	57.644	329.585	93006130

(Continuing to the next page.)

Table B.1: Observational log (Continued from the previous page.)

ID	Name	Euler Anlges			Sequence No.
		ϕ	θ	ψ	
lss319	ft950112_1902.0120	199.224	57.358	329.477	93006110
lss320	ft950113_0120.0750	199.422	57.068	329.367	93006090
lss321	ft950618_1623.0225	198.137	58.999	150.414	93007000
lss322	ft950619_0226.0840	200.118	56.117	149.350	93007010
lss323	ft950619_0840.1511	200.190	56.346	149.338	93007020
lss324	ft950619_1512.2305	200.534	56.518	149.145	93007030
lss325	ft950619_2305.0501	200.328	56.805	149.260	93007040
lss326	ft950701_0503.1030	200.467	56.290	149.181	93007050
lss327	ft950701_1030.1711	200.808	56.462	148.996	93007060
lss328	ft950702_0541.1251	200.196	57.318	149.329	93007090
lss329	ft950701_2321.0540	200.402	57.032	149.215	93007080
lss330	ft950701_1711.2320	200.605	56.750	149.106	93007070
lss331	ft950705_2213.0350	198.234	60.198	150.357	93007100
lss332	ft950706_0350.1009	198.426	59.913	150.262	93007110
lss333	ft950706_1010.1630	198.616	59.620	150.165	93007120
lss334	ft950706_1631.2259	198.811	59.333	150.066	93007130
lss335	ft950706_2300.0520	199.008	59.046	149.963	93007140
lss336	ft950707_0521.1140	199.197	58.727	154.868	93007150
lss337	ft950707_1141.1630	199.396	58.467	149.758	93007160
lss338	ft950707_1630.2300	199.597	58.180	149.653	93007170
lss339	ft950707_2300.0519	199.795	57.894	149.548	93007180
lss340	ft950708_0520.1101	199.994	57.607	149.442	93007190

Appendix C

The diffuse X-ray and background spectra

We show the diffuse X-ray emission and background spectra of each selected 11 GIS pointing for diffuse X-ray analyses. Left panels show the spectra accumulated from whole GIS field of view after subtracting the point-like sources, while right panels show the background spectra which are identical with those of blank sky, however, take account of the vignetting effect.

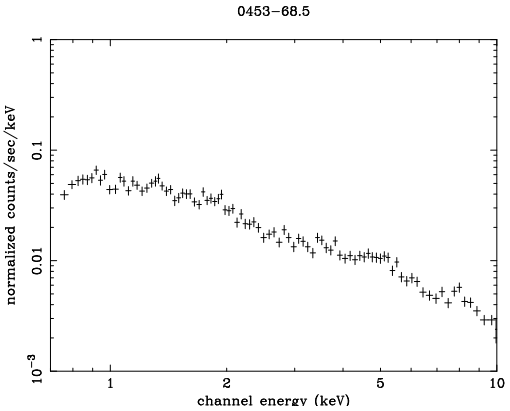

(a) GIS2+3 spectra of diffuse X-ray emission in 0453−68.5 region.

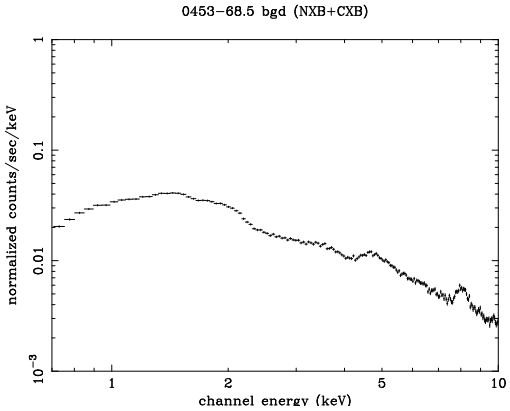

(b) GIS2+3 spectra of NXB + CXB in 0453−68.5 region.

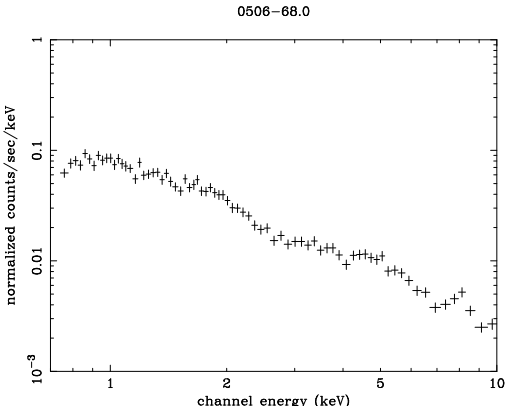

(a) GIS2+3 spectra of diffuse X-ray emission in 0506−68.0 region.

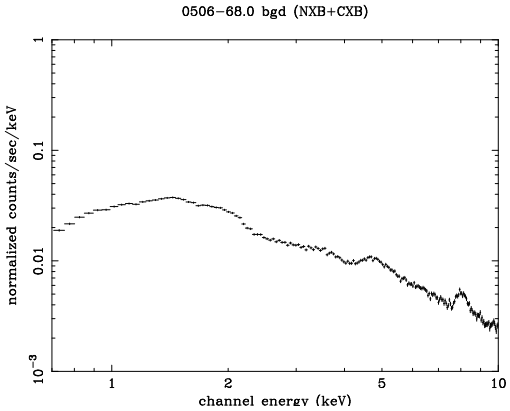

(b) GIS2+3 spectra of NXB + CXB in 0506−68.0 region.

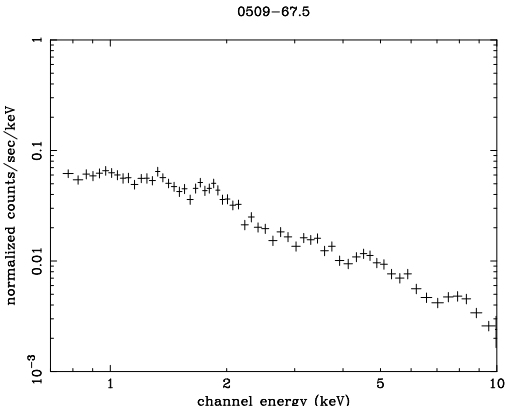

(a) GIS2+3 spectra of diffuse X-ray emission in 0509−67.5 region.

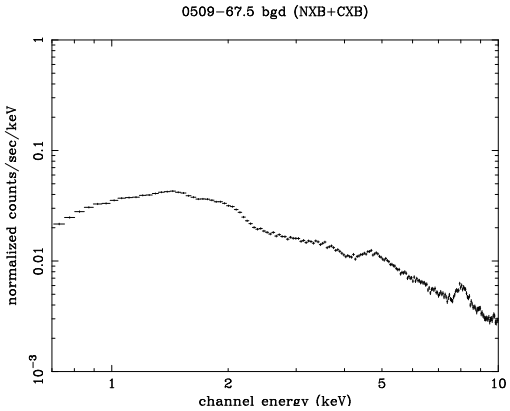

(b) GIS2+3 spectra of NXB + CXB in 0509−67.5 region.

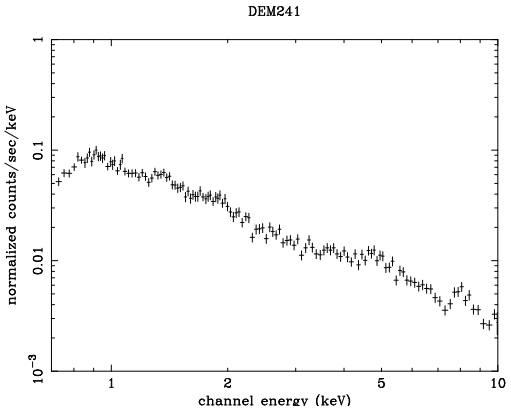

(a) GIS2+3 spectra of diffuse X-ray emission in DEM241 region.

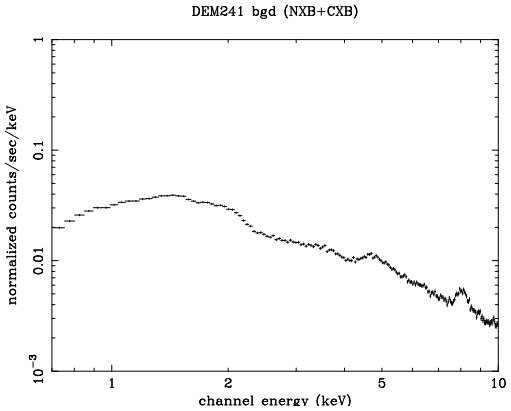

(b) GIS2+3 spectra of NXB + CXB in DEM241 region.

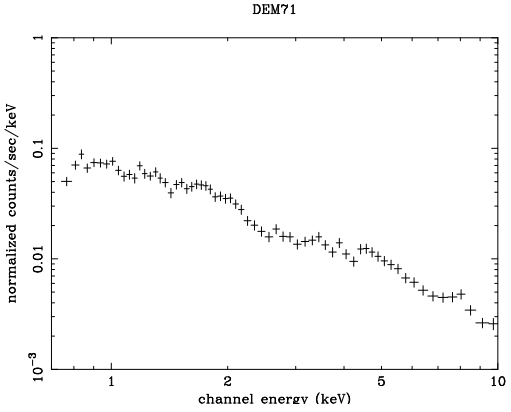

(a) GIS2+3 spectra of diffuse X-ray emission in DEM71 region.

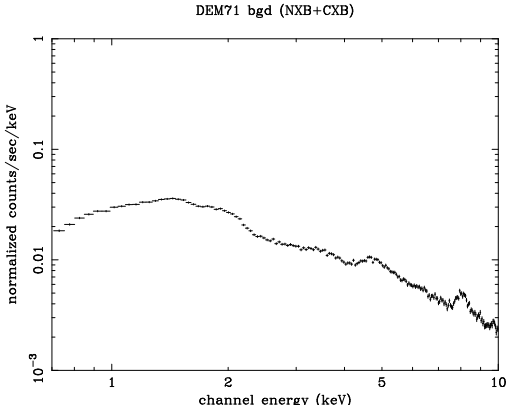

(b) GIS2+3 spectra of NXB + CXB in DEM71 region.

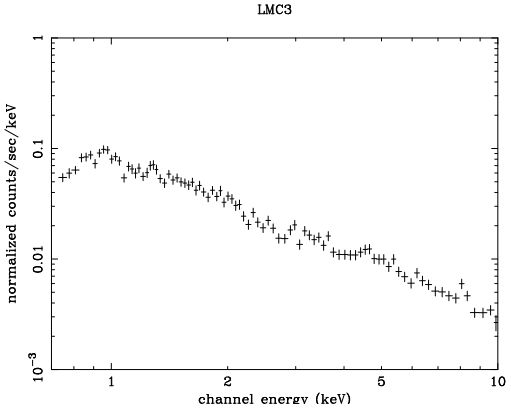

(a) GIS2+3 spectra of diffuse X-ray emission in LMC3 region.

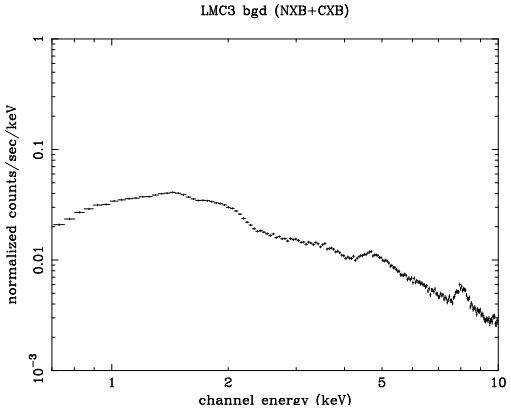

(b) GIS2+3 spectra of NXB + CXB in LMC3 region.

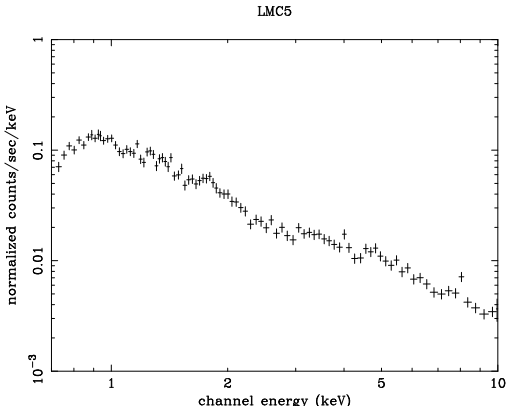

(a) GIS2+3 spectra of diffuse X-ray emission in LMC5 region.

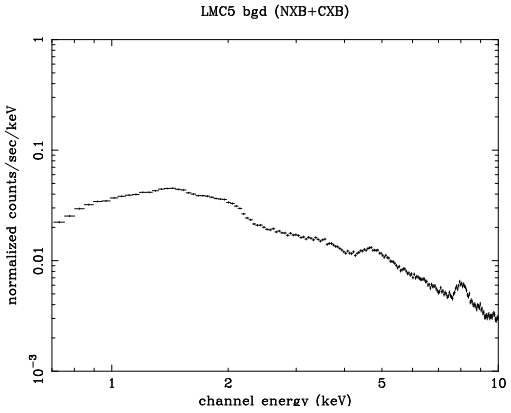

(b) GIS2+3 spectra of NXB + CXB in LMC5 region.

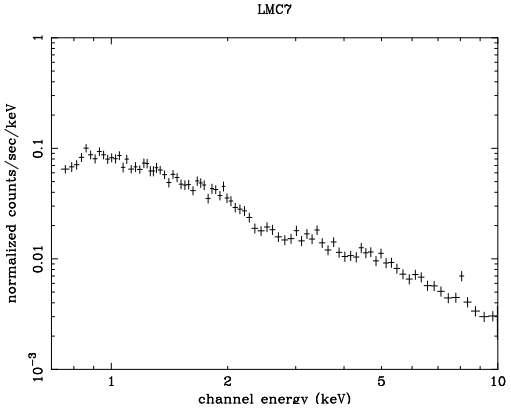

(a) GIS2+3 spectra of diffuse X-ray emission in LMC7 region.

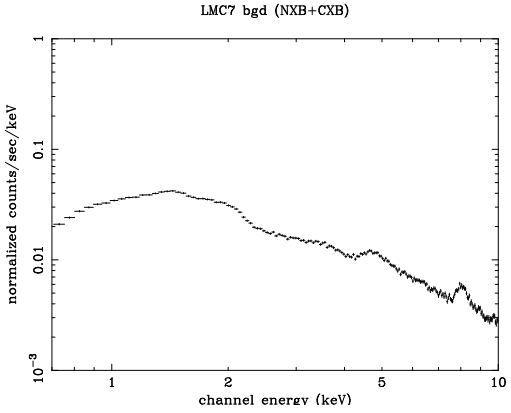

(b) GIS2+3 spectra of NXB + CXB in LMC5 region.

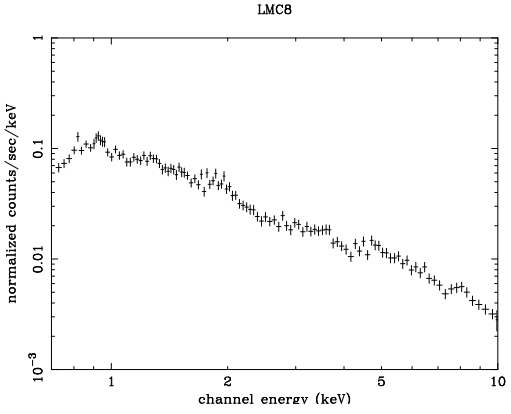

(a) GIS2+3 spectra of diffuse X-ray emission in LMC8 region.

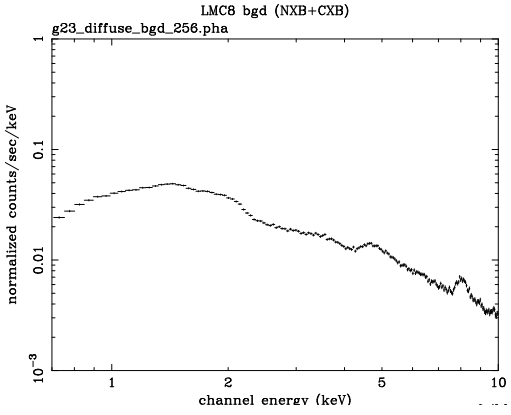

(b) GIS2+3 spectra of NXB + CXB in LMC8 region.

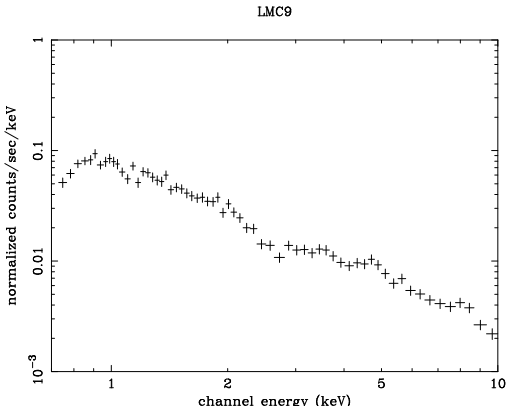

(a) GIS2+3 spectra of diffuse X-ray emission in LMC9 region.

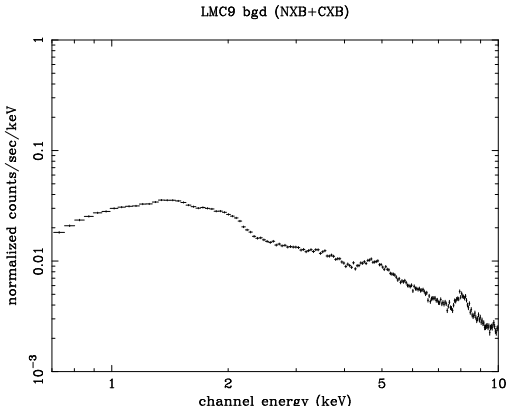

(b) GIS2+3 spectra of NXB + CXB in LMC9 region.

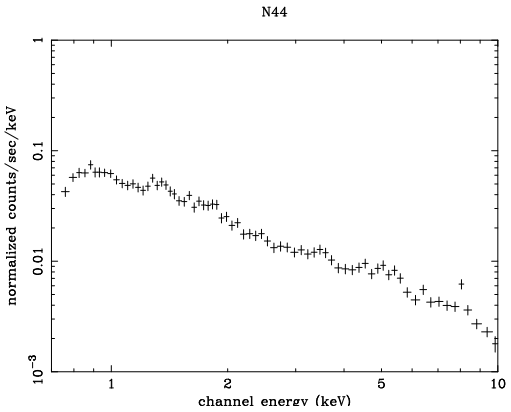

(a) GIS2+3 spectra of diffuse X-ray emission in N44 region.

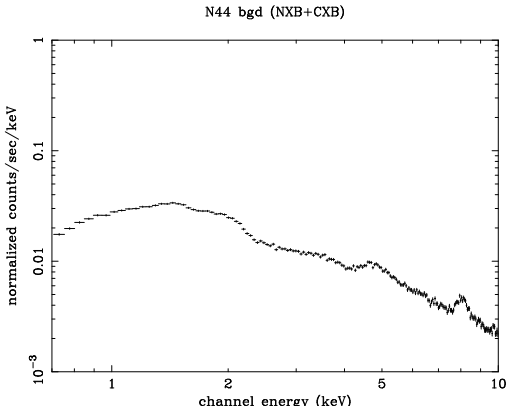

(b) GIS2+3 spectra of NXB + CXB in N44 region.

Appendix D

2-false-color X-ray image of the LMC

Here, we show the 2-false-color image of the LMC. Red color represents the X-ray photons in the soft band (0.7–2.0 keV), while blue color represents those in the hard band (2.0–7.0 keV). The brightest structure in a radial pattern at the lower left hand side is stray-light from LMC X-1. The bright red, namely soft sources, represent mostly SNRs, while blue, namely hard ones, represent X-ray binaries. With this image, you can clearly know which sources are classified into either of categories. It is obvious that the LMC contains many SNRs.

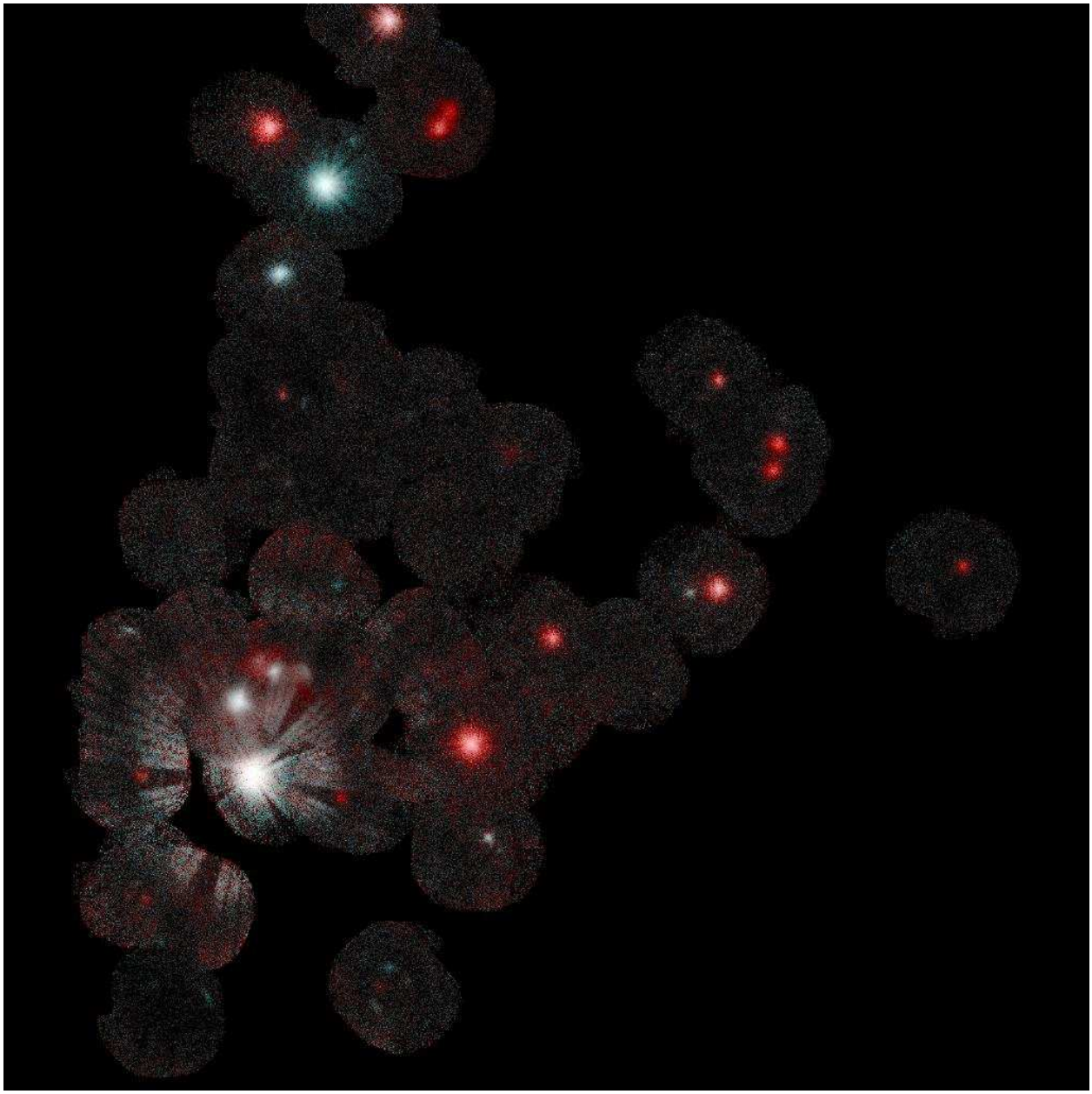

Figure D.1:

Bibliography

Allen, C. (1973). *"Astrophysical Quantities 3rd edition"*. London: Athlone.

Arnett, W. D. (1982, February). "Type I supernovae. I - Analytic solutions for the early part of the light curve". *Astrophys. J. 253*, 785–797.

Arnett, W. D., J. N. Bahcall, R. P. Kirshner, and S. E. Woosley (1989). "Supernova 1987A". *Ann. Rev. Astron. Astrophys. 27*, 629–700.

Arnett, W. D., D. Branch, and J. C. Wheeler (1985, March). "Hubble's constant and exploding carbon-oxygen white dwarf models for Type I supernovae". *Nature 314*, 337+.

Aschenbach, B., R. Egger, and J. Trumper (1995, February). "Discovery of Explosion Fragments Outside the VELA Supernova Remnant Shock-Wave Boundary". *Nature 373*, 587+.

Baade, W. & Zwicky, F. (1934). *Phys. Rev. 46*, 76+.

Bamba, A., J. Yokogawa, M. Sakano, and K. Koyama (2000, April). "Deep X-Ray Observations of Supernova Remnants G359.1-0.5 and G359.0-0.9 with ASCA". *Publ. Astron. Soc. Japan 52*, 259+.

Barbon, R., F. Ciatti, and L. Rosino (1973, November). "Light curves and characteristics of recent supernovae.". *Astron. Astrophys. 29*, 57+.

Bash, F. N., E. Green, and W. L. Peters (1977, October). "The galactic density wave, molecular clouds, and star formation". *Astrophys. J. 217*, 464–472.

Begelman, M. C. and C. L. Sarazin (1986, March). "SN 1985f - Death of a Wolf-Rayet star". *Astrophys. J. Letters 302*, L59–L62.

Bertelli, G., A. Bressan, C. Chiosi, M. Mateo, and P. R. Wood (1993, July). "The distance to the Large Magellanic Cloud - Constraints from Cepheids in Large Magellanic Cloud star clusters". *Astrophys. J. 412*, 160–172.

Blinnikov, S. I., V. S. Imshennik, and V. P. Utrobin (1982, December). "The Cygnus Superbubble as the remnant of a peculiar supernova". *Soviet Astronomy Letters 8*, 361–365.

Bocchino, F., J. Vink, F. Favata, A. Maggio, and S. Sciortino (2000, August). "A BeppoSAX and ROSAT view of the RCW86 supernova remnant". *Astron. Astrophys. 360*, 671–682.

Bomans, D. J., K. Dennerl, and M. Kurster (1994, March). "Diffuse X-Ray Emission from the Supergiant Shell Large Magellanic CLOUD-4 Detected with ROSAT". *Astron. Astrophys. 283*, L21–+.

Branch, D. (1986, January). "On the relative frequencies of the kinds of Type I supernovae". *Astrophys. J. Letters 300*, L51–L54.

Branch, D., R. Buta, S. W. Falk, M. L. McCall, A. Uomoto, J. C. Wheeler, B. J. Wills, and P. G. Sutherland (1982, January). "Interpretation of the maximum light spectrum of a Type I supernova". *Astrophys. J. Letters 252*, L61–L64.

Broeils, A. H. and H. van Woerden (1994, October). "A search for spiral galaxies with extended HI disks.". *Astron. Astrophys. Suppl. 107*, 129–176.

Chevalier, R. A. (1974, March). "The Evolution of Supernova Remnants. Spherically Symmetric Models". *Astrophys. J. 188*, 501–516.

Chevalier, R. A. and J. C. Raymond (1978, October). "Optical emission from a fast shock wave - The remnants of Tycho's supernova and SN 1006". *Astrophys. J. Letters 225*, L27–L30.

Chu, Y. (1997, May). "Supernova Remnants in OB Associations". *Astron. J. 113*, 1815+.

Chu, Y. and R. C. Kennicutt (1988a, April). "Echelle observations of supernova remnants in the Magellanic Clouds". *Astron. J. 95*, 1111–1121.

Chu, Y. and R. C. Kennicutt (1988b, December). "Environments and populations of supernova remnants in the Large Magellanic Cloud". *Astron. J. 96*, 1874–1883.

Chu, Y. and M. Mac Low (1990, December). "X-rays from superbubbles in the Large Magellanic Cloud". *Astrophys. J. 365*, 510–521.

Cox, D. P. (1972, November). "Cooling and Evolution of a Supernova Remnant". *Astrophys. J. 178*, 159–168.

Cox, D. P. and B. W. Smith (1974, May). "Large-Scale Effects of Supernova Remnants on the Galaxy: Generation and Maintenance of a Hot Network of Tunnels". *Astrophys. J. Letters 189*, L105–+.

De Vaucouleurs, G. and K. Freeman (1973). *Vistas Astron. (Pergamon Press, Oxford) 14*, 163+.

Dopita, M. A. (1977, April). "Optical Emission from Shock Waves. II. Diagnostic Diagrams". *Astrophys. J. Suppl. 33*, 437+.

Dopita, M. A. (1988). "The first nine months of SN 1987A - What have we learnt?". *Space Science Reviews 46*, 225–271.

Dotani, T. (1999). "ASCA sis calibration information. In:"A Catalogue of Galactic Supernova Remnants"". Technical report, ISAS.

Dotani, T., A. Yamashita, H. Ezuka, K. Takahashi, G. Crew, K. Mukai, and the SIS team (1997, April). "Recent Progress of SIS Calibration and Software". Technical Report 5, ISAS, MIT, NASA/GSFC.

Dufour, R. J. (1984, September). "The composition of H II regions in the Magellanic Clouds". In *IAU Symp. 108: Structure and Evolution of the Magellanic Clouds*, Volume 108, pp. 353–360.

Elias, J. H., K. Matthews, G. Neugebauer, and S. E. Pesson (1985, September). "Type I supernovae in the infrared and their use as distance indicators". *Astrophys. J. 296*, 379–389.

Falle, S. A. E. G. (1981, June). "Catastrophic cooling in supernova remnants". *Monthly Notices Roy. Astron. Soc. 195*, 1011–1028.

Falle, S. A. E. G. (1988). *"Supernova Remnants and the Interstellar Medium"*, Volume 101, pp. 419. Cambridge University Press.

Feast, M. (1999, July). "Cepheids as Distance Indicators". *PASP 111*, 775–793.

Fesen, R. A., W. P. Blair, and R. P. Kirshner (1985, May). "Optical emission-line properties of evolved galactic supernova remnants". *Astrophys. J. 292*, 29–48.

Filipovic, M. D., R. F. Haynes, G. L. White, P. A. Jones, U. Klein, and R. Wielebinski (1995, June). "A radio continuum study of the Magellanic Clouds. IV. Catalogues of radio sources in the Large Magellanic Cloud at 1.40, 2.45, 4.75, 4.85 and 8.55 GHz.". *Astron. Astrophys. Suppl. 111*, 311+.

Filipovic, M. D., G. L. White, P. A. Jones, W. Pietsch, R. F. Haynes, R. Wielebinski, and U. Klein (1996, May). "A Radio - X-ray comparison of sources in the Large Magellanic Clouds (LMC)". In *American Astronomical Society Meeting*, Volume 188, pp. 7702+.

Fink, H. H., I. Asaoka, W. Brinkmann, N. Kawai, and K. Koyama (1994, March). "The X-ray continuum of Tycho's remnant mearured with GINGA". *Astron. Astrophys. 283*, 635–641.

Gardiner, L. T. and M. Noguchi (1996, January). "N-body simulations of the Small Magellanic Cloud and the Magellanic Stream". *Monthly Notices Roy. Astron. Soc. 278*, 191–208.

Gardiner, L. T., T. Sawa, and M. Fujimoto (1994, February). "Numerical Simulations of the Magellanic System - Part One - Orbits of the Magellanic Clouds and the Global Gas Distribution". *Monthly Notices Roy. Astron. Soc. 266*, 567+.

Gaskell, C. M., E. Cappellaro, H. L. Dinerstein, D. R. Garnett, R. P. Harkness, and J. C. Wheeler (1986, July). "Type Ib supernovae 1983n and 1985f - Oxygen-rich late time spectra". *Astrophys. J. Letters 306*, L77–L80.

Girardi, L., C. Chiosi, G. Bertelli, and A. Bressan (1995, June). "Age distribution of LMC clusters from their integrated UBV colors: history of star formation.". *Astron. Astrophys. 298*, 87+.

Gull, S. F. (1973). "A numerical model of the structure and evolution of young supernovaremnants". *Monthly Notices Roy. Astron. Soc. 161*, 47+.

Haberl, F. and W. Pietsch (1999, October). "A ROSAT PSPC catalogue of X-ray sources in the LMC region". *Astron. Astrophys. Suppl. 139*, 277–295.

Harkness, R. P., J. C. Wheeler, B. Margon, R. A. Downes, R. P. Kirshner, A. Uomoto, E. S. Barker, A. L. Cochran, H. L. Dinerstein, D. R. Garnett, and R. M. Levreault (1987, June). "The early spectral phase of type Ib supernovae - Evidence for helium". *Astrophys. J. 317*, 355–367.

Hayashi, I. (1997). *"Systematic X-ray Spectroscopy of Supernova Remnants in the Magellanic Clouds"*. Ph. D. thesis, Kyoto University.

Hughes, J. P., I. Hayashi, and K. Koyama (1998, October). "ASCA X-Ray Spectroscopy of Large Magellanic Cloud Supernova Remnants and the Metal Abundances of the Large Magellanic Cloud". *Astrophys. J. 505*, 732–748.

Hughes, J. P. and K. P. Singh (1994, February). "Elemental abundances of the supernova remnant G292.0+1.8: Evidence for a massive progenitor". *Astrophys. J. 422*, 126–135.

Hughes, S. M. G., P. R. Wood, and N. Reid (1991, April). "Long-period variables in the Large Magellanic Cloud. III - Evidence of a kinematic spheroidal population". *Astron. J. 101*, 1304–1323.

Hwang, U. and E. V. Gotthelf (1997, February). "X-Ray Emission-Line Imaging and Spectroscopy of Tycho's Supernova Remnant". *Astrophys. J. 475*, 665+.

Hwang, U., J. P. Hughes, and R. Petre (1998, April). "The X-Ray Iron Emission from Tycho's Supernova Remnant". *Astrophys. J. 497*, 833+.

Ishisaki, Y. (1997). *"Spectra and Large-scale Isotropy of the Cosmic X-ray Background from ASCA Observations"*. Ph. D. thesis, Tokyo University.

Ishisaki, Y., Y. Ueda, H. Kubo, Y. Ikebe, K. Makishima, and the GIS team (1997, April). "Reproducibility of the GIS Non X-Ray Background". Technical Report 5, ISAS.

Kennicutt, R. C. (1984, February). "Constraints on the masses of supernova progenitors". *Astrophys. J. 277*, 361–366.

Kim, S. (1998, December). "An HI aperture synthesis mosaic survey of the Large Magellanic Cloud". In *American Astronomical Society Meeting*, Volume 193, pp. 2803+.

Kinugasa, K. and H. Tsunemi (1999, April). "ASCA Observation of Kepler's Supernova Remnant". *Publ. Astron. Soc. Japan 51*, 239–252.

Koyama, K., T. Ikegami, H. Inoue, N. Kawai, K. Makishima, M. Matsuoka, K. Mitsuda, T. Murakami, Y. Ogawara, T. Ohashi, K. Suzuki, Y. Tanaka, and I. Waki (1984).

"Performance verification of the gas scintillation proportional counters on board the TENMA satellite". *Publ. Astron. Soc. Japan 36*, 659–666.

Koyama, K., K. Kinugasa, K. Matsuzaki, M. Nishiuchi, M. Sugizaki, K. Torii, S. Yamauchi, and B. Aschenbach (1997, June). "Discovery of Non-Thermal X-Rays from the Northwest Shell of the New SNR RX J1713.7-3946: The Second SN 1006?". *Publ. Astron. Soc. Japan 49*, L7–L11.

Koyama, K., R. Petre, E. V. Gotthelf, U. Hwang, M. Matsura, M. Ozaki, and S. S. Holt (1995, November). "Evidence for Shock Acceleration of High-Energy Electrons in the Supernova Remnant SN:1006". *Nature 378*, 255+.

Kroupa, P. and U. Bastian (1997). "The HIPPARCOS proper motion of the Magellanic Clouds". *New Astronomy 2*, 77–90.

Kunieda, A., A. Furuzawa, M. Watanabe, and the ASCA XRT team (1995). Technical Report 3, ISAS, NASA/GSFC, Nagoya Univ.

Langer, N. and M. F. El Eid (1986, October). "The evolution of very luminous stars. I - Presupernova evolution". *Astron. Astrophys. 167*, 265–273.

Lasker, B. M. (1977, August). "Supernova remnants in the Large Magellanic Cloud - A photographic study in /O III/ and /S II/". *pasp 89*, 474–481.

Lasker, B. M. (1981, August). "Spectra and internal motions of supernova remnants and ring nebulae in the Magellanic Clouds". *PASP 93*, 422–427.

Leong, C., E. Kellogg, H. Gursky, H. Tananbaum, and R. Giacconi (1971, December). "X-Ray Emission from the Magellanic Clouds Observed by UHURU". *Astrophys. J. Letters 170*, L67–+.

Lequeux, J. (1989). *"Recent Developments of Magellanic Clouds Research"*, pp. 119+. edited by K.S.Boer, F. Spite, and G. Stasinska.

Long, K. S., D. J. Helfand, and D. A. Grabelsky (1981, September). "A soft X-ray study of the Large Magellanic Cloud". *Astrophys. J. 248*, 925–944.

Lozinskaia, T. A. (1980, April). "Kinematics of old supernova remnants". *Astron. Astrophys. 84*, 26–35.

Makishima, K., M. Tashiro, K. Ebisawa, H. Ezawa, Y. Fukazawa, S. Gunji, M. Hirayama, E. Idesawa, Y. Ikebe, M. Ishida, Y. Ishisaki, N. Iyomoto, T. Kamae, H. Kaneda, K. Kikuchi, Y. Kohmura, H. Kubo, K. Matsushita, K. Matsuzaki, T. Mihara, K. Nakagawa, T. Ohashi, Y. Saito, Y. Sekimoto, T. Takahashi, T. Tamura, T. Tsuru, Y. Ueda, and N. Y. Yamasaki (1996, April). "In-Orbit Performance of the Gas Imaging Spectrometer onboard ASCA". *Publ. Astron. Soc. Japan 48*, 171–189.

Mark, H., R. Price, R. Rodrigues, F. D. Seward, and C. D. Swift (1969, March). "Detection of X-Rays from the Large Magellanic Cloud". *Astrophys. J. Letters 155*, L143–+.

Masai, K. (1994, December). "Nonequilibria in thermal emission from supernova remnants". *Astrophys. J. 437*, 770–780.

Mathewson, D. (1985, April). "The Clouds of Magellan". *Scientific American 252*, 106–114.

Mathewson, D. S. and J. N. Clarke (1973, March). "Supernova remants in the Large Magellanic Cloud.". *Astrophys. J. 180*, 725–738.

Mathewson, D. S., M. N. Cleary, and J. D. Murray (1974, June). "The Magellanic stream". *Astrophys. J. 190*, 291–296.

Mathewson, D. S., V. L. Ford, M. A. Dopita, I. R. Tuohy, K. S. Long, and D. J. Helfand (1983, April). "Supernova remnants in the Magellanic Clouds". *Astrophys. J. Suppl. 51*, 345–355.

Mathewson, D. S., V. L. Ford, M. A. Dopita, I. R. Tuohy, B. Y. Mills, and A. J. Turtle (1984, June). "Supernova remnants in the Magellanic Clouds". *Astrophys. J. Suppl. 55*, 189–210.

Mathewson, D. S., V. L. Ford, I. R. Tuohy, B. Y. Mills, A. J. Turtle, and D. J. Helfand (1985, June). "Supernova remnants in the Magellanic Clouds. III". *Astrophys. J. Suppl. 58*, 197–200.

Maza, J. and S. van den Bergh (1976, March). "Statistics of extragalactic supernovae". *Astrophys. J. 204*, 519–529.

McCray, R. and M. Kafatos (1987, June). "Supershells and propagating star formation". *Astrophys. J. 317*, 190–196.

McKee, C. F. and L. L. Cowie (1977, July). "The evaporation of spherical clouds in a hot gas. II - Effects of radiation". *Astrophys. J. 215*, 213–225.

McKee, C. F. and J. P. Ostriker (1977, November). "A theory of the interstellar medium - Three components regulated by supernova explosions in an inhomogeneous substrate". *Astrophys. J. 218*, 148–169.

McKee, J. D., G. Fritz, R. G. Cruddace, S. Shulman, and H. Friedman (1980, May). "Soft X-ray sources in the bar of the Large Magellanic Cloud". *Astrophys. J. 238*, 93–97.

Meaburn, J. (1980, August). "The giant and supergiant shells of the Magellanic Clouds". *Monthly Notices Roy. Astron. Soc. 192*, 365–375.

Mills, B. Y., A. J. Turtle, A. G. Little, and J. M. Durdin (1984). "A new look at radio supernova remnants". *Australian Journal of Physics 37*, 321–357.

Miyaji, S. and K. Nomoto (1987, July). "On the collapse of 8-10 solar mass stars due to electron capture". *Astrophys. J. 318*, 307–315.

Miyaji, S., K. Nomoto, K. Yokoi, and D. Sugimoto (1980). "Supernova Triggered by Electron Captures". *Publ. Astron. Soc. Japan 32*, 303+.

Miyata, E. (1996). *"Spatially-Resolved X-ray Spectroscopy of the Cygnus Loop Supernova Remnant"*. Ph. D. thesis, Department of Earth Space Science, Faculity of Science, Osaka University.

Moore, B. and M. Davis (1994, September). "The Origin of the Magellanic Stream". *Monthly Notices Roy. Astron. Soc. 270*, 209+.

Murai, T. and M. Fujimoto (1980, September). "The Magellanic Stream and the Galaxy with massice halo". *Publ. Astron. Soc. Japan 32*, 581+.

Nomoto, K., F. . Thielemann, and K. Yokoi (1984, November). "Accreting white dwarf models of Type I supernovae. III - Carbon deflagration supernovae". *Astrophys. J. 286*, 644–658.

Ohashi, T., K. Ebisawa, Y. Fukazawa, K. Hiyoshi, M. Horii, Y. Ikebe, H. Ikeda, H. Inoue, M. Ishida, Y. Ishisaki, T. Ishizuka, S. Kamijo, H. Kaneda, Y. Kohmura, K. Makishima, T. Mihara, M. Tashiro, T. Murakami, R. Shoumura, Y. Tanaka, Y. Ueda, K. Taguchi, T. Tsuru, and T. Takeshima (1996, April). "The Gas Imaging Spectrometer on Board ASCA". *Publ. Astron. Soc. Japan 48*, 157–170.

Ostriker, J. P. and C. McKee (1988). Astrophysical blast waves. *Reviews of Modern Physics 60*, 1–68.

Pfeffermann, E., U. G. Briel, H. Hippmann, G. Kettenring, G. Metzner, P. Predehl, G. Reger, K. . Stephan, M. V. Zombeck, and J. Chappell (1987, February). "The focal plane instrumentation of the ROSAT telescope". *Presented at the Society for Photo-Optical Instrumentation Engineers (SPIE), Berlin, West Germany, Dec. 1986 87*, 28474+.

Piestch, W. and P. Kahabka (1993). *"New Aspects of Magellanic Clouds Research; ed. Baschek, B. Klare, G. and Lequeux, J."*, Volume 416. Lecture Notes in Physics.

Points, S., Y.-H. Chu, S. Snowden, and L. Staveley-Smith (2000). "The Supergiant Shell LMC2: II. Physical Properties of the 10^6 K Gas". *Astrophys. J.*.

Porter, A. C. and A. V. Filippenko (1987, June). "The observational properties of type 1b supernovae". *Astron. J. 93*, 1372–1380.

Putman, M., B. Gibson, L. Staveley-Smith, G. Banks, D. Barnes, M. Bhatal, R.and Disney, R. Ekers, K. Freeman, R. Haynes, P. Henning, H. Jerjen, V. Kilborn, B. Koribalski, P. Knezek, D. Malin, T. Mould, J.R.and Oosterloo, R. Price, S. Ryder, E. Sadler, I. Stewart, F. Stootman, R. Vaile, R. Webster, and A. Wright (1998, August). "Tidal disruption of the Magellanic Clouds by the Milky Way". *Nature 394*, 752+.

Rappaport, S., A. Levine, R. Doxsey, and H. V. Bradt (1975, February). "Soft X-ray survey of the Large Magellanic Cloud". *Astrophys. J. Letters 196*, L15–L18.

Raymond, J. C. (1979, January). "Shock waves in the interstellar medium". *Astrophys. J. Suppl. 39*, 1–27.

Raymond, J. C. (1984). Observations of supernova remnants. *Ann. Rev. Astron. Astrophys. 22*, 75–95.

Rohlfs, K., J. Kreitschmann, J. V. Feitzinger, and B. C. Siegman (1984, August). "A neutral hydrogen line survey of the Large Magellanic Cloud". *Astron. Astrophys. 137*, 343–357.

Rosado, M. (1986, May). "An empirical study of ring-shaped nebulae in the Galaxy and in the LMC". *Astron. Astrophys. 160*, 211–228.

Russell, S. C. and M. A. Dopita (1992, January). "Abundances of the heavy elements in the Magellanic Clouds. III - Interpretation of results". *Astrophys. J. 384*, 508–522.

Sasaki, M., F. Haberl, and W. Pietsch (2000, May). "ROSAT HRI catalogue of X-ray sources in the LMC region". *Astron. Astrophys. Suppl. 143*, 391–403.

Schwering, P. B. W. and F. P. Israel (1991, June). "Foreground dust and gas and the extinction curve of the Large Magellanic Cloud". *Astron. Astrophys. 246*, 231–242.

Sedov, L. (1959). *"Similarity and Dimensional Methods in Mechanics"*. New York: Achademic Press.

Serlemitsos, P. J., L. Jalota, Y. Soong, H. Kunieda, Y. Tawara, Y. Tsusaka, H. Suzuki, Y. Sakima, T. Yamazaki, H. Yoshioka, A. Furuzawa, K. Yamashita, H. Awaki, M. Itoh, Y. Ogasaka, H. Honda, and Y. Uchibori (1995, February). "The X-ray telescope on board ASCA". *Publ. Astron. Soc. Japan 47*, 105–114.

Shklovskii, I. (1960). *Sov. Astron. 4*, 355.

Shklovskii, I. (1962). *Sov. Astron. 6*, 162.

Smith, R. C., R. P. Kirshner, W. P. Blair, and P. F. Winkler (1991, July). "Six Balmer-dominated supernova remnants". *Astrophys. J. 375*, 652–662.

Snowden, S. L. and R. Petre (1994, December). "An X-ray image of the large magellanic cloud". *Astrophys. J. Letters 436*, L123–L126.

Sofue, Y. (1994, August). "Fate of the Magellanic Stream". *Publ. Astron. Soc. Japan 46*, 431–440.

Spitzer, L. (1978). *"Physical Process in the Interstellar Medium"*. Wiley-Interscience.

Tanaka, Y., H. Inoue, and S. S. Holt (1994, June). "The X-ray astronomy satellite ASCA". *Publ. Astron. Soc. Japan 46*, L37–L41.

Tinsley, B. (1977). in Supernovae, ed. D.N.Schramm. Dordrecht: Reidel.

Tinsley, B. M. (1975, December). "What stars become supernovae". *PAS 87*, 837–848.

Tomida, H., H. Matsumoto, M. Ozaki, Y. Tazawa, H. Awaki, T. Tsuru, K. Koyama, H. Tsunemi, and K. Yamamoto (1997, June). "Radiation Damage on X-Ray CCDs and Restoration Technique for Space Astronomy". *Publ. Astron. Soc. Japan 49*, 405–412.

Trüemper, J. (1982). "The ROSAT mission". *Advances in Space Research 2*, 241–249.

Tsujimoto, T., K. Nomoto, Y. Yoshii, M. Hashimoto, S. Yanagida, and F. . Thielemann (1995, December). "Relative frequencies of Type Ia and Type II supernovae in the chemical evolution of the Galaxy, LMC and SMC". *Monthly Notices Roy. Astron. Soc. 277*, 945–958.

Tsunemi, H., E. Miyata, and B. Aschenbach (1999, October). "Spectroscopic Study of the Vela-Shrapnel". *Publ. Astron. Soc. Japan 51*, 711+.

Tuohy, I. R., M. A. Dopita, D. S. Mathewson, K. S. Long, and D. J. Helfand (1982, October). "Optical identification of Balmer-dominated supernova remnants in the Large Magellanic Cloud". *Astrophys. J. 261*, 473–484.

Turner, T. J. and K. A. Pounds (1989, October). "The EXOSAT spectral survey of AGN". *Monthly Notices Roy. Astron. Soc. 240*, 833–880.

Ueda, Y. (1996). *"ASCA studies of faint X-ray soueces and the relation to the cosmic X-ray background"*. Ph. D. thesis, , Univ. Tokyo, (1996).

Van den Heuvel, E. and S. Rappaport (1987). *"in Physics of Be stars"*. ed. A. Slettebak, T.P. Snow.

Vink, J., J. S. Kaastra, and J. A. M. Bleeker (1996, March). "A new mass estimate and puzzling abundances of SNR Cassiopeia A.". *Astron. Astrophys. 307*, L41–L44.

Wang, Q., T. Hamilton, D. J. Helfand, and X. Wu (1991, June). "The detection of X-rays from the hot interstellar medium of the Large Magellanic Cloud". *Astrophys. J. 374*, 475–495.

Wang, Q. and D. J. Helfand (1991, June). "The detection of X-ray emission from the OB associations of the Large Magellanic Cloud". *Astrophys. J. 373*, 497–508.

Wheeler, J. C. and R. P. Harkness (1987, November). "Helium-rich supernovas". *Scientific American 257*, 50–58.

Wheeler, J. C., R. P. Harkness, E. S. Barker, A. L. Cochran, and D. Wills (1987, February). "Supernovae 1983i and 1983v - Evidence for abundance variations in type Ib supernovae". *Astrophys. J. Letters 313*, L69–L73.

Williams, R. M., Y. Chu, J. R. Dickel, R. Beyer, R. Petre, R. C. Smith, and D. K. Milne (1997, May). "Supernova Remnants in the Magellanic Clouds. I. The Colliding Remnants DEM L316". *Astrophys. J. 480*, 618+.

Williams, R. M., Y. Chu, J. R. Dickel, R. Petre, R. C. Smith, and M. Tavarez (1999, August). "Supernova Remnants in the Magellanic Clouds. III. an X-Ray Atlas of Large Magellanic Cloud Supernova Remnants". *Astrophys. J. Suppl. 123*, 467–485.

Williams, R. M., Y. Chu, J. R. Dickel, R. C. Smith, D. K. Milne, and P. F. Winkler (1999, April). "Supernova Remnants in the Magellanic Clouds. II. Supernova Remnant Breakouts from N11L and N86". *Astrophys. J. 514*, 798–817.

Woosley, S. (1990). *"in Supernovae ed. A.G. Petschek"*. New York: Springer-Verlag.

Yamashita, A. (1995). "The calibration in orbit of the X-ray CCD camera onboard ASCA (Japanese)". Master's thesis, Tokyo University.

Yamashita, A. (1998). *"Study of the Origin of the Cosmic X-ray Background from ASCA Deep Sky Observations"*. Ph. D. thesis, Tokyo University.

Yokogawa, J., K. Imanishi, M. Tsujimoto, M. Nishiuchi, K. Koyama, F. Nagase, and R. H. D. Corbet (2000, June). "A Study of the Populations of X-Ray Sources in the Small Magellanic Cloud with ASCA". *Astrophys. J. Suppl. 128*, 491–509.

Yun, M. S., P. T. P. Ho, and K. Y. Lo (1994, December). "A High-Resolution Image of Atomic Hydrogen in the M81 Group of Galaxies". *Nature 372*, 530+.

Acknowledgments

First of all, I am deeply grateful to my supervisor, Prof. K. Koyama for his continual guidance, advice and support throughout my graduate career. His patience and sometimes strict guidance led me to complete this work.

I express my thanks to Dr. I. Hayashi and Prof. J.P. Hughes, who carried out part of the systematic study of LMC SNR samples, the results of them are so amazing and wonderful. Prof. J.P. Hughes, especially, kindly gave me advices and suggestions on the LMC SNRs, which were so useful and helpful to me.

I am also greteful to my collaborators, Mr. J. Yokogawa, Mr. K. Imanishi and Mr. M. Tsujimoto, for their helpful discussion and also for providing useful softwares on the data analyses.

I greatly appreciate for Dr. R.N. Williams, who was a referee of my PASJ paper on DEM L316. She kindly read through my paper and gave me many useful comments. Her quick response was so helpful to me! Also I learned much from her work on the LMC SNRs from morphological approach, which was wonderfully summarized in her PhD thesis and many papers.

I also thank all the members of the Cosmic-ray laboratory in Kyoto University for the daily discussion and insightful comments, as well as for the kind and heartful attitude to me.

I express my gratitude to all the members of the ASCA team for their support of this study. All the observational data were obtained by the members of the ASCA team. I also thank to Dr. Ken Ebisawa and his family for their hospitality during my visit to GSFC/NASA in U.S.A..

I was financially supported by the Japan Society for the Promotion of Science.

Finally I express supreme thanks to my family, especially for my parents. They have provided me not only financial but also unstinted emotional support.